NUMERICAL SIMULATION OF FLOW SEPARATION CONTROL BY OSCILLATORY FLUID INJECTION

A Dissertation

by

CELERINO RESENDIZ ROSAS

Submitted to the Office of Graduate Studies of
Texas A&M University
in partial fulfillment of the requirements for the degree of

DOCTOR OF PHILOSOPHY

May 2005

Major Subject: Aerospace Engineering

NUMERICAL SIMULATION OF FLOW SEPARATION CONTROL

BY OSCILLATORY FLUID INJECTION

A Dissertation

by

CELERINO RESENDIZ ROSAS

Submitted to Texas A&M University
in partial fulfillment of the requirements
for the degree of

DOCTOR OF PHILOSOPHY

Approved as to style and content by:

Paul Cizmas (Chair of Committee)	
Othon K. Rediniotis (Member)	Leland A. Carlson (Member)
Ali Beskok (Member)	Helen L. Reed (Head of Department)

May 2005

Major Subject: Aerospace Engineering

ABSTRACT

Numerical Simulation of Flow Separation Control
by Oscillatory Fluid Injection. (May 2005)
Celerino Resendiz Rosas, B.S., Instituto Politecnico Nacional, Mexico;
M.S., Instituto Politecnico Nacional, Mexico
Chair of Advisory Committee: Dr. Paul Cizmas

In this work, numerical simulations of flow separation control are performed. The separation control technique studied is called "synthetic jet actuation". The developed code employs a cell centered finite volume scheme which handles viscous, steady and unsteady compressible turbulent flows. The pulsating zero mass jet flow is simulated by imposing a harmonically varying transpiration boundary condition on the airfoil's surface. Turbulence is modeled with the algebraic model of Baldwin and Lomax.

The application of synthetic jet actuators is based in their ability to energize the boundary layer, thereby providing significant increase in the lift coefficient. This has been corroborated experimentally and it is corroborated numerically in this research.

The performed numerical simulation investigates the flow over a NACA0015 airfoil. For this flow $Re = 9 \times 10^5$ and the reduced frequency and momentum coefficient are $F^+ = 1.1$ and $C_\mu = 0.04$ respectively. The oscillatory injection takes place at 12.27% chord from the leading edge. A maximum increase in the mean lift coefficient of 93% is predicted by the code. A discrepancy of approximately 10% is observed with corresponding experimental data from the literature. The general trend is, however, well captured. The discrepancy is attributed to the modeling of the injection boundary condition and to the turbulence model.

A sensitivity analysis of the lift coefficient to different values of the oscillation

parameters is performed. It is concluded that tangential injection, $F^+ \approx \mathrm{O}(1)$ and the utilized grid resolution around the site of injection are optimal. Streamline fields obtained for different angles of injection are analyzed. Flow separation and attachment as functions of the injection angle and of the velocity of injection can be observed.

It is finally concluded that a reliable numerical tool has been developed which can be utilized as a support tool in the optimization of the synthetic jet operation and in the modeling of its operation.

A mis padres, Rosa M. Rosas D. y J. Bernabé Reséndiz C.

A mi esposa Angélica M. Chávez Hernández.

A mis adoradas hijas, Ariane C. y Aimée C. Reséndiz Chávez.

A la memoria de mi hijo Jesús Orlando Reséndiz Chávez.

A mi hermana Laura Reséndiz Rosas y a su distinguida familia.

ACKNOWLEDGMENTS

I would like to thank Dr. Paul Cizmas, the chairman of my advisory committee, for his friendship, guidance, support and patience throughout my Ph.D. studies. I also would like to thank all of the faculty and staff of Texas A&M University who, in many ways, helped me all these years.

Special thanks to my wife Angélica Chávez H. for her endless love, patience and for the care she takes of our small, happy family. I wish to thank my parents, Rosa M. Rosas D. and J. Bernabé Reséndiz C. for their continued and enormous support, specially during the final steps of my stay at Texas A&M University. I also would like to thank my sister, Laura Reséndiz R. and her husband, Ariosto Andrade R., for all the help and support they provided throughout these years.

I want to thank my life-long best friend, J. Martín Reséndiz R. and his fine family for the precious help they provided all these years. Thanks to all of my friends who reside and work in the U.S. and who, at some point during my journey, provided valuable help. Furthermore, I'd like to thank my fellow graduate students Yuan Tao, Kyusup Kim and Joaquin Gargoloff for their friendship and valuable assistance.

And last, but not least, I would like to thank CONACYT of Mexico for its important financial support during my doctoral studies. Likewise, my gratitude goes to the Secretaría de Educación Pública (SEP) of Mexico for the financial support provided.

TABLE OF CONTENTS

CHAPTER Page

CHAPTER Page

LIST OF TABLES

LIST OF FIGURES

FIGURE Page

FIGURE Page

FIGURE Page

FIGURE Page

FIGURE Page

CHAPTER I

INTRODUCTION

The ability to actively or passively manipulate a flowfield to effect a desired change is of immense technological importance. The term boundary layer control includes any mechanism or process through which the boundary layer of a fluid flow is made to behave differently than it would normally do were the flow developing naturally along a smooth, flat surface. A boundary layer could be manipulated to achieve transition delay, separation postponement, lift enhancement, drag reduction, turbulence augmentation or noise reduction.

Active and passive flow control of separated flow over cylinders and airfoils at high incidences or in dynamic motion has been subject of experimental and theoretical investigation for the past decades. Application of passive and active flow controls in numerous experimental investigations (e.g. [1][2]) has demonstrated the potential of obtaining significant improvements in aerodynamic performance. Recently, control of separated flows with pulsating jets [3] yielded very encouraging results. Advances in smart, compact flow actuation, such as synthetic jets opened new horizons in flow actuation which can lead to significant improvement in aerodynamic performance of existing configurations.

In spite of all the positive progress, a through understanding of the flow over bodies at high angles of attack and its control is still lacking due to the complexity of such flows. These flowfields are inherently unsteady and no simple analytical theory is possible so far. Therefore, a full clarification of the mechanisms of unsteady control is highly desirable, which heavily relies on careful numerical simulations and

---

The journal model is *IEEE Transactions on Automatic Control.*

detailed experimental flowfield surveys. This research focuses therefore, on the code development of a tool for performing numerical simulations of this complex, unsteady flowfields.

A. Flow Separation: The Problem

Flow separation is generally accepted to be the breakaway or detachment of the fluid from a solid surface. Whether caused by a severe pressure gradient, a geometric discontinuity or by any other means, separation is generally accompanied by a significant thickening of the rotational flow region adjacent to the surface and by a significant increase in the velocity component normal to the surface. Therefore, the boundary layer assumptions do not longer apply for this regime.

Separation is almost always associated with losses of some kind, including, but not limited to, loss of lift, increase of drag and pressure recovery losses. Consequently, engineers have been preoccupied with altering the separation location or entirely avoiding it for over a century now.

B. Traditional Boundary Layer Control

A multitude and variety of hydro and aerodynamic vehicles and devices bear testimony to the tremendous advances that have been made in the development of means that avoid or modify separation. These, however, have relied on traditional boundary layer control methods which are based in the old traditional assumption of the steady flow.

Traditional boundary layer control methods involve the injection or suction of large amounts of mass in a steady fashion. Ailerons, flaps and slats prominently displayed on today's aircraft are example of successful implementations of traditional

boundary layer control methods. They are effective but they are also complex, costly, cumbersome and heavy.

The contributions in boundary layer control up to the early 1960's is compiled in the two volumes edited by Lachmann [4] which provide an exhaustive treatment of theoretical, experimental as well as applied boundary layer control methods. The contributions indicated that steady blowing or suction on a wing and on various configurations can produce significant increases in lift as well as reductions in drag. However, these boundary layer control methods fell far short of the high expectations on the 1960's because of two reasons. First, the plumbing system required for the boundary layer control introduced excessive technical complexity and weight, and second, the systems were not efficient, requiring auxiliary compressors or excessive compressor bleed in order to obtain meaningful lift enhancement ([4], pp. 463-515).

C. Flow Control by Excitation

Experimental data reveals that separation is only steady in a time-averaged sense while the rich time dependence coherence is acknowledged but not exploited [5]. There is overwhelming evidence that periodic excitation is an effective way of flow separation control (see e.g. [6] pp. 178-182 and references therein, [1], [2], [3], [7]). The unsteady control by periodic addition of momentum can attain the same degree of control authority that is achieved by traditional control methods [8], with two important differences: the cost, in terms of momentum input, and implementation simplicity.

Consider a maneuverable aircraft with no large moving parts or control surfaces; or a conical diffuser whose divergence angle exceeds 45 degrees; or a thrush vectored jet without vectoring nozzles. All of these are possible by adding periodic motion to the flow rather than traditional boundary layer control methods.

The breakthrough in flow control by excitation was the discovery that periodic perturbations in a laminar boundary layer trigger a known instability, i.e., initiate Tollmien-Schlichting waves [9]. This was employed for studying flow stability but it was also considered a tool for controlling laminar separation and transition. Since periodic perturbations trigger a premature transition to turbulence and a turbulent flow is less susceptible to separation, flow separation could be delayed by initiating transition.

Sound was initially employed to demonstrate these ideas on airfoils at low Reynolds numbers [10]. Laminar-turbulent transition could be effected and yet, the manipulation of turbulent shear flows was traditionally thought unattainable because of the belief that turbulence is a random process, largely determined by local flow conditions. However, experiments in the mixing layer [11] demonstrated that large coherent structures are primarily responsible for the transport of momentum across the flow domain.

Excitation accelerates and regulates the generation of large coherent structures, particularly when the flow is unstable, thereby transferring high momentum across the mixing layer. It has been shown that a turbulent mixing layer can be attached to a deflected surface [12] and that the ensuing attached flow separation could be delayed by periodic addition of momentum with or without the concomitant addition of mass flux [13]. The same concept has been applied to airfoils [14] as well to other applications. This method was shown to be more effective than the traditional steady blowing and at times attained a saving of two orders of magnitude in the momentum coefficient required to achieve a prescribed improvement in performance. The actuators required may thus be autonomous, small, light, energy efficient and decoupled from the main propulsive system –thereby overcoming all of the deficiencies of traditional boundary layer control methodologies.

To date, acoustic or hydrodynamic flow separation control has been demonstrated in a wide variety of relatively simple configurations (flows over a backward-facing steps and ramps, bluff bodies, various airfoils, circular cylinders, etc.). These studies laid the groundwork for a wide variety of potential future applications to both fixed wing as well as rotary wing aircraft.

1. Synthetic Jet Actuation

Synthetic jet flow control devices [3][15] (or synthetic jet actuators, SJA) employ membranes or springboards which are driven to resonance piezoelectrically or mechanically by motors and enhance the momentum of the boundary layer by zero mass vortical flow. Synthetic jets were successfully used to control flow separation of low Reynolds number incompressible flow [3]. The oscillatory jet adds momentum to the boundary layer in two ways. During the suction part of the cycle it draws the low momentum fluid in the boundary layer inside the cavity, thereby bringing the higher momentum fluid, at the boundary layer edge, near the control surface. On the other hand, during the blowing part of the cycle, it adds the same fluid with higher momentum to the flow. The average effective momentum added over the entire cycle replenishes the momentum deficit in the boundary layer. This added momentum enhances the ability of the boundary layer to overcome adverse pressure gradients downstream through the mixing it induces of the low momentum fluid near the surface with the high momentum external flow. The effectiveness of this mixing is expected to relate to the high receptivity of the shear layer emanating from the point of separation. Proper excitation of the shear layer promotes the development of its natural instability, which leads to the formation of large vortical coherent structures. These flow structures in turn promote boundary layer mixing and hence momentum exchange between the outer and inner parts of the boundary layer.

D. Computational Fluid Dynamics

Numerical investigations of post-stall flow control have been undertaken by Wu *et al.* [16] [17]. They used the Reynolds-averaged Navier-Stokes (RANS) approach on a NACA-0012 airfoil with the Baldwin-Lomax algebraic turbulence model [18]. Using periodic blowing and suction normal to the surface at 2.5% chord from the leading edge, they found that lift increase in the post-stall regime can be achieved as was reported in experiments. A variety of forcing frequencies that were harmonics of the shedding frequencies were considered.

In another numerical experiment of flow control on a NACA0012 airfoil, Hassan and JanakiRam [19] also used the RANS approach with the Baldwin-Lomax turbulence model. Using a zero net-mass suction and blowing over nearly 13% chord, they found that, with the careful selection of peak amplitude and oscillation frequency, the lift can be incresed. Direct comparison with experiment was not made in these computations.

Donovan [20] performed simulations of steady and pulsating jet flow controls. McCormick [7] developed a new concept "directed synthetic jet actuator" for boundary layer separation control. The blowing slot of this jet is curved in the downstream direction. The jet energizes the boundary layer and makes it, in the time average more resistant to separation. Calculated coefficients of the "directed synthetic jet" for airfoil static stall control [7] were in agreement with the experiment. In the present investigation, the jet exit velocity is also prescribed in a direction almost tangential to the airfoil surface.

E. Objectives, Scope and Layout

In spite of all the positive progress, briefly reviewed so far, a through understanding of the wing flow at high angles of attack and its control is still lacking due to the complexity of such flows. At such angles of attack, shear layers shed from both the leading edge and trailing edge of the wing, roll up into mutually interacting vortices [16]. Secondary and tertiary separations from the mid portion of the upper surface may also be induced. All these make the flowfield inherently unsteady and no simple analytical theory is possible. Therefore, a full clarification of the mechanisms of post-stall lift enhancement by unsteady controls is highly desirable, which heavily relies on careful numerical simulations and detailed experimental flowfield surveys.

Motivated by these needs, a series of two dimensional Navier-Stokes computations on NACA0012 and NACA0015 airfoils were undertaken to test the separation control capabilities of synthetic jet actuators. The effect of the actuators on the lift characteristics of the airfoils is investigated. Actuator location, frequency and level of forcing are examined. A close look into the controlled and uncontrolled flow fields reveals many features and physical mechanisms which cannot be obtained via experimentation.

The dissertation's layout is as follows. Chapter I highlights the need of performing numerical simulations on synthetic jet actuated flows, provides some general background information and gives a brief up-to-date review on the current status of flow separation control.

Chapter II discusses the equations that govern compressible, Newtonian fluid flows; these equations are presented in their integral, conservation form since the code developed in this research requires this form of the governing equations, as discussed next.

Chapter III offers a very detailed description of the code development stage of this research. Two codes were developed. One code was employed for the steady state computations (required to obtain the start-up flowfields for the unsteady simulations) and the other code code was developed to handle the unsteady computations. The codes can handle viscous/inviscid, steady/unsteady turbulent, compressible flows. The integral, conservation form of the full Navier-Stokes equations are discretized employing a cell centered finite volume formulation. Turbulence is modeled employing the Baldwin-Lomax algebraic model. For the steady computations, a variable, explicit time stepping methodology was employed[1] while for the unsteady case, a fully implicit method was implemented.

The boundary conditions employed in this research are standard with the exception of the condition at the site of oscillatory injection. The boundary condition at the site of injection is implemented as an alteration of the no-slip boundary condition that is conventionally employed for walls in viscous flows. Thus, in this research, consistently with oscillatory actuation, unsteady suction and blowing through the wall is modeled as a simple analytic function.

Grid generation was part of this work as well. A C-grid, highly clustered toward the airfoil surface (a viscous grid) was built. The grid is normal to the airfoil's surface. The presented results correspond to a grid with its outer boundary located at approximately 12 chords from the airfoil. For the injection cases, clustering around the injection site was included.

Chapter IV deals with the validation stage of the code developed in this research. Validation is achieved by direct comparison with experimental data and with results from other numerical simulations. Lift and pressure coefficients are compared. Con-

[1]Convergence is accelerated by employing a variable time step methodology.

vergence is closely monitored for all runs performed in this research. For the unsteady runs, comparison with experimental data was performed. Also, a grid convergence test on the site of injection site was performed.

Chapter V gives a broader discussion on flow separation fundamentals and on the physics of flow separation control achieved by the synthetic jet actuators. A discussion on the key parameters for the actuation is presented. In this chapter the numerical results of the simulations performed are presented and discussed. Results of a sensitivity analysis on the key parameters are discussed.

In Chapter VI the work presented in the dissertation is summarized, conclusions are drawn and recommendations for future work are provided.

CHAPTER II

FUNDAMENTAL EQUATIONS OF COMPRESSIBLE VISCOUS FLOW

The laws governing the unsteady motion of compressible Newtonian fluids are well established and can be formulated from the observation that the behavior of a physical system is completely determined by conservation laws. The general conservation laws for scalar and vector quantities are reviewed in this chapter. The conservation laws for mass, momentum and energy are then presented. The integral form for these laws is formulated and used throughout this dissertation. Use of the integral conservation form of the basic quantities in the numerical discretization leads to a numerical scheme that is conservative as well.

A. Conservation Principles

The concept of conservation, as mentioned above, means that the variation of a conserved (intensive) flow quantity within a given volume Ω is due to the net effect of some internal sources Q_V and of the amount of the quantity which is crossing the boundary surface $\partial\Omega$. The latter is called the flux $\vec{F}$ and its expression results from the mechanical and thermodynamical properties of the fluid.

When the studied quantity is a scalar (e.g., mass) the associated flux is a vector and when the quantity is a vector (e.g., momentum) the flux is a tensor[1]. The fluxes are generated from two contributions: one due to the convective transport of the fluid and another due to the molecular motion. Therefore, the flux vector $\vec{F}$ contains two components: a convective part $\vec{F}_C$ and a diffusive contribution $\vec{F}_D$. The latter, when present, is always active, even when the fluid is at rest.

[1]For a review on tensors see, e.g., [21].

The contribution due to molecular motion acts as a diffusive effect since differences in the intensity of the quantity being considered create a transfer in space (even for fluids at rest) such as to reduce the non-homogeneity. This contribution is proportional to the gradient of the corresponding quantity, such that it vanishes for homogeneous distributions.

It is important to notice that for a fluid at rest no diffusion of specific mass is possible since any variation of specific mass implies a displacement of fluid particles (convective transport). Therefore, there is no diffusive flux contribution to the mass conservation equation as it will be seen later. Furthermore, it is also assumed that no diffusion of momentum is possible in a fluid at rest, then there is no diffusive flux contribution to the momentum conservation equation either.

B. General Form of a Conservation Law

1. Scalar Conservation Law

Consider a scalar quantity per unit volume U, acting in an arbitrary volume Ω fixed in space and bounded by a closed surface $\partial\Omega$ (see Figure 1). The local intensity of U varies through the effect of fluxes $\vec{F}$, which express the contributions from the surrounding points to the local value, and through sources Q.

Thus, the general form of a conservation law follows from the statement that the variation per unit time of the quantity U within a volume Ω,

$$\frac{\partial}{\partial t}\int_{\Omega} U\, dV,$$

should be equal to the net contribution from the incoming fluxes $\vec{F}$ through the

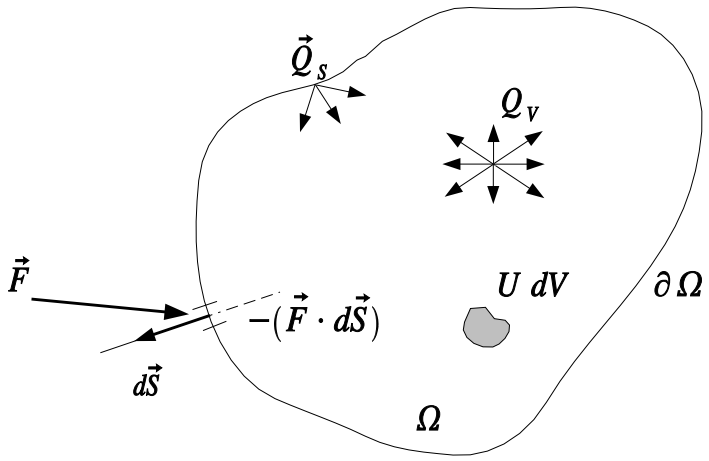

Fig. 1.: General form of a conservation law for a scalar quantity.

surface $\partial\Omega$ (with a surface element vector pointing outward $d\vec{S}$),

$$-\oint_{\partial\Omega} \vec{F}\cdot d\vec{S},$$

plus contributions from the sources of the quantity U. These sources can be divided into volume and surface sources, Q_V and $\vec{Q}_S$ respectively. Their total contribution is

$$\int_\Omega Q_V\,dV + \oint_{\partial\Omega} \vec{Q}_S\cdot d\vec{S}.$$

Hence, the general form of the conservation equation for the quantity U is

$$\frac{\partial}{\partial t}\int_\Omega U\,dV = -\oint_{\partial\Omega} \vec{F}\cdot d\vec{S} + \int_\Omega Q_V\,dV + \oint_{\partial\Omega} \vec{Q}_S\cdot d\vec{S}. \tag{2.1}$$

An essential aspect of the conservation law (2.1) lies in the observation that the internal variations of U, in the absence of volume sources, depend only on contributions through the surface $\partial\Omega$ (surface fluxes and sources) and not on the flux values inside the volume Ω.

Separation of the flux vector into convective and diffusive components gives a

more precise form of the equation

$$\frac{\partial}{\partial t}\int_{\Omega} U\,dV = -\oint_{\partial\Omega}\vec{F}_C\cdot d\vec{S} - \oint_{\partial\Omega}\vec{F}_D\cdot d\vec{S} + \int_{\Omega} Q_V\,dV + \oint_{\partial\Omega}\vec{Q}_S\cdot d\vec{S}. \tag{2.2}$$

$\vec{F}_C$ is the convective part of the flux vector and it is defined as the amount of the quantity U that is transported by a flow with velocity $\vec{v}$; that is,

$$\vec{F}_C = \vec{v}U.$$

The diffusive flux $\vec{F}_D$, on the other hand, is defined as a contribution present in fluids at rest, due to the molecular, thermal agitation. The final form of this term is individually presented for each conservation law in the following sections. The general form of the conservation law for the quantity U is then

$$\frac{\partial}{\partial t}\int_{\Omega} U\,dV = -\oint_{\partial\Omega} U\vec{v}\cdot d\vec{S} + \oint_{\partial\Omega}\vec{F}_D\cdot d\vec{S} + \int_{\Omega} Q_V\,dV + \oint_{\partial\Omega}\vec{Q}_S\cdot d\vec{S}. \tag{2.3}$$

Let V denote the volume of the domain Ω; the scalar quantity in the system is then UV (recall U is the scalar quantity in the system per unit volume). Let m denote the mass in the system, then the scalar quantity per unit mass, denoted by u, is $u = UV/m$. Since the density of the fluid is $\rho = m/V$, it follows then that $u = U/\rho$, from where

$$U = u\rho.$$

Thus, the general form of the conservation law, equation (2.3), in terms of u is

$$\frac{\partial}{\partial t}\int_{\Omega} \rho u\,dV = -\oint_{\partial\Omega} \rho u\vec{v}\cdot d\vec{S} + \oint_{\partial\Omega}\vec{F}_D\cdot d\vec{S} + \int_{\Omega} Q_V\,dV + \oint_{\partial\Omega}\vec{Q}_S\cdot d\vec{S} \tag{2.4}$$

Note that in equation (2.3) U is the scalar quantity per unit volume while in equation (2.4) u represents the scalar quantity per unit mass.

2. Vector Conservation Law

If the conserved property is described by the vector quantity per unit volume $\vec{U}$ then the flux and the surface sources become tensors, $\overline{\overline{F}}$ and $\overline{\overline{Q}}_S$ respectively. The volume source term becomes a vector $\vec{Q}_V$ and the conservation equation (2.2) is now

$$\frac{\partial}{\partial t}\int_\Omega \vec{U}\,dV = -\oint_{\partial\Omega} \overline{\overline{F}}_C \cdot d\vec{S} - \oint_{\partial\Omega} \overline{\overline{F}}_D \cdot d\vec{S} + \int_\Omega \vec{Q}_V\,dV + \oint_{\partial\Omega} \overline{\overline{Q}}_S \cdot d\vec{S}. \tag{2.5}$$

The convective component of the flux tensor in this case is given by

$$\overline{\overline{F}}_C = \vec{v} \otimes \vec{U}, \tag{2.6}$$

where the symbol $\otimes$ denotes a tensor product operation[2]. The general form of the conservation law for the quantity $\vec{U}$ is then

$$\frac{\partial}{\partial t}\int_\Omega \vec{U}\,dV = -\oint_{\partial\Omega} \vec{v} \otimes \vec{U} \cdot d\vec{S} + \oint_{\partial\Omega} \overline{\overline{F}}_D \cdot d\vec{S} + \int_\Omega \vec{Q}_V\,dV + \oint_{\partial\Omega} \overline{\overline{Q}}_S \cdot d\vec{S}. \tag{2.7}$$

The general scalar and vector forms (equations (2.3) and (2.7)) are considered as the basic formulation of a conservation law and are indeed the most generally valid expressions, since they remain valid even in the presence of discontinuous variations of the flow properties such as inviscid shock waves or contact discontinuities. The integral formulation of the conservation laws is considered to describe in the most straightforward and general way the physical reality of fluid flow phenomena.

---

[2]The tensor product is a product of two or more vectors where the unit vectors are not subject to scalar or vector operations. For example

$$\overline{\overline{D}} = \vec{A} \otimes \vec{B} = (e_i A_i)(e_j B_j) = A_i B_j\, e_i e_j.$$

In this work e_i represent the base vectors of the Cartesian coordinate system and the convention of summation over repeated indexes is employed. Therefore, the result of the purely mathematical tensor product operation in the $3D$ Euclidean space is a second order tensor with nine components.

C. Conservation Principles in Fluid Dynamics Phenomena

All analyzes concerning the motion of compressible fluid flows must begin, either directly or indirectly, with the statements of three basic physical laws governing such motions. These laws, which are independent of the nature of the particular fluid are:

1. The continuity equation or the law of conservation of mass.
2. Newton's second law of motion or law of conservation of momentum.
3. The first law of the thermodynamics or the law of conservation of energy.

In addition to these fundamental laws, it is usually necessary to bring into the analysis certain subsidiary laws relating to the particular fluid in question. Examples are the equation of state of a perfect gas, the proportionality law between shear stress and the rate of shear deformation in a Newtonian fluid, the Fourier law of heat conduction, etc.

D. The Equation of Conservation of Mass

The mass conservation principle is independent of the nature of the fluid and of the forces acting on it. It simply expresses the empirical fact that, in a fluid system, mass cannot disappear from the system nor be created.

The conserved quantity in this case is the mass m. Thus the conserved scalar quantity per unit volume is the density ρ. Equation (2.3) is then, with $U = \rho$

$$\frac{\partial}{\partial t}\int_{\Omega} \rho \, dV = -\oint_{\partial\Omega} \rho\vec{v} \cdot d\vec{S} + \oint_{\partial\Omega} \vec{F}_D \cdot \, d\vec{S} + \int_{\Omega} Q_V \, dV + \oint_{\partial\Omega} \vec{Q}_S \cdot d\vec{S}.$$

As noted before, there is no diffusive flux contribution to the continuity equation since, for a fluid at rest, any variation of mass would imply a displacement of fluid

particles. $\vec{F}_D$ is therefore equal to zero and the previous equation may be written as

$$\frac{\partial}{\partial t}\int_\Omega \rho\, dV + \oint_{\partial\Omega} \rho\vec{v}\cdot d\vec{S} = \int_\Omega Q_V\, dV + \oint_{\partial\Omega} \vec{Q}_S \cdot d\vec{S}.$$

It just remains to discuss the volume and surface sources for the continuity equation.

1. Volume and Surface Sources for the Mass Conservation Equation

As stated above, mass cannot disappear nor be created in the system. Furthermore, for single phase flows as those treated in this dissertation, no sources due to chemical reactions are to be introduced, i.e.

$$Q_V = 0,$$
$$\vec{Q}_S = 0.$$

The general mass conservation equation then finally becomes

$$\frac{\partial}{\partial t}\int_\Omega \rho\, dV + \oint_{\partial\Omega} \rho\vec{v}\cdot d\vec{S} = 0. \tag{2.8}$$

E. The Equation of Conservation of Momentum

Momentum, defined as $m\vec{v}$, is a quantity which is conserved in a physical system. Since momentum is a vectorial quantity, the conservation law will have the general form given by equation (2.7). The conserved quantity expressed per unit volume in this case is $\rho\vec{v}$. Equation (2.7) is then, with $\vec{U} = \rho\vec{v}$

$$\frac{\partial}{\partial t}\int_\Omega \rho\vec{v}\, dV = -\oint_{\partial\Omega} \left[\vec{v}\otimes(\rho\vec{v})\right]\cdot d\vec{S} - \oint_{\partial\Omega} \overline{\overline{F}}_D \cdot\, d\vec{S} + \int_\Omega \vec{Q}_V\, dV + \oint_{\partial\Omega} \overline{\overline{Q}}_S \cdot d\vec{S}. \tag{2.9}$$

Recall that the diffusive contribution of a conserved quantity is that present in the fluid at rest. Since no diffusion of momentum is possible in a fluid at rest then $\overline{\overline{F}}_D = 0$.

Furthermore, in equation (2.9), the term corresponding to the convective contri-

bution $\big[\vec{v}\otimes(\rho\vec{v})\,\big]\cdot d\vec{S}$ can be recast in a more familiar way:

$$\begin{aligned}\big[\vec{v}\otimes(\rho\vec{v})\big]\cdot d\vec{S} &= \rho\big[\vec{v}\otimes\vec{v}\big]\cdot d\vec{S}\\ &= \rho\big[v_i e_i\, v_j e_j\big]\cdot e_k dS_k = \rho\big[v_i v_j\, e_i e_j\big]\cdot e_k dS_k\\ &= \rho v_i v_j dS_k\big[e_i e_j\big]\cdot e_k = \rho v_i v_j dS_k e_i(e_j\cdot e_k)\\ &= \rho v_i v_j dS_k e_i\delta_{jk} = \rho v_i e_i\big[v_j(dS_k\delta_{jk})\big].\end{aligned}$$

Since $dS_k\,\delta_{jk} = dS_j$, $v_j dS_j = \vec{v}\cdot d\vec{S}$ and $v_i e_i = \vec{v}$ then, finally

$$\big[\vec{v}\otimes(\rho\vec{v})\big]\cdot d\vec{S} = \rho\,\vec{v}\big(\vec{v}\cdot d\vec{S}\big).$$

Equation (2.9) can then be expressed as

$$\frac{\partial}{\partial t}\int_\Omega \rho\vec{v}\,dV + \oint_{\partial\Omega}\rho\vec{v}(\vec{v}\cdot d\vec{S}) = \int_\Omega \vec{Q}_V\,dV + \oint_{\partial\Omega}\overline{\overline{Q}}_S\cdot d\vec{S}. \tag{2.10}$$

In order to determine $\vec{Q}_V$ and $\overline{\overline{Q}}_S$ in equation (2.10) it is necessary to define the sources influencing the variation of momentum. It is known, from Newton's laws, that the sources for the variation of momentum in a physical system are the forces acting on it. These sources consist of the external volume forces and of the internal forces.

The external volume forces (also known as body forces) are those which act directly on the mass of the volume. Such forces are usually due to external fields such as gravity or an applied electromagnetic potential. Let $\vec{f_e}$ to denote the resultant of the body forces per unit mass. Then the external force is $m\vec{f_e}$ and the external force per unit volume is $\rho\vec{f_e}$. The internal forces, on the other hand, are dependent of the nature of the fluid considered, and result from the assumptions made about the properties of the internal deformations within the fluid and their relation to the internal stresses.

1. Internal Stress in a Newtonian Fluid

In this dissertation it is assumed that the working fluid is Newtonian, and therefore the total internal stresses, denoted by $\overline{\overline{\sigma}}$, are taken to be

$$\overline{\overline{\sigma}} = -p\overline{\overline{I}} + \overline{\overline{\tau}}, \tag{2.11}$$

where $\overline{\overline{I}}$ is the unit Kronecker tensor defined as $\overline{\overline{I}} = e_i e_j \delta_{ij}$. Here the existence of the isotropic pressure component $p\overline{\overline{I}}$ is introduced; $\overline{\overline{\tau}}$ is the viscous shear stress tensor defined as [22] [23]

$$\overline{\overline{\tau}} = \tau_{ij}\, e_i e_j, \tag{2.12}$$

with

$$\tau_{ij} = \mu \left(\frac{\partial v_i}{\partial x_j} + \frac{\partial v_j}{\partial x_i} \right) + \delta_{ij}\, \lambda\, \frac{\partial v_k}{\partial x_k}. \tag{2.13}$$

In equation (2.13) μ is the dynamic viscosity of the fluid and λ is the second coefficient of viscosity or coefficient of bulk viscosity. A kinematic viscosity coefficient ν is also defined by $\nu = \mu/\rho$.

Equation (2.12) together with (2.13) represent the most general form for the viscous stress tensor of a Newtonian fluid. However, a simpler expression can be obtained by making use of the Stokes' relation

$$2\mu + 3\lambda = 0. \tag{2.14}$$

Thus, the components of the viscous stress tensor become

$$\tau_{ij} = \mu \left[\left(\frac{\partial v_i}{\partial x_j} + \frac{\partial v_j}{\partial x_i} \right) - \frac{2}{3}\, \delta_{ij}\, \frac{\partial v_k}{\partial x_k} \right]. \tag{2.15}$$

Up to now, with the exception of very high temperature or pressure ranges, there is no experimental evidence that the Stokes relation, equation (2.14), leading to

equation (2.15), is not satisfied. Therefore, for the rest of this work λ is not considered to be independent of μ and thus equation (2.15) is used to compute the stress tensor $\overline{\overline{\tau}}$. Plugging equation (2.15) into (2.12) gives

$$\overline{\overline{\tau}} = \mu \left[\left(\frac{\partial v_i}{\partial x_j} + \frac{\partial v_j}{\partial x_i} \right) - \frac{2}{3} \delta_{ij} \frac{\partial v_k}{\partial x_k} \right] e_i e_j. \tag{2.16}$$

Equation (2.16) will be used on any other equation where $\overline{\overline{\tau}}$ appears.

2. Volume and Surface Sources for the Momentum Conservation Equation

The source term $\vec{Q}_V$ consists of the sum of the external volume forces per unit volume $\rho \vec{f_e}$ and the sum of all the internal forces per unit volume. By definition, internal forces cancel in every point *inside* the volume. This fact has two consequences: first that

$$\vec{Q}_V = \rho \vec{f_e} + 0 \tag{2.17}$$

and second, that the only remaining internal forces within Ω are those acting on the points of the boundary surface $\partial\Omega$, since they have no opposite counterpart within the considered volume. The resultant force of these internal forces acting over all $\partial\Omega$ is

$$\oint_{\partial\Omega} \overline{\overline{\sigma}} \cdot d\vec{S}.$$

That is, $\overline{\overline{\sigma}}$ (see equation (2.11)) acts as a surface source

$$\overline{\overline{Q}}_S \; = \; \overline{\overline{\sigma}} \; = \; -p\overline{\overline{I}} + \overline{\overline{\tau}}. \tag{2.18}$$

Substitution of equations (2.17) and (2.18) into (2.10) gives

$$\frac{\partial}{\partial t} \int_\Omega \rho \vec{v} \, dV + \oint_{\partial\Omega} \rho \vec{v} (\vec{v} \cdot d\vec{S}) = \int_\Omega \rho \vec{f_e} \, dV - \oint_{\partial\Omega} p\overline{\overline{I}} \cdot d\vec{S} + \oint_{\partial\Omega} \overline{\overline{\tau}} \cdot d\vec{S},$$

where the operation $p\overline{\overline{I}} \cdot d\vec{S}$ is performed as follows

$$\begin{aligned} p\overline{\overline{I}} \cdot d\vec{S} &= p\,(e_i e_j \delta_{ij}) \cdot (e_k dS_k) = p\,\delta_{ij}\,dS_k\,(e_i e_j) \cdot (e_k) \\ &= p\,\delta_{ij}\,dS_k\,e_i\,\delta_{jk} = p\,e_j dS_j \\ &= p d\vec{S}. \end{aligned}$$

Thus the equation of conservation of momentum finally is

$$\frac{\partial}{\partial t}\int_\Omega \rho\vec{v}\,dV + \oint_{\partial\Omega} \rho\vec{v}(\vec{v}\cdot d\vec{S}) = \int_\Omega \rho\vec{f_e}\,dV - \oint_{\partial\Omega} p d\vec{S} + \oint_{\partial\Omega} \overline{\overline{\tau}} \cdot d\vec{S}. \tag{2.19}$$

F. The Equation of Conservation of Energy

The underlying principle that is used to derive the conservation equation for the energy is the first law of thermodynamics. The conserved quantity here is the scalar total energy, equal to the sum of internal, kinetic and potential energies of the fluid. This time, for convenience, the conserved quantity is expressed per unit mass and it is denoted by E. Neglecting the potential energy one has

$$E = e + \frac{|\vec{v}|^2}{2}, \tag{2.20}$$

where e is the internal energy per unit mass and $|\vec{v}|^2/2$ is the kinetic energy per unit mass.

Since the conserved quantity is a scalar expressed per unit mass, the conservation law will have the general form as in equation (2.4). That is, from equation (2.4), with $u = E$

$$\frac{\partial}{\partial t}\int_\Omega \rho E\,dV = -\oint_{\partial\Omega} \rho E\vec{v}\cdot d\vec{S} + \oint_{\partial\Omega} \vec{F}_D \cdot\, d\vec{S} + \int_\Omega Q_V\,dV + \oint_{\partial\Omega} \vec{Q}_S \cdot d\vec{S}. \tag{2.21}$$

For equation (2.21), the diffusive term $\vec{F}_D$ is written as (see [24], p. 18)

$$\vec{F}_D = -\gamma\rho\alpha\vec{\nabla}E = -\gamma\rho\alpha\vec{\nabla}\left(e + \tfrac{1}{2}|\vec{v}|^2\right).$$

However, since by definition there is no diffusive flux associated with the motion

$$\vec{F}_D = -\gamma\rho\alpha\vec{\nabla}e. \tag{2.22}$$

In equation (2.22), γ is the ratio of specific heat coefficients under constant pressure and constant volume ($\gamma = c_p/c_v$) and the coefficient α is the thermal diffusivity coefficient which needs to be determined empirically. The diffusive term, equation (2.22), describes the diffusion of heat in a medium at rest due to molecular conduction and it is generally written in the more familiar form of the Fourier's law of heat conduction (see [24], p. 18)

$$\begin{aligned} \vec{F}_D &= -\rho c_p \alpha \vec{\nabla} T \\ &= -k\vec{\nabla}T, \end{aligned} \tag{2.23}$$

where T is the absolute temperature and $k = \rho c_p \alpha$ is the thermal conductivity coefficient. With the introduction of the Prandtl number $Pr = \nu/\alpha$, where $\nu = \mu/\rho$, the thermal conductivity coefficient can be written as

$$k = \frac{\mu c_p}{Pr}. \tag{2.24}$$

Substitution of equation (2.23) into equation (2.21) finally gives

$$\frac{\partial}{\partial t}\int_\Omega \rho E\, dV + \oint_{\partial\Omega} \rho E\vec{v}\cdot d\vec{S} = \oint_{\partial\Omega} k\vec{\nabla}T\cdot d\vec{S} + \int_\Omega Q_V\, dV + \oint_{\partial\Omega}\vec{Q}_S\cdot d\vec{S}. \tag{2.25}$$

1. Volume and Surface Sources for the Energy Conservation Equation

The first law of thermodynamics states that the sources for the variation of the total energy are the work transfer of the forces acting on the system plus the heat transfer to the system. The following distinction is made regarding the sources of the energy's conservation law: the volume sources are the sum of the work transfer of the volume forces, $\rho\vec{f_e}\cdot\vec{v}$ and of the heat sources other than conduction (e.g., radiation and chemical reactions), $\dot{q}_H$. Hence, the volume sources per unit volume are

$$Q_V = \rho\vec{f_e}\cdot\vec{v} + \dot{q}_H. \tag{2.26}$$

The surface sources $\vec{Q}_S$, on the other hand, are the result of the work done on the fluid by the internal shear stresses acting on the surface of the volume considering that there are no surface heat sources

$$\begin{aligned} \vec{Q}_S &= \overline{\overline{\sigma}}\cdot\vec{v} = -p\overline{\overline{I}}\cdot\vec{v} + \overline{\overline{\tau}}\cdot\vec{v}, \\ &= -p\vec{v} + \overline{\overline{\tau}}\cdot\vec{v}. \end{aligned} \tag{2.27}$$

Substitution of (2.26) and (2.27) into (2.25) gives

$$\begin{aligned} \frac{\partial}{\partial t}\int_\Omega \rho E\, dV + \oint_{\partial\Omega} \rho E\vec{v}\cdot d\vec{S} &= \oint_{\partial\Omega} k\vec{\nabla}T\cdot d\vec{S} + \int_\Omega \left(\rho\vec{f_e}\cdot\vec{v} + \dot{q}_H\right) dV \\ &+ \oint_{\partial\Omega} \left(-p\vec{v} + \overline{\overline{\tau}}\cdot\vec{v}\right)\cdot d\vec{S}. \end{aligned}$$

Moving the term containing $p\vec{v}$ to the left hand side and doing some manipulations

$$\frac{\partial}{\partial t}\int_\Omega \rho E\, dV + \oint_{\partial\Omega}\left(E + \frac{p}{\rho}\right)\rho\vec{v}\cdot d\vec{S} =$$

$$\oint_{\partial\Omega} k\vec{\nabla}T\cdot d\vec{S} + \int_\Omega \left(\rho\vec{f_e}\cdot\vec{v} + \dot{q}_H\right) dV + \oint_{\partial\Omega}\left(\overline{\overline{\tau}}\cdot\vec{v}\right)\cdot d\vec{S}.$$

Introducing the concept of total enthalpy, $H = h + |\vec{v}|^2/2$, where h is the enthalpy of

the fluid defined as $h = e + p/\rho$. Then

$$H = e + \frac{p}{\rho} + \frac{|\vec{v}|^2}{2}.$$

Neglecting the potential energy $E = e + |\vec{v}|^2/2$, then

$$H = E + \frac{p}{\rho}.$$

The final form of the conservation equation of energy is therefore

$$\frac{\partial}{\partial t}\int_\Omega \rho E \, dV + \oint_{\partial\Omega} \rho H \vec{v} \cdot d\vec{S} =$$

$$\oint_{\partial\Omega} k\vec{\nabla}T \cdot d\vec{S} + \int_\Omega \left(\rho \vec{f_e} \cdot \vec{v} + \dot{q}_H\right) dV + \oint_{\partial\Omega} \left(\overline{\overline{\tau}} \cdot \vec{v}\right) \cdot d\vec{S}. \tag{2.28}$$

G. Equation of State and Other Complementary Equations

If the stress tensor $\overline{\overline{\tau}}$ defined by equations (2.12) and (2.15) is substituted into the momentum and energy equations (equations (2.19) and (2.28) respectively), then the five governing equations[3] for mass, momentum and energy conservation (equations (2.8), (2.19) and (2.28), respectively) have as unknowns the variables ρ, u, v, w, p, E, H, T, μ and k. That is, there are five equations for ten unknowns and therefore five more equations are needed to close the system

In this dissertation, the working fluid is air which is assumed to be an ideal gas with constant, known c_v and c_p. The gas constant for air R is available as well. Taking these into account, the complementary equations are the equation of state for

[3]Recall that the momentum equation is in vectorial form; that is, there are three scalar equations for it.

an ideal gas

$$p = \rho RT \tag{2.29}$$

and the following thermodynamic relations

$$E = c_v T + |\vec{v}|^2/2, \tag{2.30}$$

$$H = c_p T + |\vec{v}|^2/2. \tag{2.31}$$

It just remains to determine the transport properties μ and k. These coefficients have been related to the thermodynamic variables using kinetic theory. In this research, Sutherland's formula for the viscosity is employed

$$\mu = C_1 \frac{T^{3/2}}{T + C_2}, \tag{2.32}$$

where C_1 and C_2 are constants for a given gas. For air at moderate temperatures, $C_1 = 1.458 \times 10^{-6}$ kg/(m s $\sqrt{\text{K}}$) and $C_2 = 110.4$ K. The thermal conductivity k is determined in terms of μ (see equation (2.24))

$$k = \frac{c_p}{Pr}\mu. \tag{2.33}$$

This is possible because the ratio (c_p/Pr) which appears in (2.33) is approximately constant for most gases. For air at standard conditions $Pr = 0.72$.

Equations (2.29) to (2.33) close the system of equations as mentioned above.

CHAPTER III

CODE DEVELOPMENT

In this chapter the methodology followed to develop the finite volume code used in this research is explained in detail. Finite volume method is the name given to the technique by which the integral formulation of the conservation laws are discretized directly in the physical space. This ensures that the basic quantities mass, momentum and energy will also remain conserved at the discrete level. This means the resulting scheme has the property of being conservative, feature of major importance when dealing with flows with strong gradients or with discontinuous flows, such as transonic flows with shock waves [25].

The finite volume method takes full advantage of an arbitrary mesh, where a large number of options are open for the definition of the control volumes on which the conservation laws are expressed. Furthermore, great flexibility exists in the choosing of rules and accuracy for the evaluation of the fluxes through the control surfaces.

In this research, two- and three-dimensional codes are developed. These codes can handle steady or unsteady, inviscid or viscous, laminar or turbulent compressible flow problems. The scheme is cell centered and uses a structured grid (these terms are explained in following sections). The analysis presented in this chapter corresponds only to the development of the two-dimensional code. The development of the three-dimensional code follows the same principles as explained for the two-dimensional case.

In this work the spatial discretization is the same for steady and unsteady problems; the temporal discretization, however, is different. For steady problems an explicit scheme with variable time step as a convergence accelerator is employed. For unsteady problems, on the other hand, a fully implicit scheme is utilized. The details

of the implementation of the spatial and temporal discretization, plus a discussion on the required boundary conditions, turbulence modeling and grid generation are also given in this chapter.

A. Summary of the Governing Equations

As discussed in the previous chapter, the governing equations of viscous fluid flow phenomena are the Navier-Stokes equations (equations (2.8), (2.19) and (2.28)). Considering that in this research external forces and heat sources are not present, they can be recast as follows

$$\frac{\partial}{\partial t}\int_{\Omega}\rho\,dV \quad + \oint_{\partial\Omega}(\rho\vec{v})\cdot d\vec{S} = 0, \tag{3.1}$$

$$\frac{\partial}{\partial t}\int_{\Omega}\rho\vec{v}\,dV \quad + \oint_{\partial\Omega}(\rho\vec{v}\otimes\vec{v} + p\overline{\overline{I}} - \overline{\overline{\tau}})\cdot d\vec{S} = 0, \tag{3.2}$$

$$\frac{\partial}{\partial t}\int_{\Omega}\rho E\,dV \quad + \oint_{\partial\Omega}\left(\rho H\vec{v} - k\vec{\nabla}T - \overline{\overline{\tau}}\cdot\vec{v}\right)\cdot d\vec{S} = 0. \tag{3.3}$$

Where, according to equations (2.12) and (2.15)

$$\overline{\overline{\tau}} = \tau_{ij}\,e_i e_j = \mu\left[\left(\frac{\partial v_i}{\partial x_j} + \frac{\partial v_j}{\partial x_i}\right) - \frac{2}{3}\,\delta_{ij}\,\frac{\partial v_k}{\partial x_k}\right]\,e_i e_j. \tag{3.4}$$

The surface sources have the same effect on the system as the convective and diffusive flux terms (they change the local intensity of the corresponding conserved variable, denoted W, through contributions acting on $\partial\Omega$). Thus, taking all the diffusive, convective and surface source fluxes into one, single total flux $\vec{F}_T$, a general form for the governing equations can be written

$$\frac{\partial}{\partial t}\int_{\Omega} W\,dV + \oint_{\partial\Omega}\vec{F}_T\cdot d\vec{S} = 0, \tag{3.5}$$

where

$$W = \left\{ \begin{array}{c} \rho \\ \rho\vec{v} \\ \rho E \end{array} \right\} \qquad \text{and} \qquad \vec{F}_T = \left\{ \begin{array}{c} \rho\vec{v} \\ \rho\vec{v} \otimes \vec{v} + p\overline{\overline{I}} - \overline{\overline{\tau}} \\ \rho H\vec{v} - k\vec{\nabla}T - \overline{\overline{\tau}} \cdot \vec{v} \end{array} \right\}. \tag{3.6}$$

B. Conservative Property

The essential significance of equation (3.5) lies in the presence of the surface integral and the fact that the time variations of W, in the domain Ω, depend only on the flux contributions through the surface $\partial\Omega$. The flux values inside Ω cancel out and contribute nothing to the variation of W. Hence, for an arbitrary subdivision of the domain Ω into a given number N of sub-volumes Ω_I, one can write the conservation law for each sub-volume. Later, one can recover the global conservation law, equation (3.5), by adding up all of the sub-volumes' conservation laws. That is

$$\frac{\partial}{\partial t}\int_{\Omega} W\, dV = \sum_{I=1}^{N} \frac{\partial}{\partial t}\int_{\Omega_I} W\, dV, \tag{3.7}$$

$$\oint_{\partial\Omega} \vec{F}_T \cdot d\vec{S} = \sum_{I=1}^{N} \oint_{\partial\Omega_I} \vec{F}_T \cdot d\vec{S}. \tag{3.8}$$

In equation (3.8) $\partial\Omega_I$ represents the area surrounding each sub-volume Ω_I. Note that $\partial\Omega_I$ may lay inside the total domain Ω or it may be a constituent part of the surface boundary $\partial\Omega$ of the total domain.

In order for (3.8) to be true, all of the internal flux contributions must cancel out. The only remaining contributions must be those along the domain's boundary surface $\partial\Omega$. For example, if in Figure 2 the line segments AE, EB, BCA represent the domain's bounding surface $\partial\Omega$, then the total flux term of the global conservation law, equation (3.5) is

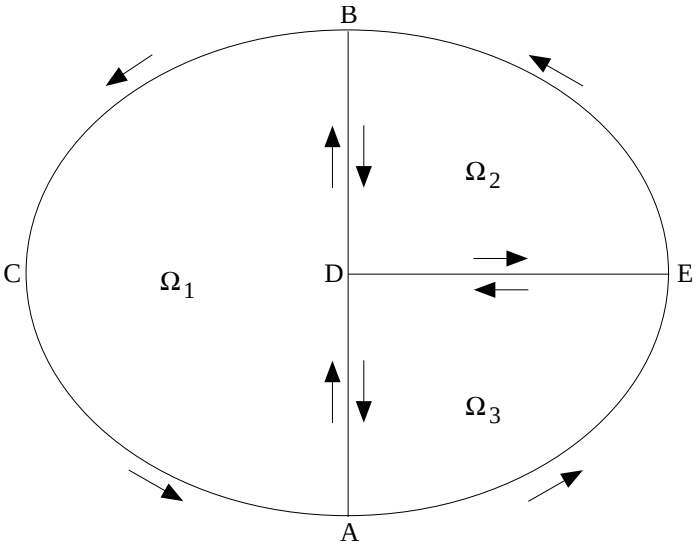

Fig. 2.: Conservation laws for sub-volumes Ω_I of volume Ω (the arrows indicate the direction of integration for each sub-volume).

$$\oint_{\partial\Omega} \vec{F_T} \cdot d\vec{S} = \int_{AE} \vec{F_T} \cdot d\vec{S} + \int_{EB} \vec{F_T} \cdot d\vec{S} + \int_{BCA} \vec{F_T} \cdot d\vec{S}. \tag{3.9}$$

But from equation (3.8), with $N = 3$

$$\oint_{\partial\Omega} \vec{F_T} \cdot d\vec{S} = \sum_{I=1}^{N=3} \oint_{\partial\Omega_I} \vec{F_T} \cdot d\vec{S} \tag{3.10}$$

where

$$\begin{aligned} \sum_{I=1}^{N=3} \oint_{\partial\Omega_I} \vec{F_T} \cdot d\vec{S} \;&=\; \int_{AD} \vec{F_T} \cdot d\vec{S} + \int_{DB} \vec{F_T} \cdot d\vec{S} + \int_{BCA} \vec{F_T} \cdot d\vec{S} + \\ &+\; \int_{DE} \vec{F_T} \cdot d\vec{S} + \int_{EB} \vec{F_T} \cdot d\vec{S} + \int_{BD} \vec{F_T} \cdot d\vec{S} + \\ &+\; \int_{AE} \vec{F_T} \cdot d\vec{S} + \int_{ED} \vec{F_T} \cdot d\vec{S} + \int_{DA} \vec{F_T} \cdot d\vec{S}. \end{aligned} \tag{3.11}$$

The first three terms on the right hand side of equation (3.11) result from using $\oint_{\partial\Omega_I} \vec{F_T} \cdot d\vec{S}$ on sub-volume Ω_1. The following three terms from the application of the

same equation to sub-volume Ω_2 and the last three when working on sub-volume Ω_3. In order of equations (3.9) and (3.10) to agree, it must be that the sum of internal flux contributions is zero

$$\int_{AD} \vec{F}_T \cdot d\vec{S} + \int_{DB} \vec{F}_T \cdot d\vec{S} + \int_{DE} \vec{F}_T \cdot d\vec{S} + \int_{BD} \vec{F}_T \cdot d\vec{S} + \int_{ED} \vec{F}_T \cdot d\vec{S} + \int_{DA} \vec{F}_T \cdot d\vec{S} = 0. \quad (3.12)$$

In equation (3.12) $\int_{AD} \vec{F}_T \cdot d\vec{S}$ and $\int_{DA} \vec{F}_T \cdot d\vec{S}$ differ only in the order of the integration limits, therefore

$$\int_{AD} \vec{F} \cdot d\vec{S} = -\int_{DA} \vec{F} \cdot d\vec{S}.$$

In the same way

$$\int_{DB} \vec{F} \cdot d\vec{S} = -\int_{BD} \vec{F} \cdot d\vec{S},$$

$$\int_{DE} \vec{F} \cdot d\vec{S} = -\int_{ED} \vec{F} \cdot d\vec{S}.$$

Equation (3.12) is thus satisfied.

The essential property that the sum of the internal flux contributions is zero must be kept by the numerical discretization of such internal fluxes in order for the scheme to be conservative. When this is not the case, that is, when after summation of the discretized equations over a certain number of adjacent sub-volumes, the resulting equation still contains flux contributions from inside the domain, the discretization is said to be non-conservative, and the internal flux contributions appear as *numerical* internal volume sources.

In this work, a numerical discretization which ensured the conservation feature is used. Emphasis is put on this issue because, as noted in Hirsch's book [24], p. 240, numerical experiments and comparisons have consistently shown that non-conservative

formulations are generally less accurate than conservative ones, particularly in the presence of strong gradients.

C. The Method of Lines

The availability of sophisticated and reliable algorithms and computer programs for the numerical computation of complicated systems of *ordinary* differential equations makes the classical method of lines attractive for a number of problems. This method states that, for a given *system of partial differential equations* one must discretize all but one of the independent variables. This semi-discrete procedure yields a coupled system of ordinary differential equations which are then numerically integrated using a suitable numerical scheme [26].

Both steady and unsteady problems are considered in this research. In the steady problems case, pseudo time-dependent methods are used. Therefore, on any case, marching in time a time-dependent equation is performed. The time dependent equation of interest in this research is equation (3.5)

$$\frac{\partial}{\partial t}\int_{\Omega} W\, dV + \oint_{\partial\Omega} \vec{F}_T \cdot d\vec{S} = 0.$$

As mentioned before, this actually represents a system of partial differential equations, the Navier-Stokes equations. The method of lines will be applied to this system in order to obtain the numerical scheme used in this work.

D. Subdivision of the Physical Space

Previous to the derivation of the numerical scheme used in this dissertation, a subdivision of the physical space, where the flow is to be computed, must be performed. The physical space is therefore divided into a number of geometrical elements called grid

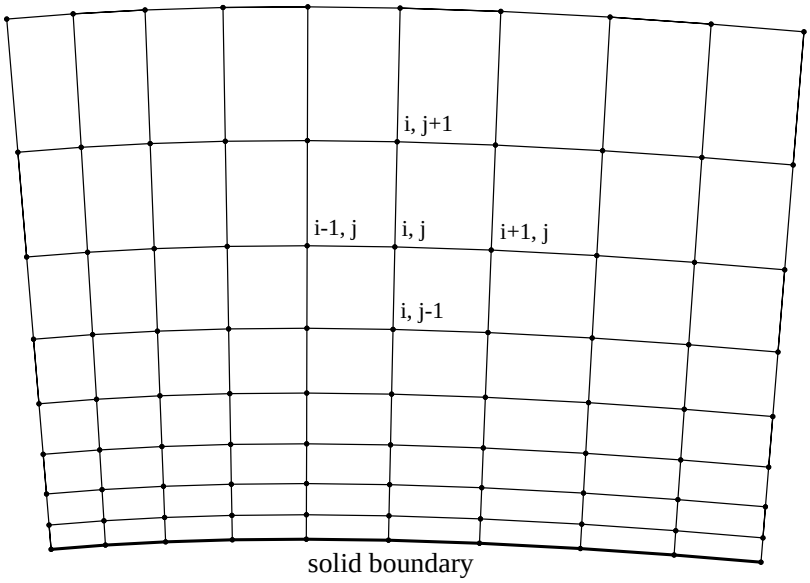

Fig. 3.: Example of structured, body-fitted grid (in two dimensions).

cells[1]. In this research, the space subdivision is accomplished with a structured grid (see Figure 3). The term structured is used when each grid point (also called node) is uniquely identified by the indices i, j and ordered in such a way that neighboring grid cells and grid points can be easily determined, just by adding or subtracting an integer value to or from the corresponding index. The evaluation of gradients, fluxes and the treatment of the boundary conditions is greatly simplified by this feature.

In this work two and three dimensional computations were performed and the cell elements are quadrilateral and hexahedral cells respectively. The utilized grid is also body fitted, that is, it closely follows the boundaries of the physical domain, as can also be seen in Figure 3.

[1]They are also called simply cells, cell elements or control volumes.

E. The Mean Value Theorem

Before proceeding with the space discretization, let the mean or average of W in a given cell Ω be defined. In the following theorem

$$\int_{\Omega} W \, dV = \overline{W} \, V(\Omega) \tag{3.13}$$

$\overline{W}$ represents the mean value or average of W inside the volume Ω. $V(\Omega)$ is the volume of Ω, i.e. $V(\Omega) = \int_{\Omega} dV$. Use of equation (3.13) into (3.5), regarding $V(\Omega)$ as independent of time, gives

$$\frac{\partial \overline{W}}{\partial t} + \frac{1}{V(\Omega)} \oint_{\partial\Omega} \vec{F}_T \cdot d\vec{S} = 0. \tag{3.14}$$

It must be stressed out that equation (3.14) is exact and that no approximations have been made up to this point.

F. Spatial Discretization of the Governing Equation

For two dimensional problems and the Cartesian coordinate system, the scalar product $\vec{F}_T \cdot d\vec{S}$ in equation (3.5) or (3.14) gives

$$\vec{F}_T \cdot d\vec{S} = \left\{ \begin{array}{lcl} (\quad \rho u \quad) \, dS_x & + & (\quad \rho v \quad) \, dS_y \\ (\quad \rho uu + p - \tau_{xx} \quad) \, dS_x & + & (\quad \rho uv - \tau_{xy} \quad) \, dS_y \\ (\quad \rho vu - \tau_{yx} \quad) \, dS_x & + & (\quad \rho vv + p - \tau_{yy} \quad) \, dS_y \\ (\quad \rho uH - k\dfrac{\partial T}{\partial x} - u\tau_{xx} - v\tau_{xy} \quad) \, dS_x & + & (\quad \rho vH - k\dfrac{\partial T}{\partial y} - u\tau_{yx} - v\tau_{yy} \quad) \, dS_y \end{array} \right\}, \tag{3.15}$$

or

$$\vec{F}_T \cdot d\vec{S} = F_{T_x} dS_x + F_{T_y} dS_y. \tag{3.16}$$

Since for the Cartesian two dimensional case (see equation (2.15))

$$\tau_{xx} = \frac{2}{3}\mu\left(2\,\frac{\partial u}{\partial x} - \frac{\partial v}{\partial y}\right)$$

$$\tau_{yy} = \frac{2}{3}\mu\left(2\,\frac{\partial v}{\partial y} - \frac{\partial u}{\partial x}\right)$$

$$\tau_{xy} = \tau_{yx} = \mu\left(\frac{\partial u}{\partial y} + \frac{\partial v}{\partial x}\right),$$

then F_{T_x} and F_{T_y} in equation (3.16) are, according to (3.15)

$$F_{T_x} = \left\{ \begin{array}{c} \rho u \\ \rho u u + p - \frac{2}{3}\mu\left(2\frac{\partial u}{\partial x} - \frac{\partial v}{\partial y}\right) \\ \rho v u - \mu\left(\frac{\partial u}{\partial y} + \frac{\partial v}{\partial x}\right) \\ \rho u H - k\frac{\partial T}{\partial x} - \frac{2}{3}\,u\mu\left(2\frac{\partial u}{\partial x} - \frac{\partial v}{\partial y}\right) - v\mu\left(\frac{\partial u}{\partial y} + \frac{\partial v}{\partial x}\right) \end{array} \right\} \tag{3.17}$$

and

$$F_{T_y} = \left\{ \begin{array}{c} \rho v \\ \rho u v - \mu\left(\frac{\partial u}{\partial y} + \frac{\partial v}{\partial x}\right) \\ \rho v v + p - \frac{2}{3}\mu\left(2\frac{\partial v}{\partial y} - \frac{\partial u}{\partial x}\right) \\ \rho v H - k\frac{\partial T}{\partial y} - u\mu\left(\frac{\partial v}{\partial x} + \frac{\partial u}{\partial y}\right) - \frac{2}{3}\,v\mu\left(2\frac{\partial v}{\partial y} - \frac{\partial u}{\partial x}\right) \end{array} \right\}. \tag{3.18}$$

Substitution of equation (3.16) into (3.5) gives

$$\frac{\partial \overline{W}}{\partial t} + \frac{1}{V(\Omega)} \oint_{\partial\Omega} (F_{Tx} dS_x + F_{Ty} dS_y) = 0. \tag{3.19}$$

At this stage, the surface integral of equation (3.19) is replaced with the mid-point integration rule which is second order accurate for uniform and smoothly varying grids[27]. For structured grids and two dimensional problems, the volumes of integration are quadrilaterals and they are denoted $\Omega_{I,J}$ (see Figure 4). It is assumed that F_{Tx} and F_{Ty} are constant along the individual face and also that they are evaluated at the mid-point of the face. Therefore, the approximation for the surface integral in equation (3.19) is

$$\frac{1}{V(\Omega)} \oint_{\partial\Omega} (F_{Tx} dS_x + F_{Ty} dS_y) \approx \frac{1}{V(\Omega_{I,J})} \sum_{m=1}^{4} \Big(F_{Tx}\, S_x + F_{Ty}\, S_y \Big)_m . \tag{3.20}$$

In equation (3.20), index m refers to the face of the cell $\Omega_{I,J}$. S_x and S_y are the Cartesian components of the vector $\vec{S}$ which is the area vector corresponding to face m (see Figure 4). The magnitude of $\vec{S}$ equals the area of face m (in two-dimensions there is a depth with a value of one), its direction is normal to m and it points outward the cell $\Omega_{I,J}$. Finally, $V(\Omega_{I,J})$ is the volume of the cell $\Omega_{I,J}$ to which the conservation laws are being applied.

For example, the spatial discretization (equation (3.20)) corresponding to the mass conservation on cell element $\Omega_{I,J}$ is (plugging the corresponding scalars of

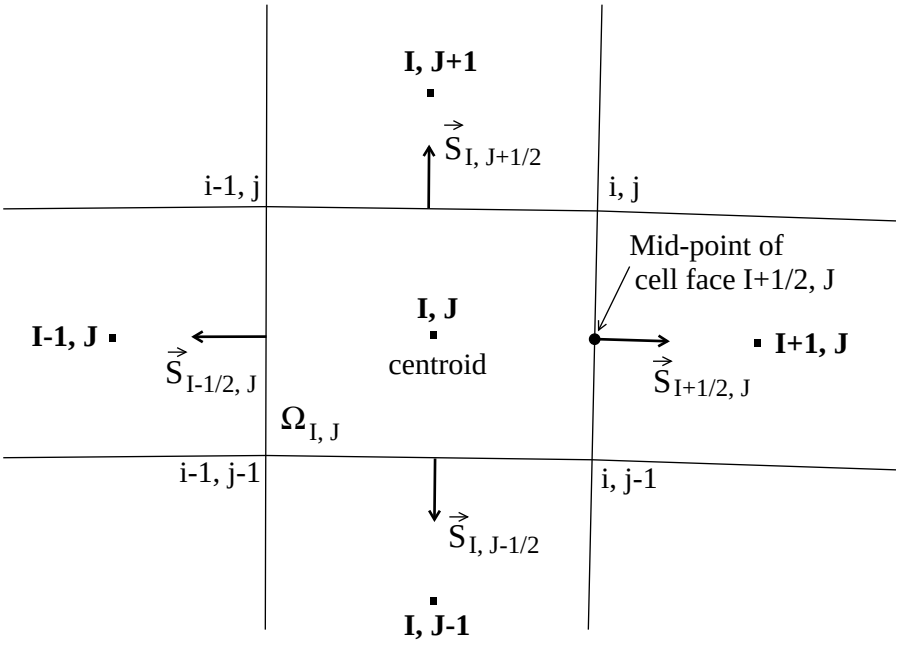

Fig. 4.: Main control volume with centroid (I, J).

equations (3.17) and (3.18) into (3.20))

$$\begin{aligned}
&\tfrac{1}{V(\Omega_{I,J})}\sum_{m=1}^{4}\Big(\big[\rho u\big]S_x+\big[\rho v\big]S_y\Big)_m=\\
&\tfrac{1}{V(\Omega_{I,J})}\Big(\big[(\rho_{I+\frac{1}{2},J})(u_{I+\frac{1}{2},J})\big][S_x]_{I+\frac{1}{2},J}+\big[(\rho_{I,J+\frac{1}{2}})(u_{I,J+\frac{1}{2}})\big][S_x]_{I,J+\frac{1}{2}}+\\
&\qquad\big[(\rho_{I-\frac{1}{2},J})(u_{I-\frac{1}{2},J})\big][S_x]_{I-\frac{1}{2},J}+\big[(\rho_{I,J-\frac{1}{2}})(u_{I,J-\frac{1}{2}})\big][S_x]_{I,J-\frac{1}{2}}+\\
&\qquad\big[(\rho_{I+\frac{1}{2},J})(v_{I+\frac{1}{2},J})\big][S_y]_{I+\frac{1}{2},J}+\big[(\rho_{I,J+\frac{1}{2}})(v_{I,J+\frac{1}{2}})\big][S_y]_{I,J+\frac{1}{2}}+\\
&\qquad\big[(\rho_{I-\frac{1}{2},J})(v_{I-\frac{1}{2},J})\big][S_y]_{I-\frac{1}{2},J}+\big[(\rho_{I,J-\frac{1}{2}})(v_{I,J-\frac{1}{2}})\big][S_y]_{I,J-\frac{1}{2}}\Big).
\end{aligned}\tag{3.21}$$

Similarly, for the x-momentum conservation equation one has

$$\tfrac{1}{V(\Omega_{I,J})}\sum_{m=1}^{4}\left(\Big[\rho uu+p-\tfrac{2}{3}\mu\left(2\tfrac{\partial u}{\partial x}-\tfrac{\partial v}{\partial y}\right)\Big]S_x+\Big[\rho uv-\mu\left(\tfrac{\partial u}{\partial y}+\tfrac{\partial v}{\partial x}\right)\Big]S_y\right)_m=$$

$$
\begin{aligned}
&\tfrac{1}{V(\Omega_{I,J})}\Bigg(\\
&\Big[(\rho_{I+\frac{1}{2},J})(u_{I+\frac{1}{2},J})(u_{I+\frac{1}{2},J})+(p_{I+\frac{1}{2},J})-\tfrac{2}{3}(\mu_{I+\frac{1}{2},J})\left(2\tfrac{\partial u}{\partial x}\Big|_{I+\frac{1}{2},J}-\tfrac{\partial v}{\partial y}\Big|_{I+\frac{1}{2},J}\right)\Big]\,[S_x]_{I+\frac{1}{2},J}+ \\
&\Big[(\rho_{I,J+\frac{1}{2}})(u_{I,J+\frac{1}{2}})(u_{I,J+\frac{1}{2}})+(p_{I,J+\frac{1}{2}})-\tfrac{2}{3}(\mu_{I,J+\frac{1}{2}})\left(2\tfrac{\partial u}{\partial x}\Big|_{I,J+\frac{1}{2}}-\tfrac{\partial v}{\partial y}\Big|_{I,J+\frac{1}{2}}\right)\Big]\,[S_x]_{I,J+\frac{1}{2}}+ \\
&\Big[(\rho_{I-\frac{1}{2},J})(u_{I-\frac{1}{2},J})(u_{I-\frac{1}{2},J})+(p_{I-\frac{1}{2},J})-\tfrac{2}{3}(\mu_{I-\frac{1}{2},J})\left(2\tfrac{\partial u}{\partial x}\Big|_{I-\frac{1}{2},J}-\tfrac{\partial v}{\partial y}\Big|_{I-\frac{1}{2},J}\right)\Big]\,[S_x]_{I-\frac{1}{2},J}+ \\
&\Big[(\rho_{I,J-\frac{1}{2}})(u_{I,J-\frac{1}{2}})(u_{I,J-\frac{1}{2}})+(p_{I,J-\frac{1}{2}})-\tfrac{2}{3}(\mu_{I,J-\frac{1}{2}})\left(2\tfrac{\partial u}{\partial x}\Big|_{I,J-\frac{1}{2}}-\tfrac{\partial v}{\partial y}\Big|_{I,J-\frac{1}{2}}\right)\Big]\,[S_x]_{I,J-\frac{1}{2}}+ \\
&\Big[(\rho_{I+\frac{1}{2},J})(u_{I+\frac{1}{2},J})(v_{I+\frac{1}{2},J})-(\mu_{I+\frac{1}{2},J})\left(\tfrac{\partial u}{\partial y}\Big|_{I+\frac{1}{2},J}-\tfrac{\partial v}{\partial x}\Big|_{I+\frac{1}{2},J}\right)\Big]\,[S_y]_{I+\frac{1}{2},J}+ \\
&\Big[(\rho_{I,J+\frac{1}{2}})(u_{I,J+\frac{1}{2}})(v_{I,J+\frac{1}{2}})-(\mu_{I,J+\frac{1}{2}})\left(\tfrac{\partial u}{\partial y}\Big|_{I,J+\frac{1}{2}}-\tfrac{\partial v}{\partial x}\Big|_{I,J+\frac{1}{2}}\right)\Big]\,[S_y]_{I,J+\frac{1}{2}}+ \\
&\Big[(\rho_{I-\frac{1}{2},J})(u_{I-\frac{1}{2},J})(v_{I-\frac{1}{2},J})-(\mu_{I-\frac{1}{2},J})\left(\tfrac{\partial u}{\partial y}\Big|_{I-\frac{1}{2},J}-\tfrac{\partial v}{\partial x}\Big|_{I-\frac{1}{2},J}\right)\Big]\,[S_y]_{I-\frac{1}{2},J}+ \\
&\Big[(\rho_{I,J-\frac{1}{2}})(u_{I,J-\frac{1}{2}})(v_{I,J-\frac{1}{2}})-(\mu_{I,J-\frac{1}{2}})\left(\tfrac{\partial u}{\partial y}\Big|_{I,J-\frac{1}{2}}-\tfrac{\partial v}{\partial x}\Big|_{I,J-\frac{1}{2}}\right)\Big]\,[S_y]_{I,J-\frac{1}{2}}\qquad\Bigg).
\end{aligned}
\tag{3.22}
$$

For the y-momentum case the spatial discretization is

$$
\begin{aligned}
&\tfrac{1}{V(\Omega_{I,J})}\sum_{m=1}^{4}\left(\Big[\rho v u-\mu\left(\tfrac{\partial v}{\partial x}+\tfrac{\partial u}{\partial y}\right)\Big]S_x+\Big[\rho v v+p-\tfrac{2}{3}\mu\left(2\tfrac{\partial v}{\partial y}-\tfrac{\partial u}{\partial x}\right)\Big]S_y\right)_m= \\
&\tfrac{1}{V(\Omega_{I,J})}\Bigg(\\
&\Big[(\rho_{I+\frac{1}{2},J})(v_{I+\frac{1}{2},J})(u_{I+\frac{1}{2},J})-(\mu_{I+\frac{1}{2},J})\left(\tfrac{\partial v}{\partial x}\Big|_{I+\frac{1}{2},J}-\tfrac{\partial u}{\partial y}\Big|_{I+\frac{1}{2},J}\right)\Big]\,[S_x]_{I+\frac{1}{2},J}+ \\
&\Big[(\rho_{I,J+\frac{1}{2}})(v_{I,J+\frac{1}{2}})(u_{I,J+\frac{1}{2}})-(\mu_{I,J+\frac{1}{2}})\left(\tfrac{\partial v}{\partial x}\Big|_{I,J+\frac{1}{2}}-\tfrac{\partial u}{\partial y}\Big|_{I,J+\frac{1}{2}}\right)\Big]\,[S_x]_{I,J+\frac{1}{2}}+ \\
&\Big[(\rho_{I-\frac{1}{2},J})(v_{I-\frac{1}{2},J})(u_{I-\frac{1}{2},J})-(\mu_{I-\frac{1}{2},J})\left(\tfrac{\partial v}{\partial x}\Big|_{I-\frac{1}{2},J}-\tfrac{\partial u}{\partial y}\Big|_{I-\frac{1}{2},J}\right)\Big]\,[S_x]_{I-\frac{1}{2},J}+ \\
&\Big[(\rho_{I,J-\frac{1}{2}})(v_{I,J-\frac{1}{2}})(u_{I,J-\frac{1}{2}})-(\mu_{I,J-\frac{1}{2}})\left(\tfrac{\partial v}{\partial x}\Big|_{I,J-\frac{1}{2}}-\tfrac{\partial u}{\partial y}\Big|_{I,J-\frac{1}{2}}\right)\Big]\,[S_x]_{I,J-\frac{1}{2}}+ \\
&\Big[(\rho_{I+\frac{1}{2},J})(v_{I+\frac{1}{2},J})(v_{I+\frac{1}{2},J})+(p_{I+\frac{1}{2},J})-\tfrac{2}{3}(\mu_{I+\frac{1}{2},J})\left(2\tfrac{\partial v}{\partial y}\Big|_{I+\frac{1}{2},J}-\tfrac{\partial u}{\partial x}\Big|_{I+\frac{1}{2},J}\right)\Big]\,[S_y]_{I+\frac{1}{2},J}+ \\
&\Big[(\rho_{I,J+\frac{1}{2}})(v_{I,J+\frac{1}{2}})(v_{I,J+\frac{1}{2}})+(p_{I,J+\frac{1}{2}})-\tfrac{2}{3}(\mu_{I,J+\frac{1}{2}})\left(2\tfrac{\partial v}{\partial y}\Big|_{I,J+\frac{1}{2}}-\tfrac{\partial u}{\partial x}\Big|_{I,J+\frac{1}{2}}\right)\Big]\,[S_y]_{I,J+\frac{1}{2}}+ \\
&\Big[(\rho_{I-\frac{1}{2},J})(v_{I-\frac{1}{2},J})(v_{I-\frac{1}{2},J})+(p_{I-\frac{1}{2},J})-\tfrac{2}{3}(\mu_{I-\frac{1}{2},J})\left(2\tfrac{\partial v}{\partial y}\Big|_{I-\frac{1}{2},J}-\tfrac{\partial u}{\partial x}\Big|_{I-\frac{1}{2},J}\right)\Big]\,[S_y]_{I-\frac{1}{2},J}+ \\
&\Big[(\rho_{I,J-\frac{1}{2}})(v_{I,J-\frac{1}{2}})(v_{I,J-\frac{1}{2}})+(p_{I,J-\frac{1}{2}})-\tfrac{2}{3}(\mu_{I,J-\frac{1}{2}})\left(2\tfrac{\partial v}{\partial y}\Big|_{I,J-\frac{1}{2}}-\tfrac{\partial u}{\partial x}\Big|_{I,J-\frac{1}{2}}\right)\Big]\,[S_y]_{I,J-\frac{1}{2}} \\
&\qquad\Bigg).
\end{aligned}
\tag{3.23}
$$

Finally, the spatial discretization for the energy equation is

$$\frac{1}{V(\Omega_{I,J})}\sum_{m=1}^{4}\Bigg(\Big[\,\rho uH - k\frac{\partial T}{\partial x} - \tfrac{2}{3}u\mu\left(2\frac{\partial u}{\partial x} - \frac{\partial v}{\partial y}\right) - v\mu\left(\frac{\partial u}{\partial y} + \frac{\partial v}{\partial x}\right)\Big]S_x + \Big[\rho vH - k\frac{\partial T}{\partial y} - u\mu\left(\frac{\partial v}{\partial x} + \frac{\partial u}{\partial y}\right) - \tfrac{2}{3}v\mu\left(2\frac{\partial v}{\partial y} - \frac{\partial u}{\partial x}\right)\Big]S_y\Bigg)_m = \frac{1}{V(\Omega_{I,J})}\Bigg(\Big[(\rho_{I+\frac{1}{2},J})(u_{I+\frac{1}{2},J})(H_{I+\frac{1}{2},J}) - (k_{I+\frac{1}{2},J})\left(\frac{\partial T}{\partial x}\Big|_{I+\frac{1}{2},J}\right) - \tfrac{2}{3}(u_{I+\frac{1}{2},J})(\mu_{I+\frac{1}{2},J})\left(2\frac{\partial u}{\partial x}\Big|_{I+\frac{1}{2},J} - \frac{\partial v}{\partial y}\Big|_{I+\frac{1}{2},J}\right) - (v_{I+\frac{1}{2},J})(\mu_{I+\frac{1}{2},J})\left(\frac{\partial u}{\partial y}\Big|_{I+\frac{1}{2},J} + \frac{\partial v}{\partial x}\Big|_{I+\frac{1}{2},J}\right)\Big][S_x]_{I+\frac{1}{2},J} + \Big[(\rho_{I,J+\frac{1}{2}})(u_{I,J+\frac{1}{2}})(H_{I,J+\frac{1}{2}}) - (k_{I,J+\frac{1}{2}})\left(\frac{\partial T}{\partial x}\Big|_{I,J+\frac{1}{2}}\right) - \tfrac{2}{3}(u_{I,J+\frac{1}{2}})(\mu_{I,J+\frac{1}{2}})\left(2\frac{\partial u}{\partial x}\Big|_{I,J+\frac{1}{2}} - \frac{\partial v}{\partial y}\Big|_{I,J+\frac{1}{2}}\right) - (v_{I,J+\frac{1}{2}})(\mu_{I,J+\frac{1}{2}})\left(\frac{\partial u}{\partial y}\Big|_{I,J+\frac{1}{2}} + \frac{\partial v}{\partial x}\Big|_{I,J+\frac{1}{2}}\right)\Big][S_x]_{I,J+\frac{1}{2}} + \Big[(\rho_{I-\frac{1}{2},J})(u_{I-\frac{1}{2},J})(H_{I-\frac{1}{2},J}) - (k_{I-\frac{1}{2},J})\left(\frac{\partial T}{\partial x}\Big|_{I-\frac{1}{2},J}\right) - \tfrac{2}{3}(u_{I-\frac{1}{2},J})(\mu_{I-\frac{1}{2},J})\left(2\frac{\partial u}{\partial x}\Big|_{I-\frac{1}{2},J} - \frac{\partial v}{\partial y}\Big|_{I-\frac{1}{2},J}\right) - (v_{I-\frac{1}{2},J})(\mu_{I-\frac{1}{2},J})\left(\frac{\partial u}{\partial y}\Big|_{I-\frac{1}{2},J} + \frac{\partial v}{\partial x}\Big|_{I-\frac{1}{2},J}\right)\Big][S_x]_{I-\frac{1}{2},J} + \Big[(\rho_{I,J-\frac{1}{2}})(u_{I,J-\frac{1}{2}})(H_{I,J-\frac{1}{2}}) - (k_{I,J-\frac{1}{2}})\left(\frac{\partial T}{\partial x}\Big|_{I,J-\frac{1}{2}}\right) - \tfrac{2}{3}(u_{I,J-\frac{1}{2}})(\mu_{I,J-\frac{1}{2}})\left(2\frac{\partial u}{\partial x}\Big|_{I,J-\frac{1}{2}} - \frac{\partial v}{\partial y}\Big|_{I,J-\frac{1}{2}}\right) - (v_{I,J-\frac{1}{2}})(\mu_{I,J-\frac{1}{2}})\left(\frac{\partial u}{\partial y}\Big|_{I,J-\frac{1}{2}} + \frac{\partial v}{\partial x}\Big|_{I,J-\frac{1}{2}}\right)\Big][S_x]_{I,J-\frac{1}{2}} + \Big[(\rho_{I+\frac{1}{2},J})(v_{I+\frac{1}{2},J})(H_{I+\frac{1}{2},J}) - (k_{I+\frac{1}{2},J})\left(\frac{\partial T}{\partial y}\Big|_{I+\frac{1}{2},J}\right) - (u_{I+\frac{1}{2},J})(\mu_{I+\frac{1}{2},J})\left(\frac{\partial v}{\partial x}\Big|_{I+\frac{1}{2},J} + \frac{\partial u}{\partial y}\Big|_{I+\frac{1}{2},J}\right) - \tfrac{2}{3}(v_{I+\frac{1}{2},J})(\mu_{I+\frac{1}{2},J})\left(2\frac{\partial v}{\partial y}\Big|_{I+\frac{1}{2},J} - \frac{\partial u}{\partial x}\Big|_{I+\frac{1}{2},J}\right)\Big][S_y]_{I+\frac{1}{2},J} + \Big[(\rho_{I,J+\frac{1}{2}})(v_{I,J+\frac{1}{2}})(H_{I,J+\frac{1}{2}}) - (k_{I,J+\frac{1}{2}})\left(\frac{\partial T}{\partial y}\Big|_{I,J+\frac{1}{2}}\right) - (u_{I,J+\frac{1}{2}})(\mu_{I,J+\frac{1}{2}})\left(\frac{\partial v}{\partial x}\Big|_{I,J+\frac{1}{2}} + \frac{\partial u}{\partial y}\Big|_{I,J+\frac{1}{2}}\right) - \tfrac{2}{3}(v_{I,J+\frac{1}{2}})(\mu_{I,J+\frac{1}{2}})\left(2\frac{\partial v}{\partial y}\Big|_{I,J+\frac{1}{2}} - \frac{\partial u}{\partial x}\Big|_{I,J+\frac{1}{2}}\right)\Big][S_y]_{I,J+\frac{1}{2}} + \Big[(\rho_{I-\frac{1}{2},J})(v_{I-\frac{1}{2},J})(H_{I-\frac{1}{2},J}) - (k_{I-\frac{1}{2},J})\left(\frac{\partial T}{\partial y}\Big|_{I-\frac{1}{2},J}\right) - (u_{I-\frac{1}{2},J})(\mu_{I-\frac{1}{2},J})\left(\frac{\partial v}{\partial x}\Big|_{I-\frac{1}{2},J} + \frac{\partial u}{\partial y}\Big|_{I-\frac{1}{2},J}\right) - \tfrac{2}{3}(v_{I-\frac{1}{2},J})(\mu_{I-\frac{1}{2},J})\left(2\frac{\partial v}{\partial y}\Big|_{I-\frac{1}{2},J} - \frac{\partial u}{\partial x}\Big|_{I-\frac{1}{2},J}\right)\Big][S_y]_{I-\frac{1}{2},J} + \Big[(\rho_{I,J-\frac{1}{2}})(v_{I,J-\frac{1}{2}})(H_{I,J-\frac{1}{2}}) - (k_{I,J-\frac{1}{2}})\left(\frac{\partial T}{\partial y}\Big|_{I,J-\frac{1}{2}}\right) - (u_{I,J-\frac{1}{2}})(\mu_{I,J-\frac{1}{2}})\left(\frac{\partial v}{\partial x}\Big|_{I,J-\frac{1}{2}} + \frac{\partial u}{\partial y}\Big|_{I,J-\frac{1}{2}}\right) - \tfrac{2}{3}(v_{I,J-\frac{1}{2}})(\mu_{I,J-\frac{1}{2}})\left(2\frac{\partial v}{\partial y}\Big|_{I,J-\frac{1}{2}} - \frac{\partial u}{\partial x}\Big|_{I,J-\frac{1}{2}}\right)\Big][S_y]_{I,J-\frac{1}{2}}\Bigg). \tag{3.24}$$

Use of the discretization, equation (3.20), into (3.19) gives, according to the method of lines, to the following system of ordinary differential equations for the

volume $\Omega_{I,J}$.

$$\frac{d\overline{W}}{dt} + \frac{1}{V(\Omega_{I,J})} \sum_{m=1}^{4} \Big(F_{Tx}\, S_x + F_{Ty}\, S_y \Big)_m = 0\,. \tag{3.25}$$

When this relationship is written down for all control volumes (i.e., for $\Omega_{I,J}$ with $1 \le I \le IMAX$ and $1 \le J \le JMAX$) a system of ordinary differential equations of first order is obtained. This system is hyperbolic in time which means that one needs to advance them in time starting from a known initial solutions. Suitable boundary conditions for the fluxes must be provided. The time advancement and boundary conditions are discussed in latter sections.

As it can be seen in equations (3.21) to (3.24), the spatial discretization can be computed if the flow variables ρ, u, v, p, H, the transport properties μ, k and the gradients $\partial u_i/\partial x_j$ and $\partial T/\partial x_i$ are known at the mid-points of the cell faces. Furthermore, the geometric quantities of the cell element (the volume of the cell element and S_x together with S_y for every cell face) are also required. The geometric quantities are discussed last in the spatial discretization analysis.

Let ζ denote any of the flow variables and transport properties needed to compute equations (3.21) to (3.24). That is, ζ takes values of ρ, u, v, p, H, μ and k (note that ζ does not represent the gradients). In the following section, the methodology employed to determine quantities ζ at the mid-point of cell face $(I+\frac{1}{2}, J)$ is presented. A discussion for the rest of cell faces is left for a latter section.

1. Computation of Quantities ζ at Mid-Point of Cell Face $(I + \frac{1}{2}, J)$

Quantities ζ are determined as function of the conserved variables W and therefore W and ζ share the same location whichever that is. As it will be seen later in detail, the solution procedure used in this work is such that in order to compute ζ at mid-points of cell faces (necessary to compute the second term of equation (3.25)), the

conserved variables $\overline{W}$ which appear in the first term of equation (3.25) should be used to compute $\overline{\zeta}$ first. Then, an interpolation scheme should be implemented between quantities $\overline{\zeta}$ to get ζ at the mid-points of the cell faces. Since the exact location of $\overline{W}$ (and therefore the location of $\overline{\zeta}$) is unknown, then no interpolation scheme can be implemented and thus the computation of quantities ζ at the mid-points of the cell faces cannot be done (using equation (3.25)).

To overcome the difficulty of not knowing where the averaged variables are, $\overline{W}$ is replaced with $W_{I,J}$ in equation (3.25). The discrete variables $W_{I,J}$ represent point values of W at a specific location within the cell $\Omega_{I,J}$. Choosing of the cell's centroid as the place where $W_{I,J}$ is positioned (see Figure 4) retains the second order accuracy [27] and makes the scheme "cell centered". That is, if $W_{I,J}$ is any of the conserved variables at the cell's centroid, then

$$W_{I,J} = \frac{1}{V}\int_{\Omega} W\, dV + O(V^2) \approx \overline{W}. \tag{3.26}$$

Equation (3.25) then becomes

$$\frac{dW_{I,J}}{dt} + \frac{1}{V(\Omega_{I,J})}\sum_{m=1}^{4}\Big(F_{T_x}\,S_x + F_{T_y}\,S_y\Big)_m = 0\,, \tag{3.27}$$

where $W_{I,J}$ now represents any of the conserved variables *at* the cell's centroid (see Figure 4).

Quantities ζ at mid-points of cell faces can now be computed by interpolation in terms of $\zeta_{I,J}$, which are determined using $W_{I,J}$, just as the solution procedure mentioned above states. The interpolation scheme used in this research is a simple arithmetic average. Thus, for face $(I+\frac{1}{2}, J)$ (see Figure 4)

$$\zeta_{I+\frac{1}{2},J} = \frac{1}{2}(\zeta_{I,J} + \zeta_{I+1,J}). \tag{3.28}$$

A similar procedure is used for finding ζ at the rest of mid-points of the grid cell $\Omega_{I,J}$

as it will bee seen in a latter section. Keep in mind that quantities ζ as obtained in equation (3.28) are those needed to compute fluxes F_{Tx} and F_{Ty} at mid-points of cell faces $(I+\frac{1}{2}, J)$ as dictated by equation (3.27), that is, they represent values of ρ, u, v, p, H, μ and k at the mid-points of cell faces $(I+\frac{1}{2}, J)$.

As it can be seen in equations (3.17) and (3.18), the gradients $\partial u_i/\partial x_j$ and $\partial T/\partial x_i$ are also required at the mid-points of cell faces in order to compute F_{Tx} and F_{Ty} at those points. Let ϕ denote any of the u_i or T scalar variables. The required gradients can then be represented in a general way as $\partial\phi/\partial x_i$. In the next section the computation of these gradients at the mid-point of cell face $(I+\frac{1}{2}, J)$ is discussed.

2. Computation of Gradients $\partial\phi/\partial x_i$ at Mid-Point of Cell Face $(I+\frac{1}{2}, J)$

A general procedure to estimate the gradients $\partial\phi/\partial x_i$, valid for an arbitrary control volume in two or three dimensions, can be derived by the application of the divergence theorem. This theorem can be considered as defining the average of the gradient of the scalar ϕ as a function of its values at the boundaries of the volume under consideration (see e.g., [24] p. 253).

Attention is placed for now on the computation of $\partial\phi/\partial x_i$ at the mid-point of cell face $(I+\frac{1}{2}, J)$ belonging to grid cell $\Omega_{I,J}$. With this purpose in mind, and in accordance with the previous paragraph, an auxiliary cell Ω' with bounding surface $\partial\Omega'$, as shown in Figure 5, is built and used. Since for this Ω' (or any other arbitrary volume)

$$\int_{\Omega'} \vec{\nabla}\phi \, dV' = \oint_{\partial\Omega'} \phi \, d\vec{S}', \tag{3.29}$$

then one can define the averaged gradients as

$$V'(\Omega') \left(\overline{\frac{\partial\phi}{\partial x}} \right) \equiv \int_{\Omega'} \frac{\partial\phi}{\partial x} \, dV' = \oint_{\partial\Omega'} \phi \, dS'_x \,, \tag{3.30}$$

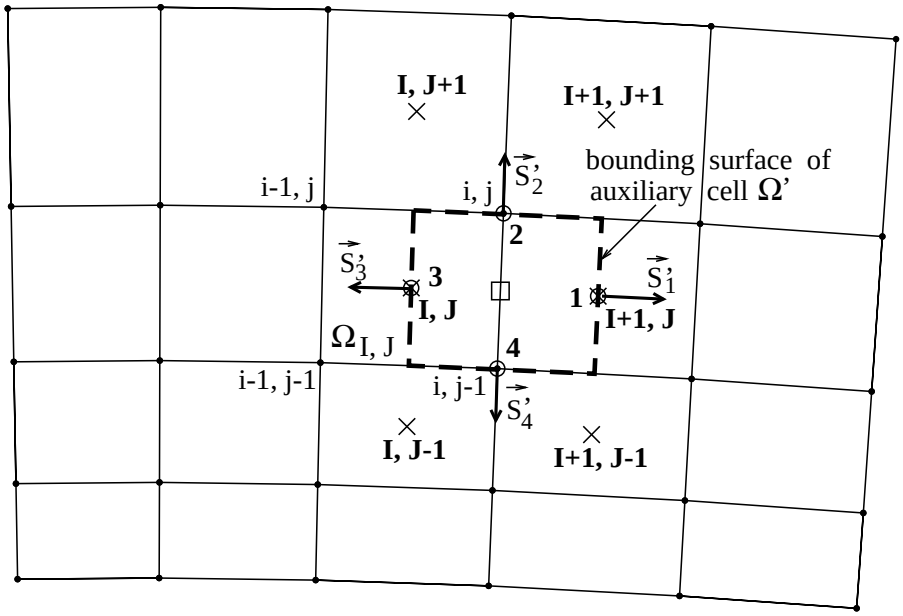

Fig. 5.: Auxiliary cell for computation of $\partial\phi/\partial x_i$ on the mid-point of cell face $(I+\frac{1}{2},\ J)$ corresponding to grid cell $\Omega_{I,J}$.

and

$$V'(\Omega')\left(\overline{\frac{\partial\phi}{\partial y}}\right) \equiv \int_{\Omega'} \frac{\partial\phi}{\partial y}\, dV' = \oint_{\partial\Omega'} \phi\, dS'_y. \tag{3.31}$$

Here again, $\overline{\frac{\partial\phi}{\partial x}}$ and $\overline{\frac{\partial\phi}{\partial y}}$ are at unknown locations inside Ω', therefore, and in the same way as in the previous section, these are replaced with specific point values. The values at the centroid of Ω' are chosen in order to maintain second order accuracy. The centroid of the auxiliary cells used to find $\partial\phi/\partial x_i$ at mid-points of faces $(I+\frac{1}{2}, J)$ for cells $\Omega_{I,J}$ are assumed to lay precisely at those points. The x-component of the

gradient is therefore

$$\left.\frac{\partial\phi}{\partial x}\right|_{I+\frac{1}{2},J} = \frac{1}{V'(\Omega')}\oint_{\partial\Omega'}\phi\, dS'_x\,, \tag{3.32}$$

while the y-component is

$$\left.\frac{\partial\phi}{\partial y}\right|_{I+\frac{1}{2},J} = \frac{1}{V'(\Omega')}\oint_{\partial\Omega'}\phi\, dS'_y\,. \tag{3.33}$$

The surface integral of equation (3.32) is approximated using the mid-point rule

$$\oint_{\partial\Omega'}\phi\, dS'_x = \sum_{m'=1}^{4}(\phi\, S'_x)_{m'} = \phi_1\, S'_{x\,1} + \phi_2\, S'_{x\,2} + \phi_3\, S'_{x\,3} + \phi_4\, S'_{x\,4}, \tag{3.34}$$

where m' now represents any of the four faces of the auxiliary cell (see Figure 5). Substitution of equation (3.34) into (3.32) gives the approximation for the term $\partial\phi/\partial x$ at the mid-point of face $(I+\frac{1}{2}, J)$ of grid cell $\Omega_{I,J}$. That is

$$\left.\frac{\partial\phi}{\partial x}\right|_{I+\frac{1}{2},J} = \frac{1}{V'(\Omega')}\Big(\phi_1\, S'_{x\,1} + \phi_2\, S'_{x\,2} + \phi_3\, S'_{x\,3} + \phi_4\, S'_{x\,4}\Big). \tag{3.35}$$

Similarly, for the y-component

$$\left.\frac{\partial\phi}{\partial y}\right|_{I+\frac{1}{2},J} = \frac{1}{V'(\Omega')}\Big(\phi_1\, S'_{y\,1} + \phi_2\, S'_{y\,2} + \phi_3\, S'_{y\,3} + \phi_4\, S'_{y\,4}\Big). \tag{3.36}$$

As it can be seen in equations (3.35) and (3.36), values of ϕ and of the components of $\vec{S}'$ are needed at the mid-points of faces for the auxiliary cell Ω' (points 1 to 4 in Figure 5). Furthermore, the volume of the auxiliary cell, $V(\Omega')$, is also required. The way these values are computed is discussed next[2]

For the particular case of the auxiliary cell of Figure 5, it is easily seen that points 1 and 3 of Ω' coincide (or are assumed to coincide) with centroids $(I+1, J)$ and (I, J)

[2]The geometric quantities for auxiliary cells Ω' are computed in terms of the geometric quantities for the domain's grid cells $\Omega_{I,J}$. The latter are discussed in other section

of the grid cells $\Omega_{I+1,J}$ and $\Omega_{I,J}$ respectively. On these centroids, all variables ϕ are available, therefore one just sets

$$\phi_1 = \phi_{I+1,J}, \tag{3.37}$$

$$\phi_3 = \phi_{I,J}, \tag{3.38}$$

(recall ϕ can be any of u_i or T and that they are available at the centroids of all sub-volumes of the domain).

Values of ϕ at points 2 and 4 of the same auxiliary cell mentioned above are determined by means of an arithmetic average between the values of ϕ at grid cell centroids surrounding the point under investigation. From Figure 5 it can be seen that for points 2 and 4

$$\phi_2 = \tfrac{1}{4}\big(\phi_{I+1,J} + \phi_{I+1,J+1} + \phi_{I,J+1} + \phi_{I,J}\big), \tag{3.39}$$

$$\phi_4 = \tfrac{1}{4}\big(\phi_{I+1,J-1} + \phi_{I+1,J} + \phi_{I,J} + \phi_{I,J-1}\big), \tag{3.40}$$

respectively.

In order to define $\vec{S}'$ and $V(\Omega')$ for the auxiliary cells, it is for now assumed that the area vectors $\vec{S}(\Omega_{I,J})$ and volumes $V(\Omega_{I,J})$ for all of the domain's cell elements are available. These will be precisely defined in a latter section.

The vector $\vec{S}'$ (i.e. ${S'}_x$ and ${S'}_y$) is computed with a simple arithmetic average between corresponding area vectors of the domain's grid cells.

For the particular case of the auxiliary cell of Figure 6, corresponding to the computation of $\partial\phi/\partial x_i$ at the mid-point of cell face $(I+\frac{1}{2}, J)$ for cell $\Omega_{I,J}$, it is easy to see that

$$S'_{x1} = \tfrac{1}{2}\Big([S_x]_{I+\frac{3}{2},J} + [S_x]_{I+\frac{1}{2},J}\Big), \tag{3.41}$$

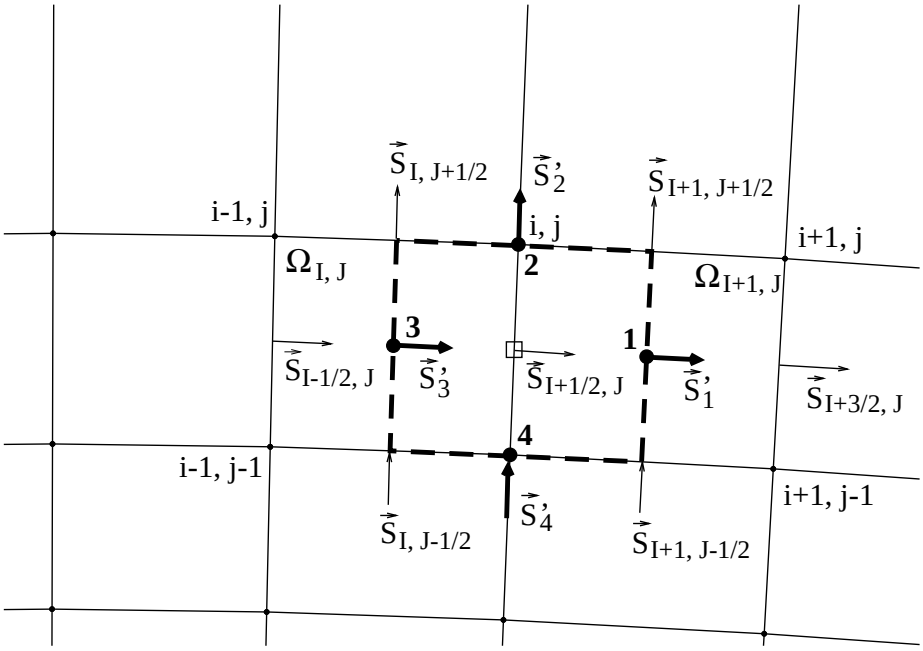

Fig. 6.: Area vectors of auxiliary cell Ω' and area vectors of the cell elements Ω for their computation.

where $(S_x)_{I+\frac{3}{2},J}$ actually is $(S_x)_{[I+1]+\frac{1}{2},J}$. That is, $(S_x)_{I+\frac{3}{2},J}$ is the *east* face of the grid cell $\Omega_{I+1,J}$ (see Figure 6). Similarly, for points 2 to 4

$$S'_{x2} = \frac{1}{2}\Big([S_x]_{I+1,J+\frac{1}{2}} + [S_x]_{I,J+\frac{1}{2}}\Big), \tag{3.42}$$

$$S'_{x3} = -\frac{1}{2}\Big([S_x]_{I-\frac{1}{2},J} + [S_x]_{I+\frac{1}{2},J}\Big), \tag{3.43}$$

$$S'_{x4} = -\frac{1}{2}\Big([S_x]_{I+1,J-\frac{1}{2}} + [S_x]_{I,J-\frac{1}{2}}\Big). \tag{3.44}$$

In order to get the y-components of $\vec{S}'$, as required in equation (3.36), one just

replaces sub-indexes x with sub-indexes y in equations (3.41) to (3.44), that is

$$S'_{y1} = \frac{1}{2}\Big([S_y]_{I+\frac{3}{2},J} + [S_y]_{I+\frac{1}{2},J}\Big), \tag{3.45}$$

$$S'_{y2} = \frac{1}{2}\Big([S_y]_{I+1,J+\frac{1}{2}} + [S_y]_{I,J+\frac{1}{2}}\Big), \tag{3.46}$$

$$S'_{y3} = -\frac{1}{2}\Big([S_y]_{I-\frac{1}{2},J} + [S_y]_{I+\frac{1}{2},J}\Big), \tag{3.47}$$

$$S'_{y4} = -\frac{1}{2}\Big([S_y]_{I+1,J-\frac{1}{2}} + [S_y]_{I,J-\frac{1}{2}}\Big). \tag{3.48}$$

Finally, it just remains to determine $V'(\Omega')$ such that equations (3.35) and (3.36) can be used to compute the gradients at mid-points of cell faces $(I+\frac{1}{2}, J)$. The volumes of the auxiliary cells $V'(\Omega')$, as mentioned above, are computed in terms of grid cell volumes $V(\Omega_{I,J})$ (defined in a latter section). Again, a simple arithmetic average is used between the two volumes where Ω' lies. For the particular case of the auxiliary cell Ω' shown in Figure 6 one has

$$V'(\Omega') = \frac{1}{2}\Big(V(\Omega_{I,J}) + V(\Omega_{I+1,J})\Big). \tag{3.49}$$

The gradient $(\partial\phi/\partial x)\big|_{I+1/2,J}$ can now be computed by using equation (3.35) with ϕ_1 to ϕ_4 defined by equations (3.41) to (3.44), S'_{x1} to S'_{x4} defined by equations (3.41) to (3.44) and with $V'(\Omega')$ as given by equation (3.49). On the other hand, in order to compute $(\partial\phi/\partial y)\big|_{I+1/2,J}$ by means of equation (3.36), one uses the same ϕ's and the same $V'(\Omega')$ as those used for $(\partial\phi/\partial x)\big|_{I+1/2,J}$ above. In addition, equations (3.45) to (3.48) must be used in order to determine S'_{y1} to S'_{y4} as dictated by equation (3.36).

The computations of the gradients $(\partial\phi/\partial x)\big|_{I+1/2,J}$ and $(\partial\phi/\partial y)\big|_{I+1/2,J}$ is then complete for the mid-point of cell face $(I+\frac{1}{2}, J)$. A brief description on the computation of quantities and gradients needed for the computation of F_{Tx} and F_{Ty} (equations (3.17) and (3.18)) on the rest of mid-points of faces is given in the next section.

3. Computation of ζ and $\partial\phi/\partial x_i$ on the Rest of Mid-Points of Cell Faces

Quantities ζ at mid-points of faces $(I, J+\frac{1}{2})$, $(I-\frac{1}{2}, J)$ and $(I, J-\frac{1}{2})$, corresponding to cell element $\Omega_{I,J}$, are computed as follows (see Figure 4)

$$\zeta_{I,J+\frac{1}{2}} = \frac{1}{2}\big(\zeta_{I,J} + \zeta_{I,J+1}\big), \tag{3.50}$$

$$\zeta_{I-\frac{1}{2},J} = \frac{1}{2}\big(\zeta_{I,J} + \zeta_{I-1,J}\big), \tag{3.51}$$

$$\zeta_{I,J-\frac{1}{2}} = \frac{1}{2}\big(\zeta_{I,J} + \zeta_{I,J-1}\big). \tag{3.52}$$

In order to compute the gradients $(\partial\phi/\partial x_i)$ at mid-points of faces $(I, J+\frac{1}{2})$, $(I-\frac{1}{2}, J)$ and $(I, J-\frac{1}{2})$, corresponding to cell element $\Omega_{I,J}$, formulas similar to (3.35) and (3.36) are used. In those formulas the mid-point of face $(I+\frac{1}{2}, J)$ is assumed to be the centroid of the auxiliary cell Ω' (see Figure 5). If in general, the mid-points $(I, J+\frac{1}{2})$, $(I-\frac{1}{2}, J)$ and $(I, J-\frac{1}{2})$ are considered to be the centroids of auxiliary cells built to compute the gradients at those points (see Figure 7), then general formulas for computation of the gradients at mid-points of cell faces corresponding to cell element $\Omega_{I,J}$ can be written

$$\left.\frac{\partial\phi}{\partial x}\right|_{\text{centroid of } \Omega'} = \frac{1}{V'(\Omega')}\Big(\phi_1\, S'_{x\,1} + \phi_2\, S'_{x\,2} + \phi_3\, S'_{x\,3} + \phi_4\, S'_{x\,4}\Big), \tag{3.53}$$

$$\left.\frac{\partial\phi}{\partial y}\right|_{\text{centroid of } \Omega'} = \frac{1}{V'(\Omega')}\Big(\phi_1\, S'_{y\,1} + \phi_2\, S'_{y\,2} + \phi_3\, S'_{y\,3} + \phi_4\, S'_{y\,4}\Big). \tag{3.54}$$

The way the right hand side of these equations is computed depends on the position and characteristics of the auxiliary cell Ω'. Since for every mid-point of the cell faces the auxiliary cell differs, then the computation of the variables on the right hand sides of equations (3.53) and (3.54) differs too[3].

[3]The procedure is similar to that described in the previous section.

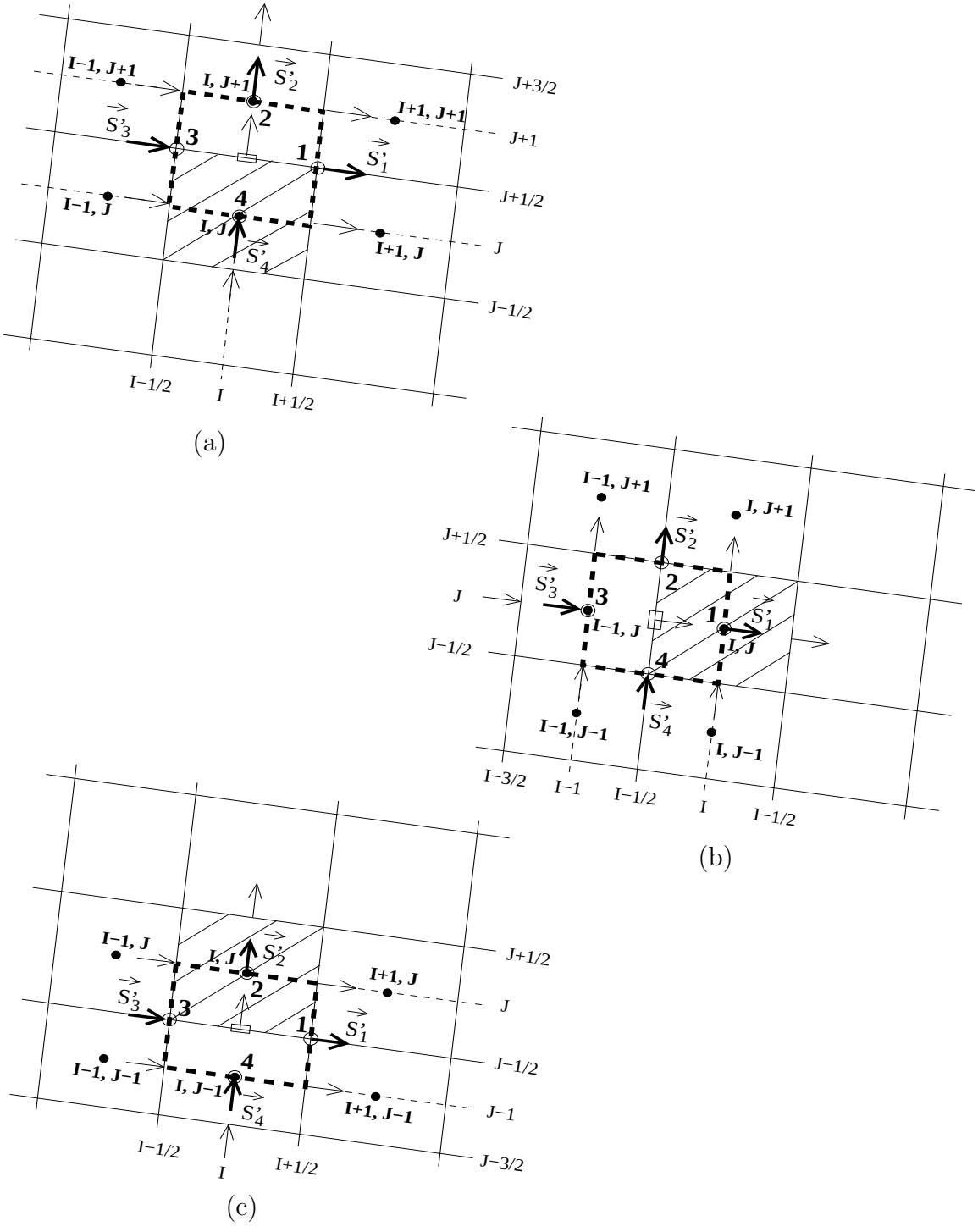

Fig. 7.: Auxiliary cells for computation of gradients on faces of $\Omega_{I,J}$.

The employed formulas for the mid-point on cell face $(I, J+\frac{1}{2})$ are (see Figure 7a)

$$\begin{aligned}
\phi_1 &= \tfrac{1}{4}(\phi_{I,J} + \phi_{I+1,J} + \phi_{I+1,J+1} + \phi_{I,J+1}), && (3.55)\\
\phi_2 &= \phi_{I,J+1}, && (3.56)\\
\phi_3 &= \tfrac{1}{4}(\phi_{I-1,J} + \phi_{I,J} + \phi_{I,J+1} + \phi_{I-1,J+1}), && (3.57)\\
\phi_4 &= \phi_{I,J}, && (3.58)
\end{aligned}$$

$$\begin{aligned}
S'_{x\,1} &= \tfrac{1}{2}\Big([S_x]_{I+\frac{1}{2},J} + [S_x]_{I+\frac{1}{2},J+1}\Big), && (3.59)\\
S'_{x\,2} &= \tfrac{1}{2}\Big([S_x]_{I,J+\frac{1}{2}} + [S_x]_{I,J+\frac{3}{2}}\Big), && (3.60)\\
S'_{x\,3} &= -\tfrac{1}{2}\Big([S_x]_{I-\frac{1}{2},J} + [S_x]_{I-\frac{1}{2},J+1}\Big), && (3.61)\\
S'_{x\,4} &= -\tfrac{1}{2}\Big([S_x]_{I,J-\frac{1}{2}} + [S_x]_{I,J+\frac{1}{2}}\Big), && (3.62)\\
V'(\Omega') &= \tfrac{1}{2}\Big(V(\Omega_{I,J}) + V(\Omega_{I,J+1})\Big). && (3.63)
\end{aligned}$$

For the mid-point of cell face $(I-\frac{1}{2}, J)$ the used formulas are (see Figure 7b)

$$\begin{aligned}
\phi_1 &= \phi_{I,J}, && (3.64)\\
\phi_2 &= \tfrac{1}{4}(\phi_{I-1,J} + \phi_{I,J} + \phi_{I,J+1} + \phi_{I-1,J+1}), && (3.65)\\
\phi_3 &= \phi_{I-1,J}, && (3.66)\\
\phi_4 &= \tfrac{1}{4}(\phi_{I-1,J-1} + \phi_{I,J-1} + \phi_{I,J} + \phi_{I-1,J}), && (3.67)
\end{aligned}$$

$$\begin{aligned}
S'_{x\,1} &= \tfrac{1}{2}\Big([S_x]_{I+\frac{1}{2},J} + [S_x]_{I-\frac{1}{2},J}\Big), && (3.68)\\
S'_{x\,2} &= \tfrac{1}{2}\Big([S_x]_{I,J+\frac{1}{2}} + [S_x]_{I-1,J+\frac{3}{2}}\Big), && (3.69)\\
S'_{x\,3} &= -\tfrac{1}{2}\Big([S_x]_{I-\frac{1}{2},J} + [S_x]_{I-\frac{3}{2},J}\Big), && (3.70)\\
S'_{x\,4} &= -\tfrac{1}{2}\Big([S_x]_{I,J-1} + [S_x]_{I-1,J-1}\Big), && (3.71)\\
V'(\Omega') &= \tfrac{1}{2}\Big(V(\Omega_{I,J}) + V(\Omega_{I-1,J})\Big). && (3.72)
\end{aligned}$$

Finally, for the mid-point of cell face $(I, J-\frac{1}{2})$ the formulas are (see Figure 7c)

$$\phi_1 = \tfrac{1}{4}(\phi_{I,J-1} + \phi_{I+1,J-1} + \phi_{I+1,J} + \phi_{I,J}), \tag{3.73}$$

$$\phi_2 = \phi_{I,J}, \tag{3.74}$$

$$\phi_3 = \tfrac{1}{4}(\phi_{I-1,J-1} + \phi_{I,J-1} + \phi_{I,J} + \phi_{I-1,J}), \tag{3.75}$$

$$\phi_4 = \phi_{I,J-1}, \tag{3.76}$$

$$S'_{x\,1} = \tfrac{1}{2}\Big([S_x]_{I+\frac{1}{2},J} + [S_x]_{I+\frac{1}{2},J-1}\Big), \tag{3.77}$$

$$S'_{x\,2} = \tfrac{1}{2}\Big([S_x]_{I,J+\frac{1}{2}} + [S_x]_{I,J-\frac{1}{2}}\Big), \tag{3.78}$$

$$S'_{x\,3} = -\tfrac{1}{2}\Big([S_x]_{I-\frac{1}{2},J} + [S_x]_{I-\frac{1}{2},J-1}\Big), \tag{3.79}$$

$$S'_{x\,4} = -\tfrac{1}{2}\Big([S_x]_{I,J-\frac{1}{2}} + [S_x]_{I,J-\frac{3}{2}}\Big), \tag{3.80}$$

$$V'(\Omega') = \tfrac{1}{2}\Big(V(\Omega_{I,J}) + V(\Omega_{I,J-1})\Big). \tag{3.81}$$

The y-versions of formulas (3.59) to (3.62), (3.68) to (3.71) and (3.77) to (3.80) (corresponding to the x-components of the area vectors for the auxiliary cells) are obtained simply by changing x-indexes to y-indexes in the corresponding formula.

4. Geometrical Quantities of a Cell Element

The geometrical quantities that are needed in order to complete the spatial discretization (see equations (3.21) to (3.24)) are the volume and the area vectors of the cell elements. Note that the geometrical quantities of the auxiliary cells used to compute the gradients at cell faces are computed in terms of these quantities.

The two-dimensional case is a special case of a three-dimensional problem where the solution is symmetric with respect to one coordinate direction. The two-dimensional problem analyzed here is symmetric with respect to the z-direction. Because of this symmetry and in order to obtain correct physical units for volume, pressure, etc.,

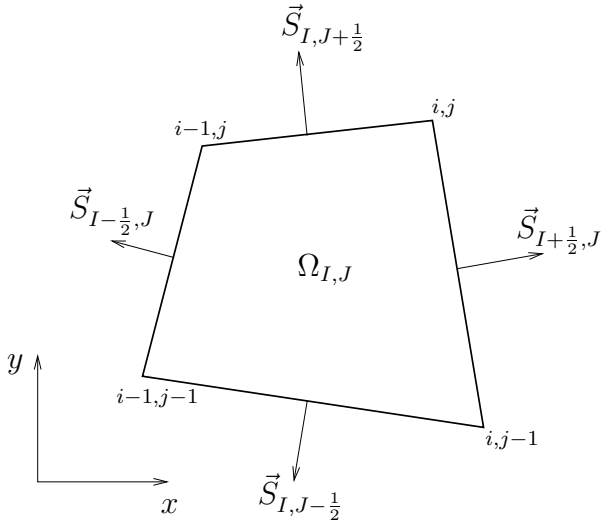

Fig. 8.: Control volume and associated face vectors for grid cell $\Omega_{I,J}$.

the depth of all grid cells is set to the constant value of one; furthermore, the two-dimensional shape and size of the cell $\Omega_{I,J}$ are kept identical along this depth. Therefore, the volume of a two-dimensional cell numerically equals the area of that cell[4]. Its units are, of course, ℓ^3.

The area of an arbitrary quadrilateral as that shown in Figure 8 is determined as half the value of the magnitude of the vector resulting from the cross product between the position vectors forming its diagonals. Let $\vec{V}_{d1}$ and $\vec{V}_{d2}$ be the position vectors corresponding to the diagonals of the cell element. That is

$$\begin{aligned} \vec{V}_{d1} &= \left[x_{(i-1,j-1)} - x_{(i,j)}\right]\hat{\imath} + \left[y_{(i-1,j-1)} - y_{(i,j)}\right]\hat{\jmath}, \\ \vec{V}_{d2} &= \left[x_{(i,j-1)} - x_{(i-1,j)}\right]\hat{\imath} + \left[y_{(i,j-1)} - y_{(i-1,j)}\right]\hat{\jmath}. \end{aligned}$$

[4]The procedure for finding the volume for general three-dimensional problems is different to that for the two dimensional case. The procedure given in [24], pp. 258-260 was followed in this research for the three-dimensional cases.

The cross product of these is

$$\vec{V}_{d1} \times \vec{V}_{d2} = \begin{vmatrix} \hat{\imath} & \hat{\jmath} & \hat{k} \\ x_{(i-1,j-1)} - x_{(i,j)} & y_{(i-1,j-1)} - y_{(i,j)} & 0 \\ x_{(i,j-1)} - x_{(i-1,j)} & y_{(i,j-1)} - y_{(i-1,j)} & 0 \end{vmatrix},$$

$$\begin{aligned} \vec{V}_{d1} \times \vec{V}_{d2} \;\; = \;\; & \hat{k} \Big\{ \big[x_{(i-1,j-1)} - x_{(i,j)}\big] \big[y_{(i,j-1)} - y_{(i-1,j)}\big] - \\ & \big[x_{(i,j-1)} - x_{(i-1,j)}\big] \big[y_{(i-1,j-1)} - y_{(i,j)}\big] \Big\}. \end{aligned}$$

This is a vector with a single component in the positive direction of z (positive because of the disposition of the vectors forming the cross product). Therefore the magnitude of this vector equals the value of the z-component

$$\begin{aligned} \Big|(\vec{V}_{d1} \times \vec{V}_{d2})\Big| \;\; = \;\; & \big[x_{(i-1,j-1)} - x_{(i,j)}\big] \big[y_{(i,j-1)} - y_{(i-1,j)}\big] - \\ & \big[x_{(i,j-1)} - x_{(i-1,j)}\big] \big[y_{(i-1,j-1)} - y_{(i,j)}\big]. \end{aligned}$$

Finally, the area of the quadrilateral (or the volume of the two-dimensional cell) is

$$\begin{aligned} V(\Omega_{I,J}) = \frac{1}{2} \Big|(\vec{V}_{d1} \times \vec{V}_{d2})\Big| \;\; = \;\; & \frac{1}{2} \Big\{ \big[x_{(i-1,j-1)} - x_{(i,j)}\big] \big[y_{(i,j-1)} - y_{(i-1,j)}\big] - \\ & \big[x_{(i,j-1)} - x_{(i-1,j)}\big] \big[y_{(i-1,j-1)} - y_{(i,j)}\big] \Big\}. \end{aligned} \tag{3.82}$$

The cross product between the position vectors forming the face's diagonals gives a vector which is normal to the face and whose magnitude equals the double of the area of the face. Therefore, this cross product can be used to determine the area vectors too. As mentioned above, for two-dimensional problems it is considered that the shape and size of the cell $\Omega_{I,J}$ are kept identical along the depth which is set to one (the depth runs along the z-direction). With this in mind, the area vectors as shown in Figure 8 can be computed as follows (disregarding the k-index in the x and

y coordinates forming the result of the cross product —because $x_{(i,j,k)} = x_{(i,j,k-1)}$ and $y_{(i,j,k)} = y_{(i,j,k-1)}$ for all $_{i,j}$)

$$\vec{S}_{I+\frac{1}{2},J} = [\, y_{(i,j)} - y_{(i,j-1)} \,]\, \hat{\imath} - [\, x_{(i,j)} - x_{(i,j-1)} \,]\, \hat{\jmath},$$

$$\vec{S}_{I,J+\frac{1}{2}} = [\, y_{(i-1,j)} - y_{(i,j)} \,]\, \hat{\imath} - [\, x_{(i-1,j)} - x_{(i,j)} \,]\, \hat{\jmath},$$

$$\vec{S}_{I-\frac{1}{2},J} = [\, y_{(i-1,j-1)} - y_{(i-1,j)} \,]\, \hat{\imath} - [\, x_{(i-1,j-1)} - x_{(i-1,j)} \,]\, \hat{\jmath},$$

$$\vec{S}_{I,J-\frac{1}{2}} = [\, y_{(i,j-1)} - y_{(i-1,j-1)} \,]\, \hat{\imath} - [\, x_{(i,j-1)} - x_{(i-1,j-1)} \,]\, \hat{\jmath}.$$

From where obviously

$$[S_x]_{I+\frac{1}{2},J} = y_{(i,j)} - y_{(i,j-1)}, \qquad [S_y]_{I+\frac{1}{2},J} = -x_{(i,j)} + x_{(i,j-1)}, \tag{3.83}$$

$$[S_x]_{I,J+\frac{1}{2}} = y_{(i-1,j-1)} - y_{(i-1,j)}, \qquad [S_y]_{I,J+\frac{1}{2}} = -x_{(i-1,j-1)} + x_{(i-1,j)}, \tag{3.84}$$

$$[S_x]_{I-\frac{1}{2},J} = y_{(i-1,j-1)} - y_{(i-1,j)}, \qquad [S_y]_{I-\frac{1}{2},J} = -x_{(i-1,j-1)} + x_{(i-1,j)}, \tag{3.85}$$

$$[S_x]_{I,J-\frac{1}{2}} = y_{(i,j-1)} - y_{(i-1,j-1)}, \qquad [S_y]_{I,J-\frac{1}{2}} = -x_{(i,j-1)} + x_{(i-1,j-1)}. \tag{3.86}$$

This completes the spatial discretization. All the quantities required to compute equations (3.21) to (3.24) have been derived. As mentioned in the previous sections, the scheme is cell centered and the basic idea of this kind of scheme is to be able to compute the total fluxes at a face of the control volume from the arithmetic average of the involved variables on both sides of the face. This, however, leads to odd-even decoupling of the solution (generation of two independent solutions of the discretized equations) and wiggles in regions containing severe pressure gradients in the neighborhood of shock waves or stagnation points [28]. Therefore, it is necessary to augment the finite volume scheme by the addition of artificial dissipative terms.

The artificial dissipation (or artificial viscosity) is discussed in the next section.

G. Artificial Dissipation

The concept of artificial dissipation was introduced by Von Neumann in a classic paper with R. D. Ritchmeyer [29]. Since the appearance of the original paper by Von Neumann, the concept of artificial viscosity has been discussed and/or utilized by several researchers, of which perhaps the most important is that of Lax and Wendroff [30] who provide a detailed theoretical discussion of the corrective role played by the artificial viscosity. In particular, they show how certain schemes exhibit error modes which change sign at alternate grid points leading to oscillatory type of numerical solutions and how the artificial viscosity tends to counteract these oscillations by simulating the effects of physical viscosity on the scale of the mesh.

In the context of fluid dynamics phenomena, artificial dissipation was probably first used by MacCormack and Baldwin [31]. The derivation of good dissipation operators does not follow prescribed, fixed rules but it is a matter of trial and error and making use of those which work most effectively.

In this research, the popular and widely used operator derived by Jameson [28] was utilized. Jameson, by means of numerical experiments, established that an effective operator is a blend of first and third differences of the conserved variables, with coefficients which depend on the local pressure gradient. Let the artificial dissipation operator be denoted as $D(W_{I,J})$ with $W_{I,J}$ representing any of the conserved variables

at centroid of the cell element $\Omega_{I,J}$. Therefore

$$D(W_{I,J}) = \left\{ \begin{array}{l} D([\rho]_{I,J}) \\ D([\rho u]_{I,J}) \\ D([\rho v]_{I,J}) \\ D([\rho E]_{I,J}) \end{array} \right\}. \tag{3.87}$$

The addition of this operator to the original governing equation (equation (3.27)) gives the following new governing equation which is solved in this work.

$$V(\Omega_{I,J})\frac{dW_{I,J}}{dt} + \sum_{m=1}^{4} \Big(F_{Tx}\, S_x + F_{Ty}\, S_y \Big)_m - D(W_{I,J}) = 0. \tag{3.88}$$

Let the following operator for the above spatial discretization be introduced

$$Q([\rho]_{I,J}) = \sum_{m=1}^{4} \Big(\big[\rho u\big] S_x + \big[\rho v\big] S_y \Big)_m, \tag{3.89}$$

$$Q([\rho u]_{I,J}) = \sum_{m=1}^{4} \left(\left[\rho uu + p - \tfrac{2}{3}\mu \left(2\tfrac{\partial u}{\partial x} - \tfrac{\partial v}{\partial y} \right) \right] S_x + \left[\rho uv - \mu \left(\tfrac{\partial u}{\partial y} + \tfrac{\partial v}{\partial x} \right) \right] S_y \right)_m, \tag{3.90}$$

$$Q([\rho v]_{I,J}) = \sum_{m=1}^{4} \left(\left[\rho vu - \mu \left(\tfrac{\partial v}{\partial x} + \tfrac{\partial u}{\partial y} \right) \right] S_x + \left[\rho vv + p - \tfrac{2}{3}\mu \left(2\tfrac{\partial v}{\partial y} - \tfrac{\partial u}{\partial x} \right) \right] S_y \right)_m, \tag{3.91}$$

$$\begin{aligned} Q([\rho E]_{I,J}) = \sum_{m=1}^{4} \Bigg(& \left[\rho uH - k\tfrac{\partial T}{\partial x} - \tfrac{2}{3}u\mu \left(2\tfrac{\partial u}{\partial x} - \tfrac{\partial v}{\partial y} \right) - v\mu \left(\tfrac{\partial u}{\partial y} + \tfrac{\partial v}{\partial x} \right) \right] S_x + \\ & \left[\rho vH - k\tfrac{\partial T}{\partial y} - u\mu \left(\tfrac{\partial v}{\partial x} + \tfrac{\partial u}{\partial y} \right) - \tfrac{2}{3}v\mu \left(2\tfrac{\partial v}{\partial y} - \tfrac{\partial u}{\partial x} \right) \right] S_y \Bigg)_m. \end{aligned} \tag{3.92}$$

The left hand sides of equations (3.89) to (3.92) can be written in a simplified way

as $Q(W_{I,J})$, that is

$$Q(W_{I,J}) = \left\{ \begin{array}{l} Q([\rho]_{I,J}) \\ Q([\rho u]_{I,J}) \\ Q([\rho v]_{I,J}) \\ Q([\rho E]_{I,J}) \end{array} \right\}, \tag{3.93}$$

while the right hand sides of equations (3.89) to (3.92) are computed using equations (3.21) to (3.24). The governing equation (3.88) can then be written as

$$V(\Omega_{I,J})\frac{dW_{I,J}}{dt} + Q(W_{I,J}) - D(W_{I,J}) = 0. \tag{3.94}$$

The construction of the dissipative term for each of the conserved variables is identical and therefore the general variable W is used in its derivation (that is, W in the derivation below represents any of the conserved variables ρ, ρu, ρv or ρE). The dissipative term is defined by the following equation

$$D(W_{I,J}) = D_x(W_{I,J}) + D_y(W_{I,J}), \tag{3.95}$$

where $D_x(W_{I,J})$ and $D_y(W_{I,J})$ are the corresponding contributions for the two coordinate directions and they are defined as

$$D_x(W_{I,J}) = d_{I+\frac{1}{2},J}(W_{I,J}) - d_{I-\frac{1}{2},J}(W_{I,J}), \tag{3.96}$$

$$D_y(W_{I,J}) = d_{I,J+\frac{1}{2}}(W_{I,J}) - d_{I,J-\frac{1}{2}}(W_{I,J}). \tag{3.97}$$

The derivation of the terms $d_{I+\frac{1}{2},J}(W_{I,J})$, $d_{I-\frac{1}{2},J}(W_{I,J})$, etc., follows next.

As mentioned above, the dissipation operator is formed by a blend of two dissipative terms. The first term is obtained by forming the third differences of the conserved variables. The resulting term is third order accurate and provide the required coupling without compromising the second order accuracy of the scheme. The

third order accurate term is constructed as

$$d_{I+\frac{1}{2},J}(W_{I,J}) = -\frac{V(\Omega_{I,J})}{\Delta t_{I,J}}\,\kappa^{(4)}\Big(W_{I+2,J} - 3W_{I+1,J} + 3W_{I,J} - W_{I-1,J}.\Big) \tag{3.98}$$

The factor $V(\Omega_{I,J})/\Delta t_{I,J}$ appearing in equation (3.98) balances the same factor that arises when the temporal discretization is performed (i.e., when the first term of equation (3.27) is discretized); $\Delta t_{I,J}$ is the time step for grid cell $\Omega_{I,J}$ and theoretical aspects for its determination are discussed in Section III.I. The coefficient $\kappa^{(4)}$, together with $\kappa^{(2)}$ and with the Courant (CFL) number[5] of the scheme must be tunned up to obtain the best overall convergence rate. What it is usually done is to maximize the Courant number for the given time-stepping scheme and then to choose $\kappa^{(4)}$ and $\kappa^{(2)}$ such that the scheme is stable.

In order to capture shocks without any pre-shock oscillation a second dissipative term needs to be added. This term is of order of one in the neighborhood of the shock wave and it is easily obtained by forming the first differences of $W_{I,J}$. It is, however, necessary to capture shocks sharply and, at the same time, to retain second order accuracy away from the immediate vicinity of the shock wave. Furthermore, it has also been found necessary to switch off the fourth differences term near shocks to prevent oscillations. These necessities are satisfied by employing a pressure-based sensor, sensitive to the normalized second differences in the pressure

$$\Upsilon_I = \frac{\left|p_{I+1,J} - 2p_{I,J} + p_{I-1,J}\right|}{p_{I+1,J} + 2p_{I,J} + p_{I-1,J}}. \tag{3.99}$$

This quantity is of second order in smooth regions of the flow and is of order one in regions containing steep pressure gradients. Afterwards, the following coefficients are

[5] $\kappa^{(2)}$ is other artificial dissipation coefficient discussed next and the CFL (Courant-Friedrichs-Lewy) number is a necessary condition for explicit schemes' stability, discussed in a section below.

defined

$$\varepsilon^{(2)}_{I+\frac{1}{2},J} = \kappa^{(2)} \max\big(\Upsilon_{I+1}, \Upsilon_I\big) \tag{3.100}$$

$$\varepsilon^{(4)}_{I+\frac{1}{2},J} = \max\big(0, \kappa^{(4)} - \varepsilon^{(2)}_{I+\frac{1}{2},J}\big). \tag{3.101}$$

In equation (3.100) the parameter $\kappa^{(2)}$ is of order of one. The right hand side of the equation for $d_{I+\frac{1}{2},J}(W_{I,J})$ (equation (3.98)) is then replaced by

$$d_{I+\frac{1}{2},J}(W_{I,J}) = \frac{V(\Omega_{I,J})}{\Delta t_{I,J}} \left\{ \begin{array}{l} \varepsilon^{(2)}_{I+\frac{1}{2},J}\big(W_{I+1,J} - W_{I,J}\big) - \\ \\ \varepsilon^{(4)}_{I+\frac{1}{2},J}\big(W_{I+2,J} - 3W_{I+1,J} + 3W_{I,J} - W_{I-1,J}\big) \end{array} \right\}, \tag{3.102}$$

where of course, $\varepsilon^{(2)}_{I+\frac{1}{2},J}$ and $\varepsilon^{(4)}_{I+\frac{1}{2},J}$ are computed using equations (3.100) and (3.101), respectively. The fourth differences in equation (3.102) provide background dissipation throughout the domain, except when switched off in the neighborhood of a shock wave, where the pressure sensor Υ_I is of order one and therefore the second differences in equation (3.102) become the dominant dissipative terms.

Equation (3.102) defines the term $d_{I+\frac{1}{2},J}(W_{I,J})$ of equation (3.96). The rest of the d terms in equations (3.96) and (3.97) are constructed in a very similar way as equation (3.102). They are

$$d_{I-\frac{1}{2},J}(W_{I,J}) = \frac{V(\Omega_{I,J})}{\Delta t_{I,J}} \left\{ \begin{array}{l} \varepsilon^{(2)}_{I-\frac{1}{2},J}\big(W_{I,J} - W_{I-1,J}\big) - \\ \\ \varepsilon^{(4)}_{I-\frac{1}{2},J}\big(W_{I+1,J} - 3W_{I,J} + 3W_{I-1,J} - W_{I-2,J}\big) \end{array} \right\},$$

$$d_{I,J+\frac{1}{2}}(W_{I,J}) = \frac{V(\Omega_{I,J})}{\Delta t_{I,J}} \left\{ \begin{array}{l} \varepsilon^{(2)}_{I,J+\frac{1}{2}}\big(W_{I,J+1} - W_{I,J}\big) - \\ \\ \varepsilon^{(4)}_{I,J+\frac{1}{2}}\big(W_{I,J+2} - 3W_{I,J+1} + 3W_{I,J} - W_{I,J-1}\big) \end{array} \right\},$$

$$d_{I,J-\frac{1}{2}}(W_{I,J}) = \frac{V(\Omega_{I,J})}{\Delta t_{I,J}} \left\{ \begin{array}{l} \varepsilon^{(2)}_{I,J-\frac{1}{2}}\big(W_{I,J} - W_{I,J-1}\big) - \\ \\ \varepsilon^{(4)}_{I,J-\frac{1}{2}}\big(W_{I,J+1} - 3W_{I,J} + 3W_{I,J-1} - W_{I,J-2}\big) \end{array} \right\}.$$

where

$$\varepsilon^{(2)}_{I-\frac{1}{2},J} = \kappa^{(2)} \max\big(\Upsilon_{I-1}, \Upsilon_I\big), \tag{3.103}$$

$$\varepsilon^{(4)}_{I-\frac{1}{2},J} = \max\Big(0, \kappa^{(4)} - \varepsilon^{(2)}_{I-\frac{1}{2},J}\Big).$$

Here, Υ_I (and Υ_{I-1} or Υ_{I+1}) are computed using equation (3.99) by shifting I index accordingly. Furthermore

$$\varepsilon^{(2)}_{I,J+\frac{1}{2}} = \kappa^{(2)} \max\big(\Upsilon_{J+1}, \Upsilon_J\big), \tag{3.104}$$

$$\varepsilon^{(4)}_{I,J+\frac{1}{2}} = \max\Big(0, \kappa^{(4)} - \varepsilon^{(2)}_{I,J+\frac{1}{2}}\Big),$$

$$\varepsilon^{(2)}_{I,J-\frac{1}{2}} = \kappa^{(2)} \max\big(\Upsilon_{J-1}, \Upsilon_J\big), \tag{3.105}$$

$$\varepsilon^{(4)}_{I,J-\frac{1}{2}} = \max\Big(0, \kappa^{(4)} - \varepsilon^{(2)}_{I,J-\frac{1}{2}}\Big).$$

In equations (3.104) and (3.105), Υ_J (and Υ_{J-1} or Υ_{J+1}) are computed using the following equation

$$\Upsilon_J = \frac{\big|p_{I,J+1} - 2p_{I,J} + p_{I,J-1}\big|}{p_{I,J+1} + 2p_{I,J} + p_{I,J-1}} \tag{3.106}$$

with J index shifted accordingly. The coefficients $\kappa^{(2)}$ and $\kappa^{(4)}$ for the artificial dissipation in the previous formulas are set, in this dissertation, to the following values

$$\kappa^{(2)} = \frac{1}{4} \qquad \text{and} \qquad \kappa^{(4)} = \frac{1}{250}$$

The artificial dissipation operator $D(W_{I,J})$ defined by equation (3.95) can now be computed. The next step is the temporal discretization; that is, the discretization of the first term of the augmented governing equation (3.94).

H. Temporal Discretization

As mentioned at the beginning of this chapter, two different implementations for the time-advancement of equation (3.94) are utilized in this research. One for steady problems and the other for unsteady ones. The technique employed for the steady problems can be used for unsteady runs[6] but, as it will be seen later, if viscous grids[7] are used the working global time step would be extremely small. According to the physics of the problem a small time step may or may not be desirable. Details on these implementations are given in the following sub-sections.

1. Explicit Time-Stepping Scheme for Steady Problems

For the governing equation

$$V(\Omega_{I,J})\frac{dW_{I,J}}{dt} + Q(W_{I,J}) - D(W_{I,J}) = 0,$$

let the following notation be introduced for the spatial and artificial dissipation operators

$$R(W_{I,J}) = Q(W_{I,J}) - D(W_{I,J}). \tag{3.107}$$

Therefore, the governing equation can be written as

$$V(\Omega_{I,J})\frac{dW_{I,J}}{dt} = -R(W_{I,J}). \tag{3.108}$$

The term $R(W_{I,J})$ in equation (3.108) is known as the residual and it includes all the spatial discretization, the added artificial dissipation and the source (if any)

[6]One just uses a constant, globally allowable time step instead of the variable, locally allowable time step used as a convergence accelerator for steady problems.

[7]Grids that are highly stretched toward solid boundaries or toward regions where large gradients are known to exist.

terms. For explanation purposes, a very basic explicit scheme to time-advance the governing equation (3.108) is reviewed first. This scheme is as follows.

$$V(\Omega_{I,J})\,\frac{\Delta W^n_{I,J}}{\Delta t_{I,J}} = -R(W^n_{I,J}), \tag{3.109}$$

with

$$\Delta W^n_{I,J} = W^{n+1}_{I,J} - W^n_{I,J}$$

being the solution correction. Equation (3.109) can then be written as

$$W^{n+1}_{I,J} = W^n_{I,J} - \frac{\Delta t_{I,J}}{V(\Omega_{I,J})} R(W^n_{I,J}). \tag{3.110}$$

The superscripts n and $n+1$ denote the time levels with n being the current one. Furthermore, $\Delta t_{I,J}$ represents the time step for grid cell $\Omega_{I,J}$. Thus the time at the n-th time level for cell $\Omega_{I,J}$ is $t = n\,\Delta t_{I,J}$.

The explicit scheme (equation (3.110)) utilized to time-advance the governing equation (3.108) starts from a known solution (or initial guess) $W^n_{I,J}$ and employs the corresponding residual $R(W^n_{I,J})$ in order to obtain a new solution at time $(t + \Delta t)$. In other words, the new solution $W^{n+1}_{I,J}$ depends solely on the values already known. This fact makes the explicit schemes simple and easy to implement.

The scheme represented by equation (3.110) is a single-stage scheme because a new solution $W^{n+1}_{I,J}$ is obtained by evaluating the residual just once. This scheme is of no practical value, since it is stable only if combined with a first order accurate upwind spatial discretization. To alleviate this restriction, multistage time-stepping schemes can be used. These are better known as Runge-Kutta schemes and in them the solution is advanced in several stages and the residual is evaluated at intermediate stages.

When in a multi-stage Runge-Kutta scheme the residual $R(W_{I,J})$ is computed us-

ing equation (3.107) and it is evaluated at all intermediate stages, the resulting scheme is particularly suitable when the spatial term of the governing equation has been discretized using an upwind approach. In this research, however, a central discretization approach is employed for such term and, for this kind of spatial discretization, the hybrid multi-stage methodology performs more efficiently (see [32] p. 183). These type of schemes treat the convective and dissipative terms in a distinct fashion. The residual $R(W_{I,J})$ in equation (3.107) is thus split as

$$R(W_{I,J}) = R_c(W_{I,J}) + R_d(W_{I,J}) \tag{3.111}$$

where, for each conserved variable

$$\begin{aligned}
R_c([\rho]_{I,J}) &= \sum_{m=1}^{4} \Big(\big[\rho u\big] S_x + \big[\rho v\big] S_y \Big)_m, \\
R_c([\rho u]_{I,J}) &= \sum_{m=1}^{4} \Big(\Big[\rho uu + p\Big] S_x + \Big[\rho uv\Big] S_y \Big)_m, \\
R_c([\rho v]_{I,J}) &= \sum_{m=1}^{4} \Big(\Big[\rho vu\Big] S_x + \Big[\rho vv + p\Big] S_y \Big)_m, \\
R_c([\rho E]_{I,J}) &= \sum_{m=1}^{4} \Big(\Big[\rho uH\Big] S_x + \Big[\rho vH\Big] S_y \Big)_m,
\end{aligned}$$

$$\begin{aligned}
R_d([\rho]_{I,J}) &= -D([\rho]_{I,J}), \\
R_d([\rho u]_{I,J}) &= \sum_{m=1}^{4} \left(\Big[-\tfrac{2}{3}\mu \left(2\tfrac{\partial u}{\partial x} - \tfrac{\partial v}{\partial y} \right) \Big] S_x + \Big[-\mu \left(\tfrac{\partial u}{\partial y} + \tfrac{\partial v}{\partial x} \right) \Big] S_y \right)_m - D([\rho u]_{I,J}), \\
R_d([\rho v]_{I,J}) &= \sum_{m=1}^{4} \left(\Big[-\mu \left(\tfrac{\partial v}{\partial x} + \tfrac{\partial u}{\partial y} \right) \Big] S_x + \Big[-\tfrac{2}{3}\mu \left(2\tfrac{\partial v}{\partial y} - \tfrac{\partial u}{\partial x} \right) \Big] S_y \right)_m - D([\rho v]_{I,J}),
\end{aligned}$$

$$R_d([\rho E]_{I,J}) = \sum_{m=1}^{4} \Bigg(\Big[-k\frac{\partial T}{\partial x} - \tfrac{2}{3}u\mu\left(2\frac{\partial u}{\partial x} - \frac{\partial v}{\partial y}\right) - v\mu\left(\frac{\partial u}{\partial y} + \frac{\partial v}{\partial x}\right)\Big] S_x + \Big[-k\frac{\partial T}{\partial y} - u\mu\left(\frac{\partial v}{\partial x} + \frac{\partial u}{\partial y}\right) - \tfrac{2}{3}v\mu\left(2\frac{\partial v}{\partial y} - \frac{\partial u}{\partial x}\right)\Big] S_y \Bigg)_m - D([\rho E]_{I,J}).$$

The terms in the summation symbols are computed as in equations (3.21) to (3.24) while the artificial dissipation terms $D(W_{I,J})$, with $W = [\rho, \rho u, \rho v, \rho E]^T$ are computed as described in the previous section.

Using the splitting given by equation (3.111) a particularly effective four-stage scheme with two evaluations of the dissipation term (see Jameson [33]) is adopted for this research. Such scheme is derived starting from (let $V_{I,J}$ denote $V(\Omega_{I,J})$)

$$\begin{aligned}
W_{I,J}^{(0)} &= W_{I,J}^{(n)} \\
W_{I,J}^{(1)} &= W_{I,J}^{(0)} - \alpha_1 \tfrac{\Delta t_{I,J}}{V_{I,J}} \left[R_c^{(0)} + R_d^{(0)} \right] \\
W_{I,J}^{(2)} &= W_{I,J}^{(0)} - \alpha_2 \tfrac{\Delta t_{I,J}}{V_{I,J}} \left[R_c^{(1)} + R_d^{(1)} \right] \\
W_{I,J}^{(3)} &= W_{I,J}^{(0)} - \alpha_3 \tfrac{\Delta t_{I,J}}{V_{I,J}} \left[R_c^{(2)} + R_d^{(2)} \right] \\
W_{I,J}^{(4)} &= W_{I,J}^{(0)} - \alpha_4 \tfrac{\Delta t_{I,J}}{V_{I,J}} \left[R_c^{(3)} + R_d^{(3)} \right] \\
W_{I,J}^{(n+1)} &= W_{I,J}^{(4)},
\end{aligned} \tag{3.112}$$

where

$$\begin{aligned}
R_c^{(0)} &= R_c\left(W_{I,J}^{(0)}\right) & R_d^{(0)} &= R_d\left(W_{I,J}^{(0)}\right) \\
R_c^{(1)} &= R_c\left(W_{I,J}^{(1)}\right) & R_d^{(1)} &= \beta_2 R_d\left(W_{I,J}^{(1)}\right) + (1-\beta_2) R_d^{(0)} \\
R_c^{(2)} &= R_c\left(W_{I,J}^{(2)}\right) & R_d^{(2)} &= \beta_3 R_d\left(W_{I,J}^{(2)}\right) + (1-\beta_3) R_d^{(1)} \\
R_c^{(3)} &= R_c\left(W_{I,J}^{(3)}\right) & R_d^{(3)} &= \beta_4 R_d\left(W_{I,J}^{(3)}\right) + (1-\beta_4) R_d^{(2)}.
\end{aligned} \tag{3.113}$$

The coefficients α_k and β_k in equations (3.112) and (3.113) are chosen to maximize the stability region of the scheme and for the final scheme used in this research they are as shown in Table I. These coefficients are optimized in order to expand the stability region of the scheme, improve its damping properties and, hence, its convergence rate

and robustness. Depending on the stage coefficients and the number of stages, a multistage scheme of this kind can be extended to second or higher order of accuracy in time.

Table I.: Hybrid multistage scheme; optimized stage (α) and blending (β) coefficients.

Stage	α	β
1	$\frac{1}{3}$	1
2	$\frac{4}{15}$	$\frac{1}{2}$
3	$\frac{5}{9}$	0
4	1	0

Use of the coefficients β_k of Table I and of the definitions given by equations (3.113) into (3.112) gives the final hybrid, explicit, Runge-Kutta scheme used in this research for steady state computations[8]

$$\begin{aligned}
W_{I,J}^{(0)} &= W_{I,J}^{(n)} \\
W_{I,J}^{(1)} &= W_{I,J}^{(0)} - \alpha_1 \frac{\Delta t_{I,J}}{V_{I,J}} \left[R_c \left(W_{I,J}^{(0)} \right) + R_d \left(W_{I,J}^{(0)} \right) \right] \\
W_{I,J}^{(2)} &= W_{I,J}^{(0)} - \alpha_2 \frac{\Delta t_{I,J}}{V_{I,J}} \left[R_c \left(W^{(1)} \right) + \tfrac{1}{2} R_d \left(W_{I,J}^{(1)} \right) + \tfrac{1}{2} R_d \left(W_{I,J}^{(0)} \right) \right] \\
W_{I,J}^{(3)} &= W_{I,J}^{(0)} - \alpha_3 \frac{\Delta t_{I,J}}{V_{I,J}} \left[R_c \left(W^{(2)} \right) + \tfrac{1}{2} R_d \left(W_{I,J}^{(1)} \right) + \tfrac{1}{2} R_d \left(W_{I,J}^{(0)} \right) \right] \\
W_{I,J}^{(4)} &= W_{I,J}^{(0)} - \alpha_4 \frac{\Delta t_{I,J}}{V_{I,J}} \left[R_c \left(W^{(3)} \right) + \tfrac{1}{2} R_d \left(W_{I,J}^{(1)} \right) + \tfrac{1}{2} R_d \left(W_{I,J}^{(0)} \right) \right] \\
W_{I,J}^{(n+1)} &= W_{I,J}^{(4)}.
\end{aligned} \tag{3.114}$$

Advantages of explicit multistage time-stepping schemes are that they can be employed in connection with any spatial discretization scheme, they are numerically

[8]Note that, effectively, it is a four-stage scheme with two evaluations of the dissipation term $R_d(W)$.

cheap and require only a small amount of computer memory. On the other hand, the maximum permissible time step is severely restricted by the characteristics of the governing equations as well as by the grid geometry. Particularly for viscous flows and highly stretched grid cells, the convergence to steady state slows down considerably. To alleviate this problem, a fully implicit scheme is implemented in this work such that no restriction on the time step size exists. Such implementation is discussed in the next section.

2. Implicit Time-Stepping Scheme for Unsteady Problems

The phenomena investigated here is that of flow separation control by means of unsteady fluid injection. The frequencies of injection employed in this research ranged from 300 to 1500 Hz. A frequency of 700 Hz and a cycle resolution of 12 intervals gives a physical time step of of the order of 1×10^{-4} s. However, the explicit scheme of the previous section, together with the flow conditions, grid features, etc., allow for a maximum, *global* time step of the order of (fill) (if the scheme is set to solve the flow accurately in time). This is a problem because it would take a prohibitively long time to solve the flow with the fluid injection at the mentioned frequency.

This problem can be solved if an explicit Runge-Kutta scheme as that described in the previous section (which reaches convergence relatively fast) is utilized as a driver for a fully implicit time stepping scheme [33]. The implicit scheme would allow for a freely chosen time step size, solely based on the physics of the problem. The mentioned fully implicit scheme is obtained by approximating equation (3.27) as follows (with operator $Q(W_{I,J})$ for the spatial discretization –equations (3.89) to (3.92)– and multiplying all the equation by the cell's volume)

$$V(\Omega_{I,J})\, D_t(W_{I,J}^{n+1}) + Q(W_{I,J}^{n+1}) = 0. \tag{3.115}$$

D_t represents a k^{th} order accurate backward difference operator of the form

$$D_t(W_{I,J}^{n+1}) = \frac{1}{\Delta t_{phys}} \sum_{q=1}^{k} \frac{1}{q} \left[\Delta^-(W_{I,J}^{n+1})\right]^q \tag{3.116}$$

where

$$\begin{aligned} \left[\Delta^-(W_{I,J}^{n+1})\right]^1 &= W_{I,J}^{n+1} - W_{I,J}^{n}, \\ \left[\Delta^-(W_{I,J}^{n+1})\right]^2 &= \Delta^-\Big(\left[\Delta^-(W_{I,J}^{n+1})\right]^1 \Big) = W_{I,J}^{n+1} - 2W_{I,J}^{n} + W_{I,J}^{n-1}, \\ &\vdots \end{aligned}$$

In equation (3.116) Δt_{phys} denotes the time step which is set solely based in the physics of the problem to be simulated; that is, Δt_{phys} is a user defined parameter.

In the current implementation, a second order accurate backward difference operator is utilized (i.e., $k = 2$ in equation (3.116)). Substitution of equation (3.116), with $k = 2$, into equation (3.115) gives

$$V(\Omega_{I,J})\Big(\frac{3}{2\Delta t_{phys}}\Big[W_{I,J}^{n+1}\Big] - \frac{2}{\Delta t_{phys}}\Big[W_{I,J}^{n}\Big] + \frac{1}{2\Delta t_{phys}}\Big[W_{I,J}^{n-1}\Big]\Big) + Q(W_{I,J}^{n+1}) = 0. \tag{3.117}$$

Or defining a modified spatial discretization operator

$$Q^*(W_{I,J}^{n+1}) = 0, \tag{3.118}$$

where obviously

$$Q^*(W_{I,J}^{n+1}) = V(\Omega_{I,J})\Big(\frac{3}{2\Delta t_{phys}}\Big[W_{I,J}^{n+1}\Big] - \frac{2}{\Delta t_{phys}}\Big[W_{I,J}^{n}\Big] + \frac{1}{2\Delta t_{phys}}\Big[W_{I,J}^{n-1}\Big]\Big) + Q(W_{I,J}^{n+1}).$$

Introduction of a pseudo time term in equation (3.118) allows the utilization of the techniques previously discussed to find a $W_{I,J}^{n+1}$ such that equation (3.118) is

satisfied. Equation (3.118) plus the mentioned pseudo time term gives

$$V(\Omega_{I,J})\frac{d\,W_{I,J}^{n+1}}{dt^*} + Q^*(W_{I,J}^{n+1}) = 0, \tag{3.119}$$

where t^* is the pseudo time. Equation (3.119) is now treated as a modified steady state problem to be solved for W^{n+1} (denoted $W_{I,J}^*$ from now on for simplicity[9]) by means of an explicit Runge-Kutta scheme. This scheme employs a variable pseudo time stepping technique and it is very similar to that presented in the previous section.

Here too, as for truly steady problems, artificial dissipation must be added for stability reasons. Thus, equation (3.119) is modified as follows

$$V(\Omega_{I,J})\frac{dW_{I,J}^*}{dt^*} + Q^*(W_{I,J}^*) - D^*(W_{I,J}^*) = 0, \tag{3.120}$$

where, as mentioned above, $W_{I,J}^*$ is an approximation to $W_{I,J}^{n+1}$. The artificial dissipation operator $D^*(W_{I,J}^*)$ is computed as it was seen in Section III.G with $W_{I,J}$, $\Delta t_{I,J}$ and $p_{I,J}$ replaced by $W_{I,J}^*$, $\Delta t_{I,J}^*$ and $p_{I,J}^*$ respectively. $\Delta t_{I,J}^*$ is the pseudo time step for the Runge-Kutta explicit scheme utilized to solve equation (3.120). The determination of the pseudo time step is reviewed in the next section.

A modified residual can now be defined for the unsteady problems

$$\begin{aligned} R^*(W_{I,J}^*) &= V(\Omega_{I,J})\Big(\frac{3}{2\Delta t_{phys}}\Big[W_{I,J}^*\Big] - \frac{2}{\Delta t_{phys}}\Big[W_{I,J}^n\Big] + \frac{1}{2\Delta t_{phys}}\Big[W_{I,J}^{n-1}\Big]\Big) + \\ &+ Q(W_{I,J}^*) - D^*(W_{I,J}^*). \end{aligned} \tag{3.121}$$

Denoting the last two terms of equation (3.121) as

$$R(W_{I,J}^*) = Q(W_{I,J}^*) - D^*(W_{I,J}^*) \tag{3.122}$$

[9]When solving equation (3.117) for W^{n+1} with a (fictitious) time stepping technique, a superscript n or $n+1$ is used *on top of the already existing one,* this would result in a cumbersome, confusing notation.

one has a modified residual as follows

$$R^*(W^*_{I,J}) = V(\Omega_{I,J})\Big(\frac{3}{2\Delta t_{phys}}\Big[W^*_{I,J}\Big] - \frac{2}{\Delta t_{phys}}\Big[W^n_{I,J}\Big] + \frac{1}{2\Delta t_{phys}}\Big[W^{n-1}_{I,J}\Big]\Big) + R(W^*_{I,J}).$$

The operator $S[W^n_{I,J}, W^{n-1}_{I,J}]$ is called the source term and it is introduced to collect the fixed, known terms of the modified residual. $S[W^n_{I,J}, W^{n-1}_{I,J}]$ is computed using solutions which are available from previous time levels and is treated as a constant throughout the time-marching procedure in fictitious time. That is

$$S[W^n_{I,J}, W^{n-1}_{I,J}] = V(\Omega_{I,J})\Big(-\frac{2}{\Delta t_{phys}}\Big[W^n_{I,J}\Big] + \frac{1}{2\Delta t_{phys}}\Big[W^{n-1}_{I,J}\Big]\Big).$$

If furthermore, a splitting of the term $R(W^*_{I,J})$, equation (3.122), in convective and diffusive parts is introduced[10], then the modified residual above may be rewritten as

$$R^*(W^*_{I,J}) = V(\Omega_{I,J})\frac{3}{2\Delta t_{phys}}\Big[W^*_{I,J}\Big] + R_c(W^*_{I,J}) + R_d(W^*_{I,J}) + S[W^n_{I,J}, W^{n-1}_{I,J}]. \quad (3.123)$$

Equation (3.123) is the residual to be used for the modified governing equation (equation (3.120)). Thus

$$V(\Omega_{I,J})\frac{dW^*_{I,J}}{dt^*} = -R^*(W^*_{I,J}). \quad (3.124)$$

Equation (3.124) can be solved using a technique very similar to that shown in the previous section. For example, a single stage explicit scheme as that of equation (3.110) is

$$[W^*_{I,J}]^{n+1} = [W^*_{I,J}]^n - \frac{\Delta t^*_{I,J}}{V(\Omega_{I,J})}\, R^*\big([W^*_{I,J}]^n\big), \quad (3.125)$$

(recall that $W^*_{I,J}$ is an approximation to $W^{n+1}_{I,J}$ where $n+1$ represents the real time level, while the $n+1$ or n in equation (3.125) represent the fictitious time level).

[10]This splitting is exactly as that in equation (3.111) and the purpose of its introduction is, in general, the scheme's improvement in convergence rate and robustness.

Introducing equation (3.123) into equation (3.125)

$$[W^*_{I,J}]^{n+1} = [W^*_{I,J}]^n - \frac{3\Delta t^*_{I,J}}{2\Delta t_{phys}}[W^*_{I,J}]^n - \\ -\frac{\Delta t^*_{I,J}}{V(\Omega_{I,J})}\Big(R_c([W^*_{I,J}]^n) + R_d([W^*_{I,J}]^n) + S[W^n_{I,J}, W^{n-1}_{I,J}]\Big). \tag{3.126}$$

The scheme of equation (3.126) is just a single stage explicit scheme in t^*. A four stage Runge-Kutta scheme to solve the governing equation (3.120), similar to that of equation (3.114) is (letting $V_{I,J}$ denote $V(\Omega_{I,J})$)

$$\begin{aligned}
W^{*(0)}_{I,J} &= W^{*(n)}_{I,J} \\
W^{*(1)}_{I,J} &= W^{*(0)}_{I,J} - \alpha_1 \tfrac{\Delta t^*_{I,J}}{V_{I,J}} \left\{ V_{I,J} \tfrac{3}{2\Delta t_{phys}} \left[W^{*(0)}_{I,J} \right] + R^{(0)}_c + R^{(0)}_d + S[W^n_{I,J}, W^{n-1}_{I,J}] \right\} \\
W^{*(2)}_{I,J} &= W^{*(0)}_{I,J} - \alpha_2 \tfrac{\Delta t^*_{I,J}}{V_{I,J}} \left\{ V_{I,J} \tfrac{3}{2\Delta t_{phys}} \left[W^{*(1)}_{I,J} \right] + R^{(1)}_c + R^{(1)}_d + S[W^n_{I,J}, W^{n-1}_{I,J}] \right\} \\
W^{*(3)}_{I,J} &= W^{*(0)}_{I,J} - \alpha_3 \tfrac{\Delta t^*_{I,J}}{V_{I,J}} \left\{ V_{I,J} \tfrac{3}{2\Delta t_{phys}} \left[W^{*(2)}_{I,J} \right] + R^{(2)}_c + R^{(2)}_d + S[W^n_{I,J}, W^{n-1}_{I,J}] \right\} \\
W^{*(4)}_{I,J} &= W^{*(0)}_{I,J} - \alpha_4 \tfrac{\Delta t^*_{I,J}}{V_{I,J}} \left\{ V_{I,J} \tfrac{3}{2\Delta t_{phys}} \left[W^{*(3)}_{I,J} \right] + R^{(3)}_c + R^{(3)}_d + S[W^n_{I,J}, W^{n-1}_{I,J}] \right\} \\
W^{*(n+1)}_{I,J} &= W^{*(4)}_{I,J}.
\end{aligned} \tag{3.127}$$

The definitions of $R^{(k)}_c$ and $R^{(k)}_d$ of scheme (3.127) are provided later, when the final scheme had been derived. Arnone et al. [34] pointed out that the scheme given by equations (3.127) becomes unstable when the physical time step Δt_{phys} is of the order of the fictitious time step Δt^* or smaller. Melson et al. [35] demonstrated that the instability is caused by the term $(3W^*_{I,J})/(2\Delta t_{phys})$ in the modified residual which becomes significant for small Δt_{phys}. In this research, therefore, an approach similar to that of Melson [35] is employed such that the resulting scheme is unconditionally stable for any size of real time step Δt_{phys}.

In Melson's approach, the portion of the discrete real time operator at real time level $n+1$ (i.e., the term $3W^*_{I,J}/2\Delta t_{phys}$ in equation (3.127)) is treated implicitly in the fictitious time-marching process. Therefore, the scheme represented by equations

(3.127) is changed to

$$
\begin{aligned}
W_{I,J}^{*\,(0)} &= W_{I,J}^{*\,(n)} \\
W_{I,J}^{*\,(1)} &= W_{I,J}^{*\,(0)} - \alpha_1 \tfrac{\Delta t^*}{V_{I,J}} \left\{ V_{I,J} \tfrac{3}{2\Delta t_{phys}} \left[W_{I,J}^{*\,(1)} \right] + R_c^{(0)} + R_d^{(0)} + S[W_{I,J}^n, W_{I,J}^{n-1}] \right\} \\
W_{I,J}^{*\,(2)} &= W_{I,J}^{*\,(0)} - \alpha_2 \tfrac{\Delta t^*}{V_{I,J}} \left\{ V_{I,J} \tfrac{3}{2\Delta t_{phys}} \left[W_{I,J}^{*\,(2)} \right] + R_c^{(1)} + R_d^{(1)} + S[W_{I,J}^n, W_{I,J}^{n-1}] \right\} \\
W_{I,J}^{*\,(3)} &= W_{I,J}^{*\,(0)} - \alpha_3 \tfrac{\Delta t^*}{V_{I,J}} \left\{ V_{I,J} \tfrac{3}{2\Delta t_{phys}} \left[W_{I,J}^{*\,(3)} \right] + R_c^{(2)} + R_d^{(2)} + S[W_{I,J}^n, W_{I,J}^{n-1}] \right\} \\
W_{I,J}^{*\,(4)} &= W_{I,J}^{*\,(0)} - \alpha_4 \tfrac{\Delta t^*}{V_{I,J}} \left\{ V_{I,J} \tfrac{3}{2\Delta t_{phys}} \left[W_{I,J}^{*\,(4)} \right] + R_c^{(3)} + R_d^{(3)} + S[W_{I,J}^n, W_{I,J}^{n-1}] \right\} \\
W_{I,J}^{*\,(n+1)} &= W_{I,J}^{*\,(4)}.
\end{aligned}
\tag{3.128}
$$

It can be seen now that, for stages $k = 1$ to 4 in (3.128), the seeked variable $W_{I,J}^{*\,(k)}$ appears in both sides of the equations[11]. Solving for $W_{I,J}^{*\,(k)}$ in all the four stages of (3.128) gives the final form of the Runge-Kutta scheme used in this dissertation

$$
\begin{aligned}
W_{I,J}^{*\,(0)} &= W_{I,J}^{*\,(n)} \\
W_{I,J}^{*\,(1)} &= \left(1 + \alpha_1 \tfrac{3\Delta t^*}{2\Delta t_{phys}}\right)^{-1} \left(W_{I,J}^{*\,(0)} - \alpha_1 \tfrac{\Delta t^*}{V_{I,J}} \left\{ R_c^{(0)} + R_d^{(0)} + S[W_{I,J}^n, W_{I,J}^{n-1}] \right\} \right) \\
W_{I,J}^{*\,(2)} &= \left(1 + \alpha_2 \tfrac{3\Delta t^*}{2\Delta t_{phys}}\right)^{-1} \left(W_{I,J}^{*\,(0)} - \alpha_2 \tfrac{\Delta t^*}{V_{I,J}} \left\{ R_c^{(1)} + R_d^{(1)} + S[W_{I,J}^n, W_{I,J}^{n-1}] \right\} \right) \\
W_{I,J}^{*\,(3)} &= \left(1 + \alpha_3 \tfrac{3\Delta t^*}{2\Delta t_{phys}}\right)^{-1} \left(W_{I,J}^{*\,(0)} - \alpha_3 \tfrac{\Delta t^*}{V_{I,J}} \left\{ R_c^{(2)} + R_d^{(2)} + S[W_{I,J}^n, W_{I,J}^{n-1}] \right\} \right) \\
W_{I,J}^{*\,(4)} &= \left(1 + \alpha_4 \tfrac{3\Delta t^*}{2\Delta t_{phys}}\right)^{-1} \left(W_{I,J}^{*\,(0)} - \alpha_4 \tfrac{\Delta t^*}{V_{I,J}} \left\{ R_c^{(3)} + R_d^{(3)} + S[W_{I,J}^n, W_{I,J}^{n-1}] \right\} \right) \\
W_{I,J}^{*\,(n+1)} &= W_{I,J}^{*\,(4)},
\end{aligned}
$$

with

$$
\begin{aligned}
R_c^{(0)} &= R_c\left(W_{I,J}^{*\,(0)}\right) & R_d^{(0)} &= R_d\left(W_{I,J}^{*\,(0)}\right) \\
R_c^{(1)} &= R_c\left(W_{I,J}^{*\,(1)}\right) & R_d^{(1)} &= \beta_2 R_d\left(W_{I,J}^{*\,(1)}\right) + (1-\beta_2)\, R_d^{(0)} \\
R_c^{(2)} &= R_c\left(W_{I,J}^{*\,(2)}\right) & R_d^{(2)} &= \beta_3 R_d\left(W_{I,J}^{*\,(2)}\right) + (1-\beta_3)\, R_d^{(1)} \\
R_c^{(3)} &= R_c\left(W_{I,J}^{*\,(3)}\right) & R_d^{(3)} &= \beta_4 R_d\left(W_{I,J}^{*\,(3)}\right) + (1-\beta_4)\, R_d^{(2)}.
\end{aligned}
\tag{3.129}
$$

[11] This is the only difference between schemes (3.127) and (3.128)

The coefficients α_k and β_k are exactly as given by Table I. Use of the suggested β_k and of the definitions given in (3.129) gives the final form of the Runge-Kutta scheme utilized in this dissertation to time march equation (3.120) in t^*.

$$
\begin{aligned}
W_{I,J}^{*\,(0)} &= W_{I,J}^{*\,(n)} \\
W_{I,J}^{*\,(1)} &= \frac{\left(W_{I,J}^{*\,(0)} - \alpha_1 \frac{\Delta t^*}{V_{I,J}} \left\{ R_c(W_{I,J}^{*\,(0)}) + R_d(W_{I,J}^{*\,(0)}) + S[W_{I,J}^{n}, W_{I,J}^{n-1}] \right\}\right)}{\left(1 - \alpha_1 \frac{3\Delta t^*}{2\Delta t_{phys}}\right)} \\
W_{I,J}^{*\,(2)} &= \frac{\left(W_{I,J}^{*\,(0)} - \alpha_2 \frac{\Delta t^*}{V_{I,J}} \left\{ R_c(W_{I,J}^{*\,(1)}) + \frac{1}{2} R_d(W_{I,J}^{*\,(1)}) + \frac{1}{2} R_d(W_{I,J}^{*\,(0)}) + S[W_{I,J}^{n}, W_{I,J}^{n-1}] \right\}\right)}{\left(1 - \alpha_2 \frac{3\Delta t^*}{2\Delta t_{phys}}\right)} \\
W_{I,J}^{*\,(3)} &= \frac{\left(W_{I,J}^{*\,(0)} - \alpha_3 \frac{\Delta t^*}{V_{I,J}} \left\{ R_c(W_{I,J}^{*\,(2)}) + \frac{1}{2} R_d(W_{I,J}^{*\,(1)}) + \frac{1}{2} R_d(W_{I,J}^{*\,(0)}) + S[W_{I,J}^{n}, W_{I,J}^{n-1}] \right\}\right)}{\left(1 - \alpha_3 \frac{3\Delta t^*}{2\Delta t_{phys}}\right)} \\
W_{I,J}^{*\,(4)} &= \frac{\left(W_{I,J}^{*\,(0)} - \alpha_4 \frac{\Delta t^*}{V_{I,J}} \left\{ R_c(W_{I,J}^{*\,(3)}) + \frac{1}{2} R_d(W_{I,J}^{*\,(1)}) + \frac{1}{2} R_d(W_{I,J}^{*\,(0)}) + S[W_{I,J}^{n}, W_{I,J}^{n-1}] \right\}\right)}{\left(1 - \alpha_4 \frac{3\Delta t^*}{2\Delta t_{phys}}\right)} \\
W_{I,J}^{*\,(n+1)} &= W_{I,J}^{*\,(4)}.
\end{aligned}
\tag{3.130}
$$

Here again, n denotes the current and $n+1$ the new fictitious time level, respectively and Δt_{phys} is set at will, solely based on the physics of the problem. In this work, the (fictitious) time marching process is started with a corresponding converged solution for the steady problem. The process on every dual time step is continued until $W_{I,J}^{*\,n+1}$ approximates $W_{I,J}^{n+1}$ with sufficient accuracy, usually when the residual $R^*(W_{I,J}^*)$ given by equation (3.123) is reduced by two or three orders of magnitude. After that, the next physical time step is conducted.

I. Determination of the Maximum Time Step for the Explicit and Implicit Schemes

Both reviewed schemes from the last two sections are considered to be explicit schemes and to reach steady states. One of the schemes reaches a truly steady state by marching in real time t. The other one reaches a fictitious steady state by marching in fictitious time t^*. The determination of the time steps $\Delta t_{I,J}$ and $\Delta t^*_{I,J}$ for both time-advancement schemes is identical and it is reviewed in this section.

Every explicit time stepping scheme remains stable only up to a certain value of the time step. To be stable, a time stepping scheme must fulfill the so-called *Courant-Friedrichs-Lewy* (*CFL*) condition. This condition states that the domain of dependence of the numerical method must include the domain of dependence of the partial differential equation under study. The magnitude of the *CFL* number depends on the type and on the parameters of the time stepping scheme, as well as on the form of the spatial discretization scheme.

The maximum time step can be determined for linear model equations with the aid of the Von Neumann stability analysis. However, the maximum time step can be calculated only approximately for multidimensional, non-linear governing equations, like the Navier-Stokes equations themselves.

For steady state calculations, in real and in fictitious time, a faster expulsion of the disturbances can be achieved by locally using the maximum allowable time step. This means that a maximum allowable time step is computed and used for each one of the control volumes. In the present work, for the two-dimensional Navier-Stokes equations, the local time step limit $\Delta t_{I,J}$ for a given control volume $\Omega_{I,J}$ is estimated accounting for both the convective $[\Delta t_c]_{I,J}$ and diffusive $[\Delta t_d]_{I,J}$ contributions as follows

$$\Delta t_{I,J} = \Delta t^*_{I,J} = \sigma \frac{[\Delta t_c]_{I,J}\,[\Delta t_d]_{I,J}}{[\Delta t_c]_{I,J} + [\Delta t_d]_{I,J}}, \tag{3.131}$$

where σ is the *CFL* , or Courant, number. For two dimensional problems the convective contribution is

$$[\Delta t_c]_{I,J} = \frac{V(\Omega_{I,J})}{\left|\vec{v}_{I,J}\cdot\vec{S}_I\right| + \left|\vec{v}_{I,J}\cdot\vec{S}_J\right| + c_{I,J}\left(\left|\vec{S}_I\right| + \left|\vec{S}_J\right|\right)}. \tag{3.132}$$

In equation (3.132), $c_{I,J}$ is the speed of sound for the control volume $\Omega_{I,J}$, computed as follows

$$c_{I,J} = \sqrt{\gamma\, R\, T_{I,J}}.$$

$\vec{S}_I$ and $\vec{S}_J$ in equation (3.132) are average area vectors. They refer to the control volume $\Omega_{I,J}$ and are defined as follows (assuming the area vectors of cell volume $\Omega_{I,J}$ are oriented as in Figure 4)

$$\vec{S}_I = \frac{1}{2}\left([S_x]_{I+\frac{1}{2},J} - [S_x]_{I-\frac{1}{2},J}\right)\hat{\imath} - \frac{1}{2}\left([S_y]_{I+\frac{1}{2},J} - [S_y]_{I-\frac{1}{2},J}\right)\hat{\jmath}$$

$$\vec{S}_J = \frac{1}{2}\left([S_x]_{I,J+\frac{1}{2}} - [S_x]_{I,J-\frac{1}{2}}\right)\hat{\imath} - \frac{1}{2}\left([S_y]_{I,J+\frac{1}{2}} - [S_y]_{I,J-\frac{1}{2}}\right)\hat{\jmath}$$

Finally, $\left|\vec{S}_I\right|$ and $\left|\vec{S}_J\right|$ in equation (3.132) denote the magnitudes of vectors $\vec{S}_I$ and $\vec{S}_J$, respectively. The viscous contribution to the time step for the two dimensional case is

$$[\Delta t_d]_{I,J} = \frac{V(\Omega_{I,J})^2}{K_t \frac{\gamma}{\rho_{I,J}}\frac{\mu_{I,J}}{Pr}\left(\left|\vec{S}_I\right|^2 + \left|\vec{S}_J\right|^2\right)}. \tag{3.133}$$

K_t is a constant whose value in this dissertation is set equal to 4. The molecular viscosity, $\mu_{I,J}$, is computed as function of the temperature as it was stated in the previous chapter (see equation (2.32)); Pr is the Prandtl number and, as stated in Chapter II, it is a constant with value 0.72 for air.

With the aid of equations (3.131), (3.132) and (3.133), the local time step can be obtained. This time step is valid for one control volume only. Use of local time

stepping technique helps to reach convergence faster in both implicit and explicit schemes from the previous sections. Only the implicit scheme is time-accurate though. The explicit scheme can be made time-accurate by employing a global time step, Δt_{global}, defined as follows

$$\Delta t_{\text{global}} = \min\left(\Delta t_{I,J}\right), \tag{3.134}$$

for all interior I and J and with $\Delta t_{I,J}$ computed using equation (3.131). This Δt_{global} is then used in the scheme (3.114) instead of $\Delta t_{I,J}$ (for all interior I and J).

Equations (3.131), (3.132) and (3.133) complete the determination of the time step for both time-advancement schemes reviewed in the last two sections.

J. Turbulence Modeling

The basic equations for the numerical solutions under consideration are the Navier-Stokes equations (see summary of governing equations (3.1) to (3.3) and equation (3.4)). In this research, the effects of turbulence are simulated by an eddy viscosity coefficient denoted as $\mu_{T\,I,J}$. This eddy viscosity coefficient is stored at all cell centers of the flow field. However, $\mu_{T\,I,J}$ is computed only in a user defined region, close to the wall and to the wake cut[12], where the turbulence effects are known to be important. On the rest of the flow field $\mu_{T\,I,J}$ is set to zero. What is done next is to replace the molecular viscosity, μ[13], by a total viscosity defined as $(\mu + \mu_T)$ on everyplace where μ appears (only when the flow being simulated is turbulent).

Note that, for the discretized energy and momentum equations, the total viscosity is required at the mid-points of cell faces (see equations (3.22) to (3.24)). Because

[12]There is a user defined parameter that lets the user choose how far from the wall and from the wake cut he wants the turbulence model to be applied.

[13]Computed using equations (2.32) and stored at all cell centers as well.

μ and μ_T are available at cell centers only, the total viscosity $(\mu + \mu_T)$ at the mid-points of cell faces is obtained by computing μ and μ_T at such mid-points by simple arithmetic average and then adding the result. For example, the total viscosity at mid-points of cell face $(I + \frac{1}{2}, J)$ is computed as follows

$$\left(\mu + \mu_T\right)_{I+\frac{1}{2},J} = \frac{\left(\mu_{I,J} + \mu_{I+1,J}\right)}{2} + \frac{\left(\mu_{T\,I,J} + \mu_{T\,(I+1,J)}\right)}{2}.$$

Furthermore, in the discretized energy equation, the "laminar" thermal conductivity $k = c_p\,(\mu/Pr)$ is required at the mid-points of cell faces (see equation (3.24)). This laminar thermal conductivity must be replaced by a "total" thermal conductivity when the flow is turbulent. The total thermal conductivity is defined as $c_p\,(\mu/Pr + \mu_T/Pr_T)$, and for the specific case of cell face $(I + \frac{1}{2}, J)$ it is

$$c_p\left(\frac{\mu}{Pr} + \frac{\mu_T}{Pr_T}\right)_{(I+\frac{1}{2},J)} = c_p\left(\frac{\mu_{I,J} + \mu_{I+1,J}}{2\,Pr} + \frac{\mu_{T\,I,J} + \mu_{T\,I+1,J}}{2\,Pr_T}\right). \tag{3.135}$$

Pr_T in the expressions for the total thermal conductivity is the "turbulent" Prandtl number which is considered to have a constant value of 0.90 for air, the working fluid in this dissertation. Finally, the quantity $\mu_{I,J}/Pr$ in the expression for $[\Delta t_d]_{I,J}$, (see equation (3.133)), is changed to $(\mu_{I,J}/Pr + \mu_{T\,I,J}/Pr_T)$. Note that here, no averaging is required.

The turbulent viscosity $\mu_{T\,I,J}$ mentioned above is determined by means of the algebraic turbulence model of Baldwin and Lomax [18]. This model is patterned after that of Cebeci [36] with modifications that avoid the necessity for finding the edge of the boundary layer. It is a two-layer algebraic eddy viscosity model in which $\mu_{T\,I,J}$ is given by

$$\mu_{T\,I,J} = \begin{cases} (\mu_{T\,I,J})_{\text{inner}} & y_{I,J} \le y_{\text{crossover}} \\ (\mu_{T\,I,J})_{\text{outer}} & y_{\text{crossover}} < y_{I,J} \end{cases}$$

where $y_{I,J}$ denotes the normal distance from the wall to cell center (I,J) and $y_{\text{crossover}}$

is the smallest value of $y_{I,J}$ at which values from the inner and outer formulas are equal.

The Prandtl-Van Driest formulation is used for the inner region

$$(\mu_{T\,I,J})_{\text{inner}} = \rho_{I,J}\,\ell_{I,J}^2\,|\vec{w}_{I,J}|, \tag{3.136}$$

where $|\vec{w}_{I,J}|$ is the magnitude of the vorticity vector, defined as follows (for two-dimensional problems)

$$|\vec{w}_{I,J}| = \sqrt{\left(\left.\frac{\partial u}{\partial y}\right|_{I,J} - \left.\frac{\partial v}{\partial x}\right|_{I,J}\right)^2}. \tag{3.137}$$

The derivatives in this equation are computed as described in Sections III.F.2 and III.F.3 with the difference that here they are computed at grid cell centers and not at mid-points of cell faces. No auxiliary control volumes are therefore required and the derivatives in equation (3.137) are computed in terms of velocities at mid-points of cell faces and of the volume of the cell.

In equation (3.136) the term $\ell_{I,J}$ is computed as

$$\ell_{I,J} = k\;y_{I,J}\;\left[1 - \exp\left(-\frac{y^+_{I,J}}{A^+}\right)\right], \tag{3.138}$$

where A^+ and k are constants that are defined at the end of this formulation. The symbol $y^+_{I,J}$ in the same equation is known as the *y-plus number* and it is defined as

$$y^+_{I,J} = \frac{\rho_{I,\frac{1}{2}}\,u_\tau\,y_{I,J}}{\mu_{I,\frac{1}{2}}}. \tag{3.139}$$

In equation (3.139) subscripts $(I, \frac{1}{2})$ denote values at the wall[14] and u_τ represents the

[14]Sometimes these and other values at the wall are denoted with the subscript w when discussing turbulence model implementation.

friction velocity which is defined as

$$u_\tau = \sqrt{\frac{\tau_{I,\frac{1}{2}}}{\rho_{I,\frac{1}{2}}}}. \tag{3.140}$$

The term $\tau_{I,\frac{1}{2}}$ in equation (3.140) denotes the shear stress at the wall. A discussion about its determination is given in Section III.L.5 and, for now, only the formula for its computation is given

$$\tau_{I,\frac{1}{2}} = \mu_{I,\frac{1}{2}} \left.\frac{\partial u_\varepsilon}{\partial \eta}\right|_{I,\frac{1}{2}}. \tag{3.141}$$

In this equation, ε and η denote a local tangential-normal coordinate system. u_ε is the velocity component along the ε-direction (see Figure 9).

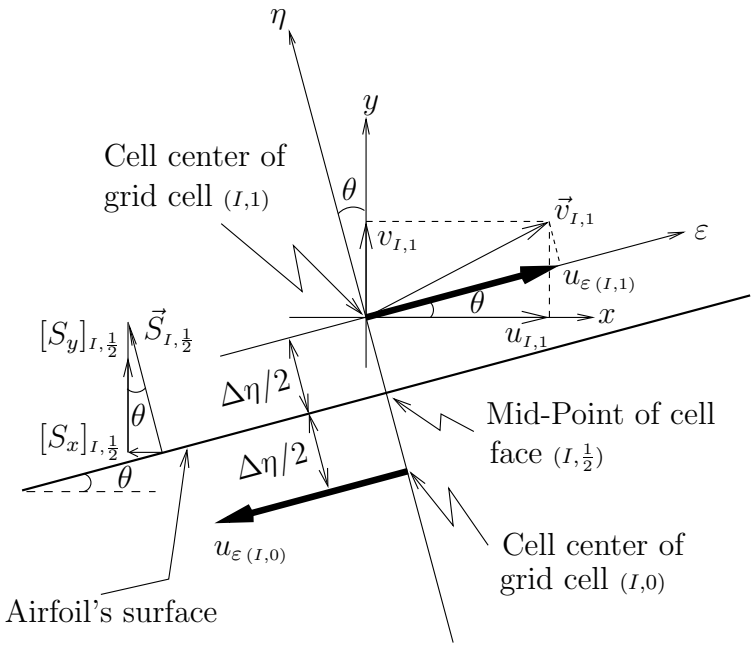

Fig. 9.: Cartesian velocity components at grid cell $(I, 1)$ and their projection to the tangential-to-the-wall direction (ε).

The term $\left.\frac{\partial u_\varepsilon}{\partial \eta}\right|_{I,\frac{1}{2}}$ is expressed in terms of the available Cartesian components of $\vec{v}$ at

cell center $(I,1)$

$$\left.\frac{\partial u_\varepsilon}{\partial \eta}\right|_{I,\frac{1}{2}} = \frac{u_{\varepsilon(I,1)} - u_{\varepsilon(I,0)}}{2\left(\frac{\Delta\eta}{2}\right)}, \tag{3.142}$$

(see Figure 9). Because of the no-slip boundary condition $u_{\varepsilon(I,0)} = -u_{\varepsilon(I,1)}$. Equation (3.142) then reduces to

$$\left.\frac{\partial u_\varepsilon}{\partial \eta}\right|_{I,\frac{1}{2}} = \frac{2u_{\varepsilon(I,1)}}{\Delta\eta}. \tag{3.143}$$

The velocity component $u_{\varepsilon\,(I,1)}$ is expressed in terms of the available Cartesian components of $\vec{v}_{I,1}$

$$u_{\varepsilon\,(I,1)} = u_{I,1}\cos\theta + v_{I,1}\sin\theta, \tag{3.144}$$

where, as it can be verified in Figure 9

$$\cos\theta = \frac{[S_y]_{I,\frac{1}{2}}}{\left|\vec{S}_{I,\frac{1}{2}}\right|} \qquad \text{and} \qquad \sin\theta = \frac{-[S_x]_{I,\frac{1}{2}}}{\left|\vec{S}_{I,\frac{1}{2}}\right|}. \tag{3.145}$$

Finally, the term $\Delta\eta$ equals the height of the grid cells adjacent to the airfoil. Due to the nature of the grid built in this work (see Section III.O.1) this is constant for a given grid and is computed as follows

$$\Delta\eta = \sqrt{(x_{(I,1)} - x_{(I,0)})^2 + (y_{(I,1)} - y_{(I,0)})^2} \tag{3.146}$$

for any I over the airfoil. Substitution of equations (3.144), (3.145) and (3.146) into (3.143) gives the final formula to compute $\left.\frac{\partial u_\varepsilon}{\partial \eta}\right|_{I,\frac{1}{2}}$ in terms of Cartesian components (for $\vec{v}_{I,1}$, $\vec{S}_{I,\frac{1}{2}}$) and coordinates (for $\Delta\eta$). The formula is

$$\left.\frac{\partial u_\varepsilon}{\partial \eta}\right|_{I,\frac{1}{2}} = \frac{2\big(u_{I,1}\,[S_y]_{I,\frac{1}{2}} - v_{I,1}\,[S_x]_{I,\frac{1}{2}}\big)}{\left|\vec{S}_{I,\frac{1}{2}}\right|\sqrt{(x_{(I,1)} - x_{(I,0)})^2 + (y_{(I,1)} - y_{(I,0)})^2}}.$$

This expression is utilized to compute $\tau_{I,\frac{1}{2}}$, equation (3.141). Substitution of equation

(3.140) into (3.139) allows to rewrite the expression for $y^+_{I,J}$ as follows

$$y^+_{I,J} = \frac{\sqrt{\rho_{I,\frac{1}{2}}\,\tau_{I,\frac{1}{2}}}}{\mu_{I,\frac{1}{2}}}\; y_{I,J}.$$

This is the expression that must be used in equation (3.138).

On the other hand, for the outer region, the following formula is utilized

$$(\mu_{TI,J})_{\text{outer}} = K\,(C_{CP}\,)\,\rho_{I,J} F_{WAKE}\,F_{KLEB}\,(y_{I,J}) \tag{3.147}$$

where K is the Clauser constant and C_{CP} is an additional constant (both specified in Table II). F_{WAKE} is defined as the smaller value between $y_{MAX}\,F_{MAX}$ and $C_{WK}\,y_{MAX}\,(U_{DIF}\,)^2/F_{MAX}$. Employing the "Min" intrinsic Fortran function[15]

$$F_{WAKE} = \text{Min}\Big(y_{MAX}\,F_{MAX}\,,\; C_{WK}\,y_{MAX}\,(U_{DIF}\,)^2/F_{MAX}\,\Big). \tag{3.148}$$

The constant C_{WK} is specified in Table II. The quantities y_{MAX} and F_{MAX} of the same equation are determined from the function

$$F(y_{I,J}) = y_{I,J}\,|\vec{w}_{I,J}|\,\left[1 - \exp\!\left(-\frac{y^+_{I,J}}{A^+}\right)\right]. \tag{3.149}$$

In wakes, the exponential term of equation (3.149) is set equal to zero [18]. The quantity F_{MAX} is the maximum value of $F(y_{I,J})$ that occurs in a profile and y_{MAX} is the value of $y_{I,J}$ at which it occurs. The quantity U_{DIF} in equation (3.148) represents

---

[15] Min(A-1, A-2, ..., A-n)

Min: 'INTEGER' or 'REAL' function, the exact type being the result of cross-promoting the types of all the arguments.

A: 'INTEGER' or 'REAL'; at least two such arguments must be provided; scalar; INTENT(IN).

Intrinsic groups: (standard FORTRAN 77).

Description: Returns the argument with the smallest value.

the difference between maximum and minimum total velocity in the profile. Thus, for a fixed I station, for which all cell centers are normal to the airfoil, one has

$$U_{DIF} = \left(\sqrt{u^2+v^2}\,\right)_{MAX} - \left(\sqrt{u^2+v^2}\,\right)_{MIN} .$$

The second term of this equation is taken to be zero (except in wakes).

Finally, the function $F_{KLEB}\,(y_{I,J})$ in equation (3.147) is the Klebanoff intermittency factor given by

$$F_{KLEB}\,(y_{I,J}) = \left[1 + 5.5\left(\frac{C_{KLEB}\,y_{I,J}}{y_{MAX}}\right)^6\right]^{-1}$$

where C_{KLEB} denotes the Klebanoff constant. The constants appearing in all of the previous relations have been determined by requiring agreement with the Cebeci [36] formulation for constant pressure boundary layers at transonic speeds. The values of the constants are given in Table II.

Table II.: Values of constants appearing in the Baldwin-Lomax turbulence modeling.

Constant notation	*Value*
A^+	26
C_{CP}	1.60
C_{KLEB}	0.30
C_{WK}	0.25
k	0.40
K	0.0168

The outer formulation (equations (3.147) and (3.148)) can be used in wakes as well as in attached and separated boundary layers. In this model, the distribution of

vorticity is used to determine the length scales so that the necessity for finding the outer edge of the boundary layer (or of the wake) is removed.

K. Fluid Injection Simulation

In this research a numerical study is conducted to investigate the effect of a zero-mass synthetic jet on the aerodynamic characteristics of the NACA0015 and NACA0012 airfoils. An unsteady surface transpiration boundary condition is enforced at a user defined location on the airfoil's upper surface to simulate the time variation of the mass flux out from and into the airfoil's surface. It is important to note that a control technique which simulates the effects of surface blowing/suction without any actual mass transfer (e.g. the zero-mass synthetic jet investigated in this work) is highly desirable since it eliminates the need of complex air management systems (as it would be the case, for example, for a steady blowing jet).

The mechanics of the jet is that associated with the outward and inward flows observed when one moves a piston forward and backward in a cylinder having a single orifice like-port (see figure on page 146). Air moves out of the cylinder when the piston is moved forward displacing the volume of air ahead of it. When the piston is moved backward, air is drawn into the cylinder by virtue of the low level suction pressure created in the cylinder cavity. If the displaced volumes associated with the motion of the piston are equal, then the net mass transfer across the port, for all practical purposes, is equal to zero.

For a given jet exit cross section, the interaction between the jet and the surrounding fluid can be simulated using a relative simple time-dependent boundary condition. As perceived by an observer standing next to the exit port, periodic flow out of and into the cavity is seen. The boundary condition for the jet is therefore

one which represents an oscillating velocity vector in the direction of the jet, simply described using a harmonic function

$$v_{jet} = V_{jet\ max}\ \sin\left(2\pi\, f_{SJA}\, t\right). \tag{3.150}$$

In equation (3.150), f_{SJA} denotes the frequency of injection in [Hz], $V_{jet\ max}$ denotes the amplitude of the sine function in [m/s] and t denotes the time in [s]. The amplitude and frequency of the sinusoidal variation are user defined parameters whose values for the simulations performed in this dissertation are widely discussed in the following chapters. Figure 10 depicts the temporal variation of the jet velocity, v_{jet}. Note that the positive jet velocity is associated with the blowing portion of the cycle and that the negative jet velocity is associated with the suction portion of the cycle.

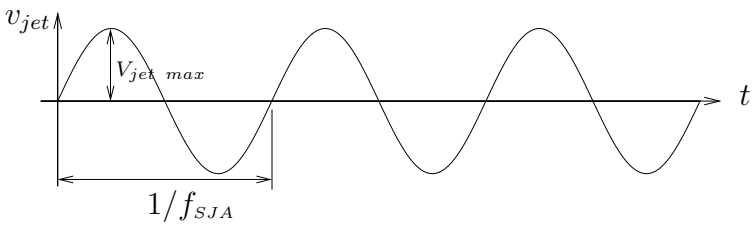

Fig. 10.: Variation of the injection velocity, v_{jet}, with respect to time.

In the code developed in this research, the number of cell faces where injection of fluid takes place is a user defined parameter. Furthermore, the user can also set the angle of fluid injection, measured with respect to the wall at the point of injection. For the numerical experiments performed in this dissertation, the angle of injection is set to 2 degrees. That is, the fluid is injected nearly tangentially to the airfoil and in direction of the flow as schematically shown in Figure 11.

To demonstrate the effects of the jet on the aerodynamic characteristics of the NACA0015 a set of numerical simulations were performed for a number of different

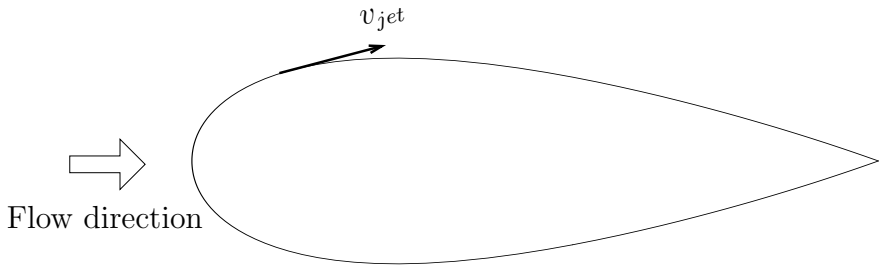

Fig. 11.: Tangential fluid injection.

angles of attack. All the time accurate predictions were started from a corresponding steady solution (i.e., from the solution of a simulation without injection at the desired angle of attack, freestream Mach number and Reynolds number). In the following chapters the impact of the injection parameters is widely discussed.

L. Boundary Conditions

In this dissertation, the flow around an isolated NACA0015 airfoil is numerically simulated. For this problem, only a finite region surrounding the solid body can be covered by the numerical simulation and there exists, therefore, a truncation of the domain. This truncation leads to non-natural (or artificial) boundaries –the *farfield boundaries*– where values of certain quantities must be prescribed. This type of boundary condition is discussed in this section.

There are, furthermore, solid walls which are exposed to the flow and which represent natural boundaries –the *wall boundaries*– of the physical domain. Another type of artificial boundary encountered in this work is the *coordinate wake cut*. As it will be seen in the corresponding subsection below, this type of boundary condition appears for the C-grid topology (among others) and the flow variables and their gradients must be continuous across the cut. Finally, the boundary conditions in the

region of fluid injection are presented in this section.

The numerical treatment of the boundary conditions require particular care since an improper implementation can result in inaccurate simulation of the real system. Additionally, the stability and the convergence speed of the solution scheme can be negatively influenced. In the subsections below, the implementation of the boundary conditions is reviewed.

1. Concept of Dummy Cells

The approach known as *dummy cells* for the application of the boundary conditions is employed in this work (see e.g., [32], pp. 268-269). The dummy cells approach consists of an additional layer of control volumes or cells completely surrounding the physical domain. This is sketched in Figure 12 for the case of two-dimensional problems.

In Figure 12 the connected `x` symbols represent two standard stencils of a second-order cell centered scheme (for the convective terms). One stencil is applied to a boundary cell of the domain and the other is applied to an interior cell. The dummy cells are not physically generated as the grid for the interior domain; rather, they are only virtual but with some geometrical quantities, like volume or face vectors, associated with them.

The purpose of the dummy cells is to simplify the computation of fluxes, gradients, dissipation, etc., along the boundaries. This is achieved by extending the stencil of the spatial discretization scheme beyond the boundaries. The dummy cells' job is to cover the part of the stencil which lays outside. As it can be seen in Figure 12, the same discretization scheme is utilized at boundary cells and at interior cells. Thus, the governing equations can be solved in exactly the same way in all physical cells. This makes the discretization scheme much easier to implement since no special

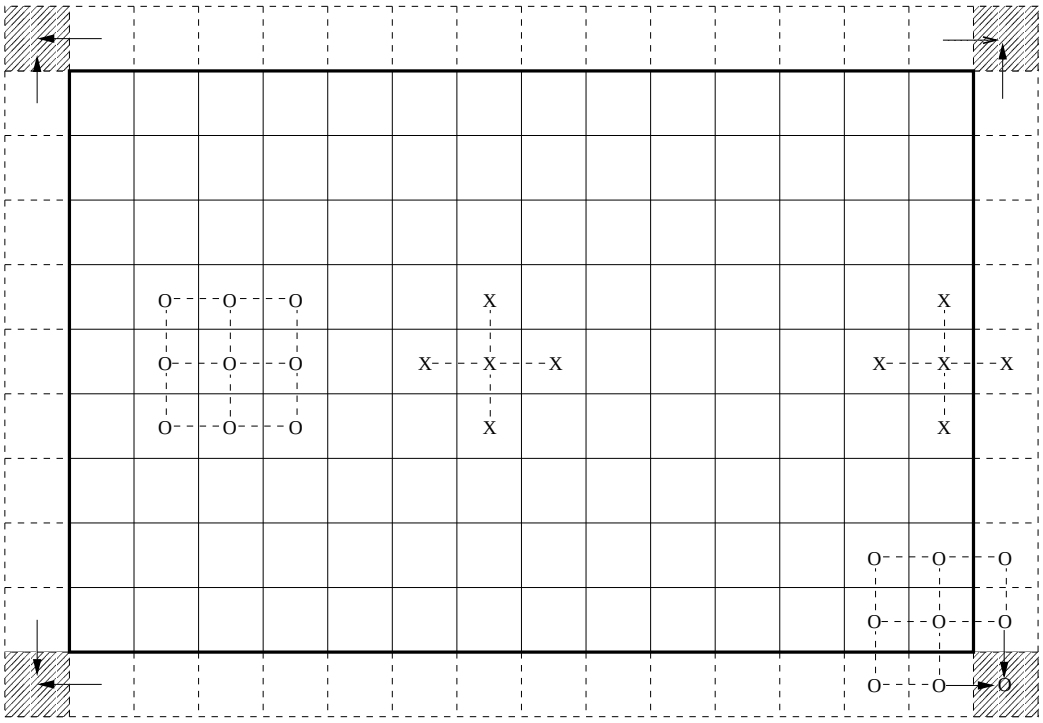

Fig. 12.: One layer of dummy cells (dashed line) around the computational domain (thick line) in 2D.

treatment is required when the solver is working on the boundary cells.

The condition is of course that the dummy cells' centroids contain appropriate values of the conservative variables and of the required geometrical quantities. The conservative variables at the centroids of the dummy cells are obtained from the boundary conditions. The geometrical quantities are taken from the corresponding control volumes at the boundaries. In the case of coordinate wake cut boundaries, all flow variables and the geometry are obtained directly from a corresponding, opposite cell (see appropriate sub-section below).

The gray-shadowed dummy cells in Figure 12 represent a challenge, since it is not quite clear how to set their values (when there is not adjacent grid block, like

in a multi-block approach). These values are not required by the standard cross-type discretization 4-point stencil (as shown in Figure 12). However, they become necessary for the determination of the velocity and temperature gradients; i.e., for the computation of viscous and heat fluxes at mid-points of cell faces. For a given (I, J) cell, the computation of the gradients at all cell faces requires a nine-point stencil as shown in Figure 12 by the "o" connected symbols. In this research, a simple average of the values from the adjacent "regular" dummy cells, as indicated by the arrows in Figure 12, is utilized.

2. Natural Boundaries of the Physical Domain

a. Solid Walls for Inviscid Flow

At solid walls, a single physical boundary condition must be imposed. For the inviscid flow case, this condition is expressed by the vanishing of the normal-to-the-wall velocity or the *no-penetration condition*

$$\vec{v}_{I,\frac{1}{2}} \cdot \vec{S}_{I,\frac{1}{2}} = 0, \tag{3.151}$$

where subindex $(_{I,\frac{1}{2}})$ refers to values at the wall and $\vec{S}_{I,\frac{1}{2}}$ is the normal-to-the wall vector pointing toward the interior domain (see Figure 13). Physically, this means that, when the flow is assumed to be inviscid, the fluid slips over the solid surface but does not penetrate such surface. In this work, condition (3.151) is achieved by setting the Cartesian velocity components at the corresponding ghost cell such that (see Figure 13)

$$v_{\eta\,(I,\frac{1}{2})} = 0. \tag{3.152}$$

This is the single boundary condition that must be imposed at the solid wall. On the other hand, the tangential velocity component at the wall, and the rest of flow

quantities, must be extrapolated from the interior. The tangential velocity at the wall is obtained using a first order extrapolation from the interior (see Figure 13)

$$v_{\varepsilon\,(I,\frac{1}{2})} = v_{\varepsilon\,(I,1)} \tag{3.153}$$

In equations (3.152), (3.153) and in Figure 13, ε and η denote tangential and normal directions to the wall, respectively. More specifically, ε-η denote a local coordinate system where the η-axis points toward the domain and ε-axis is such that the coordinate system is right-handed. Conditions (3.152) and (3.153) lead to

$$v_{\varepsilon\,(I,0)} = v_{\varepsilon\,(I,1)} \tag{3.154}$$

$$v_{\eta\,(I,0)} = -v_{\eta\,(I,1)} \tag{3.155}$$

such that

$$\begin{aligned} v_{\varepsilon\,(I,\frac{1}{2})} &= \tfrac{1}{2}\left(v_{\varepsilon\,(I,1)} + v_{\varepsilon\,(I,0)}\right) = v_{\varepsilon\,(I,1)} \\ v_{\eta\,(I,\frac{1}{2})} &= \tfrac{1}{2}\left(v_{\eta\,(I,1)} + v_{\eta\,(I,0)}\right) = 0. \end{aligned}$$

The seeked x- and y-components of $\vec{v}_{I,0}$ are determined by performing a component transformation of $\vec{v}_{I,0}$ from the ε-η to the x-y coordinate system (see Figure 13). The transformation is

$$\begin{aligned} u_{I,0} &= v_{\varepsilon\,(I,0)}\cos\theta - v_{\eta\,(I,0)}\sin\theta \\ v_{I,0} &= v_{\varepsilon\,(I,0)}\sin\theta + v_{\eta\,(I,0)}\cos\theta. \end{aligned} \tag{3.156}$$

In (3.156), the angle θ must be measured counter-clockwise, from the positive x-axis to the positive ε-axis. The inclination of the ε-axis is readily determined using the grid geometry (nodes $(i,0)$ and $(i-1,0)$ in Figure 13). Use of equations (3.154) and (3.155) into transformation (3.156) gives

$$\begin{aligned} u_{I,0} &= v_{\varepsilon\,(I,1)}\cos\theta + v_{\eta\,(I,1)}\sin\theta \\ v_{I,0} &= v_{\varepsilon\,(I,1)}\sin\theta - v_{\eta(I,1)}\cos\theta. \end{aligned} \tag{3.157}$$

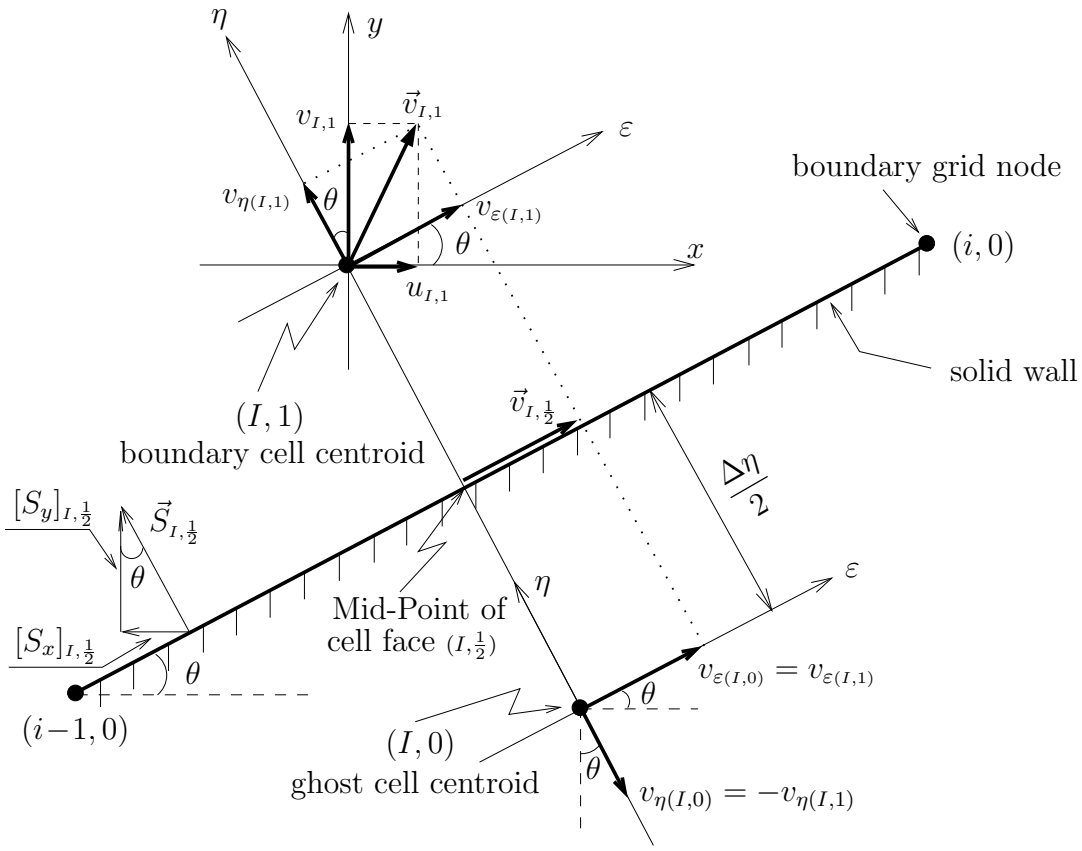

Fig. 13.: Velocity components at cell centers $(I,1)$, $(I,0)$ and at mid-point of cell face $(I,\frac{1}{2})$.

The problem therefore reduces to the determination of $v_{\varepsilon(I,1)}$ and $v_{\eta(I,1)}$.

The x- and y-components of $\vec{v}_{I,1}$ are known at all times from the flow solver. The angle θ, as mentioned previously, is also known; therefore, a component transformation of $\vec{v}_{I,1}$ from the x-y to the ε-η systems will give the required $v_{\varepsilon(I,1)}$ and $v_{\eta(I,1)}$. The transformation is as follows

$$\begin{aligned} v_{\varepsilon\,(I,1)} &= u_{I,1}\cos\theta + v_{I,1}\sin\theta \\ v_{\eta\,(I,1)} &= -u_{I,1}\sin\theta + v_{I,1}\cos\theta. \end{aligned} \tag{3.158}$$

The final formulas utilized in this work, for the determination of $u_{I,0}$ and $v_{I,0}$ in a solid

wall boundary condition and inviscid flow, are determined by substituting equations (3.158) into (3.157). The result is

$$u_{I,0} = u_{I,1}\left(\cos\theta\cos\theta - \sin\theta\sin\theta\right) + v_{I,1}\left(2\sin\theta\cos\theta\right) \tag{3.159}$$

$$v_{I,0} = u_{I,1}\left(2\sin\theta\cos\theta\right) - v_{I,1}\left(\cos\theta\cos\theta - \sin\theta\sin\theta\right). \tag{3.160}$$

In this work, the angle θ is not actually computed. Instead, the $\cos\theta$ and $\sin\theta$ terms in the equations above are determined in terms of the available area vector and its component

$$\cos\theta = \frac{[S_y]_{I,\frac{1}{2}}}{\left|\vec{S}_{I,\frac{1}{2}}\right|} \qquad \text{and} \qquad \sin\theta = \frac{-[S_x]_{I,\frac{1}{2}}}{\left|\vec{S}_{I,\frac{1}{2}}\right|}. \tag{3.161}$$

These formulas are general, valid for any orientation of the grid segment $(i,0)$, $(i-1,0)$. Using equations (3.161) into equations (3.159) and (3.160) yields

$$u_{I,0} = \frac{u_{I,1}}{\left|\vec{S}_{I,\frac{1}{2}}\right|}\left([S_y]^2_{I,\frac{1}{2}} - [S_x]^2_{I,\frac{1}{2}}\right) - 2\,\frac{v_{I,1}}{\left|\vec{S}_{I,\frac{1}{2}}\right|}\left([S_x]_{I,\frac{1}{2}}\,[S_y]_{I,\frac{1}{2}}\right) \tag{3.162}$$

$$v_{I,0} = -2\,\frac{u_{I,1}}{\left|\vec{S}_{I,\frac{1}{2}}\right|}\left([S_x]_{I,\frac{1}{2}}\,[S_y]_{I,\frac{1}{2}}\right) - \frac{u_{I,1}}{\left|\vec{S}_{I,\frac{1}{2}}\right|}\left([S_y]^2_{I,\frac{1}{2}} - [S_x]^2_{I,\frac{1}{2}}\right) \tag{3.163}$$

As mentioned above, the variables other than the normal velocity must be obtained from the interior flow. In the current solid wall boundary implementation for the inviscid flow, the density at the wall, denoted as $\rho_{I,\frac{1}{2}}$, is extrapolated from the first interior node. That is, it is considered that $\rho_{I,\frac{1}{2}} = \rho_{I,1}$. This implies that the value at the corresponding ghost cell must be set as

$$\rho_{I,0} = \rho_{I,1}. \tag{3.164}$$

The next step in the implementation of the inviscid solid wall boundary condition is the determination of the pressure at the ghost cell $(I,0)$. The numerical determination of $p_{I,0}$ for inviscid flows is an essential element in any computation with solid boundaries (see Figure 15). The method employed here consists in discretiz-

ing directly the normal-to-the-wall, inviscid, momentum equation. Such equation is (see [37], pp. 381-383)

$$\frac{1}{R_{I,\frac{1}{2}}}\, v^2_{\varepsilon\,(I,\frac{1}{2})} = \frac{1}{\rho_{I,\frac{1}{2}}}\, \frac{\partial p}{\partial \eta}\bigg|_{I,\frac{1}{2}} \tag{3.165}$$

In equation (3.165), $R_{I,\frac{1}{2}}$ is the wall radius of curvature, $\rho_{I,\frac{1}{2}}$ (equal to $\rho_{I,1}$) is the density at the wall and $v^2_{\varepsilon(I,\frac{1}{2})}$ is the total velocity at the wall, replaced with $\left|\vec{v}_{I,\frac{1}{2}}\right|^2$ and computed as

$$\left|\vec{v}_{I,\frac{1}{2}}\right|^2 \;=\; u^2_{(I,\frac{1}{2})} + v^2_{(I,\frac{1}{2})} \;=\; \left[\tfrac{1}{2}\big(u_{I,0} + u_{I,1}\big)\right]^2 + \left[\tfrac{1}{2}\big(v_{I,0} + v_{I,1}\big)\right]^2. \tag{3.166}$$

The term $(\partial p/\partial \eta)\big|_{I,\frac{1}{2}}$ is discretized using a second order, central finite difference scheme as follows (see Figure 13)

$$\frac{\partial p}{\partial \eta}\bigg|_{I,\frac{1}{2}} = \frac{p_{I,1} - p_{I,0}}{2\left(\dfrac{\Delta\eta}{2}\right)} = \frac{p_{I,1} - p_{I,0}}{\Delta\eta}. \tag{3.167}$$

This is possible since the grid used in this work is orthogonal to the wall; $\Delta\eta$ is twice the distance from the cell centroid $(I,1)$ (or $(I,0)$) to the mid-point of the grid segment $(i,0)$ to $(i-1,0)$ (see Figure 13). This distance is equal to the height of the first grid cell closest to the wall and it is computed as

$$\Delta\eta = \sqrt{\left[x_{(i,1)} - x_{(i\text{–}1,0)}\right]^2 + \left[y_{(i,1)} - y_{(i\text{–}1,0)}\right]^2}. \tag{3.168}$$

This quantity is constant for a given grid in this work and it is computed only once, at the beginning of the computation. The *inverse* of the radius of curvature $1/R_{I,\frac{1}{2}}$ can be computed analytically if the definition of the wall is defined analytically. For the simulation over the NACA0015 airfoil performed in this dissertation, the wall is defined as

$$y = a\,\sqrt{x} + b\,x + c\,x^2 + d\,x^3 + e\,x^4 \tag{3.169}$$

where the coefficients a to e are, with $\tau = 0.15$ for the thickness of the airfoil

$$\begin{aligned} a &= 1.4845\,\tau &&= 0.222675 \\ b &= -0.6300\,\tau &&= -0.094500 \\ c &= -1.7685\,\tau &&= -0.265275 \\ d &= 1.4215\,\tau &&= 0.213225 \\ e &= -0.5075\,\tau &&= -0.076125. \end{aligned}$$

The formula to analytically compute the inverse of the radius of curvature is (see [38], p. 697)

$$\frac{1}{R} = \frac{|f'(t)g''(t) - g'(t)f''(t)|}{[(f'(t))^2 + (g'(t))^2]^{\frac{3}{2}}}.$$

Here, $f(t)$ and $g(t)$ are the parametric equations describing the wall of the NACA0015 with t denoting the parameter. More specifically

$$\begin{aligned} x &= t = f(t) \\ y &= a\sqrt{t} + b\,t + c\,t^2 + d\,t^3 + e\,t^4 = g(t). \end{aligned}$$

Therefore

$$\begin{aligned} f'(t) &= 1 \\ f''(t) &= 0 \\ g'(t) &= \frac{1}{2}\,a\,(t^{-\frac{1}{2}}) + b + 2\,c\,(t) + 3\,d\,\left(t^2\right) + 4\,e\,\left(t^3\right) && (3.170) \\ g''(t) &= -\frac{1}{4}\,a\,(t^{-\frac{3}{2}}) + 2\,c + 6\,d\,(t) + 12\,e\,\left(t^2\right). && (3.171) \end{aligned}$$

Thus, finally

$$\frac{1}{R} = \frac{\mid\ g''(t)\ \mid}{\left[1 + \left(g'(t)\right)^2\right]^{\frac{3}{2}}} = \frac{\mid\ g''(x)\ \mid}{\left[1 + \left(g'(x)\right)^2\right]^{\frac{3}{2}}} \qquad (0 \le x \le 1) \qquad (3.172)$$

Since the radius of curvature is required at mid-points of cell faces over the airfoil's

surface, then equation (3.172) is finally changed to a discrete form

$$\frac{1}{R_{I,\frac{1}{2}}} = \frac{\left| \; g''\left(\frac{x_{(I,0)}+x_{(I-1,0)}}{2}\right) \; \right|}{\left[1+\left(g'\left(\frac{x_{(I,0)}+x_{(I-1,0)}}{2}\right)\right)^2\right]^{\frac{3}{2}}} \qquad ITE \leq I \leq IM-(ITE-1)\,, \tag{3.173}$$

with functions g' and g'' defined by equations (3.170) and (3.171), respectively. The inverse of the radius of curvature is constant throughout the simulation and it is computed only once, at the beginning of the run. A plot showing these values is presented in Figure 14. Note the airfoil is not to 1:1 scale.

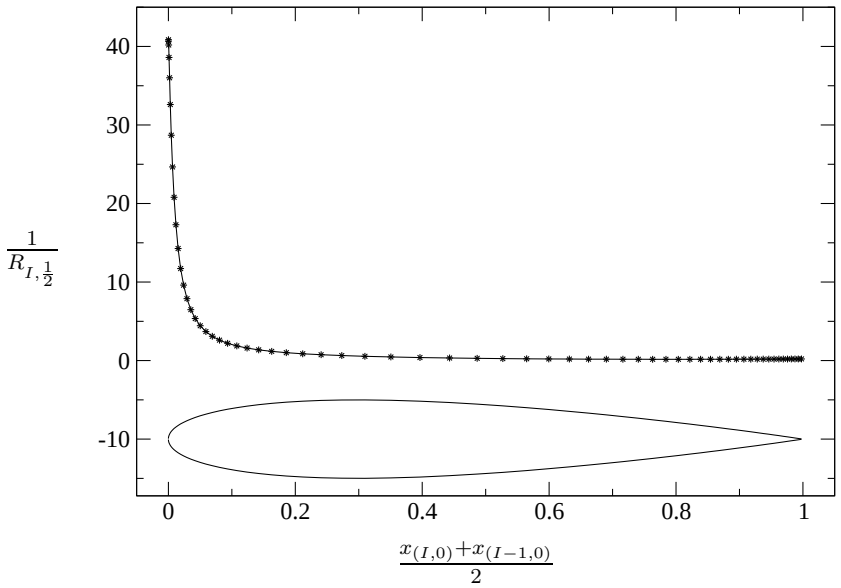

Fig. 14.: Inverse of the radius of curvature for the NACA0015 airfoil (not shown to scale).

Equations (3.165), (3.167), (3.168) and (3.173) give the final expression for the

pressure at the ghost cell $(I, 0)$

$$p_{I,0} = p_{I,1} - \Delta\eta \, \frac{\rho_{I,\frac{1}{2}}}{R_{I,\frac{1}{2}}} \left|\vec{v}_{I,\frac{1}{2}}\right|^2 . \tag{3.174}$$

An easier way of setting the pressure at the wall, $p_{I,\frac{1}{2}}$, would be a first order extrapolation of the pressure from the closest interior cell. This gives the following formula for obtaining $p_{I,0}$

$$p_{I,0} = p_{I,1}. \tag{3.175}$$

This is equivalent to setting $1/R_{I,\frac{1}{2}} = 0$ in equation (3.174)[16]. Figure 15 shows pressure contour plots from two steady, inviscid fluid flow computations for an isolated airfoil NACA0015 with $M_\infty = 0.3$ and $Re_\infty = 1 \times 10^6$. For the results shown in the top Figure, where the contour pressure lines close to the airfoil are smoother, equation (3.174) was utilized to set $p_{I,0}$ in the wall region. For the bottom Figure, equation (3.175) was utilized for the same purpose. The difference can be easily seen. The rest of variables required by the inviscid flow solver at "solid wall" ghost cells are the total energy E and the total enthalpy H, both per unit mass. These quantities are determined algebraically by using the relations (2.30) and (2.31). That is, $E_{I,0}$ and $H_{I,0}$ are determined as follows

$$E_{I,0} = c_v T_{I,0} + \left|\vec{v}_{I,0}\right|^2/2 \tag{3.176}$$

$$H_{I,0} = c_p T_{I,0} + \left|\vec{v}_{I,0}\right|^2/2, \tag{3.177}$$

with $T_{I,0}$ determined algebraically from the equation of state (equation (2.29))

$$T_{I,0} = \frac{p_{I,0}}{R\,\rho_{I,0}} \tag{3.178}$$

and $\left|\vec{v}_{I,0}\right|^2/2$ computed using $u_{I,0}$ and $v_{I,0}$ from equations (3.162) and (3.163).

[16] $1/R_{I,\frac{1}{2}} = 0$ corresponds to flat solid surfaces.

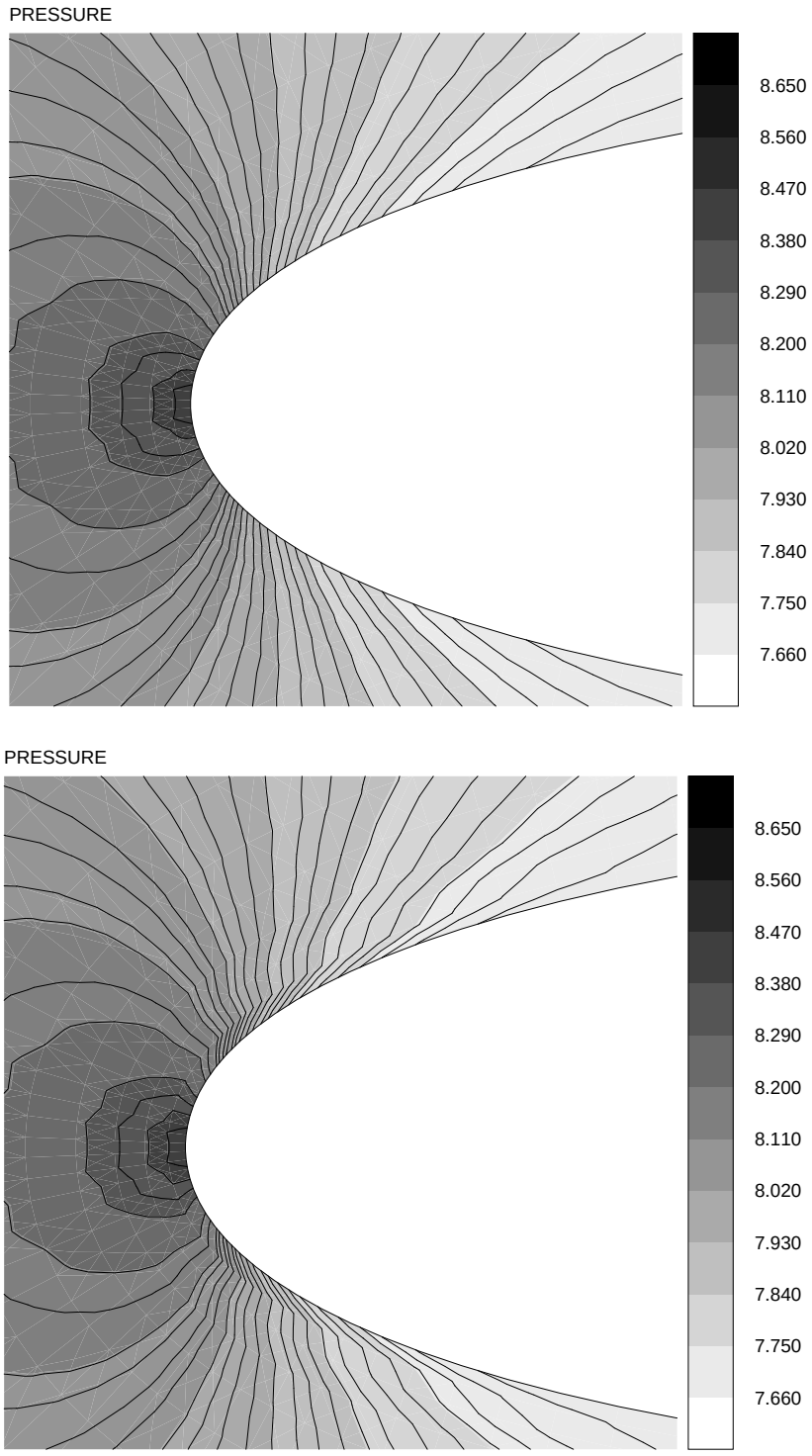

Fig. 15.: Contour plots of non-dimensional pressure for different wall boundary condition for the pressure. Top Figure: Eq. (3.174); bottom Figure: Eq. (3.175).

The solid wall boundary conditions for inviscid flow are thus computed using equations (3.162), (3.163), (3.164), (3.174), (3.176), (3.177) and (3.178).

b. Solid Walls for Viscous Flow

When a viscous fluid flows along a solid wall, physical experience must be employed in order to determine the nature of the boundary condition to be imposed. Within the framework of continuum mechanics, all known experiments indicate that the relative velocity between the fluid and the solid wall is zero. This is called the no-slip condition and is expressed by

$$\vec{v}_{\text{(of fluid at wall)}} = \vec{v}_{\text{(of the wall)}}.$$

If the velocity of the wall is zero, as it is the case in this work, and denoting the velocity of the fluid at the wall as usual (i.e., as $\vec{v}_{I,\frac{1}{2}}$) then the no-slip boundary condition can be written as

$$\vec{v}_{I,\frac{1}{2}} = 0,$$

This condition is implemented by means of the dummy cells concept

$$u_{I,0} = -u_{I,1} \tag{3.179}$$

$$v_{I,0} = -v_{I,1}. \tag{3.180}$$

Adiabatic boundary conditions are specified at the solid walls. That is, a prescribed zero heat flux is enforced at the wall. Therefore, the normal derivative of temperature, T, at the wall must be zero, $\partial T/\partial \eta\big|_{I,\frac{1}{2}} = 0$. This leads to the following equation for the determination of T at the ghost cells in the solid wall region (by performing a second-order finite difference approximation)

$$T_{I,0} = T_{I,1}. \tag{3.181}$$

The second thermodynamic variable at the solid wall for the case of viscous flows could be obtained by applying the normal pressure equation. At a solid wall with a no-slip condition, the momentum equation projected on the normal direction reduces to (see [37] p. 602)

$$\left.\frac{\partial p}{\partial \eta}\right|_{I,\frac{1}{2}} = \left(\vec{\nabla}\cdot\overline{\overline{\tau}}\right)_{\eta} \tag{3.182}$$

where η denotes the normal-to-the-wall direction. Assuming the shear layers are thin at high Reynolds numbers, equation (3.182) is replaced by $\left.\partial p/\partial \eta\right|_{I,\frac{1}{2}} = 0$ (see [37] p. 602). This in turn leads to the following equation for the determination of p at the ghost cells in the solid wall region

$$p_{I,0} = p_{I,1}. \tag{3.183}$$

Finally, the rest of the required variables ($\rho_{I,0}$, $E_{I,0}$ and $H_{I,0}$) are algebraically determined using relations (2.29), (2.30) and (2.31) respectively. That is

$$\rho_{I,0} = \frac{p_{I,0}}{R\,T_{I,0}} \tag{3.184}$$

$$E_{I,0} = c_v T_{I,0} + \left|\vec{v}_{I,0}\right|^2/2 \tag{3.185}$$

$$H_{I,0} = c_p T_{I,0} + \left|\vec{v}_{I,0}\right|^2/2, \tag{3.186}$$

In equations (3.185) and (3.186), $\left|\vec{v}_{I,0}\right|^2/2$ is computed using $u_{I,0}$ and $v_{I,0}$ from equations (3.179) and (3.180).

The solid wall boundary conditions for viscous flows are thus computed using equations (3.179), (3.180), (3.181), (3.183), (3.184), (3.185) and (3.186).

3. Artificial Boundary Conditions

As previously mentioned, when numerically simulating the flow over an isolated airfoil, a truncation of the domain must be introduced. The truncation must be placed

"far enough" such that its influence does not have notable effects on the flow solution as compared to the infinite domain. The approach utilized in this dissertation to deal with the farfield boundaries is as that used by Whitfield and Janus [39] for the cases of subsonic inflow and outflow. This approach utilizes the concept of characteristic variables which states that depending on the sign of the eigenvalues of the convective flux Jacobians (see Appendix A.9, equation (A.63) or (A.67) of Blazek [32]), the information is transported out or into the computational domain along the characteristics. According to the one-dimensional theory of Kreiss [40], the number of conditions to be imposed from outside at the boundary should be equal to the number of incoming characteristics. The remaining conditions should be determined from the solution inside the domain.

At the farfield boundary the flow can either enter or leave the domain as sketched in Figure 16. A discussion on the numerical implementation of the boundary conditions corresponding to these situations is given below.

a. Farfield Boundary Condition for Subsonic Inflow

Here, three characteristics enter and one leaves the physical domain. Therefore three characteristic variables are prescribed based on the freestream values and one characteristic variable is extrapolated from the interior physical domain. This leads to the following set of boundary conditions [39]

$$\begin{aligned} p_b &= \tfrac{1}{2}\big\{p_a + p_d - \rho_0 c_0 \left[n_x(u_a - u_d) + n_y(v_a - v_d)\right]\big\} \\ \rho_b &= \rho_a + (p_b - p_a)/c_0^2 \\ u_b &= u_a - n_x(p_a - p_b)/(\rho_0 c_0) \\ v_b &= v_a - n_y(p_a - p_b)/(\rho_0 c_0), \end{aligned} \tag{3.187}$$

where ρ_0 and c_0 represent a reference state. This state is set equal to the state at the

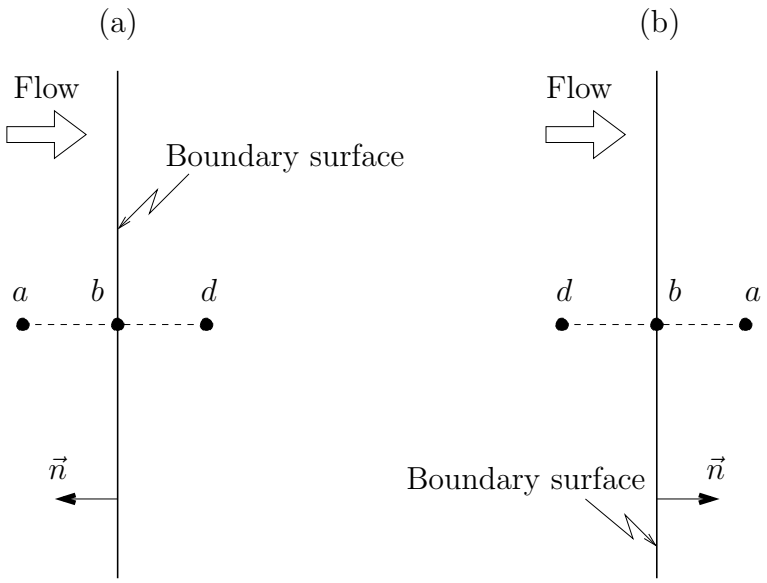

Fig. 16.: Farfield boundary: inflow (a) and outflow (b) situation. Position a is outside, b on the boundary and position d is inside the physical domain. The unit normal vector $\vec{n} = [n_x, n_y]^T$ points out of the domain.

interior point (point d in Figure 16). The values at point a are determined from the freestream state.

b. Farfield Boundary Condition for Subsonic Outflow

For this case, three flow variables –density and the two velocity components– must be extrapolated from the interior of the physical domain. The remaining fourth variable –the pressure– must be specified externally. This leads to the following set

of boundary conditions [39]

$$\begin{aligned} p_b &= p_a \\ \rho_b &= \rho_d + (p_b - p_d)/c_0^2 \\ u_b &= u_d + n_x(p_d - p_b)/(\rho_0 c_0) \\ v_b &= v_d + n_y(p_d - p_b)/(\rho_0 c_0), \end{aligned} \tag{3.188}$$

in which p_a is the freestream static pressure and ρ_0 and c_0 represent a reference state equal to the state at interior point d.

The required values for the dummy cells at the farfield for both cases, inflow or outflow, are obtained by linear extrapolation from the states d and b. That is, if the ghost cell's indexes are $(I, JM+1)$ for $I = 1$ to IM and fixed $J = JM$, then

$$\rho_{I,JM+1} = 2\,\rho_b - \rho_{I,JM} \tag{3.189}$$

$$u_{I,JM+1} = 2\,u_b - \rho_{I,JM} \tag{3.190}$$

$$v_{I,JM+1} = 2\,v_b - \rho_{I,JM} \tag{3.191}$$

$$p_{I,JM+1} = 2\,p_b - \rho_{I,JM}. \tag{3.192}$$

Finally, $E_{I,JM+1}$ and $H_{I,JM+1}$ are determined algebraically utilizing relations (2.30) and (2.31) which require $T_{I,JM+1}$. The latter can be determined algebraically as well using the equation of state for a perfect gas, equation (2.29). Therefore

$$E_{I,JM+1} = c_v\,T_{I,JM+1} + |\vec{v}_{I,JM+1}|^2/2 \tag{3.193}$$

$$H_{I,JM+1} = c_p\,T_{I,JM+1} + |\vec{v}_{I,JM+1}|^2/2, \tag{3.194}$$

$$T_{I,JM+1} = \frac{p_{I,JM+1}}{R\,\rho_{I,JM+1}} \tag{3.195}$$

In equations (3.193) and (3.194) $|\vec{v}_{I,JM+1}|^2/2$ is computed using $u_{I,JM+1}$ and $v_{I,JM+1}$ from equations (3.190) and (3.191).

Equations (3.189) to (3.195) represent the boundary conditions for the farfield boundaries. In equations (3.189) to (3.192), the variables ρ_b, u_b, v_b and p_b are computed according to the *subsonic* flow situation, inflow or outflow, using equations (3.187) or (3.188) respectively.

c. Coordinate Wake Cut

This type of boundary condition represents an artificial boundary that is used for the C-grid utilized in this work. For the two-dimensional problems treated in this dissertation, this boundary is a line composed of two sets of grid points with different computational coordinates but identical physical location.

The coordinate cut boundary condition is implemented using the dummy cells concept. As shown in Figure 17, the dummy cells are not virtual, but they coincide with the grid cells on the opposite side of the cut. Hence, the values of physical quantities in the dummy cell centroids are obtained directly from the opposite cells. With this approach, the needed variables at cell faces along the cut can be obtained by simple averaging. Furthermore, the determination of fluxes is exactly as the computation of fluxes for the interior field (no special logic is required).

Let ζ be any of the variables ρ, u, v, p, T, E or H. For the ghost cell centroids corresponding to the cut region shown in Figure 17, one has

$$\begin{aligned} \zeta_{1,0} &= \zeta_{IM,1}, & \zeta_{IM,0} &= \zeta_{1,1}, \\ \zeta_{2,0} &= \zeta_{IM-1,1}, & \zeta_{IM-1,0} &= \zeta_{2,1}, \\ &\vdots \end{aligned}$$

Thus, the following general formula applies for the wake cut boundary

$$\zeta_{I,0} = \zeta_{IM-(I-1),1} \qquad (1 \le I \le ITE-1) \cup (IM-ITE+2 \le I \le IM). \tag{3.196}$$

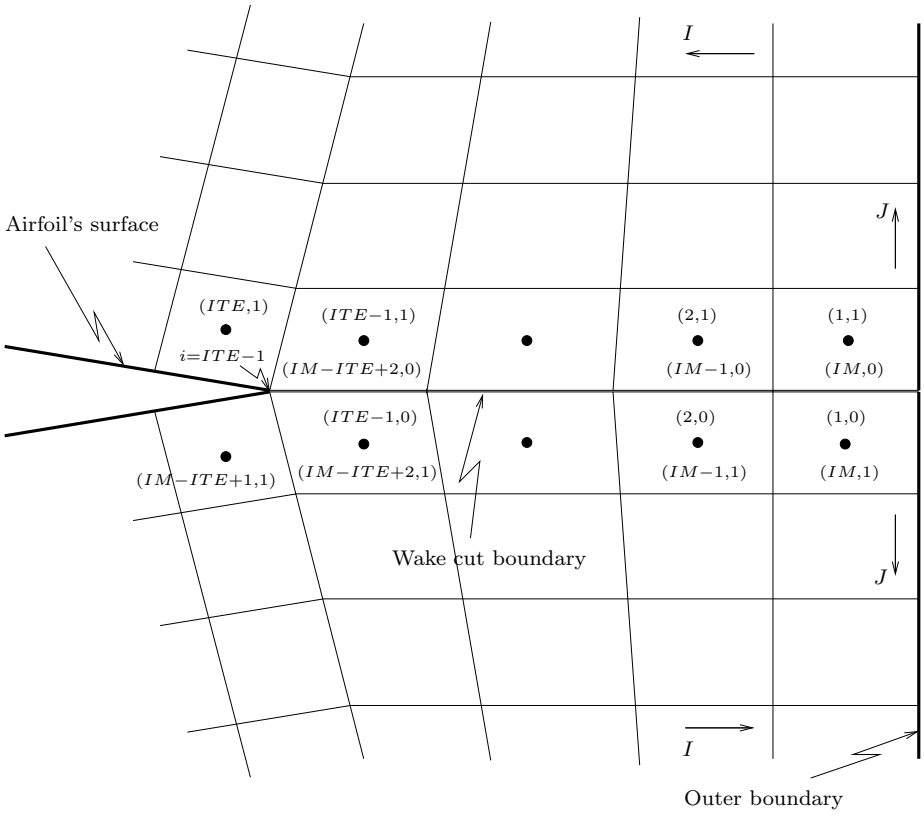

Fig. 17.: Coordinate cut boundary condition.

In equation (3.196) IM is the maximum number of nodes in the i-direction and $ITE-1$ denotes the lower i-index of the grid point at the trailing edge of the airfoil.

Equation (3.196) with ζ replaced by ρ, u, v, p, T, E or H (for the stated range in I) is employed to implement the boundary conditions at the wake cut.

d. Fluid Injection Boundary Condition

Aerodynamic design and integration have a whole new set of challenges with the introduction of unsteady flow control. One of these challenges is modeling the actuator-

induced flows for implementation as simplified boundary conditions[17]. In this research, consistently with oscillatory actuation, unsteady suction and blowing through the wall is modeled as a simple analytic function. This approach is implemented using a harmonic source generator. An equal amount of mass injected by blowing is extracted by suction so that zero net mass is added to the boundary layer.

Although the disturbances may be generated by random frequency input, disturbances of interest can be forced with known frequencies. Essentially, this disturbance generator is an alteration to the no-slip boundary conditions that are conventionally used for the wall condition in a viscous flow problem. The velocity at the wall is thus (see equation (3.150) and Figure 10)

$$v_{jet} = V_{jet\ max}\ \sin(2\pi\, f_{SJA}\, t).$$

where f_{SJA} and $V_{jet\ max}$ are the user defined frequency of injection and the amplitude of the sinusoidal function, respectively; t denotes the time. Other user defined parameters are the angle of injection relative to the airfoil's surface, θ_{jet}, and the injection location[18]. Optimum values for these parameters are discussed in Section III.O.2. The availability of the relative angle of injection, θ_{jet}, and of the injection location allow the computation of the absolute angle of injection $\theta_{jet\ abs}$. This angle is measured with respect to the general, positive x-axis direction (see Figure 18).

For the implementation of the fluid injection boundary condition, the concept of dummy cell is also employed. The velocity vector is seeked at the cell center of the dummy cell on whose boundary face the fluid injection is taking place. This is done

[17]The alternative would be coupling a structural finite-element model of the actuator to CFD code or fluid model[41].

[18]An increased grid resolution is used in the region where the pulsating jet is considered (see Section III.O.2).

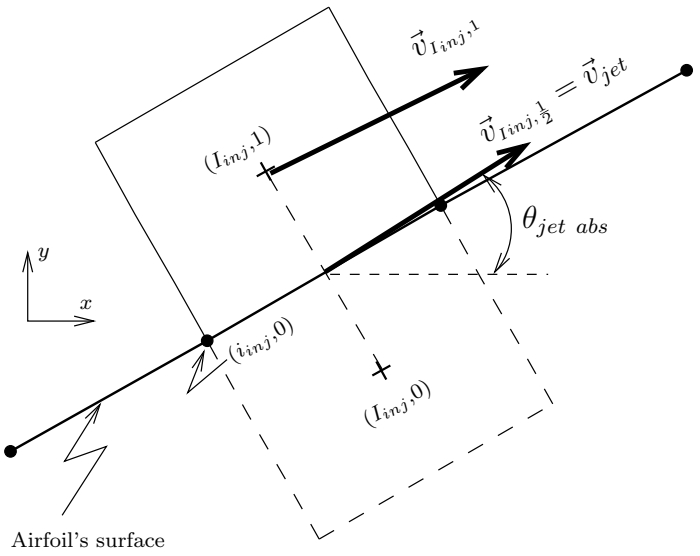

Fig. 18.: Boundary condition at fluid injection site.

by linear extrapolation as follows (see Figure 18)

$$\begin{aligned} u_{I_{inj},0} &= 2\left|\vec{v}_{inj,\frac{1}{2}}\right|\cos\theta_{jet\ abs} - u_{I_{inj},1} \\ v_{I_{inj},0} &= 2\left|\vec{v}_{inj,\frac{1}{2}}\right|\sin\theta_{jet\ abs} - v_{I_{inj},1} \end{aligned} \tag{3.197}$$

where I_{inj} denotes the index for the cell where the injection is taking place. The temperature, pressure and density at the injection dummy cell are computed using the methodology employed in Section III.L.2.b. That is

$$\begin{aligned} T_{I_{inj},0} &= T_{I_{inj},1}, \\ p_{I_{inj},0} &= p_{I_{inj},1}, \\ \rho_{I_{inj},0} &= \frac{p_{I_{inj},0}}{R\,T_{I_{inj},0}}. \end{aligned}$$

The variables directly related to the fluid's velocity at the dummy cell are finally

corrected as follows

$$\begin{aligned} E_{I_{inj},0} &= c_v T_{I_{inj},0} + \left|\vec{v}_{I_{inj},0}\right|^2/2 \\ H_{I_{inj},0} &= c_p T_{I_{inj},0} + \left|\vec{v}_{I_{inj},0}\right|^2/2. \end{aligned}$$

where $\left|\vec{v}_{I_{inj},0}\right|^2$ is computed using equations (3.197). This completes the implementation of the fluid injection boundary condition for the viscous case only.

4. Boundary Conditions for Turbulence Modeling

This type of boundary condition must be implemented for the solid wall, the wake cut and for the farfield boundaries. The implementation for the solid wall case takes advantage of the fact that, at the wall (i.e., at cell faces $(I, \frac{1}{2})$ over the airfoil), $\mu_{T\,I,\frac{1}{2}}$ must be zero (see equation (3.136)). Because the value of $\mu_{T\,I,\frac{1}{2}}$ at the wall is an average between values at cell centers $(I, 1)$ and $(I, 0)$ it follows that

$$\mu_{T\,I,0} = -\mu_{T\,I,1}$$

for all I over the airfoil's surface.

The technique employed in Section III.L.3.c is also applied for the wake cut. That is, in equation (3.196) ζ is also replaced by μ_T for the wake cut region.

Finally, it is assumed that in the farfield boundary $\mu_T = 0$ and therefore μ_T at the farfield ghost cells is set to zero.

5. Influence of the Farfield Boundary Location on the Lift Coefficient

In this section, the variation of the lift coefficient per unit span (C_L) due to the distance airfoil–farfield boundary is investigated. For this section only, the results

presented are obtained by employing just the Euler part of the flow solver[19]. That is, only the pressure contribution to the lift coefficient is taken into account. The viscous contribution to the lift (due to the shear stress distribution), although not taken into account for the results in this section is nonetheless included in the equation utilized to compute the lift force. This is done because the final results presented in the following chapters take into account all the effects that contribute to the lift (i.e., pressure and shear stress distributions).

In external flow problems the farfield boundaries are assumed to be located "far enough" from the flow region of interest so that the influence of a finite computational domain does not affect the results. The far field boundary conditions are usually reflective and they introduce non-physical flow disturbances that pollute the numerical solution. Since these disturbances generally require long distances to damp out, the boundaries need to be situated, in practice, at an appreciable distance from the source of disturbances (50 chords between the airfoil and the far-field boundary is not uncommon [37] p. 385).

The influence on the lift coefficient of the farfield boundary position with respect to the airfoil is investigated by computing C_L for various distances from the airfoil to the farfield boundary. The lift coefficient per unit span is computed using the following equation

$$C_L = \frac{L'}{q_\infty C} \quad , \tag{3.198}$$

where L' is the lift force per unit span, q_∞ is the freestream's dynamic pressure (equal to $\rho_\infty \left|\vec{v}_\infty^{\,2}\right| /2$) and C is the airfoil's chord. Note that the C_L is a *global* coefficient

[19]The results on C_L obtained using the Euler solver alone are very close to those obtained using the full solver (i.e., taking the viscous effects into account). This is verified in the following chapter.

while the pressure coefficient, defined as

$$C_{p\,(I,\frac{1}{2})} = \frac{p_{I,\frac{1}{2}} - p_\infty}{q_\infty} \qquad \text{for all } I \text{ over the airfoil,} \tag{3.199}$$

is a *local* coefficient. Plots of the pressure coefficient are presented in the next chapter, while the discussion in this section concentrates on the lift coefficient only (equation (3.198)).

The lift force L' is a component (together with the drag force D') of the resultant force $\vec{R}'$ that the airfoil, moving through the fluid, experiments as a result of the net effect of the pressure and shear stress distributions integrated over the complete airfoil's surface (see Figure 20 or 21). The resultant force $\vec{R}'$ is computed by integrating over the complete airfoil's surface the force exerted by the fluid on the differential surface element. That is

$$\vec{R}' = \int_{\text{airfoil}} d\vec{F}_s. \tag{3.200}$$

In equation (3.200) the term $d\vec{F}_s$ is the stress vector and it represents the force acting on a solid wall's elemental surface that is in contact with the fluid (see Figure 19). The stress vector is computed as follows (see [42], p. 57)

$$d\vec{F}_s = \overline{\overline{\sigma}} \cdot d\vec{S},$$

or employing equation (2.11)

$$d\vec{F}_s = \left(-p\overline{\overline{I}} + \overline{\overline{\tau}}\right) \cdot d\vec{S}. \tag{3.201}$$

In the last two equations, the term $d\vec{S}$ denotes the elemental area vector that is normal to the area over which the computation is being performed and it points *toward* the interior domain (see Figure 19).

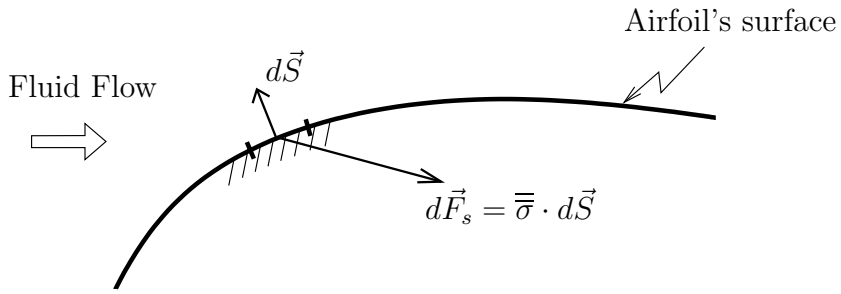

Fig. 19.: Force exerted by the fluid on a solid surface elemental area.

The stress vector acting on an surface's elemental area can be decomposed into normal and shear (tangential) stress forces[20], denoted $d\vec{F}_n$ and $d\vec{F}_\tau$, respectively. The components of such forces are determined by scalarly multiplying the stress vector times the unit normal and unit tangential vectors, denoted $\vec{n}$ and $\vec{t}$, respectively. That is

$$\begin{aligned} d\vec{F}_n &= \left[\left(\overline{\overline{\sigma}} \cdot d\vec{S}\right) \cdot \vec{n}\,\right]\vec{n} \\ d\vec{F}_\tau &= \left[\left(\overline{\overline{\sigma}} \cdot d\vec{S}\right) \cdot \vec{t}\,\right]\vec{t}. \end{aligned}$$

In particular, the unit normal vector is computed as

$$\vec{n} = \frac{d\vec{S}}{|d\vec{S}|} = \frac{d\vec{S}}{dS}, \tag{3.202}$$

where $dS = |d\vec{S}|$ represents the actual area of the surface element and it is, therefore, a positive quantity all the time. From equation (3.202) $d\vec{S} = \vec{n}dS$. The shear stress

[20]Normal and tangential to the surface element under study.

at the wall, denoted τ_w, can be computed as follows

$$\begin{aligned} \tau_w &= \frac{\left(\overline{\overline{\sigma}} \cdot d\vec{S}\right) \cdot \vec{t}}{dS} = \frac{\left(\overline{\overline{\sigma}} \cdot \vec{n}\, dS\right) \cdot \vec{t}}{dS} \\ &= \left(\overline{\overline{\sigma}} \cdot \vec{n}\right) \cdot \vec{t}. \end{aligned} \tag{3.203}$$

Equation (3.200) is discretized as follows

$$\vec{R}\,' = \sum_{\text{airfoil}} d\vec{F}_{s_{(I,\frac{1}{2})}} = \sum_{\text{airfoil}} \left(-p\overline{\overline{I}} + \overline{\overline{\tau}}\right)_{(I,\frac{1}{2})} \cdot \vec{S}_{(I,\frac{1}{2})}, \tag{3.204}$$

where $\vec{S}_{(I,\frac{1}{2})}$ denotes the discrete area vectors corresponding to the area elements (or length elements in 2D problems) defining the airfoil. The components of the vector $\vec{R}\,'$ in equation (3.204) will run along the coordinate axis in which the involved quantities utilized for its computations are described. In this dissertation, the simulation of the flow field around an airfoil at a given angle of attack, α_∞, as that shown in Figure 20, is performed employing a rotated Cartesian coordinate system denoted $x\,'$-$y\,'$ (see Figure 21)[21]. The theory developed so far employs such $x\,'$-$y\,'$ reference system, but without the "prime" symbol for notation simplicity.

It is clear that the $\hat{\imath}$- and $\hat{\jmath}$-components of equation (3.204), expressed in the $x\,'$-$y\,'$ coordinate system (see Figure 21), result in forces along the $x\,'$- and $y\,'$-coordinate axes, respectively. That is, equation (3.204) gives rise to the axial force component ($A\,'$) along the airfoil's chord, and to the normal force component ($N\,'$) perpendicular to the airfoil's chord (see Figure 21). Expanding equation (3.204) one therefore has (see equation (3.4) for the definition of $\overline{\overline{\tau}}$)

$$A\,' = \sum_{\text{airfoil}} \left(-p + \frac{2}{3}\,\mu \left[2\frac{\partial u}{\partial x} - \frac{\partial v}{\partial y}\right]\right)\Bigg|_{I,\frac{1}{2}} [S_x]_{(I,\frac{1}{2})} + \left(\mu \left[\frac{\partial u}{\partial y} + \frac{\partial v}{\partial x}\right]\right)\Bigg|_{I,\frac{1}{2}} [S_y]_{(I,\frac{1}{2})} \tag{3.205}$$

[21]The resulting pressure and shear stress distributions are identical for both configurations. This is so because the solution of the Navier-Stokes equations is independent of the orientation of the reference system in which the equations are expressed.

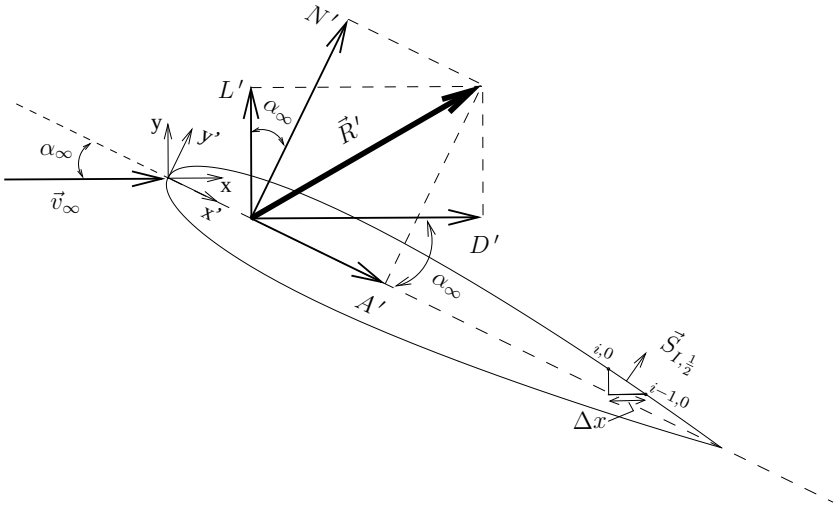

Fig. 20.: Resultant aerodynamic force and the components into which it splits.

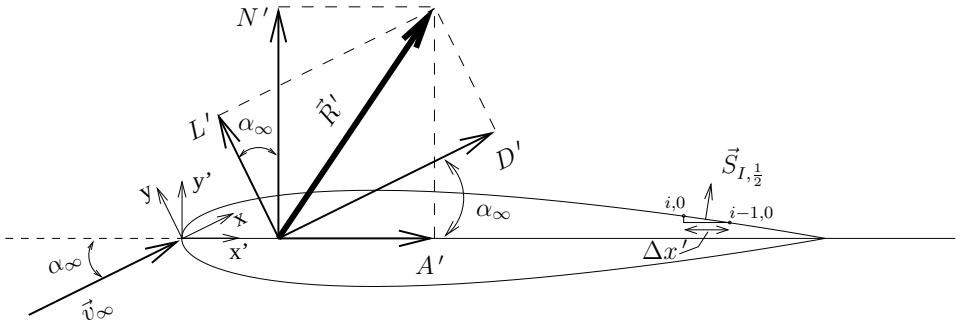

Fig. 21.: Airfoil at the same flow conditions as those in Figure 20 but observed from a frame rotated α degrees (observe that $\alpha = \alpha_\infty$).

and

$$N' = \sum_{\text{airfoil}} \left(\mu \left[\frac{\partial u}{\partial y} + \frac{\partial v}{\partial x} \right] \right) \Bigg|_{I,\frac{1}{2}} [S_x]_{(I,\frac{1}{2})} + \left(-p + \frac{2}{3}\,\mu \left[2\frac{\partial v}{\partial y} - \frac{\partial u}{\partial x} \right] \right) \Bigg|_{I,\frac{1}{2}} [S_y]_{(I,\frac{1}{2})} \quad (3.206)$$

The required lift force, L', is obtained by determining the component of the resultant force $\vec{R}$ along the original y-axis (see Figure 21). This can be accomplished by performing a vector component transformation from the x'-y' to the x-y coordinate system as follows

$$L' = N' \cos \alpha_\infty - A' \sin \alpha_\infty, \quad (3.207)$$

where α_∞ is the angle of attack. Equations (3.198), (3.205), (3.206) and (3.207) are employed in the computation of the lift coefficient used in the investigations performed in this dissertation.

The influence of the distance from the airfoil to the farfield boundary is shown in Figure 22. Table III is included for validation purposes. It shows numerical and experimental results for a NACA0012 airfoil at $M_\infty = 0.3$, $\alpha = 4$ deg and $Re = 1 \times 10^6$. The numerical results were obtained using (1) a vortex panel method (VPM)[22], (2) the Thin Shear Layer Navier-Stokes (TSL N-S) solver of R.K. Agarwal et al. [43] and (3) The Euler solver also developed by Agarwal et al. [43]. The experimental results are taken from C. D. Harris report [44].

As shown in Figure 22 and in Table III, the results of the code developed in this dissertation are accurate if the farfield boundary conditions are located at more that twelve chord distances from the airfoil. Therefore, the final grid used in this work places the farfield boundary at twelve chord distances from the airfoil.

[22]The employed VPM is a code developed by the Fluids Department of the Virginia Polytechnic Institute and State University. The VPM is available on the world wide web in the form of an engineering applet and it can be run on-line. Documentation about the applet can be found at http://www.engapplets.vt.edu/fluids/vpm/.

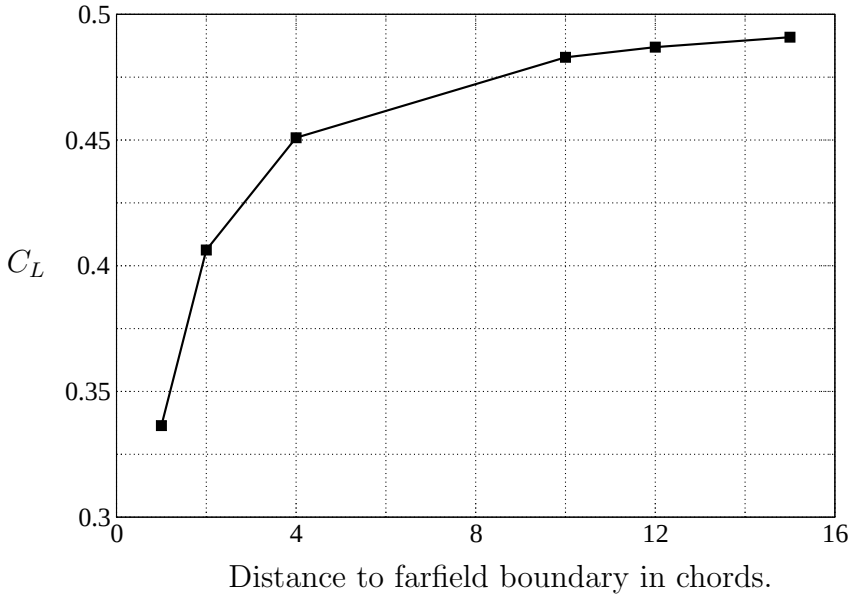

Fig. 22.: Effect of the distance to the farfield boundary on the lift coefficient. NACA0012 airfoil, $M_\infty = 0.3$, $\alpha_\infty = 4$ deg, $Re = 1 \times 10^6$.

M. Initial Conditions

An initial guess of the solution is required to start the marching process, equations (3.114) or (3.130). User defined freestream values of density, pressure, Mach number and inlet flow angle (ρ_∞, p_∞, M_∞ and α_∞, respectively) are used to determine an initial guess for the primitive variables (p, ρ and $\vec{v}$) throughout the interior domain ($1 \leq I \leq IM$ and $1 \leq J \leq JM$)[23]. The initial guess generator (a program independent of the flow solver) delivers the variables p, ρ and $\vec{v}$ for all the interior domain to the flow solver, which in turn process them, at a startup routine, to get the variables it requires to start the marching process (the conservative and other variables like T and H).

The user defined freestream variables ρ_∞, p_∞, M_∞ are placed in an input file.

[23]Recall that the boundary ghost cell's indexes are $I = 0$, $J = 0$, $I = IM + 1$ and $J = JM + 1$

Table III.: Lift coefficient results from different authors. NACA0012 airfoil, $M_\infty = 0.3$, $\alpha = 4\,\text{deg}$, $Re = 1 \times 10^6$.

Method	*Lift coefficient*
Vortex panel method	0.4826
TSL N-S solver of R. K. Agarwal et al. [43]	0.4740
Euler solver of R. K. Agarwal et al. [43]	0.5360
Experimental measurements of C. D. Harris [44]	0.4646

The initial guess generator then reads these values and sets the following

$$\begin{aligned} p_{I,J} &= p_\infty \\ \rho_{I,J} &= \rho_\infty. \end{aligned} \qquad \text{for} \quad 1 \le I \le IM \quad \text{and} \quad 1 \le J \le JM\,.$$

The total freestream velocity ($|\vec{v}_\infty|$) is then computed as follows: from the Mach number definition one gets $|\vec{v}_\infty| = M_\infty\, c_\infty$. The freestream Mach number is already available but the freestream speed of sound c_∞ must be computed as $c_\infty = \sqrt{\gamma\, p_\infty/\rho_\infty}$. Thus

$$|\vec{v}_\infty| = M_\infty \sqrt{\gamma\, p_\infty/\rho_\infty}. \tag{3.208}$$

All the freestream variables and the gas constant for air in the right hand side of (3.208) are known. Finally, to obtain the initial guess for the interior velocity field, one sets

$$\begin{aligned} u_{I,J} &= |\vec{v}_\infty| \\ v_{I,J} &= 0. \end{aligned} \qquad \text{for} \quad 1 \le I \le IM \quad \text{and} \quad 1 \le J \le JM\,.$$

This completes the initial guess generation.

N. Convergence Criteria

As seen in Sections III.H.1 and III.H.2, explicit schemes are utilized to solve the governing equations for both steady and unsteady problems. For both cases, convergence is claimed to be reached when the average residuals are less than a user defined tolerance. The residuals are defined by equations (3.107) and (3.121) for steady and unsteady problems, respectively. The average residuals for each component have the same form and they are

$$R^{\text{ avg}}(W_{I,J}) = \frac{\sum_{I,J} |R(W_{I,J})|}{N_{\text{cells}}} \qquad \text{and} \qquad R^{*\text{ avg}}(W^*_{I,J}) = \frac{\sum_{I,J} |R^*(W^*_{I,J})|}{N_{\text{cells}}},$$

for all interior (I, J) indexes.

The other convergence indicator utilized in this dissertation is the conservation of mass. This is defined as

$$\dot{m}_{\text{error}} = \oint_{\partial\Omega} \rho\vec{v} \cdot d\vec{S}, \tag{3.209}$$

where $\partial\Omega$ denotes the boundary of the domain, namely the farfield boundary and the line (surface for 3-D case) defining the airfoil. Ideally this should be zero; in reality, and for a converged solution, it should be very small. Equation (3.209) measures the difference of mass flows entering and leaving the domain. That is

$$\oint_{\partial\Omega} \rho\vec{v} \cdot d\vec{S} = \dot{m}_{\text{out}} + \dot{m}_{\text{in}},$$

where $\dot{m}_{\text{out}}$ and $\dot{m}_{\text{in}}$ denote, respectively, the mass entering and leaving the domain through its boundaries. It will be seen below that $\dot{m}_{\text{out}} > 0$ and $\dot{m}_{\text{in}} < 0$. In practice, the mass conservation indicator is implemented as follows

$$\dot{m}_{\text{error}} = \frac{|\dot{m}_{\text{out}} + \dot{m}_{\text{in}}|}{\dot{m}_{\text{out}}} \times 100, \tag{3.210}$$

Mass entering *or* leaving the domain through a given discrete boundary surface

element $\vec{S}$ is computed by evaluating $(\rho\vec{v}\cdot\vec{S})$ at the midpoint of such surface element. The boundary area vector $\vec{S}$ can also be written as $\vec{S}=\vec{n}S$, where $\vec{n}$ is a unit normal vector pointing out of the domain and S is the actual (positive) area of the surface element. Thus, if the fluid is entering the domain one has that $(\rho\vec{v}\cdot\vec{S})<0$ since the protection of $\vec{v}$ along $\vec{n}$ is negative. On the contrary, if fluid is leaving the domain then $\rho\vec{v}\cdot\vec{S}>0$.

In order to compute $\dot{m}_{in}$ and $\dot{m}_{out}$, the expression $(\rho\vec{v}\cdot\vec{S})$ must be evaluated at the mid-points of all the surface elements forming the boundaries of the domain. Addition of all the negative results of $(\rho\vec{v}\cdot\vec{S})$ gives $\dot{m}_{in}$, while addition of the positive values gives $\dot{m}_{out}$. Typical convergence histories are presented in Figures 23 and 24 where the $\log_{10}$ has been taken for the respective errors. Note that the error in mass conservation, equation (3.210), is given as a percentage.

O. Grid Generation

For this work, two kinds of grids were algebraically generated and utilized, namely the grids for problems with and without fluid injection. In both cases the grids are C-type grids around NACA0012 and NACA0015 airfoils. For the no injection cases, the node distribution over the airfoil is clustered toward the leading and trailing edges of the airfoil. The grid for the injection problems have, besides the clustering just mentioned, a clustered region at the injection site. The generation of these two kinds of grids is discussed in the following subsections.

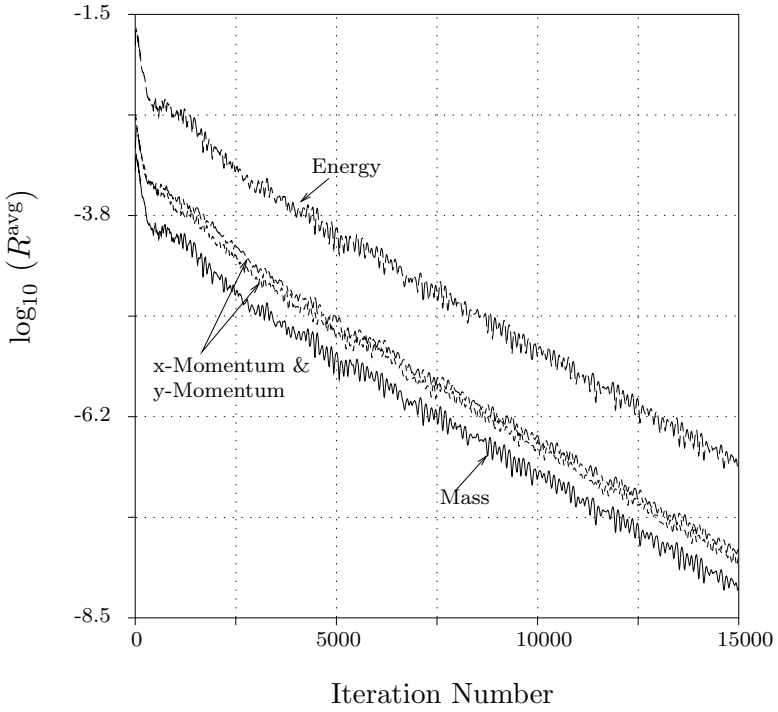

Fig. 23.: Typical histories of the average residuals.

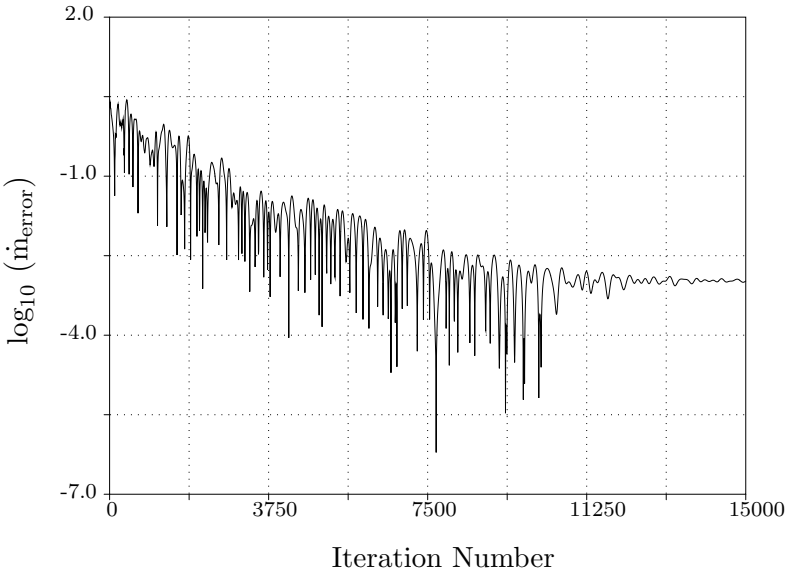

Fig. 24.: Typical history of the mass conservation error.

1. Computational Grid for Problems without Fluid Injection

The grid for this kind of problems is as that shown in Figure 25. The airfoils utilized in this dissertation are defined analytically using equation (3.169). This airfoil definition data is then utilized by the grid generator program[24] to, as a first step, determine the node distribution from $i=0$ to $i=ILE$, where ILE denotes the i-index of the grid point at leading edge of airfoil.

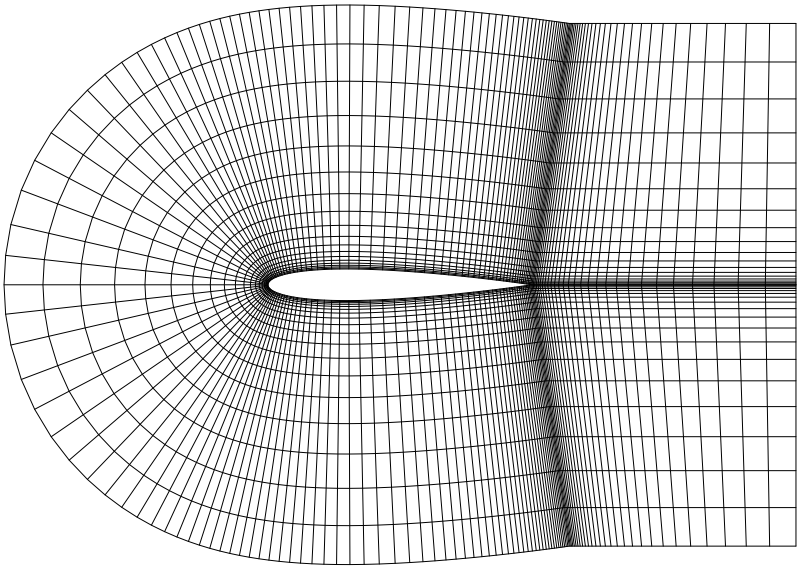

Fig. 25.: C-type grid with one chord distance from airfoil to farfield boundary.

Figure 26 shows a typical output of this first step of the grid generator program. Note that the origin of the Cartesian coordinate system is located at the leading edge of the airfoil.

[24]The grid generator program is independent of the flow solver and of the initial guess generator.

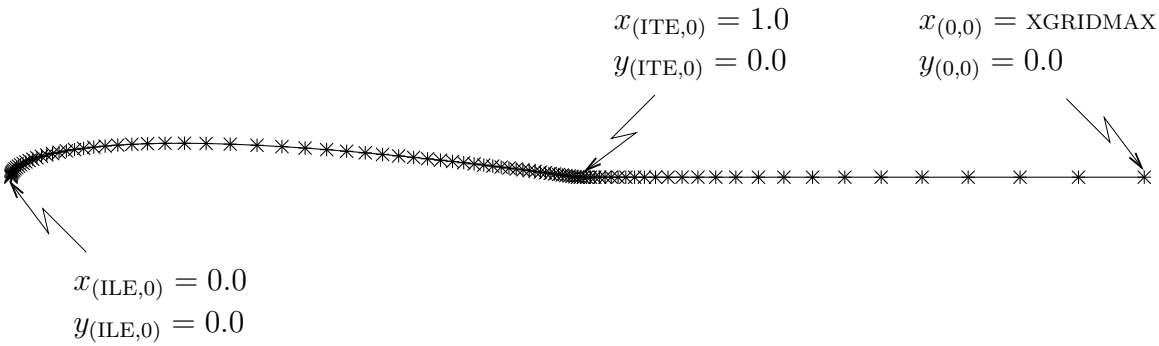

Fig. 26.: i-node distribution on the upper half of coordinate line $j = 0$ (from $i = 0$ to $i = ILE$). ITE denotes the lower i-index of the grid point at trailing edge of the airfoil.

The parameters involved in this first grid generation task are placed in an input file and they are 1) the number of nodes defining the upper half of the airfoil; 2) the number of nodes from $i = 0$ to $i = ITE$; 3) the physical x-coordinate corresponding to $i = 0$; 4) the ratio of successive elements from the leading edge to the middle of the airfoil; 5) the ratio of successive elements from the trailing edge to the middle of the airfoil and 6) the ratio of successive elements from the trailing edge to $i = 0$.

For this first step of grid generation, the three utilized ratios of successive elements, for $j = 0$, are constant and less than 1.3 as recommended by experience in order to have good accuracy and convergence rate features. For example, for the segment from $i = ITE$ to $i = 0$ (see Figure 26) one has

$$\begin{aligned} x_{(ITE\quad,0)} &= 1.0 \\ x_{(ITE-1,0)} &= 1.0 + \ell \\ x_{(ITE-2,0)} &= 1.0 + \ell + \ell\, r \\ x_{(ITE-3,0)} &= 1.0 + \ell + \ell\, r + \ell\, r^2 \\ &\vdots \end{aligned} \tag{3.211}$$

where ℓ is the size of the first grid element to the right of the trailing edge. That is (see Figure 26) $\ell = x_{(ITE-1,0)} - x_{(ITE,0)}$. The ratios between successive elements for equations (3.211) are

$$\begin{aligned}
\frac{x_{(ITE-2,0)} - x_{(ITE-1,0)}}{x_{(ITE-1,0)} - x_{(ITE\quad,0)}} &= \frac{1.0 + \ell + \ell\, r - (1.0 + \ell)}{1.0 + \ell - 1.0} = r \\
\frac{x_{(ITE-3,0)} - x_{(ITE-2,0)}}{x_{(ITE-2,0)} - x_{(ITE-1,0)}} &= \frac{1.0 + \ell + \ell\, r + \ell\, r^2 - (1.0 + \ell + \ell\, r)}{1.0 + \ell + \ell\, r - (1.0 + \ell)} = r \\
&\vdots
\end{aligned}$$

The same principle is applied for the node distribution over the airfoil but, instead of using $(x_{(i,0)} - x_{(i-1,0)})$ for a given element size, one uses $\Delta\varepsilon_{(i,0)}$ with

$$\Delta\varepsilon_{(i,0)} = \sqrt{[x_{(i+1,0)} - x_{(i,0)}]^2 + [y_{(i+1,0)} - y_{(i,0)}]^2}.$$

The next step in the C-grid generation process used is to build the grid above the upper half of the airfoil[25]. This is a grid orthogonal to the airfoil and, as a first step, it is uniformly distributed along the j-direction (see Figure 27). This kind of grid is obtained using the following formulas

$$\begin{aligned}
x_{(i,j)} &= x_{(i,0)} + \eta \sin\theta \\
y_{(i,j)} &= y_{(i,0)} + \eta \cos\theta
\end{aligned} \qquad ITE \le i \le ILE, \quad 0 \le j \le JM,$$

where $\eta = j\,\Delta\eta$ and

$$\Delta\eta = \frac{\text{c-grid thickness}}{JM}, \qquad \cos\theta = \frac{S_{avg_y}}{|\vec{S}_{avg}|}, \qquad \sin\theta = \frac{S_{avg_x}}{|\vec{S}_{avg}|}.$$

The parameters "c-grid thickness" and "JM" are user defined for this phase of the C-grid generation process. The "thickness" of the C-grid can be thought of as the

[25]That is, for $ITE \le i \le ILE$ and $0 \le j \le JM$ (see Figure 26)

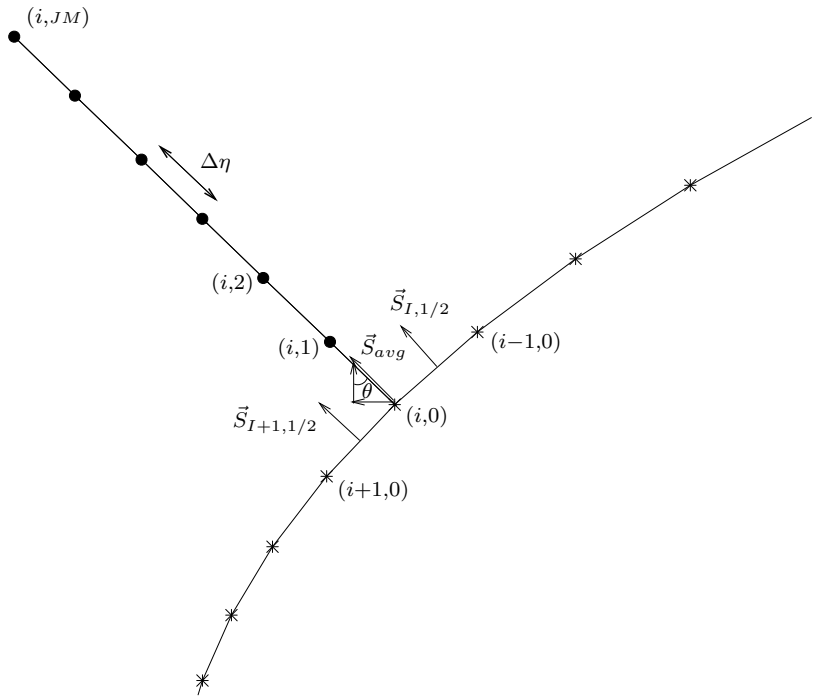

Fig. 27.: Uniform node distribution over upper part of airfoil.

distance from the leading edge of the airfoil to the farfield boundary in front of it[26]. Furthermore, S_{avg_x} and S_{avg_y} (from which $|\vec{S}_{avg}|$ can be obtained) are computed by averaging the corresponding area vector components of faces $(I+1, 1/2)$ and $(I, 1/2)$ (see Figure 27). S_{avg_x} and S_{avg_y} can be computed using equations (3.86) with $J = 1$.

The next step in the grid generation process is the construction of the grid in the region above the cut of the C-grid. This is constructed algebraically using the previously determined node distributions along lines $j = \text{const} = 0$ (with $0 \leq i \leq ITE$,

[26]The parameter "c-grid thickness" actually is the shortest distance from a given point on the airfoil to the farfield boundary.

see Figure 26) and $i = \text{const} = ITE$ (with $0 \leq j \leq JM$)

$$\begin{aligned} y_{(i,j)} &= y_{(ITE,j)} \\ x_{(i,j)} &= x_{(i+1,j)} + \left(x_{(0,0)} - x_{(ITE,j)}\right) \left(\frac{x_{(i,0)} - x_{(i+1,0)}}{x_{(0,0)} - x_{(ITE,0)}}\right), \end{aligned}$$

for $0 \leq i \leq (ITE - 1)$ and $1 \leq j \leq JM$.

Before mirroring the upper half of the grid thus far generated to the lower half, a clustering toward the coordinate line $j = 0$ is performed[27]. This clustering is algebraic and takes advantage of the lines $i = \text{const}$ (for $0 \leq i \leq ILE$) so far generated

$$\begin{aligned} x_{(i,j)} &= x_{(i,j-1)} + \left(r_{(j)} - r_{(j-1)}\right) \left(x_{(i,JM)} - x_{(i,0)}\right) \\ y_{(i,j)} &= y_{(i,j-1)} + \left(r_{(j)} - r_{(j-1)}\right) \left(y_{(i,JM)} - y_{(i,0)}\right), \end{aligned} \tag{3.212}$$

for $0 \leq i \leq ILE$ and $1 \leq j \leq JM - 1$. In equations (3.212) $r_{(j)}$ is a clustered distribution over a y-oriented line with unit length, composed with a number of segments equal to JM (the number of segments of the C-grid in the j-direction). Specifically

$$r_{(JM-j)} = 1 + \frac{\tanh\left(-\dfrac{\eta}{2} \log \dfrac{1+b}{1-b}\right)}{\tanh\left(\quad \dfrac{1}{2} \log \dfrac{1+b}{1-b}\right)}, \qquad 0 \leq j \leq JM \tag{3.213}$$

where $\eta = j\,\Delta\eta$ with $\Delta\eta = 1.0/JM$ and b is the clustering parameter, $0 \leq b < 1$, that sets the degree of clustering, being this more intense as it gets closer to 1.0 from below. Figure 28 shows a sample of the output of formula (3.213) when $b = 0.85$ and $JM = 7$.

The last step in the C-grid generation process is to mirror the upper half of the C-grid thus far generated to the lower half. This is achieved employing the following

[27]Only if a user defined flag to perform this task is *on*. If not, the already defined uniform distribution in the j-direction is employed.

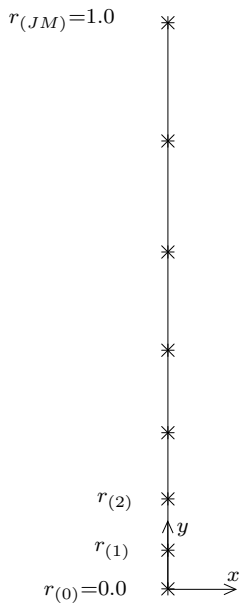

Fig. 28.: Clustering on the unit length segment.

formulas

$$\begin{aligned} x_{(IM-i,j)} &= x_{(i,j)} \\ y_{(IM-i,j)} &= -y_{(i,j)} \end{aligned} \qquad 0 \le i \le ILE-1, \quad 0 \le j \le JM.$$

This completes the grid generation process for the simulations without fluid injection performed in this dissertation. Application of the procedure just described produces grids as that of Figure 25.

2. Computational Grid for Problems with Fluid Injection

The cases with fluid injection simulated in this dissertation were chosen to match the specifications of the experiments of flow separation control performed by Gilarranz [15] in the wind tunnel facilities of the Aerospace Engineering Department at Texas A&M University. A specialized grid was designed to match the geometry of

those experiments.

The airfoil used is a NACA0015 with a chord length of 0.375 m. The injection takes place on the upper half of the airfoil only, through a gap 0.002 m wide. The center of the gap is located at an x-coordinate equal to 0.046 m from the leading edge of the airfoil. These parameters are shown in Table IV in non-dimensional form. The non-dimensionalization is performed using the chord length as a reference length.

Table IV.: Geometric details for fluid-injection problems.

Parameter	*Non-dimensional value*
Chord length	1.0
Gap width	5.333×10^{-3}
x-coordinate for mid-point of gap	0.122666

With the data from Table IV an appropriate node distribution from $i = 0$ to $i = ILE$ is built. The procedure from the previous section is then applied to construct the final grid (see Figure 29) utilized for the fluid injection simulations performed in this dissertation.

In this work, the fluid injection takes place through one boundary cell face only (see Figure 30). The x-location of the mid-point of this injection face and its length are as stated in Table IV. Furthermore, as mentioned above, the grid for fluid injection problems is clustered around the injection site as shown in Figure 31. Finally, the grid generation parameters are set such that the resulting grid is a 231×55 viscous grid;[28] with a distance to the farfield boundary equal to twelve chord distances (see Figure 29).

[28]That is, a grid highly clustered toward the airfoil's surface.

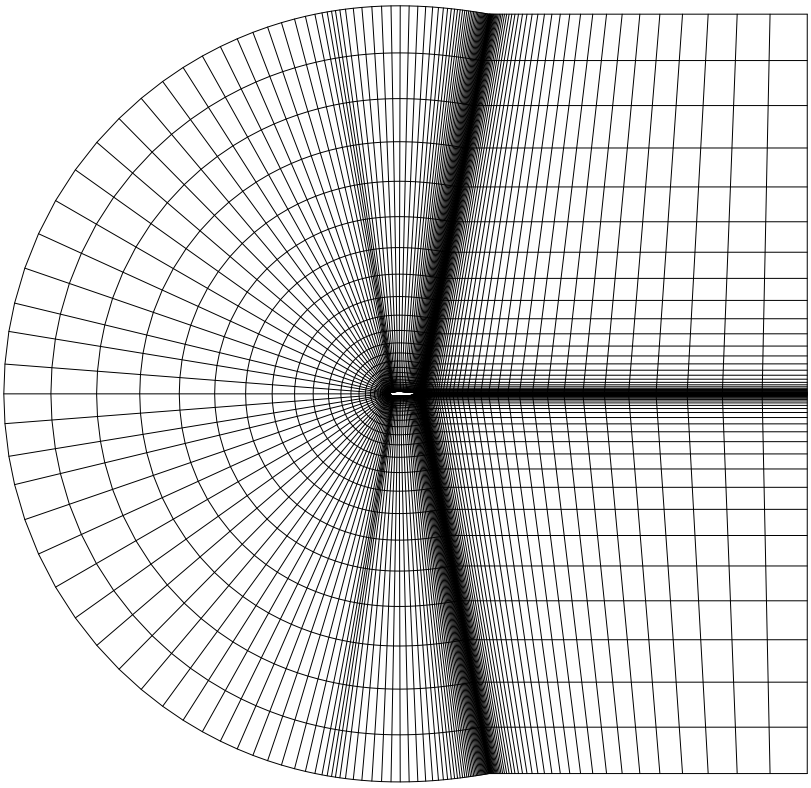

Fig. 29.: Full grid for fluid injection problems.

P. Computer Resources and Post-Processing Software

The code was written in the Fortran 90 programming language for UNIX/Linux platforms. Double precision was utilized for all the computations and two of the supercomputers from the Supercomputing Center of the Texas A&M University were employed. Furthermore, two DEC-alpha computers from the Aerospace Engineering Department were utilized for the numerical computations.

The software utilized for the post-processing of the results was: grafic, Fieldview, Tecplot and xmgrace. This software was used to generate x-y graphs, scalar and vector fields, plots of grids and movies of the unsteady simulations.

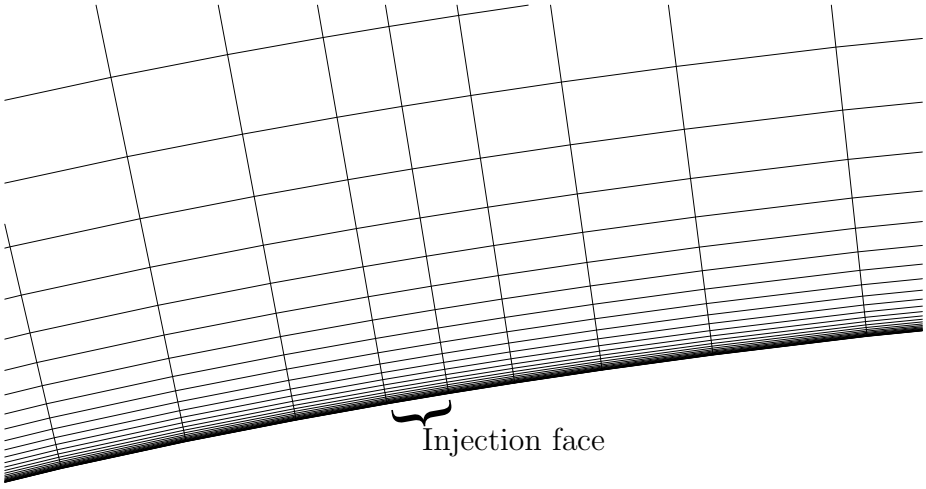

Fig. 30.: Fluid injection site.

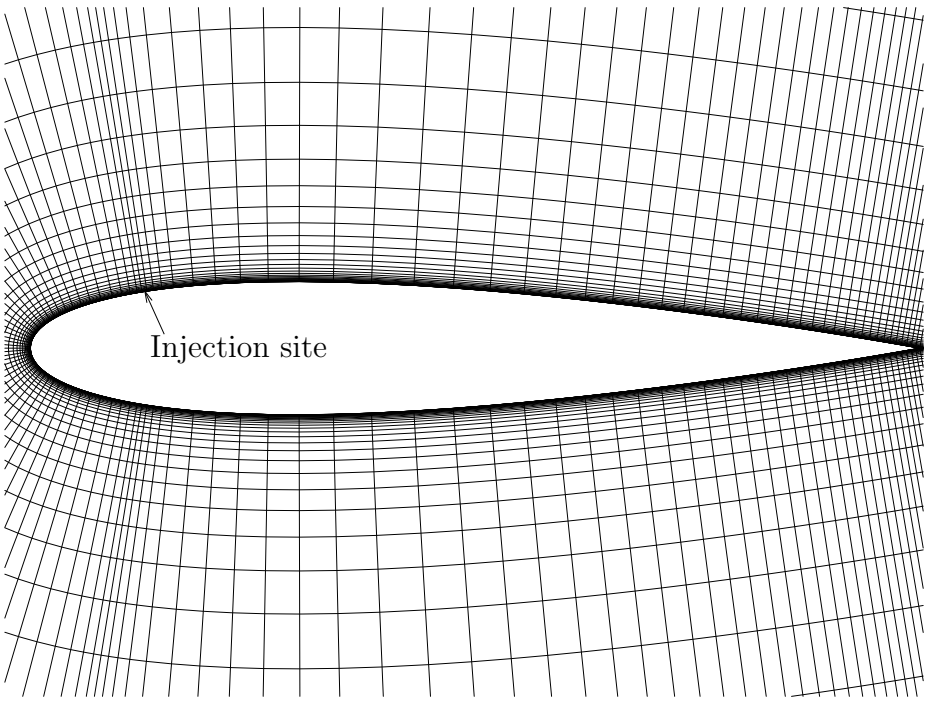

Fig. 31.: Full airfoil grid view for fluid injection problems.

CHAPTER IV

CODE VALIDATION STUDIES

In this chapter, some validation studies are performed. The validation of the code is achieved by comparison of the results obtained in this research versus experimental data and versus numerical results from other authors. The compared quantities are the lift coefficient, the pressure coefficient and the normal force coefficient. The pressure and lift coefficients are computed using equations (3.199) and (3.198), respectively, while the normal force coefficient is introduced below. As mentioned before, the lift and normal force coefficients are global quantities and the pressure coefficient is a local quantity.

The aim of this chapter is to show the reliability of the code generated in this dissertation for steady simulations of flows around NACA0012 airfoils. For the fluid injection simulations, comparisons with corresponding Gilarranz [15] experimental (unsteady) data are performed but this takes place until the following chapter.

The information in this chapter is presented as follows: 1.) Numerical results obtained using the code developed in this research are compared versus experimental data provided by Harris [44]. The compared quantities are pressure and normal force coefficients for a flow around a NACA0012 airfoil at various angles of attack, $M_\infty = 0.3$ and a $Re = 3 \times 10^6$. 2.) Numerical results obtained using the code developed in this research are compared against different numerically obtained results as presented in Agarwal et al. [43]. The compared quantities in this case are pressure and lift coefficients for a flow around a NACA0012 airfoil at different angles of attack, $M_\infty = 0.3$ and $Re = 1 \times 10^6$. For this study, an experimentally obtained C_L versus angle of attack plot is also included.

The grid employed for these studies was a viscous, C-grid with a distance to the

farfield boundary of 15 chords. It had 241×60 grid points and 129 nodes defining the whole NACA0012 airfoil. The grid was normal to the airfoil's wall and the height of the first grid cell (closest to the wall) is constant and equal to 1.41074×10^{-5} chords.

In some of the graphs of results mentioned above, results obtained using the vortex panel method (VPM) are included. The VPM is a method employed for the computation of the aerodynamic characteristics of airfoil sections assuming ideal fluid flow and it is available on-line as an engineering applet.

A. Introductory Remarks

Some concepts employed in this chapter that have not been discussed so far are reviewed in this section. Several comments are also given.

1. The Normal Force Coefficient

As mentioned above, the results of two-dimensional wind tunnel tests on a NACA0012 airfoil, performed by Harris [44] in the Langley Research Center's 8-foot Transonic Pressure Tunnel, are used for comparison with the numerical results obtained in this research. It is very important to point out that the results provided in Harris' report are the C_p plots with their corresponding *normal* (not lift) force coefficient for each tested angle of attack. The normal force coefficient, denoted as C_n, differs to the lift coefficient discussed in Section III.L.5 because the former employs the normal force component, N', for its calculation while the latter employs the lift force (see equation (3.198)). The normal force coefficient is computed as follows

$$C_n = \frac{N'}{q_\infty C} \, . \tag{4.1}$$

In equation (4.1), N' is a vector force component, perpendicular to the airfoil's chord

(see Figures 20 or 21). Specifically, N' is a component (the normal-to-the-airfoil component) of the resultant force $\vec{R}$ that the airfoil undergoes as a result of the net effect of the pressure and shear stress distributions, integrated over the complete airfoil's surface. Furthermore, in equation (4.1), q_∞ is the dynamic pressure (equal to $\rho_\infty \left|\vec{v}_\infty^{\,2}\right| /2$) and C is the airfoil's chord.

In Harris' report [44] the normal force component, N', is computed using the pressure contributions only (see [44] p. 2). Therefore, for the cases when the comparisons are made versus experimental Harris' data *or* when the results come from the Euler part of the solver, the formula utilized to compute N' employs the pressure contribution only[1]. That is

$$N' = \sum_{\text{airfoil}} -\left(p\, S_y\right)\Big|_{I,\frac{1}{2}}. \tag{4.2}$$

As it was explained in Section III.L.5, the chosen reference system to work out this dissertation problems was the x'-y' coordinate system shown in Figure 21. It can be seen in Figure 21 that $[S_y]_{I,\frac{1}{2}} = -\Delta x'_{I,\frac{1}{2}} = -\left[x'(_{i,0}) - x'(_{i-1,0})\right]$; however, as mentioned in Section III.L.5, the " $'$ " symbol is dropped for notation simplicity. Thus

$$N' = \sum_{\text{airfoil}} \left(p\, \Delta x\right)\Big|_{I,\frac{1}{2}}$$

and therefore (see equation (4.1))

$$C_n = -\,\frac{1}{q_\infty C} \sum_{\text{airfoil}} \left(p\, \Delta x\right)\Big|_{I,\frac{1}{2}}, \tag{4.3}$$

with Δx determined from the airfoil's geometry defined in the x'-y' coordinate system (see Figure 21). The pressure obtained using this research's code and the airfoil's geometry defined in the x'-y' coordinate system are employed in formulas (3.198)

[1]Bear in mind, though, that the simulation was performed employing the full (viscous, turbulent) Navier-Stokes code.

and (4.3) to determine C_p and C_n which are then compared with Harris' experimental data [44], Agarwal's et al. (and other's) numerical results [43] and with the numerical results of the vortex panel method.

2. Corrections for the Experimental Data

In his report, Harris [44] states that the basic experimental data obtained in his tests (and utilized in this section for validation purposes) is presented without corrections for wall effects because of the uncertainty in the wall-induced lift interference. He, however, gives an indication of the tunnel walls' influence on the flow over the airfoil by rotating part of the C_n versus angle of attack curve as shown in Figure 32. The rotated line is the dashed one and indicates the correction that must be introduced to the angle of attack due to wall interference.

The slope m of the rotated curve is *approximately* equal to $m = 0.1117 \left[\frac{1}{\text{deg}}\right]$. This slope, together with the value of the normal force coefficient C_n (available at all the C_p plots provided in Harris report [44]), allows one to compute a corrected angle of attack as follows

$$\alpha^*_\infty = \frac{C_n}{m} \ \text{[deg]}, \tag{4.4}$$

with α^*_∞ denoting the corrected angle of attack.

As it can be seen in Figure 32, the correction curve covers up to approximately 11 deg. For this reason, only angles below this angle of attack are employed for the comparisons with Harris' experimental data. Table V shows a summary of Harris' angles of attack utilized for the comparisons, the corrected angles obtained by means of equation (4.4), and the different C_n's obtained by different methods/authors and those obtained in the present research.

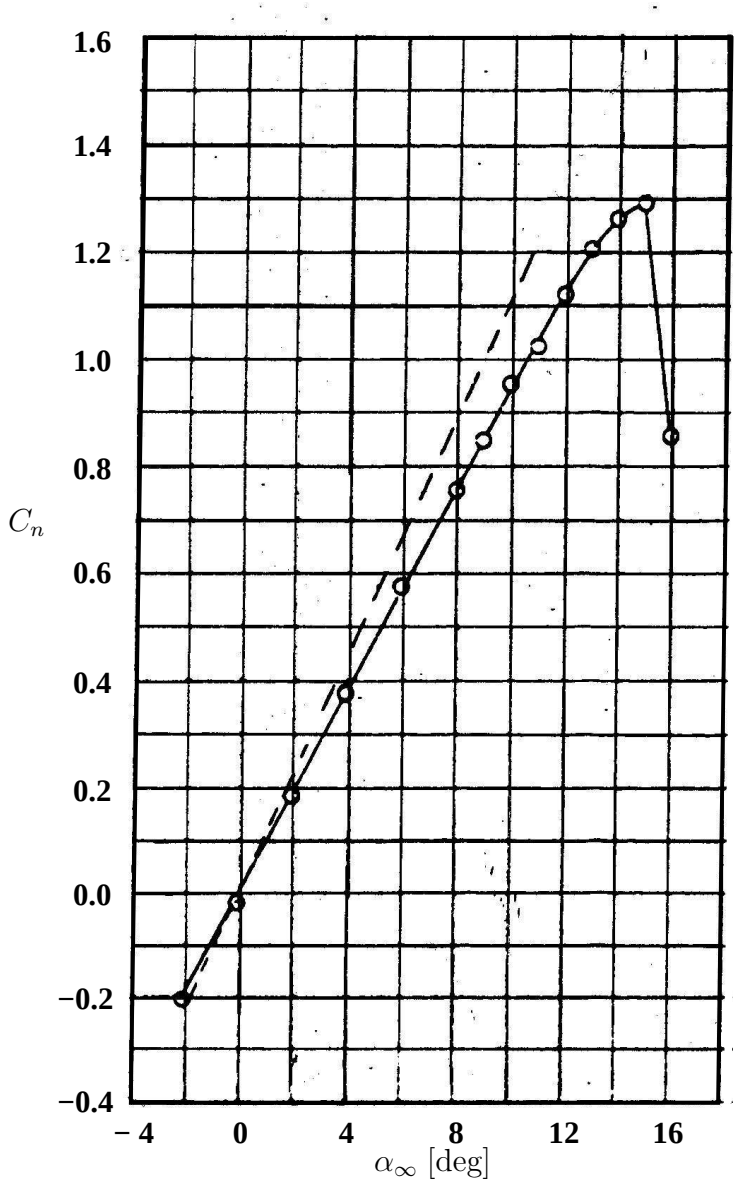

Fig. 32.: Normal force coefficient for a NACA0012 airfoil as reported in Harris [44]; $M_\infty = 0.30$ and $Re = 3.0 \times 10^6$. The dashed line indicates angle of attack correction for wall interference.

3. Computation of the Normal Force Coefficient in the Vortex Panel Method

The vortex panel method (VPM) takes as input data the airfoil's dimensionless geometry x'/C, y'/C (defined in the x'-y' coordinate system as shown in Figure 21) and the angle of attack, α_∞. The results provided by the VPM are $u'_{I,\frac{1}{2}}/u_\infty$, $v'_{I,\frac{1}{2}}/u_\infty$, $\left|\vec{v}_{I,\frac{1}{2}}\right|/u_\infty$, $[C_p]_{I,\frac{1}{2}}$, and C_L. Note that C_n is not provided and therefore it is necessary to compute it. It can be proved that the *normal* coefficient can be approximated by numerically evaluating the following integral

$$C_n = \oint_{\text{airfoil}} C_p \, d\left(\frac{x'}{C}\right).$$

This integral is directly evaluated counterclockwise using an "xmgrace" utility. The program "xmgrace"is the post-processing program utilized to plot the $C_p - \dfrac{x'}{C}$ and other graphs.

B. Code Validation Using Experimental Data

In this section, the C_p results obtained from different sources are presented for comparison purposes. The C_p data comes from 1) the experimental work of Harris [44], 2) from the code developed in this research and 3) from the vortex panel method developed at the Virginia Tech Institute. The convergence history of the normal force coefficient obtained by the present code is presented as well for each case.

Figures 33, 34 and 35 present the results for C_p from the mentioned different sources and Figures 36, 37 and 38 show the C_n convergence histories for each case.

1. Discussion

A summary of the results for C_n is given in Table V. Regarding the $C_p - \dfrac{x}{C}$ plot, for the case of $\alpha_\infty = -0.14$ ($\alpha^*_\infty = -0.16123$), the comparison between numerical and

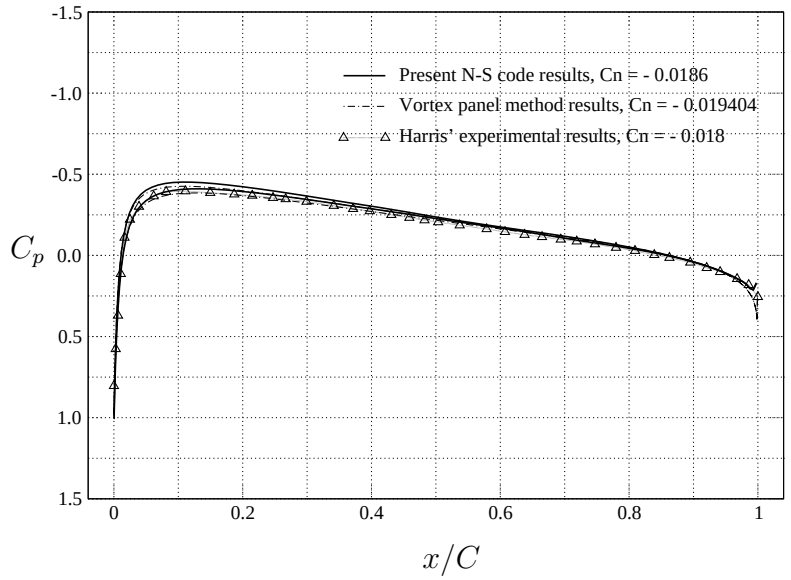

Fig. 33.: Comparison of different C_p and C_n results for the flow over a NACA0012 airfoil at flow conditions of $M_\infty = 0.3$, $Re = 3 \times 10^6$ and $\alpha_\infty = -0.14$ deg (corrected angle of attack is $\alpha^*_\infty = -0.16123$ deg).

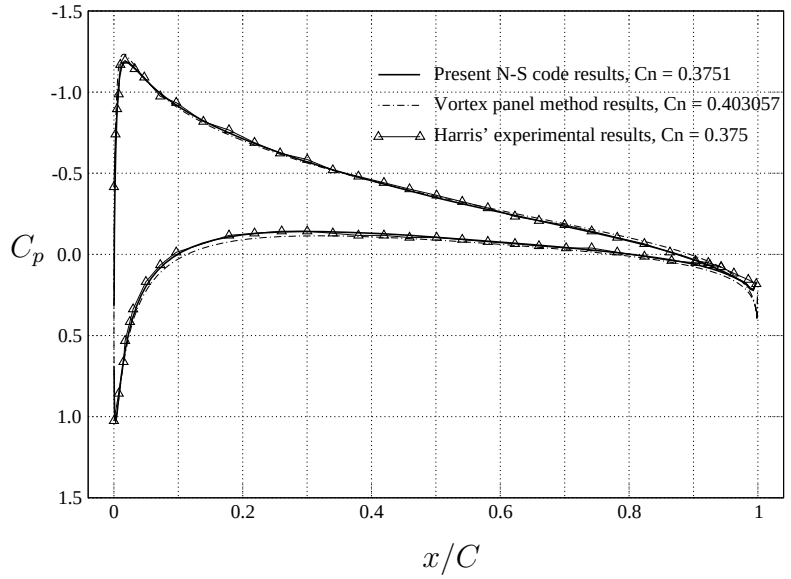

Fig. 34.: Comparison of different C_p and C_n results for the flow over a NACA0012 airfoil at flow conditions of $M_\infty = 0.3$, $Re = 3 \times 10^6$ and $\alpha_\infty = 3.86$ deg (corrected angle of attack is $\alpha^*_\infty = 3.3567$ deg).

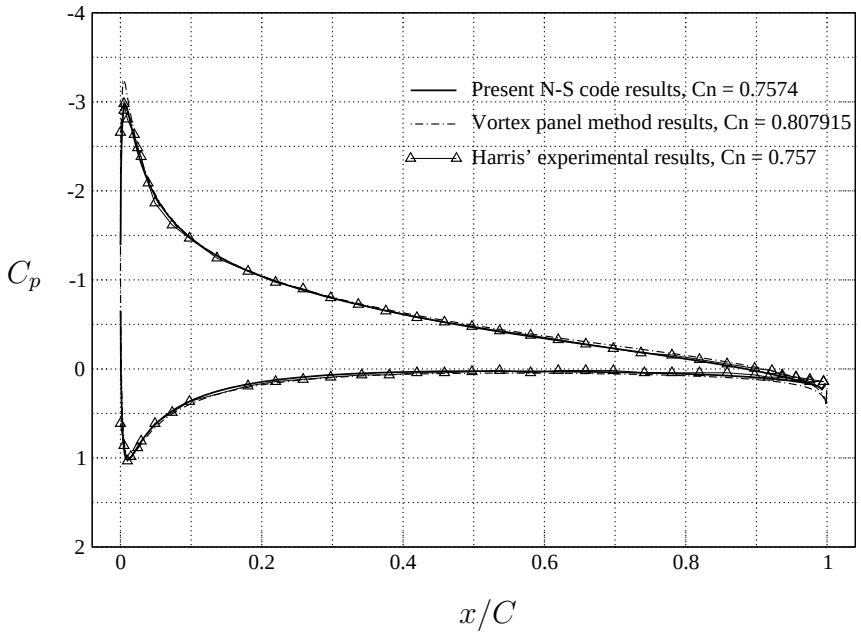

Fig. 35.: Comparison of different C_p and C_n results for the flow over a NACA0012 airfoil at flow conditions of $M_\infty = 0.3$, $Re = 3\times10^6$ and $\alpha_\infty = 7.86$ deg (corrected angle of attack is $\alpha^*_\infty = 6.776$ deg).

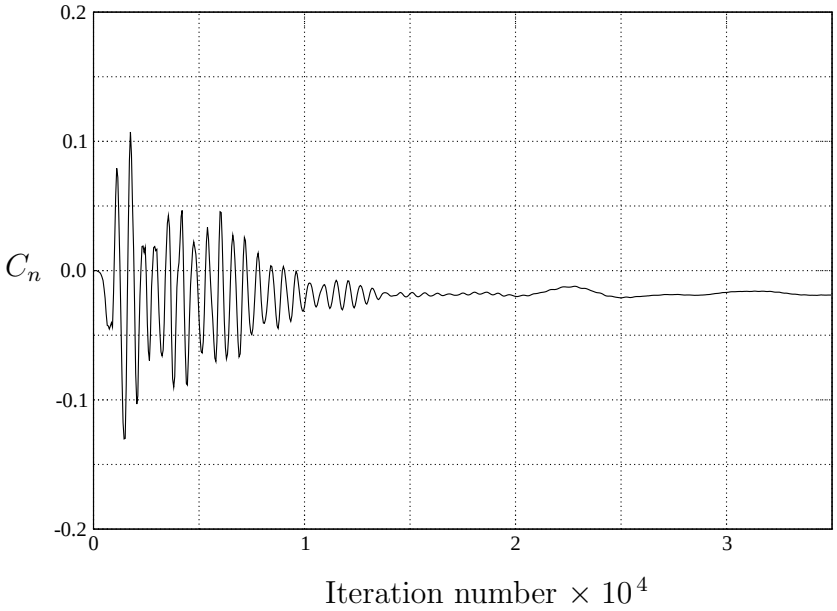

Fig. 36.: Present code C_n history; $M_\infty = 0.3$, $Re = 3\times10^6$ and $\alpha^*_\infty = -0.16123$ deg.

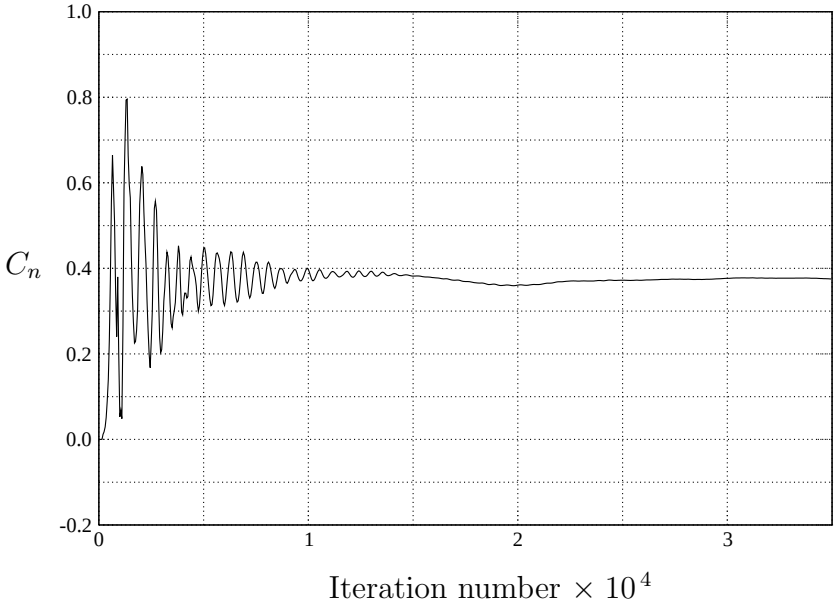

Fig. 37.: Present code C_n history; $M_\infty = 0.3$, $Re = 3 \times 10^6$ and $\alpha^*_\infty = 3.3567$ deg.

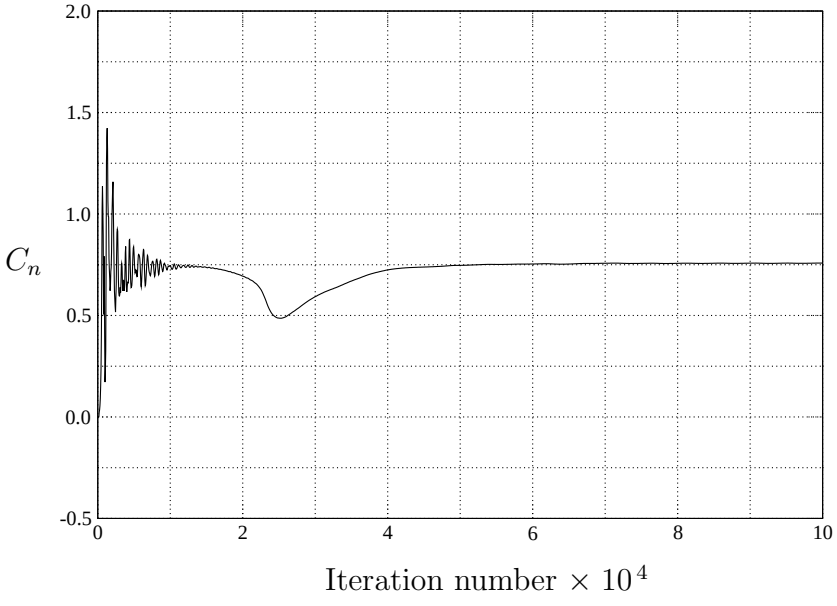

Fig. 38.: Present code C_n history; $M_\infty = 0.3$, $Re = 3 \times 10^6$ and $\alpha^*_\infty = 6.776$ deg.

experimental data is difficult since for this specific, very small angle, the experimental upper and lower C_p plots are *almost* overlapped (see Figure 9.b in [44]). What it was done was to digitalize an imaginary line approximately placed in the middle of the upper and lower experimental C_p graph. Even with this problem, the agreement between the C_p plots and C_n values for this case is good as it can be seen in Figure 33.

Table V.: Summary of C_n results from several authors/methods for code validation.

α_∞ [deg] (from [44])	α^*_∞ [deg] (from eq. (4.4)	C_n (from [44])	C_n (Present code results)	C_n (VPM)
-0.14	-0.16123	-0.018	-0.0186	-0.019404
3.86	3.356731	0.375	0.3751	0.403057
7.86	6.776122	0.757	0.7574	0.807915

For the rest of the cases, the agreement between the experimental data and the results obtained with the present full Navier-Stokes code is excellent, as it can be verified in Table V and in the Figures presented in this section. However, Table V also shows that the agreement with the VPM is not as good. This is so because the theory behind the vortex panel method is for ideal fluid flow, contrary to the real fluid experiments by Harris and contrary to the real fluid flow theory of the full Navier-Stokes code developed in this dissertation. It will be seen in the next section that the results of the VPM agree excellently with the results of the Euler part of the code developed in this research.

C. Comparison with Other Numerical Results

In this section a comparison between this research results and numerical results obtained by other authors/methods is presented. As mentioned above, the numerical results obtained using the vortex panel method are also included. No experimental results for the pressure coefficient are presented for comparison in this section[2]; however, the C_p numerical results reviewed here, including this research results, are indirectly validated through the lift coefficient by means of the experimental data of Harris as shown in [43].

The comparisons for this section are shown in Figures 39 and 40. Figure 41 shows the lift coefficient versus angle of attack obtained by various means. Here, experimentally obtained data is also included for validation purposes.

1. Discussion

As it can be seen in Figure 39, the agreement between the results of the vortex panel method and the results obtained using the Euler part of the code developed in this research is very good. The agreement between Agarwal's et al. [43] simulations and the present research results (for both, Euler and Navier-Stokes solvers) is not as good though (see Figure 40). Regarding this disagreement, it is pointed out that there are no C_p experimental results available to verify which of the shown results are closer to reality. An indirect indication of correctness for the pressure coefficient plots shown in Figure 40 is the value of the lift coefficients, C_L. These are compared with available experimental data.

It can be seen in Figure 41 that the C_L versus angle of attack graph obtained

[2]Comparisons of pressure coefficient results and experimental data has been already presented in the previous section.

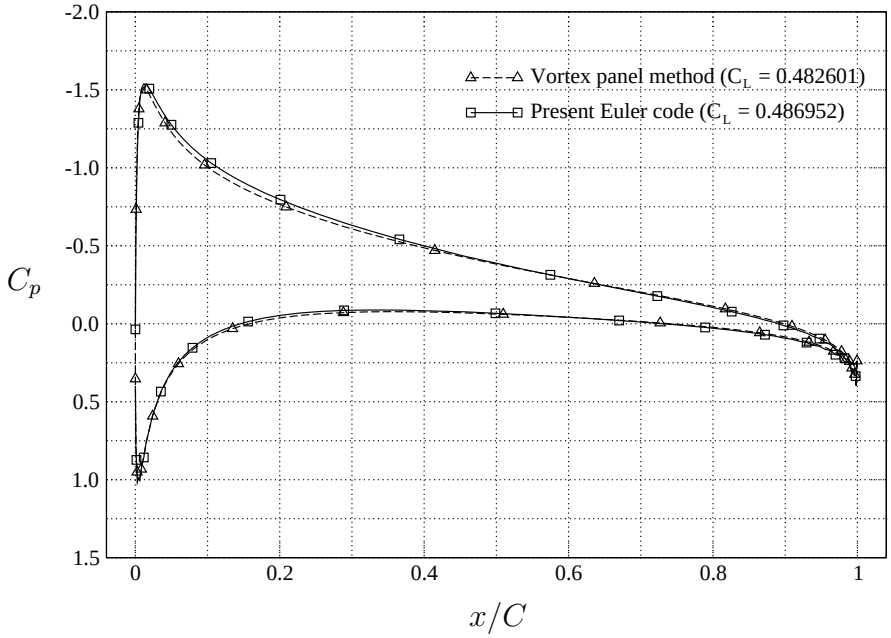

Fig. 39.: Comparison of present research results versus numerical results of the vortex panel method for the flow around a NACA0012 airfoil. $M_\infty = 0.3$, $Re = 1 \times 10^6$ and $\alpha_\infty = 4$ deg.

in this research is reasonably close to the graph obtained experimentally. It can also be seen that the graph obtained with the present research code is closer to the experimental data than all of the data presented in the figure. Despite this, a small over-prediction of the lift coefficient can be seen. This is so because, in general, there exists a difficulty for numerical approaches to match the lift (or normal) coefficient for angles of attack above the separation angle (see the numerical results by Anderson's et al. [45] in Figure 41). Despite this small over-prediction, it is concluded that the code developed in this research is a reliable tool to perform the fluid injection study. Results of such studies are presented in the following chapter.

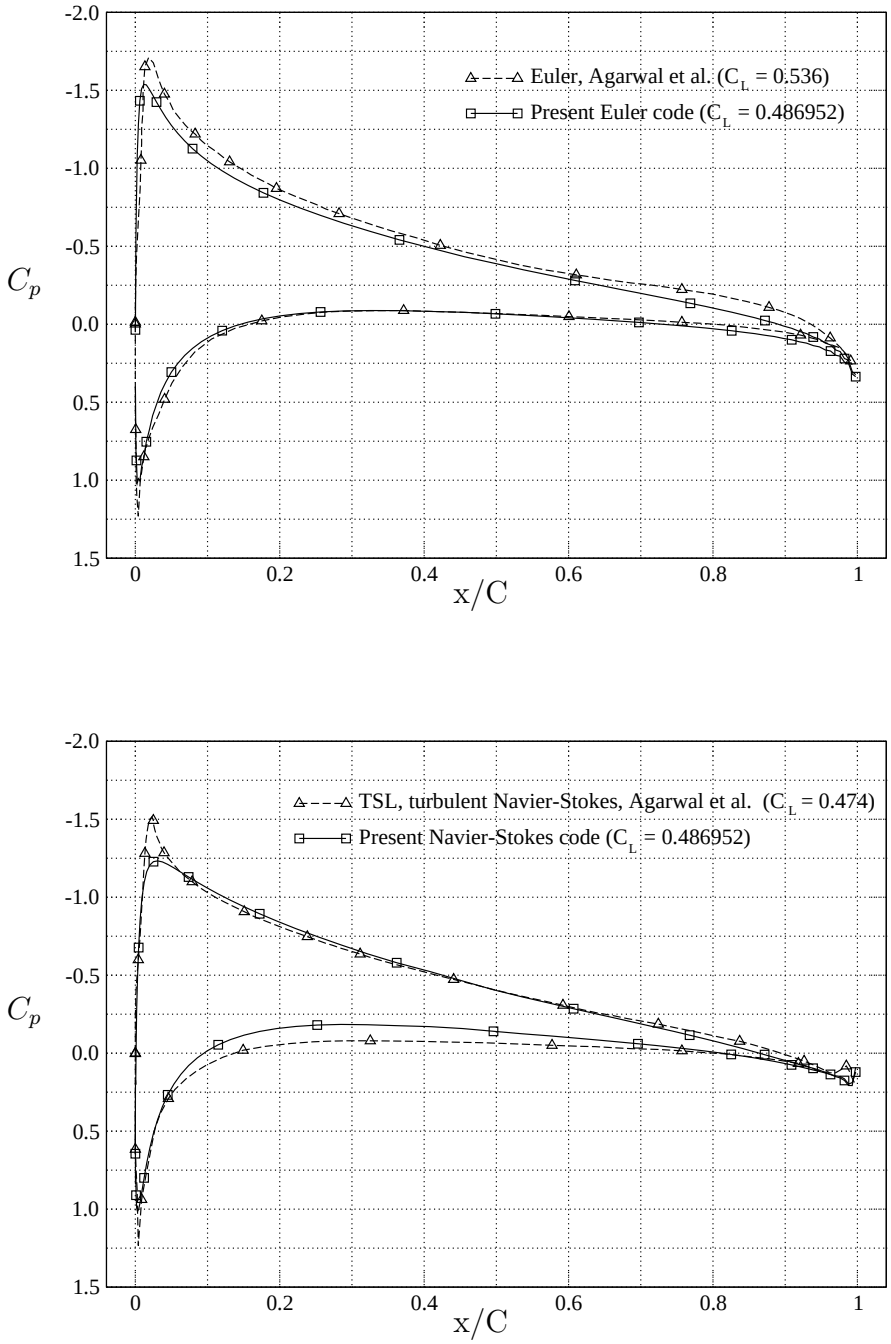

Fig. 40.: Comparison of present research results versus numerical results of Agarwal et al. [43] for the flow around a NACA0012 airfoil. $M_\infty = 0.3$, $Re = 1\times10^6$ and $\alpha_\infty = 4$ deg.

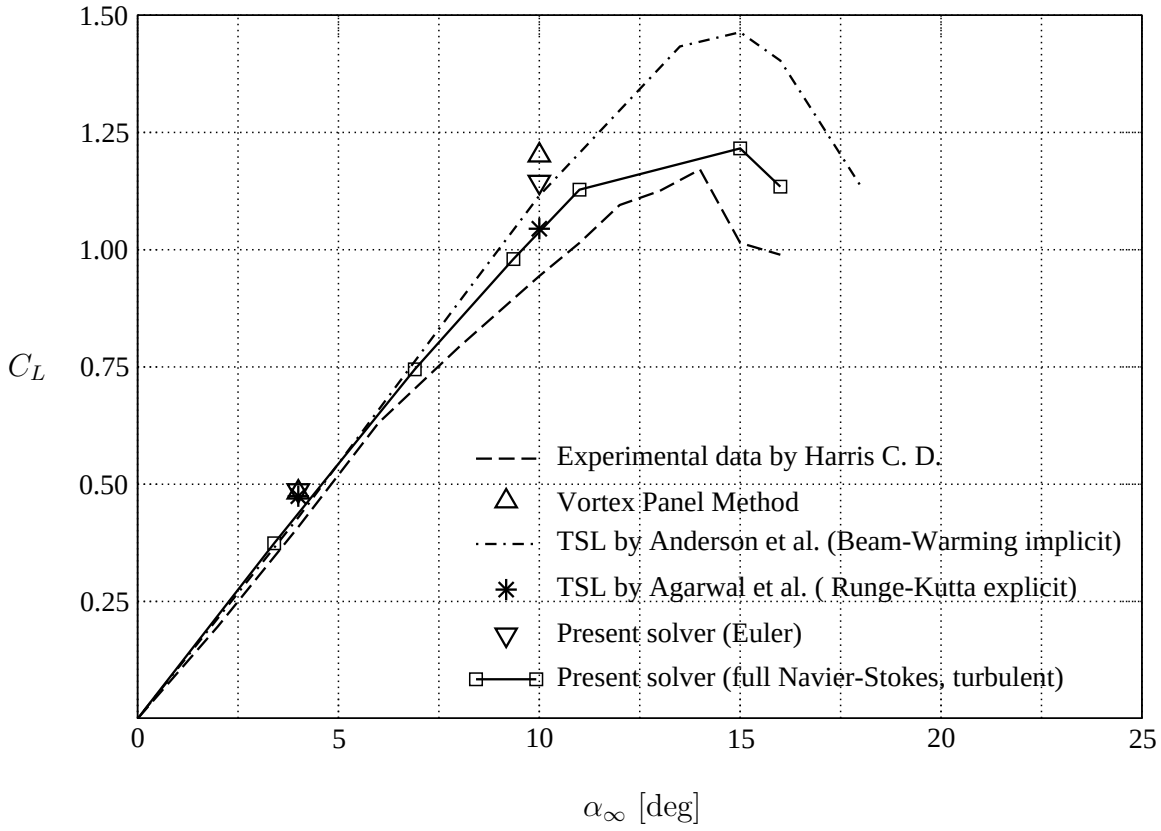

Fig. 41.: Comparison of C_L results from various numerical solutions with experimental results for the case of the flow around a NACA0012 airfoil, $M_\infty = 0.3$ and $Re = 1{\times}10^6$.

CHAPTER V

FLOW SEPARATION CONTROL BY SYNTHETIC JET ACTUATORS

This chapter discusses the flow separation control technique known as "synthetic jet actuation". Physics involving flow separation and flow separation control itself is introduced. Important parameters for unsteady separation control and their optimum values are discussed. Results of the numerical experiments performed on controlled NACA0015 and NACA0012 airfoils are presented and discussed. A study of the sensitivity of the solution to the variation of some unsteady control parameters is performed. These include angle of injection, θ_{jet}, reduced frequency of injection F^+ and grid clustering around the site of injection. Comments on the presented results are provided and a summary concludes this chapter.

A. Flow Separation Fundamentals

For the flow around a body with sharp leading edge, the boundary layer on any surface will grow from zero thickness at the upstream edge of the body. For a typical airfoil shape, with bluff nose, boundary layers will develop on top and bottom surfaces from the front stagnation point, but will have no zero thickness there. On proceeding downstream along the surface, large shearing gradients and stresses will develop adjacent to the surface because of the relative large velocities in the mainstream and the condition of no slip at the surface. Initially, this shearing action occurs only at the body surface and retards the layers of fluid immediately adjacent to the surface. These layers, since they are now moving more slowly than those beyond them, will then influence the latter and so retard them. In this way, as the fluid near the surface travels downstream, the retarding action penetrates farther and farther away from the surface and the boundary layer of retarded fluid thickens up (see Figure 42).

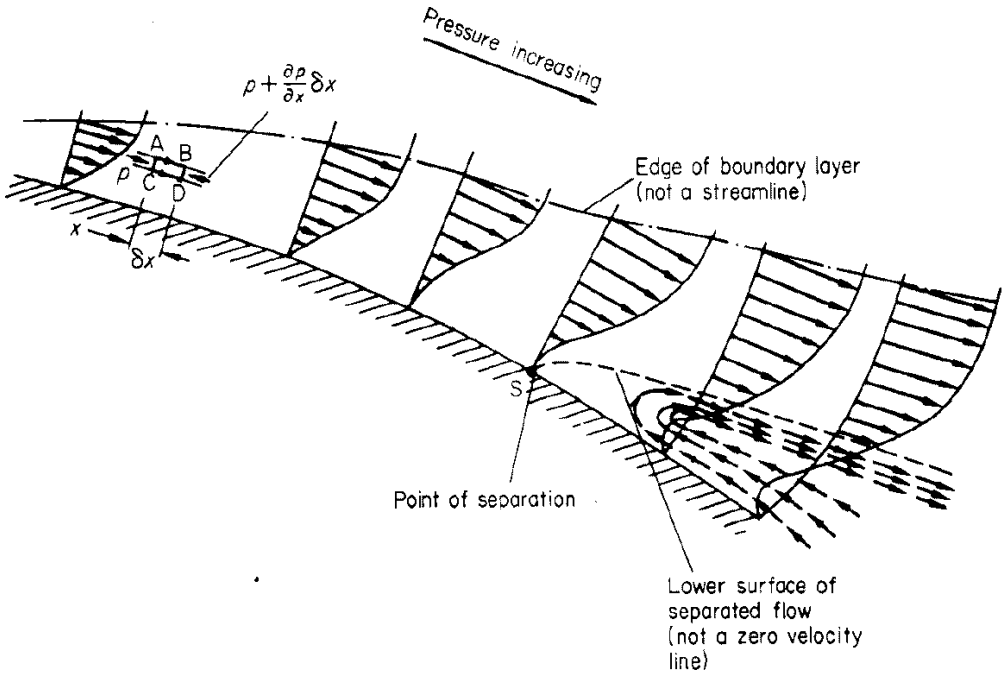

Fig. 42.: Evolution of the velocity profile in the vicinity of the separation point (taken from [15]).

Figure 42 shows a length of surface which has a gradual but steady convex curvature, such as the surface of an airfoil beyond the point of maximum thickness. In such a flow region, because of the retardation of the mainstream flow, the static pressure in the mainstream will rise (conservation of energy). On the other hand, the variation in static pressure along a normal to the surface through the boundary layer thickness is essentially zero, so that the pressure at any point in the mainstream, adjacent to the edge of the boundary layer, is transmitted unaltered through the layer to the surface. In the light of this, consider the small element of fluid marked ABCD in Figure 42. On face AC, the pressure is p, while on face BD the pressure has increased to $p + (\partial p/\partial x)\delta x$ where x denotes the streamwise direction. Thus, the net pressure force on the element is tending to retard its velocity. This retarding force is

in addition to the viscous shears which act along AB and CD and it will continuously slow the element down as it travels downstream.

This slowing effect will be more pronounced near the surface where the elements are remote from the accelerating effect, via shearing actions, of the mainstream, so that successive profile shapes in the streamwise direction will change as shown. Ultimately, at a point S on the surface, the profile slope $(\partial u/\partial y)_w$ becomes zero (u denotes the streamwise velocity component while y denotes a direction normal to the surface; subindex w refers to values at the wall). The shape of the velocity profile changes and under the new conditions, the layer must thicken up in order to satisfy continuity. Downstream of point S, the flow adjacent to the surface may well be in an upstream direction, so that a circulatory movement, in a plane normal to the surface, may take place near the surface. A line (shown dashed in Figure 42) may be drawn from point S such that the mass flow above this line corresponds to the mass flow ahead of point S. This line represents the continuation of the lower surface of the upstream boundary layer, so that, in effect, the original boundary layer separates from the surface at point S.

The result of separation on the rear half of an airfoil is to increase the thickness of the wake flow, with a consequent reduction in the pressure rise which should occur near the trailing edge. This latter means that the forward acting pressure force components on the rear part of the airfoil do not develop to offset the rearward acting pressures near the front stagnation point, and the pressure drag of the airfoil increases. If the airfoil incidence is sufficiently large, the separation may take may take place not far downstream of the maximum suction point, and a very large wake will develop. This will cause such a redistribution of the flow over the airfoil that the large area of low pressure near the upper surface leading edge is seriously reduced, with the result that the lift force is also greatly reduced.

B. Flow Control Separation Techniques

As discussed above, the reason for flow separation is the depletion of streamwise momentum from the fluid flowing immediately adjacent to the surface. Such depletion is due to the presence of the wall and the action of viscosity. Flow separation control techniques must, therefore, look for ways to replenish the lost momentum and thus delay, or even eliminate, the flow separation. In this section some control techniques that have been developed and tested are mentioned. Techniques for flow separation delay or manipulation are based on many principles. A summary of such principles and techniques is given in Table VI.

The second column in Table VI presents the flow separation control principle while the third column denotes the techniques that accomplish the control by applying the corresponding principle. In this research, focus is placed on techniques that modify the velocity profile in the boundary layer by enhancing the mixing in the shear layer.

The first category is flow control via modification of the velocity profile within the boundary layer. This can be achieved by removing the low energy fluid from the boundary layer by means of fluid suction through slots or orifices. This results in an entrainment of high energy fluid from the upper layers of the boundary layer. Another method within the first category is the use of moving boundaries. This method employs the no-slip condition at the surface in order to energize the fluid close to the wall. The flow separation control using moving boundaries has already been studied in the past. For example, rotating cylinders have been used to delay separation at the leading and trailing edges of airfoils [46].

The momentum of the boundary layer may also be increased by means of steady injection of a high energy fluid into the near wall vicinity (steady blowing). When

Table VI.: Flow separation control techniques.

FLOW SEPARATION CONTROL	Modification of velocity profile in boundary layer	Steady suction
		Moving boundaries
		Tangential steady blowing
		Oscillatory blowing and suction
	Reduction of steepness of Adverse pressure gradient	Surface streamlining
	Enhancement of mixing in shear layer	Vortex generators, turbulators, etc.
		Normal steady blowing
		Pulsed jets
		Oscillatory blowing and suction
	Control of fluid's viscosity near the wall	Heat transfer to/from the fluid
		Injection of secondary fluid with higher/lower viscosity
		Cavitation
		Chemical reaction
	Additional (active) control methods	Acoustic excitations
		Oscillating flap or wire
		Oscillatory surface heating

the fluid is injected tangentially (tangential steady blowing) the momentum of the boundary layer is directly increased and thus the velocity profile in the boundary layer is replenished. This additional momentum may be provided actively[1] (by an external source or by locally redirecting accelerated fluid into the wall region) or passively[2]. Passive blowing through leading edge slats and trailing edge flaps are commonly used in aircraft wings. Even though the amount of blowing is small (set by the wing's pressure differentials), the effect on the aerodynamic characteristics of the wings is outstanding. The effect of the leading edge slats and trailing edge flaps can also be enhanced actively by using high pressure air bled from the engine's compressor (internally blown slats and flaps) or by directly deflecting the exhaust jet from the engine (externally blown flap).

Mixing enhancement in the shear layer is of interest in this research. This mixing increases the turbulence level and hence, the energy of the fluid in the neighborhood of the wall. One way to accomplishing this energizing of the shear layer is using auxiliary devices such as vortex generators, turbulators, etc.

Other method employed to enhance the momentum in the boundary layer is to steadily inject fluid perpendicularly to the wall (normal steady blowing). This would increase the mixing rate in the shear layer. There is a large amount of literature available in the area of steady blowing [6].

Furthermore, in recent years, the use of pulsed jets emanating from the surface has also shown to have benefits as separation control devices [47][48]. These pulsed jets have the ability to produce a large amount of vorticity and to enhance the mo-

[1]In this case "active" refers to techniques in which energy is expended to modify the flow.

[2]Passive techniques do not require additional power but they have an associated drag penalty in this case.

mentum transport within the boundary layer, thus achieving good flow separation control attributes.

A technique of interest that has not been discussed so far is the oscillatory blowing and suction (see Table VI). This technique employs fluid blowing and suction alternatively and it has proven to be more efficient than steady blowing or steady suction alone [49]. One way of achieving the oscillatory blowing and suction is to use a device called zero-mass jet (or synthetic jet) actuators. These devices occupy the central attention of this research and a detailed description of them and of their operation principles is given in the next sections.

C. Synthetic Jet Actuator (SJA)

The advantage of implementing several of the previously discussed techniques in air vehicles is evident since they provide a lift increase and/or a drag reduction. Many of those techniques, however, 1) face serious technical difficulties, 2) require relative large amounts of power (active techniques) or 3) incur in drag penalties (passive techniques). For example, a steady blowing jet requires a permanent supply of air. This is typically implemented in the aircraft by bleeding the jet engines. As a result the engine's power available for producing thrust is reduced. Moreover, it needs additional plumbing to transfer this air from the engine to the site where the control is required, i.e., to the aircraft's wing[3]. This means additional parts and thus weight as well as additional maintenance. Oscillatory blowing and suction from an existing air supply also suffers from this drawback.

These problems can be overcome by using the relatively novel concept of synthetic

[3]If the wing is fixed, this might not represent a great technical difficulty; however, for the case of a rotary wing (e.g., an helicopter blade), the situation gets real complex since there would exist the need to transfer, via pneumatic connections, the air from a fixed air source to the rotating frame of the wing.

jet actuation. A synthetic jet actuator (SJA) is a small device that generates a high frequency jet by inhaling and exhaling fluid from the flow that is being controlled. Specifically, the SJA consists of an enclosed cavity which communicates with the external flow to be controlled only through an orifice or slot. The change of volume that causes the inhaling and exhaling of the SJA is induced by the oscillatory motion of a piston which is connected to a driving mechanism (see Figure 43). The flows of the inhaling and exhaling SJA cycles are assumed to be incompressible, therefore the air mass inhaled is the same as that exhaled. The difference between the inhaling and exhaling flows is that the inhaled flow is drawn from a much larger cross-sectional area (the area surrounding the orifice) than that through which the exhaled flow is directed. Therefore, the average air speed during inhaling is a lot smaller than that during exhaling. The net result of the high frequency inhaling and exhaling SJA cycles is consequently a continuous jet. This jet is "synthetic" in the sense that no net mass is supplied to the flow: the same mass that is ingested during the inhaling is expelled during exhaling. That is why such actuator is also called "zero-mass flux" actuator.

The synthetic jet actuators do not require a permanent supply of air or plumbing like steady blowing actuators and other flow control devices do. It can be perfectly self-contained and the entire unit can be installed at the site where it is needed. Its only connection with the rest of the aircraft would be electrical wires that provide power to the piston driving mechanism.

The goal of this research is to further increase the knowledge on flow separation control using synthetic jet actuators. The literature review on the subject suggests that, to date, there aren't analytical tools available to determine the range of parameters such as jet location, jet momentum coefficient, injection frequency and injection flow angle for which flow control methods are most effective. As a result, for every

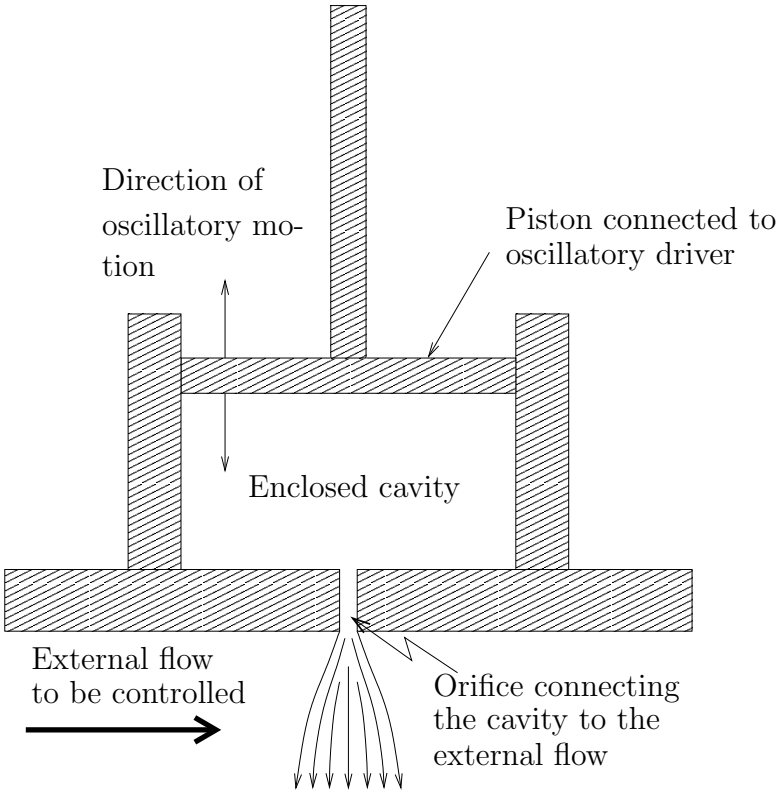

Fig. 43.: Principle of operation of a synthetic jet actuator.

new airfoil shape at fixed incidences, or for pitching airfoils with different unsteady parameters such as oscillation amplitude or rate, the flow actuation parameters are determined heuristically. Numerical solutions here can play a key role by performing sensitive analysis of the flow control parameters.

1. Principle of Operation of the SJA's

The application of synthetic jets to flow separation control is based their ability to energize the boundary layer. For the case of synthetic jet actuators equipped with tangential slots as those employed in this research, the actuator adds momentum to the boundary layer in several ways. First, during the suction part of the cycle, the

SJA draws the low momentum fluid from the near wall region into the cavity, thereby bringing the higher momentum fluid at the boundary layer edge closer to the wall. On the other hand, during the blowing part of the cycle, the SJA adds the same fluid with higher momentum into the flow, almost tangentially to the surface. Finally, the oscillatory nature of the flow field generated by the SJA promotes the mixing of the low momentum fluid near the wall with the higher energy fluid close to the edge of the boundary layer.

In order to understand why the mentioned mixing takes place, one needs to take a closer look into the physics of the flow field generated by the SJA. Vortex shedding accompanies the flow separation at high angles of attack. Vortices are periodically formed over the airfoil and travel downstream with a speed comparable to but somewhat lower than the freestream velocity. The frequency at which the vortices are shed is the shedding frequency f_{sh}. This frequency depends on the airfoil's angle of attack, chord length and on the freestream velocity. The Strouhal number, St, is a non-dimensional parameter that relates, for a fixed angle of attack, the shedding frequency, f_{sh}, the airfoil's chord length, C and the freestream velocity, U_∞, in the following way

$$St = \frac{f_{\mathrm{sh}}\, C}{U_\infty}.$$

St is a constant of O(1) and it denotes the ratio of the convection (or residence) time scale, C/U_∞, and the oscillation time scale $1/f_{\mathrm{sh}}$.

The formation and shedding of vortices enhance the mixing of the high speed, high momentum fluid away from the airfoil wall with the low speed, low momentum fluid close to the airfoil's wall. One of the important consequences of this mixing is that, if the mixing is strong enough, the low momentum flow close to the wall is energized by the entrained high momentum flow, a process which in turn causes flow

reattachment and thus reduction or even elimination of the separated region [50].

A very effective way of intensifying this mixing is through external, periodic excitation at a frequency equal or close to the natural shedding frequency. The periodic excitation generated by an SJA can be used as the required external excitation. Thus, an added benefit of the synthetic jet actuator is the promoting of the mixing and hence of the momentum exchange between the outer and inner parts of the boundary layer. Note that steady techniques (e.g. steady blowing) for separation control lack of any kind of periodicity and thus do not reinforce the mentioned mixing and momentum exchange.

D. Important Parameters in Flow Separation Control

The reduced excitation frequency, F^+, the jet momentum coefficient, C_μ, and the angle of injection, θ_{jet}, (all defined below) are the non-dimensional parameters employed when studying unsteady flow separation control by means of oscillatory blowing and suction [51]. The choice of these non-dimensional parameters focuses on the impact of the characteristics of the jet with respect to the global airfoil flow field, as opposed to a local scale in the boundary layer.

The reduced excitation frequency relates the period of the jet cycle to the convection time of the flow over the airfoil and it is defined as

$$F^+ \equiv \frac{f_{SJA}\, x_{te}}{U_\infty}\,. \tag{5.1}$$

In this equation, f_{SJA} is the actuator's frequency, x_{te} is the distance from the location on the body's surface at which excitation is provided to the end of the body (see Figure 44) and U_∞ is the value of the freestream velocity. Seifert et al. [52] claim that the optimal location of injection is the baseline separation region since, for most

applications, the excitation would be significantly attenuated otherwise.

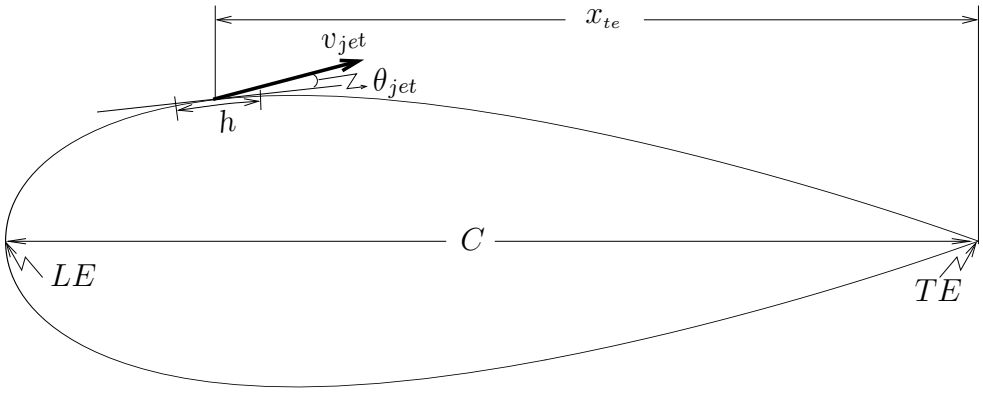

Fig. 44.: Schematic of injection site and parameter's notation.

The oscillatory blowing momentum coefficient, C_μ, quantifies the excitation introduced by the active device into the boundary layer [2]. The level of oscillatory momentum due to the actuator's excitation is referred to freestream conditions to arrive at the jet momentum coefficient

$$C_\mu \equiv \frac{h\,\rho_{jet}\,V_{jet\ max}^2}{q_\infty\,C}. \tag{5.2}$$

In equation (5.2), $V_{jet\ max}$ denotes the jet velocity oscillation amplitude (see Figure 10), h is the width of the jet's exit and C is airfoil's chord length (see Figure 44). Furthermore, in equation (5.2), q_∞ is the freestream's dynamic pressure defined as $q_\infty = \frac{1}{2}\rho_\infty\,U_\infty^2$.

The last injection parameter specifies the direction of the jet exit velocity with respect to the airfoil's surface. This parameter is called the injection flow angle and it is denoted as θ_{jet} (see Figure 44).

E. Parameters Utilized in the Present Numerical Simulation

The main theme in this research is that efforts must be directed towards utilizing the natural flow instability, enhanced by the periodic addition of momentum, to interact with the large scale coherent structures of the flow. The addition of the momentum is achieved through oscillatory injection of fluid. Such injection must be applied at the appropriate location (x_{te}), with the appropriate direction (θ_{jet}), amplitude ($V_{jet\ max}$) and frequency of oscillation (f_{SJA}).

For the case of turbulent flow it has been found that the most effective oscillation frequencies of the periodic forcing are widely disparate from those of the turbulence [52]. A monitoring of the dependence of the periodic injection effectiveness on F^+ in conjunction with C_μ was therefore undertaken by Greenblatt D. and Wygnanski I. J. [5]. They proposed a generic deflected flap configuration as an example on which the controlling parameters could be isolated. It was found that, independently of the Reynolds number and the levels of freestream turbulence, $F^+ \approx 1$ is the optimum reduced frequency to control turbulent separated flow. This result has been corroborated in a number of turbulent, separated flow control experiments (see e.g. [5])

Moreover, recent work (see e.g. [2] and [8]) has repeatedly shown that low amplitude oscillatory blowing (of the order of at least 0.002) can delay separation and enhance lift over a wide range of Reynolds numbers, including those corresponding to aircraft takeoff and landing [50]. These experiments have demonstrated several consistent results, including that:

1. The most effective location for unsteady forcing is near the point of separation,
2. The optimum reduced frequency for the oscillations is approximately $F^+ \approx 1$ and

3. The amplitude of the oscillations required for effective separation control is about two orders of magnitude lower than that for steady blowing (which needs amplitudes of $O(10^{-1})$ in order to produce any noticeable effects).

Regarding the appropriate direction of injection of the fluid (θ_{jet}), it has been found in numerical experiments [51] that no effective flow separation control can be achieved for a jet exiting normally to the airfoil surface ($\theta_{jet} = 90$ deg). It was also found, on the other hand, that for $\theta_{jet} = 30$ deg large amplitude oscillations of the computed loads (e.g. lift and drag forces) are obtained. This load oscillation is undesirable and therefore a jet exit angle $\theta_{jet} \leq 5$ deg is recommended by the numerical simulations.

From the literature review on the fluid injection parameters (briefly outlined above), it was decided that the following parameters were employed for the two numerical simulations performed in this research (see Table VII).

F. Numerical Simulation Results

Two numerical simulations using two different sets of injection parameters were performed. The objective was to investigate the effect of the flow control parameters on the flowfield. Two different geometries were employed and the injection flow angle was kept constant such that for both numerical experiments the fluid was injected almost tangentially into the flowfield. The results of these two numerical simulations are presented in the following sections. Experimental data are used to validate the numerically results when available.

Table VII.: Parameters used in the present research numerical experiments.

Parameter	*Numerical simulation 1*	*Numerical simulation 2*
Airfoil Type	NACA0015	NACA0012
Chord length, C	0.375 m	0.15 m
Freestream velocity, U_∞	35 m/s	101.88 m/s
Freestream Mach numb., M_∞	0.1	0.3
Reynolds number, Re	9×10^5	1×10^6
Frequency of injection, f_{SJA}	120 Hz	691.085 Hz
Injection location from LE	12.27 %C	1.72 %C
x_{te} (see equation 5.1)	0.329 m	0.147421 m
Max. inject. vel., $V_{jet\ max}$	73.81 m/s	47.162 m/s
Angle of injection, θ_{jet}	2 deg	2 deg
Slot width, h	2×10^{-3} m	1.4×10^{-3} m
Reduced frequency, F^+	1.128	1.0
Momentum coefficient, C_μ	0.04743	0.004

1. Results for the Simulation of the NACA0015 Airfoil

The freestream and injection parameters for this simulations are as shown in Table VII. Figures 45 to 47 show the lift coefficient, C_L, versus the *non-dimensional* time, t. These figures correspond to the controlled case only. In this research, a controlled experiment refers to one on which the periodic excitation by oscillatory fluid injection is taking place. Furthermore, Figure 48 shows the *mean* converged C_L, corresponding to the controlled simulations, against the corresponding angle of attack, α_∞. This Figure also includes experimental results for controlled and uncontrolled cases, obtained

by Gilarranz [15].

Figure 48 clearly shows the benefits of the oscillatory excitation through the increase in the mean lift coefficient of the controlled case with respect to the lift coefficient for the uncontrolled one. Figure 48 also shows that the numerical results closely follow the experimental data with the exception of a small region at high angle of attack, between approximately 18 to 23 degrees. One possible reason for this discrepancy can be attributed to local geometry variations due to actuators placement on the NACA0015 used in the experiments. Some additional discrepancies between computational and experimental performance can be linked to variations in the methods used to determine C_L.

2. Results for the Simulation of the NACA0012 Airfoil

A second numerical experiment was performed in this research in order to compare the effect of different injection parameters and geometry. The parameters for this simulation are shown in Table VII.

Figures 49 to 53 show the lift coefficient, C_L, versus non-dimensional time, t. Figure 54 compares the numerically obtained lift coefficients (for controlled and uncontrolled cases) against the corresponding angles of attack. In this Figure, experimental data for the uncontrolled case obtained by C. D. Harris [44] is also included. The observed increase in the lift coefficient with respect to the steady coefficient (see Figure 54) shows the benefits of the periodic excitation. This is discussed further in the following section.

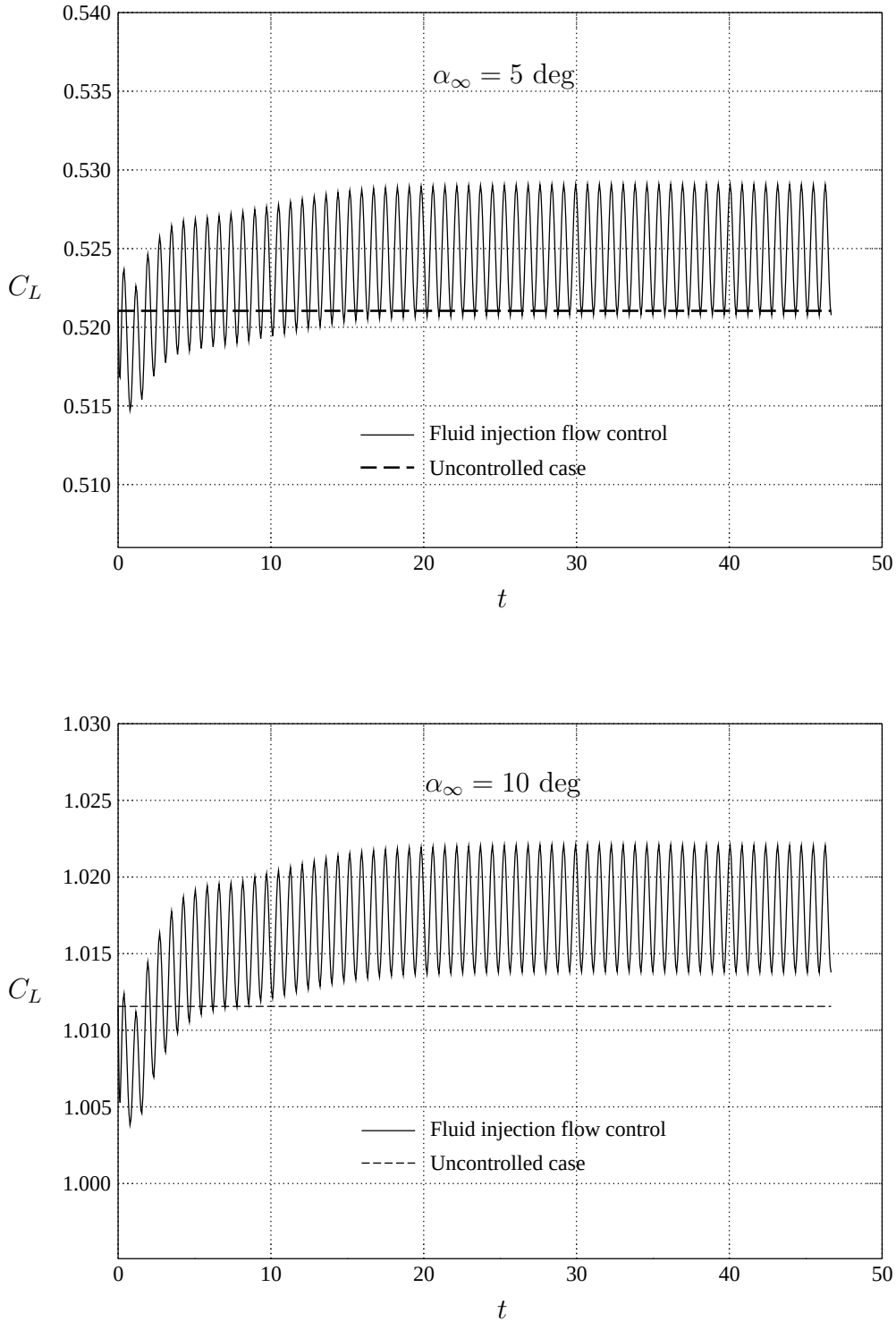

Fig. 45.: Effect of oscillatory flow separation control on C_L for a NACA0015 airfoil at $\alpha_\infty = 5$ and 10 deg. $M_\infty = 0.1$, $Re = 0.9 \times 10^6$, $F^+ = 1.13$ and $C_\mu = 0.0474$.

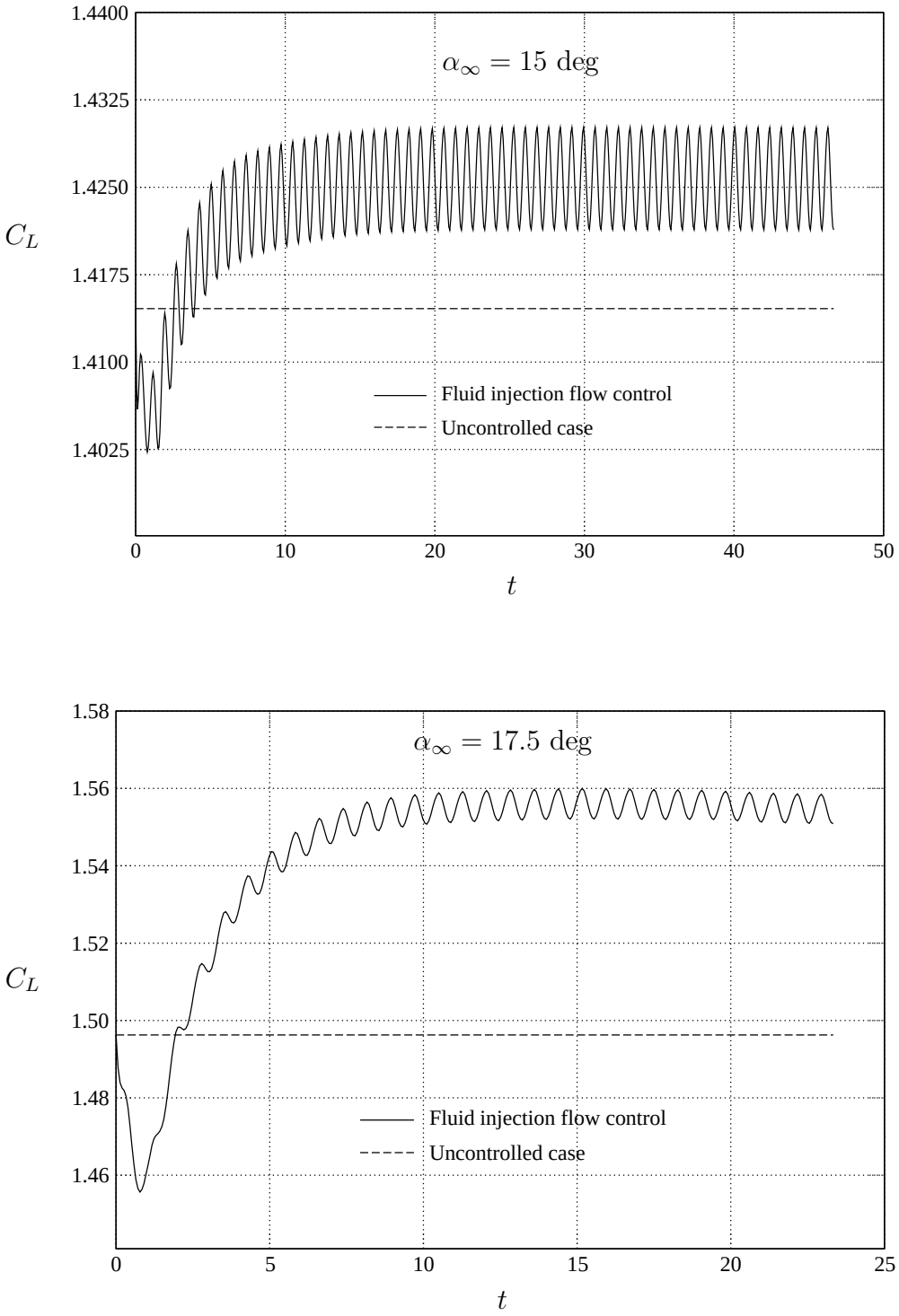

Fig. 46.: Effect of oscillatory flow separation control on C_L for a NACA0015 airfoil at $\alpha_\infty = 15$ and 17.5 deg. M_∞=0.1, Re=0.9 $\times$ 10^6, F^+=1.13 and C_μ=0.0474.

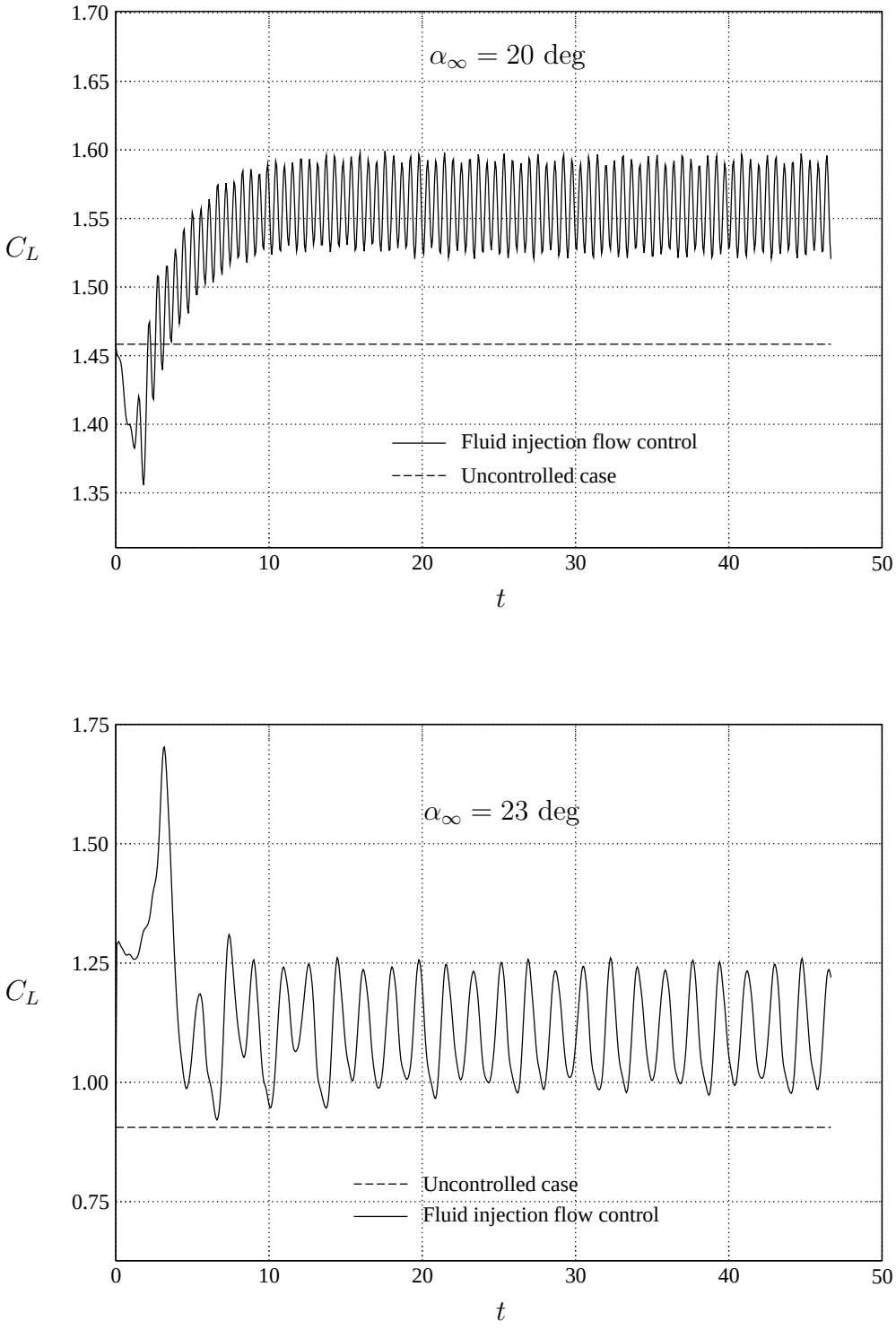

Fig. 47.: Effect of oscillatory flow separation control on C_L for a NACA0015 airfoil at $\alpha_\infty = 20$ and 23 deg. $M_\infty = 0.1$, $Re = 0.9 \times 10^6$, $F^+ = 1.13$ and $C_\mu = 0.0474$.

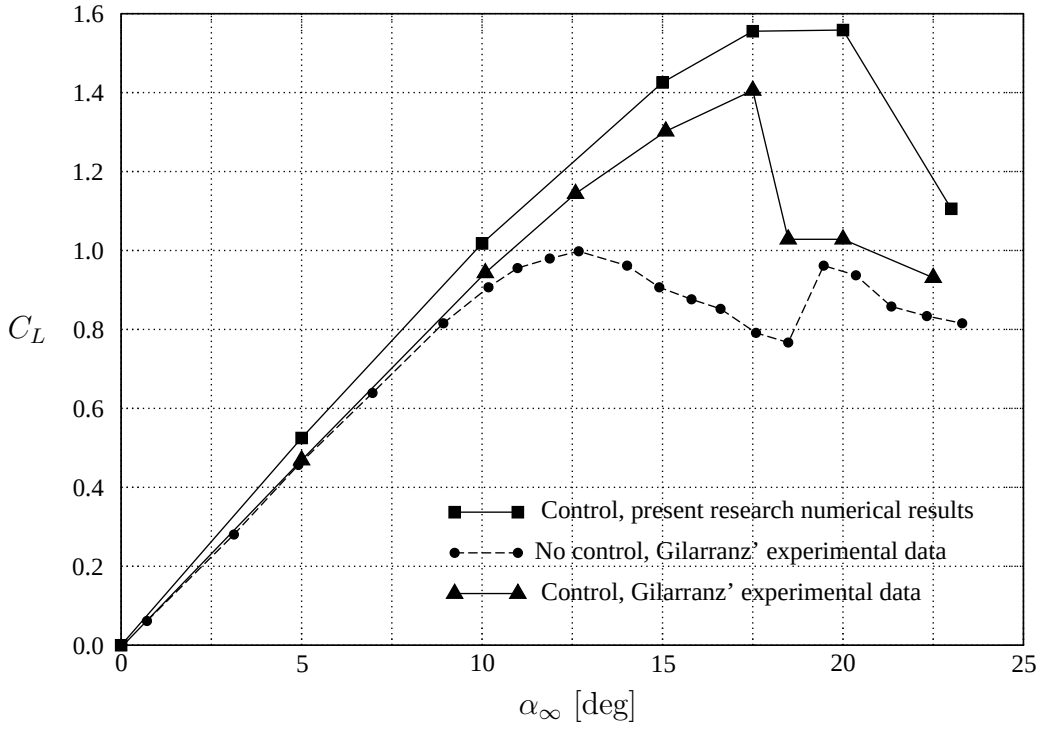

Fig. 48.: Comparison of numerical results versus Gilarranz [15] experimental data regarding the effect of SJA actuation on the lift coefficient. NACA0015 airfoil, $M_\infty = 0.1$, $Re = 0.9 \times 10^6$, $F^+ = 1.13$ and $C_\mu = 0.0474$.

G. Discussion of Results

The computed lift coefficient on the NACA0015 airfoil is over-predicted as it can be observed in Figure 55. While experimental data show an increase of up to approximately 80% in the lift coefficient, the numerical simulation reports an increase of up to approximately 93%. The general trend is, though, correctly captured.

There can be several reasons for this discrepancy. Firstly, most codes generally over-predict the lift coefficient (see e.g. the results by Anderson et al. [43] shown in Figure 41). Other probable reasons for the discrepancy may be the influence of the

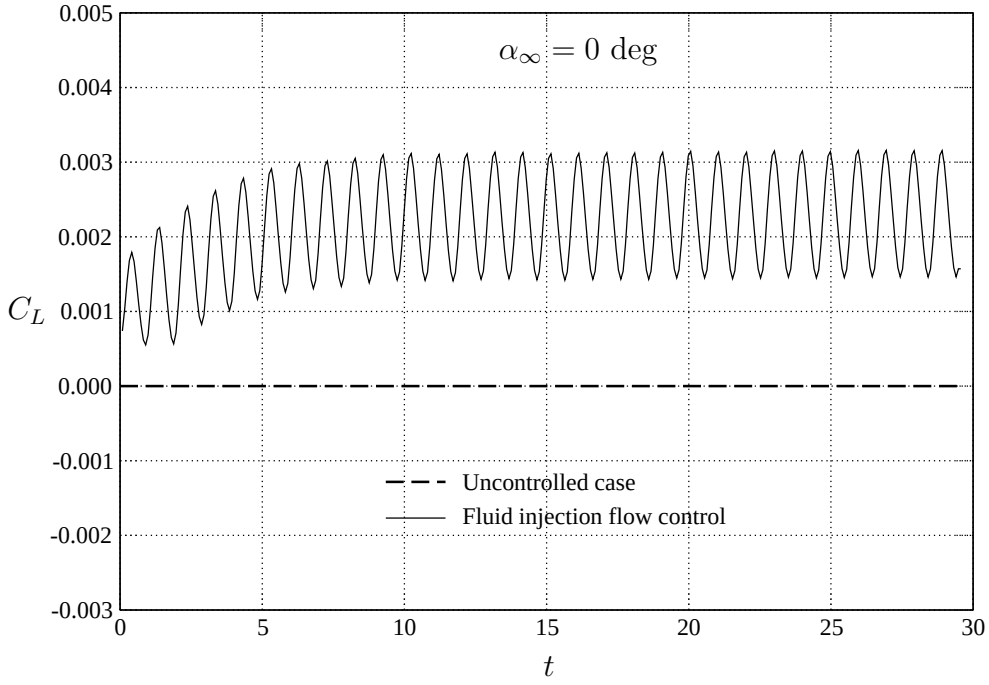

Fig. 49.: Effect of oscillatory flow separation control on C_L for a NACA0012 airfoil at $\alpha_\infty = 0$ deg. $M_\infty = 0.3$, $Re = 1.0 \times 10^6$, $F^+ = 1.0$ and $C_\mu = 0.004$.

turbulence model or the modeled boundary condition for the oscillatory injection. Poor grid resolution at the injection site has been already ruled out by means of the grid convergence study at the site of injection presented in Section V.H.3 below.

The simulation on the NACA0012 airfoil, on the other hand, shows a more conservative lift coefficient increase with respect to the corresponding experimental, baseline data. As shown in Figure 56, an increase of up to 30% in the lift coefficient is predicted for this set of injection parameters. This suggests that the injection parameters on the first numerical simulation are closer to optimum values.

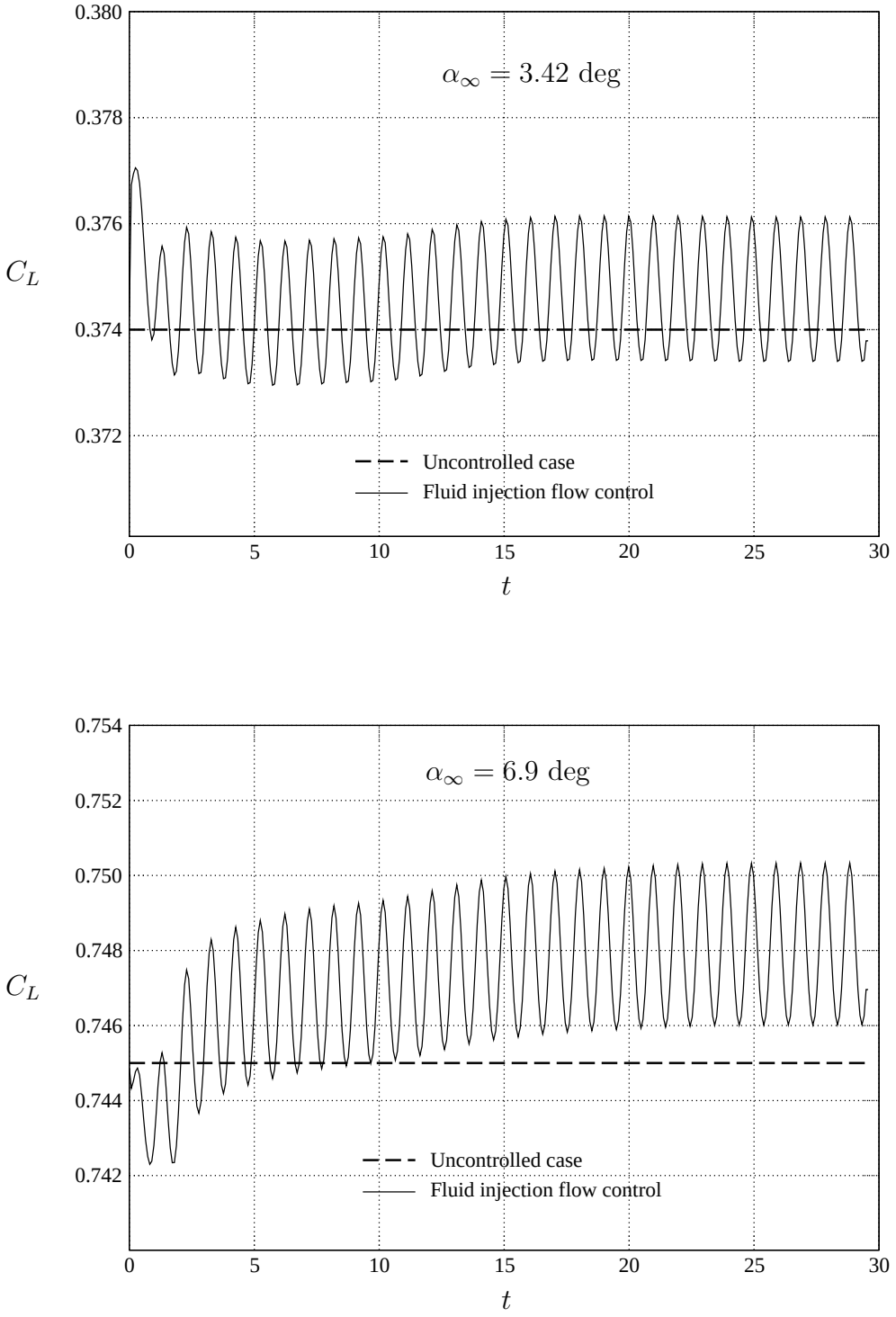

Fig. 50.: Effect of oscillatory flow separation control on C_L for a NACA0012 airfoil at $\alpha_\infty = 3.42$ and 6.9 deg. M_∞=0.3, Re=1.0 $\times$ 10^6, F^+=1.0 and C_μ=0.004.

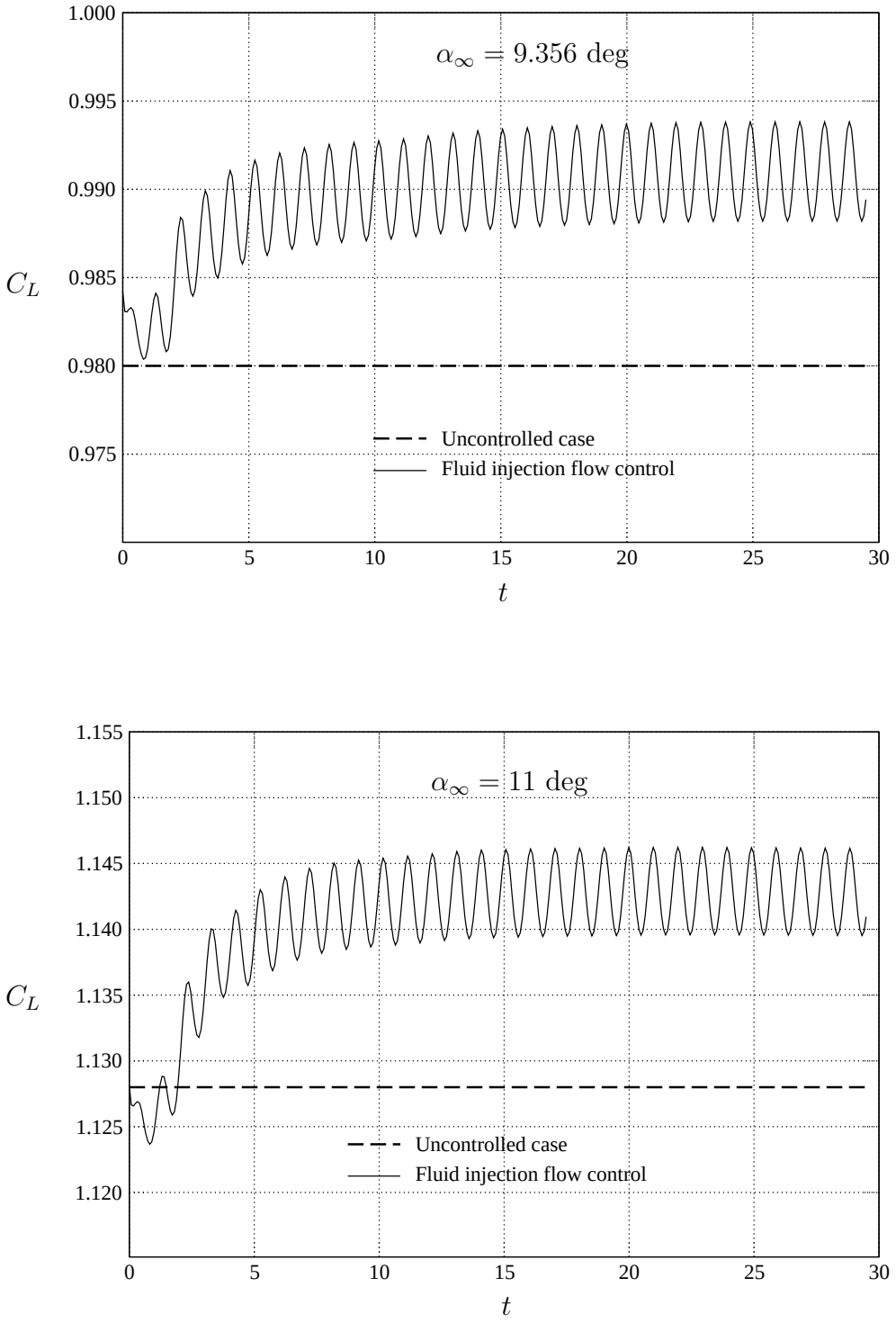

Fig. 51.: Effect of oscillatory flow separation control on C_L for a NACA0012 airfoil at $\alpha_\infty = 9.356$ and 11 deg. $M_\infty = 0.3$, $Re = 1.0 \times 10^6$, $F^+ = 1.0$ and $C_\mu = 0.004$.

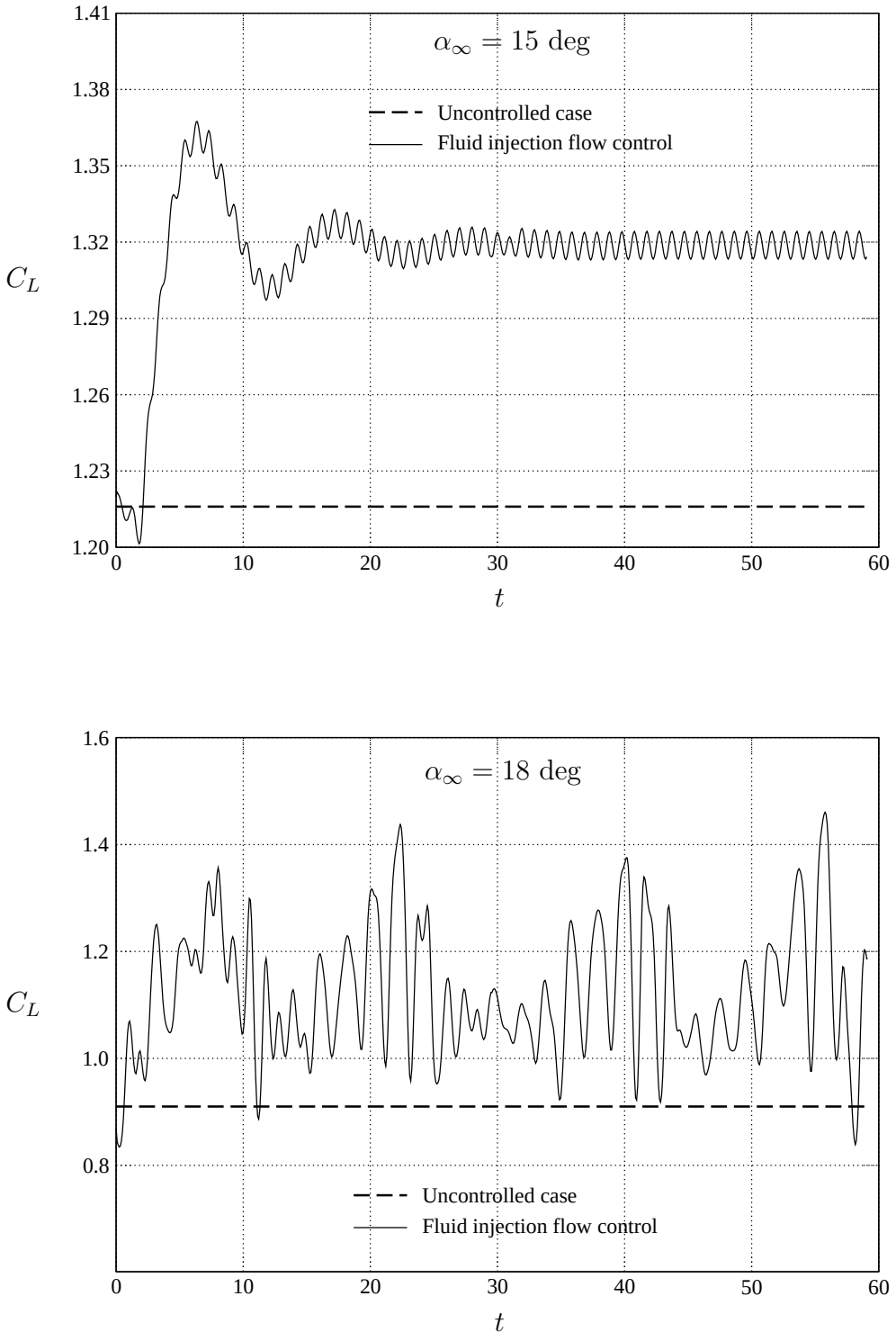

Fig. 52.: Effect of oscillatory flow separation control on C_L for a NACA0012 airfoil at $\alpha_\infty = 15$ and 18 deg. $M_\infty = 0.3$, $Re = 1.0 \times 10^6$, $F^+ = 1.0$ and $C_\mu = 0.004$.

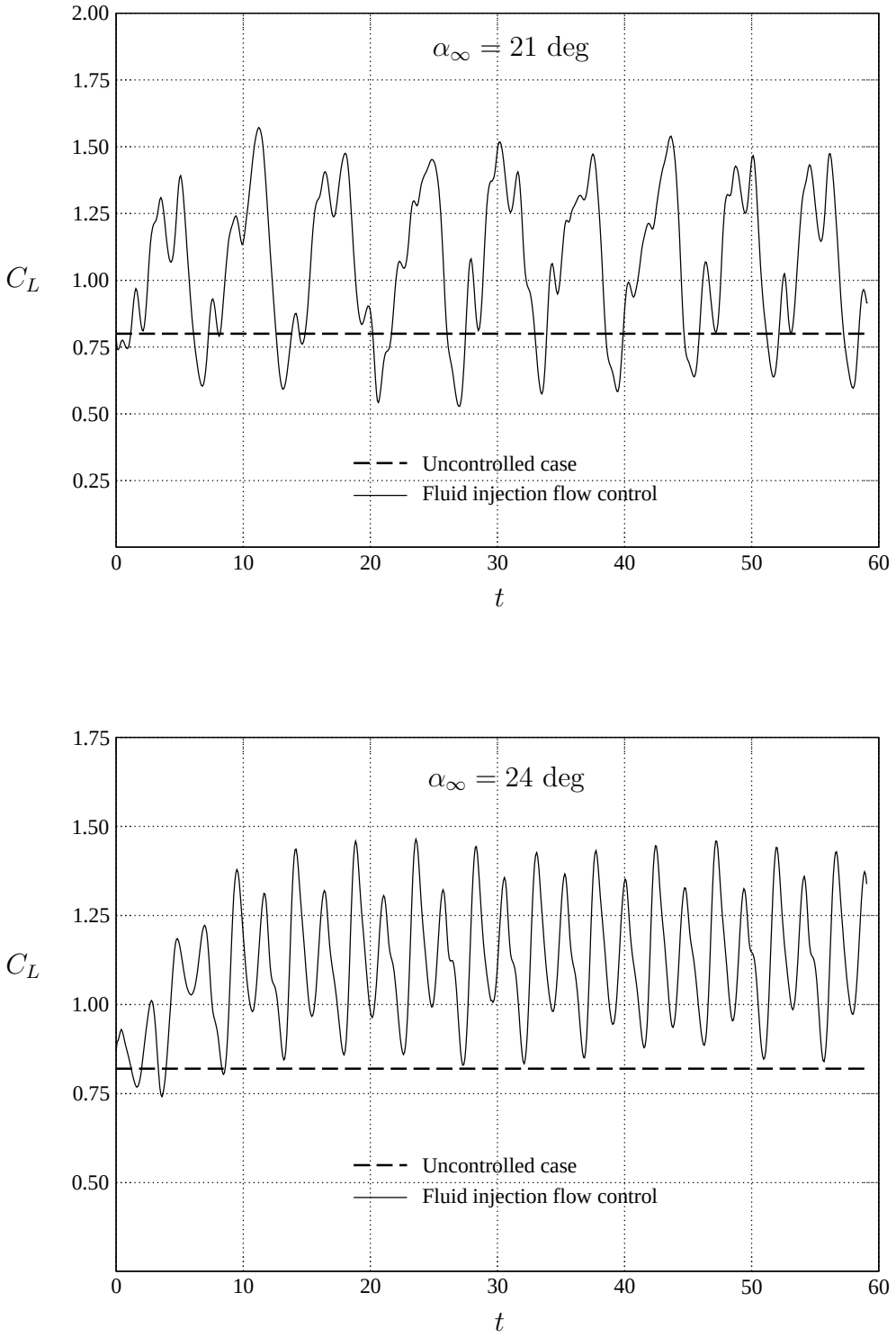

Fig. 53.: Effect of oscillatory flow separation control on C_L for a NACA0012 airfoil at $\alpha_\infty = 21$ and 24 deg. $M_\infty = 0.3$, $Re = 1.0 \times 10^6$, $F^+ = 1.0$ and $C_\mu = 0.004$.

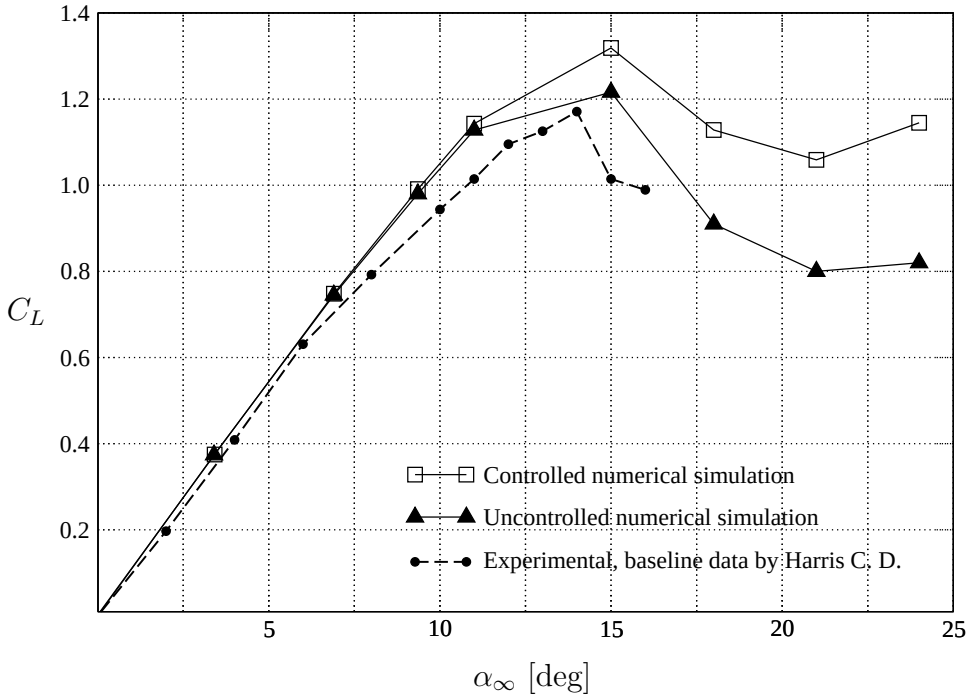

Fig. 54.: C_L versus angle of attack for the NACA0012 airfoil. The experiment and the no-controlled numerical simulation are performed using $M_\infty = 0.3$ and $Re = 1 \times 10^6$. For the controlled simulation, $F^+ = 1.0$ and $C_\mu = 0.004$.

H. Influence of Unsteady Control Parameters and Grid on the Lift Coefficient

In this section, the impact of the parameters described in the previous section on the effectiveness of the unsteady control is analyzed. Furthermore, a grid convergence study around the injection site is performed in order to assure that the unsteady solutions are grid independent. All the studies in this section are performed on a NACA0015 airfoil at an angle of attack $\alpha_\infty = 14$ deg and $M_\infty = 0.3$. The freestream velocity $U_\infty = 101.88$ m/s and the chord length of the airfoil is $C = 0.15$ m. The Reynolds number of these simulations was $Re = 1 \times 10^6$.

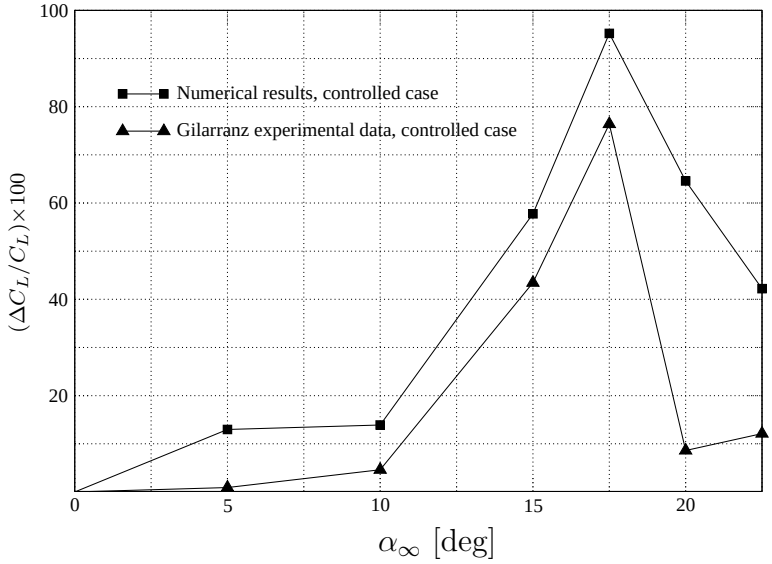

Fig. 55.: Increase in the lift coefficient with respect to the non-controlled experimental data of Gilarranz [15]. NACA0015 airfoil, $M_\infty = 0.1$, $Re = 0.9 \times 10^6$, $F^+ = 1.13$ and $C_\mu = 0.0474$.

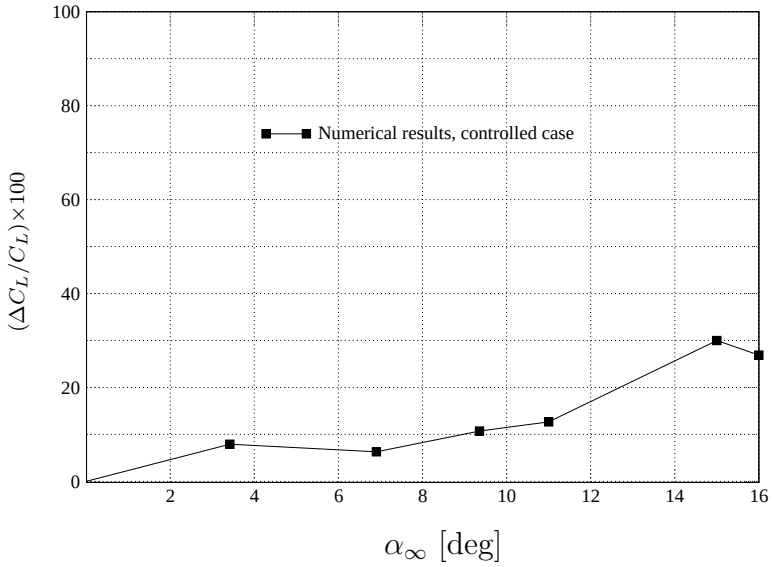

Fig. 56.: Increase in the lift coefficient with respect to the non-controlled experimental data of Harris [44]. NACA0012 airfoil, $M_\infty = 0.3$, $Re = 1 \times 10^6$, $F^+ = 1$ and $C_\mu = 0.004$.

1. Effect of the Angle of Injection

For this experiments, the angle of injection θ_{jet} was set to 2, 5 and 10 deg. The rest of parameters were kept constant and set as follows: frequency of oscillation, $f_{SJA} = 776.6$ Hz; oscillation amplitude, $V_{jet\ max} = 48.5$ m/s; injection location, $x_{te} = 0.1312$ m; slot width, $h = 0.165 \times 10^{-2}$ m. These parameters give $F^+ = 1$ and $C_\mu = 0.005$. The results of these numerical simulations are presented in Figure 57.

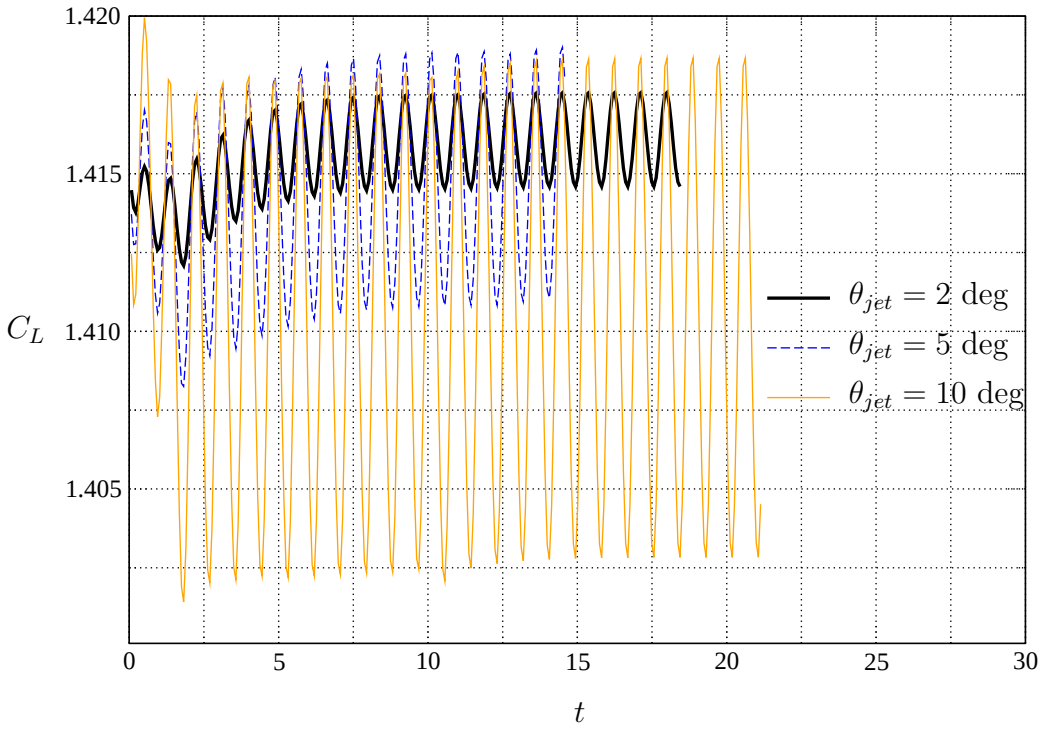

Fig. 57.: Influence of the variation of θ_{jet} on C_L. Simulations correspond to injection parameters $F^+ = 1$ and $C_\mu = 0.005$ on a NACA0015 airfoil, $M_\infty = 0.3$, $\alpha_\infty = 14$ deg and $Re = 1 \times 10^6$.

It can be observed in Figure 57 that the mean lift coefficients for $\theta_{jet} = 2$, $\theta_{jet} = 5$ and $\theta_{jet} = 10$ are 1.416, 1.414 and 1.410 respectively. Thus, $\theta_{jet} = 2$ is optimum

(although not a big difference is observed). For angles $\theta_{jet} > 2$ big (undesired) oscillations in the lift coefficient are observed and lower mean lift coefficients are obtained. A study on the flowfield generated by the oscillatory injection at these conditions and injection angles is presented in Section V.I.

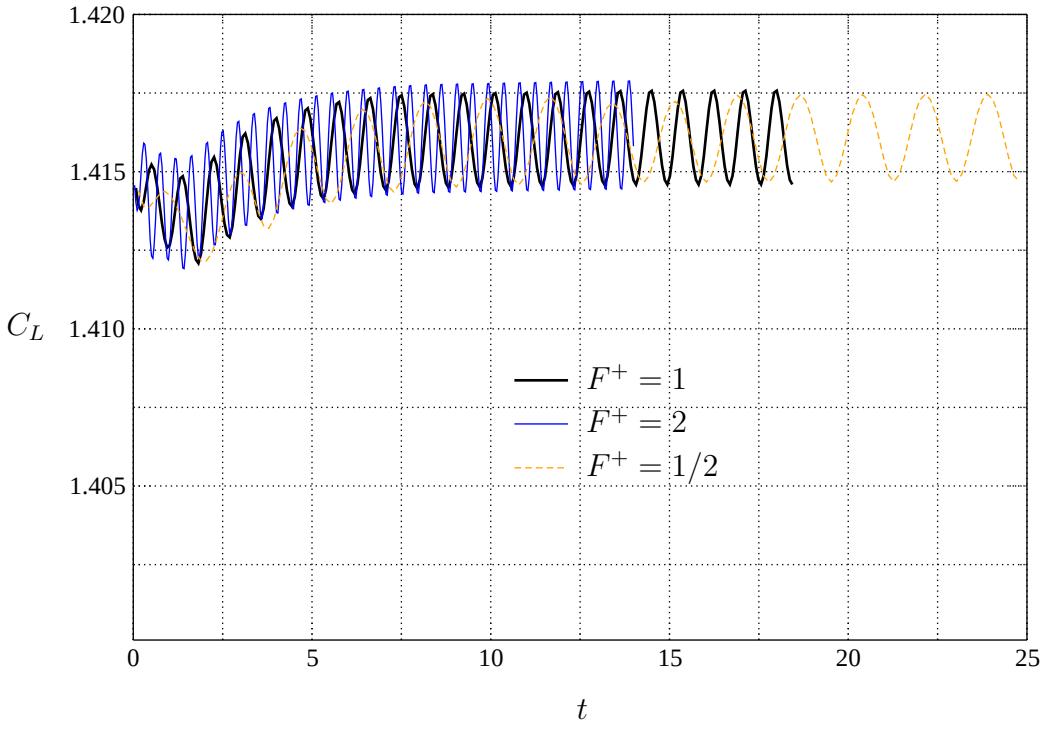

Fig. 58.: Influence of the variation of F^+ on C_L. Simulations correspond to injection parameters $\theta_{jet} = 2$ deg and $C_\mu = 0.005$ on a NACA0015 airfoil, $M_\infty = 0.3$, $\alpha_\infty = 14$ deg and $Re = 1 \times 10^6$.

2. Effect of the Non-Dimensional Frequency

In these simulations, the non-dimensional frequency F^+ was set to 1/2, 1 and 2. This was accomplished through the variation of the injection frequency f_{SJA} (see equation (5.1)) which was set to 388.33, 776.6 and 1553.312 Hz, respectively. The injection angle $\theta_{jet} = 2$ deg. The results of these numerical simulations are presented in Figure 58.

Figure 58 shows that for the three employed frequencies, the mean lift coefficients remain basically unchanged (1.41604, 1.41606 and 1.41615 for $F^+ = 1/2$, 1 and 2, respectively). This is probably so because the difference between the tested frequencies is not big enough. Orders of magnitude of difference may be required to see any noticeable effects. On the other hand, it is good that the frequency of the actuator of about 388 Hz ($F^+ = 1/2$) provides good results[4] since, as noted in Gilarranz experimental work [15], this number is ideal for rotary motor actuation.

3. Grid Converge Analysis

In order to observe how grid clustering at the injection site influences the solution, a series of simulations were performed where the number of nodes at the injection site was varied. Figure 59 shows how the grids look like at the injection site for the coarse, medium and fine grid.

[4]Similar to those of the generally accepted optimum frequency, $F^+ = 1$.

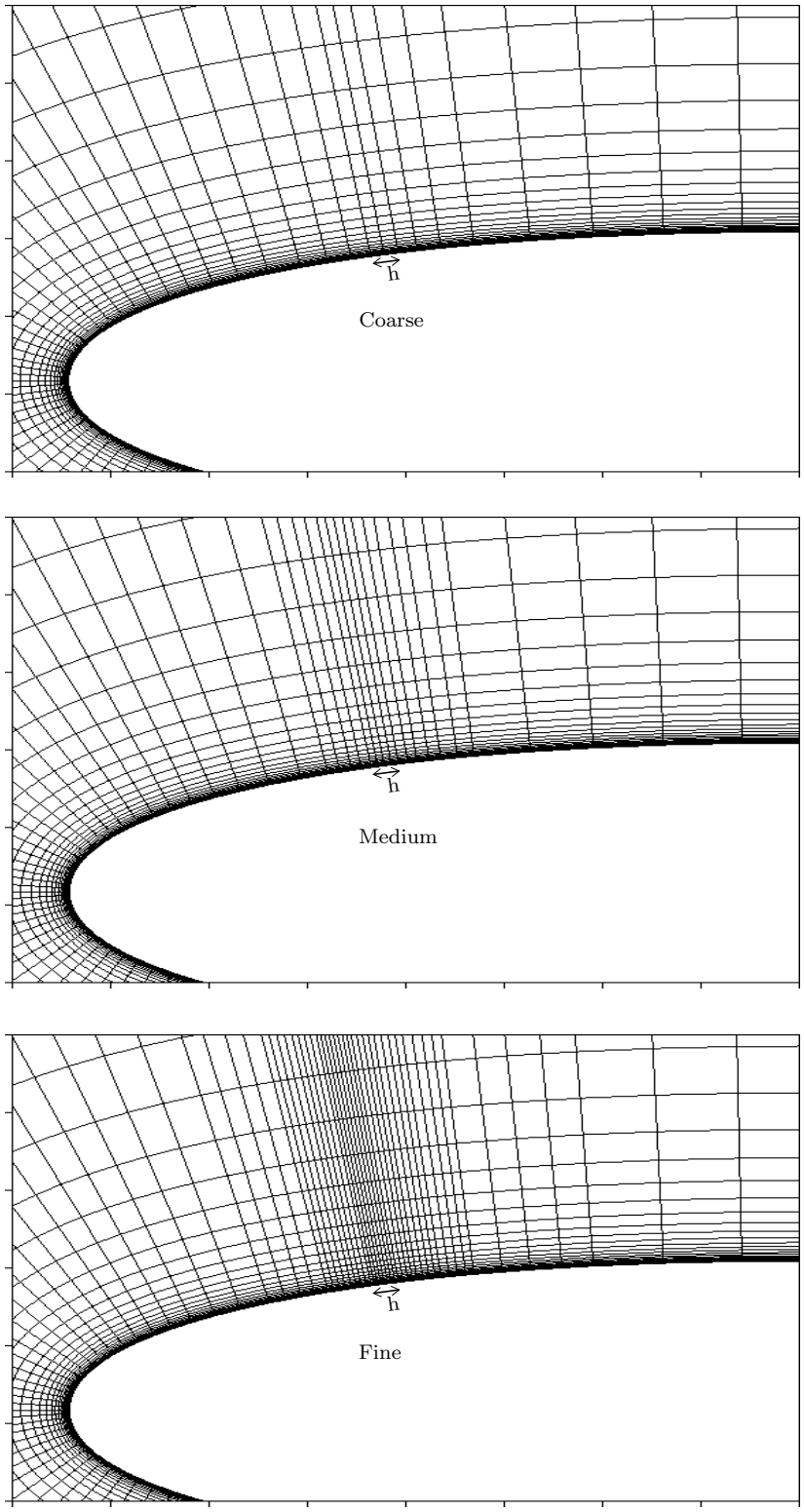

Fig. 59.: Grid clustering (at site of injection) for the NACA0015 airfoil.

Even though the clustering was achieved by halving the coarse grid in the injection region only, the number of nodes defining the entire airfoil for each case is employed as a the varying parameter. Thus the airfoil-defining node numbers employed in these experiments are 137, 151 and 187 nodes for coarse, medium and fine grids, respectively. Figure 60 shows how the *mean* lift coefficient, C_L, varies with the node number.

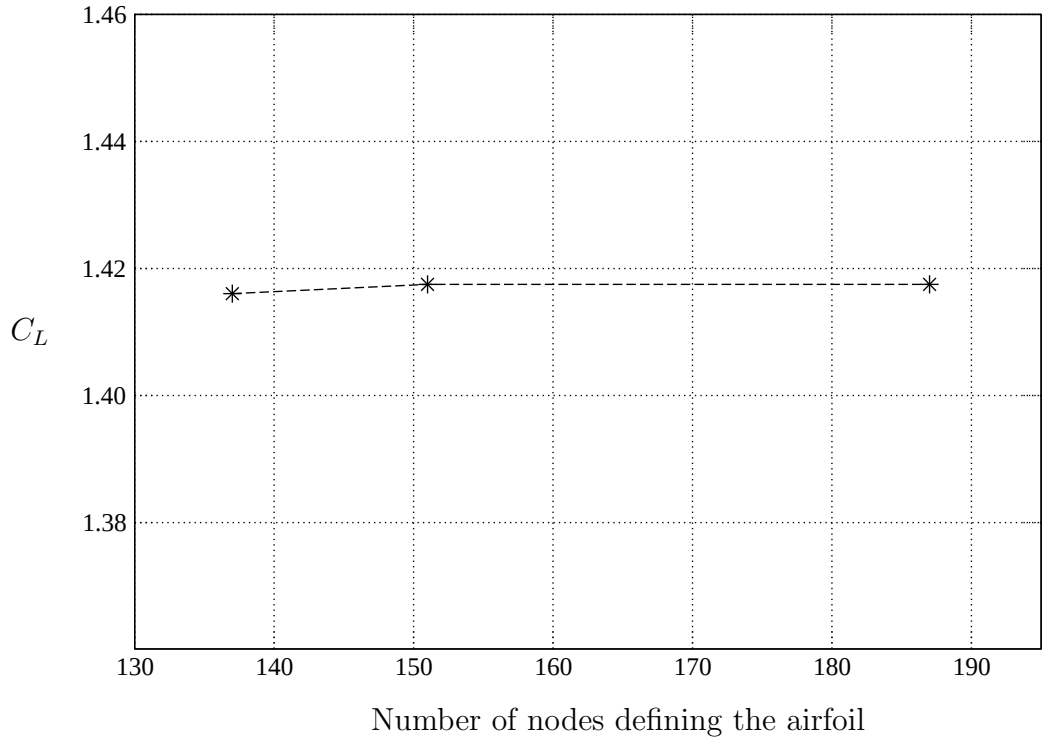

Fig. 60.: Effect of grid clustering on the lift coefficient. Simulations correspond to injection parameters $F^+ = 1$, $C_\mu = 0.005$ and $\theta_{jet} = 2$ deg on a NACA0015 airfoil, $M_\infty = 0.3$, $\alpha_\infty = 14$ deg and $Re = 1 \times 10^6$.

Figure 60 shows that the lift coefficient is practically independent of the number of nodes around the injection site. It is therefore concluded that the grid labeled as

"coarse" (see Figure 59) is appropriate for the the numerical experiments performed in this research. Note that the grids employed in the rest of simulations have a similar number of nodes as the coarse grid employed in this study.

I. Flowfield Survey

In order to understand the reason of the big variations in the instantaneous lift coefficient with variations of the angle of injection (see Section V.H.1) a flowfield survey is performed. Figure 61 shows a few computed streamlines on the full airfoil geometry.

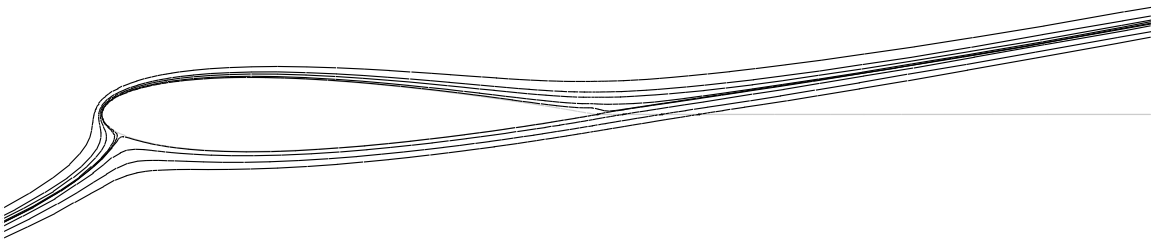

Fig. 61.: Sample of streamlines field around the full airfoil. Simulations correspond to injection parameters $F^+ = 1$, $C_\mu = 0.005$ and $\theta_{jet} = 2$ deg on a NACA0015 airfoil, $M_\infty = 0.3$, $\alpha_\infty = 14$ deg and $Re = 1 \times 10^6$.

In Figures 62 to 67 instantaneous streamlines are presented. The site of injection and the trailing edge region of the airfoil are zoomed-in and shown in windows with identical dimensions and at identical locations. The streamlines are generated at identical places for all injection cases and at (other) identical places for all trailing edge cases.

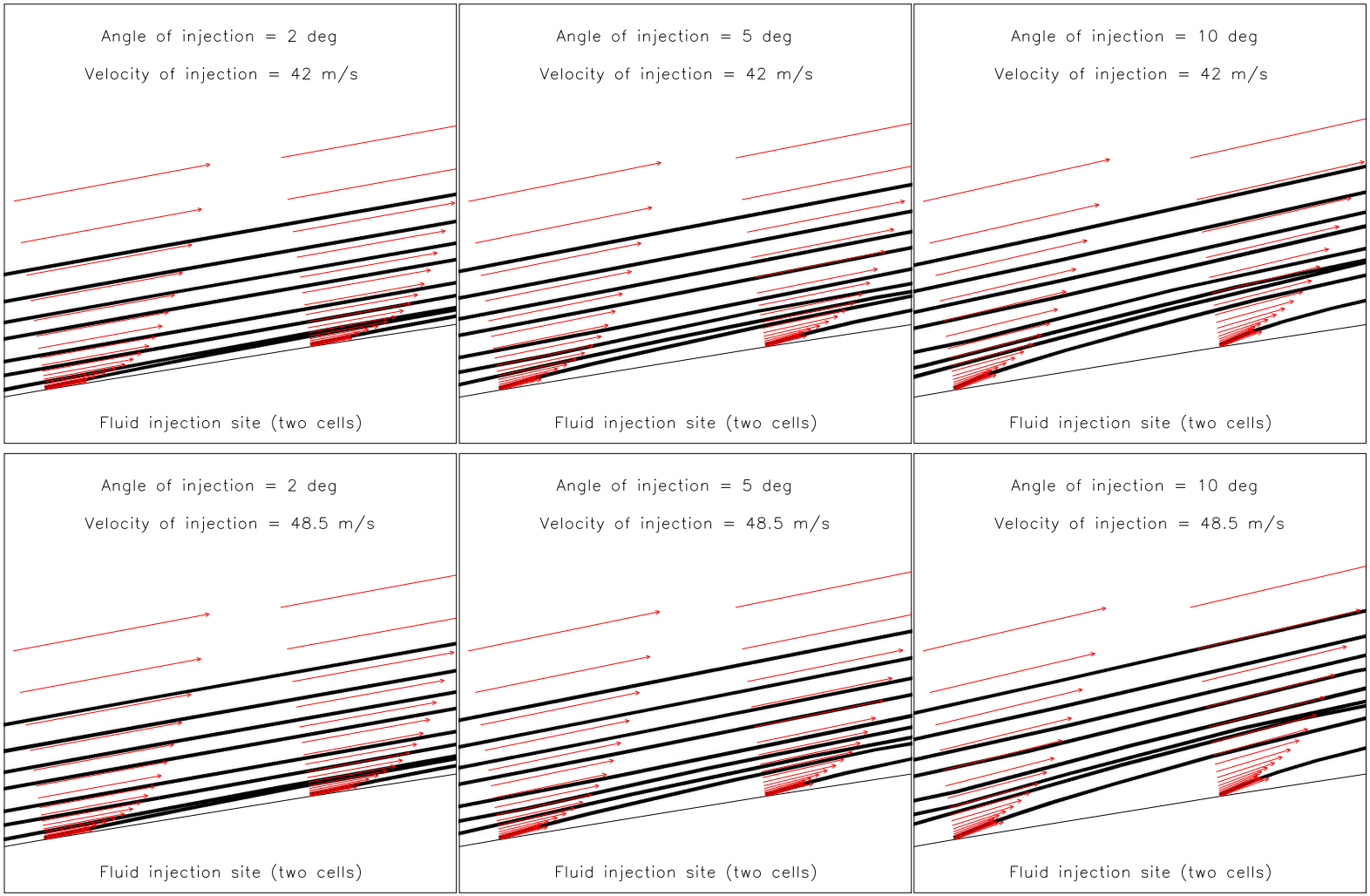

Fig. 62.: Streamlines at site of injection. $\theta_{jet} = 2, 5, 10$ deg and $v_{jet} = 42, 48.5$ m/s.

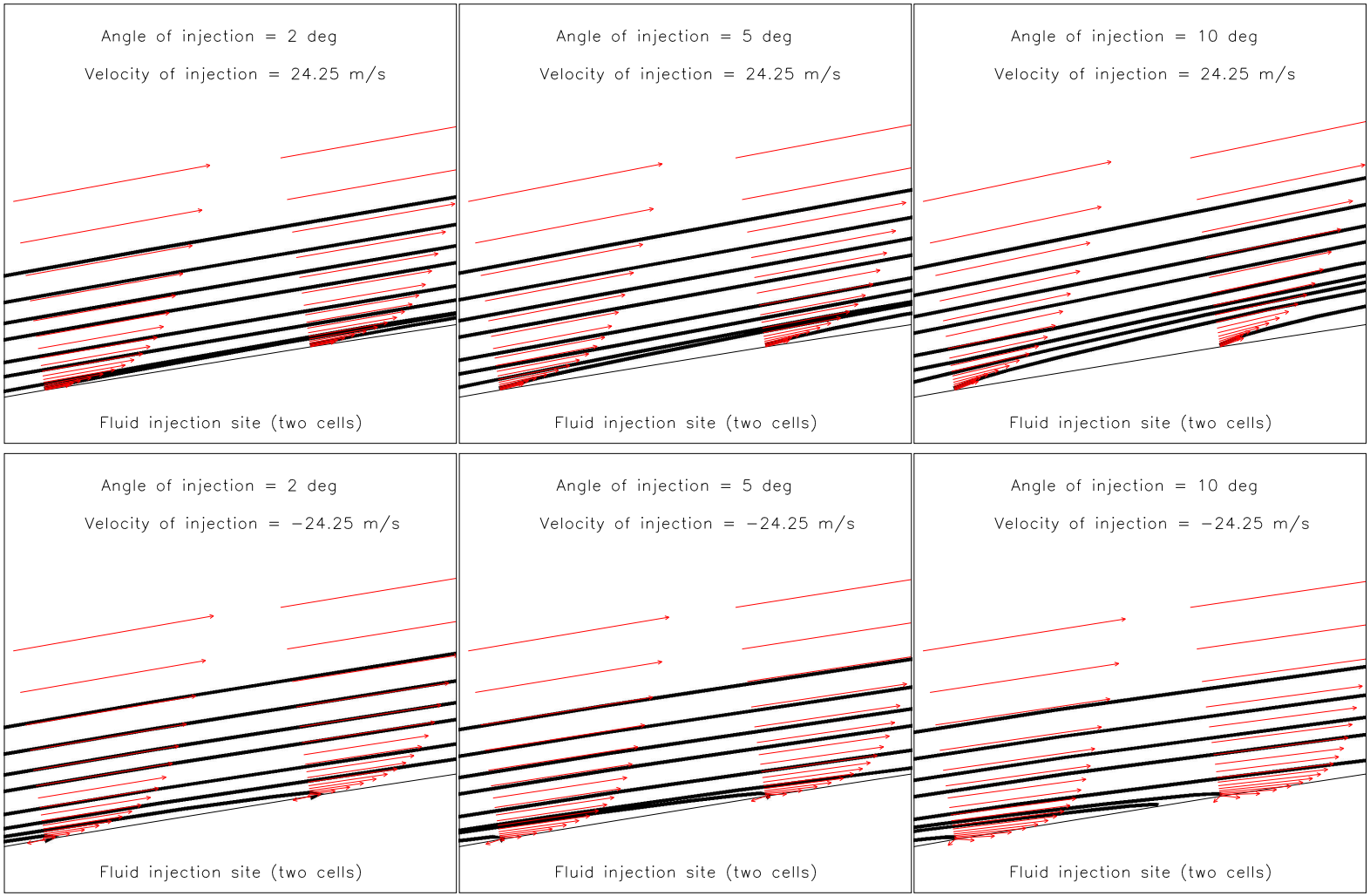

Fig. 63.: Streamlines at site of injection. $\theta_{jet} = 2, 5, 10$ deg and $v_{jet} = 24.25, -24.25$ m/s.

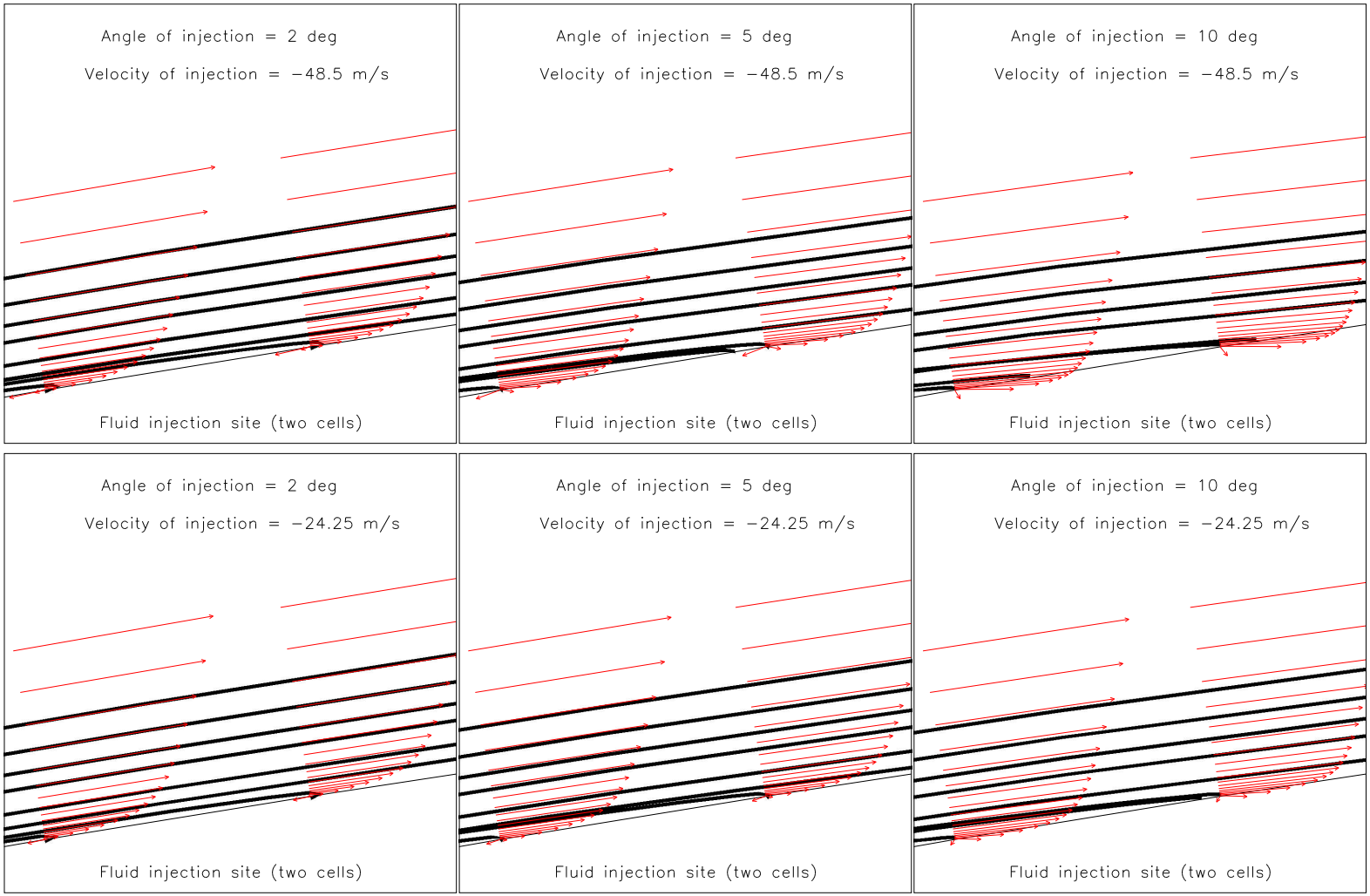

Fig. 64.: Streamlines at site of injection. $\theta_{jet} = 2, 5, 10$ deg and $v_{jet} = -48.5, -24.25$ m/s.

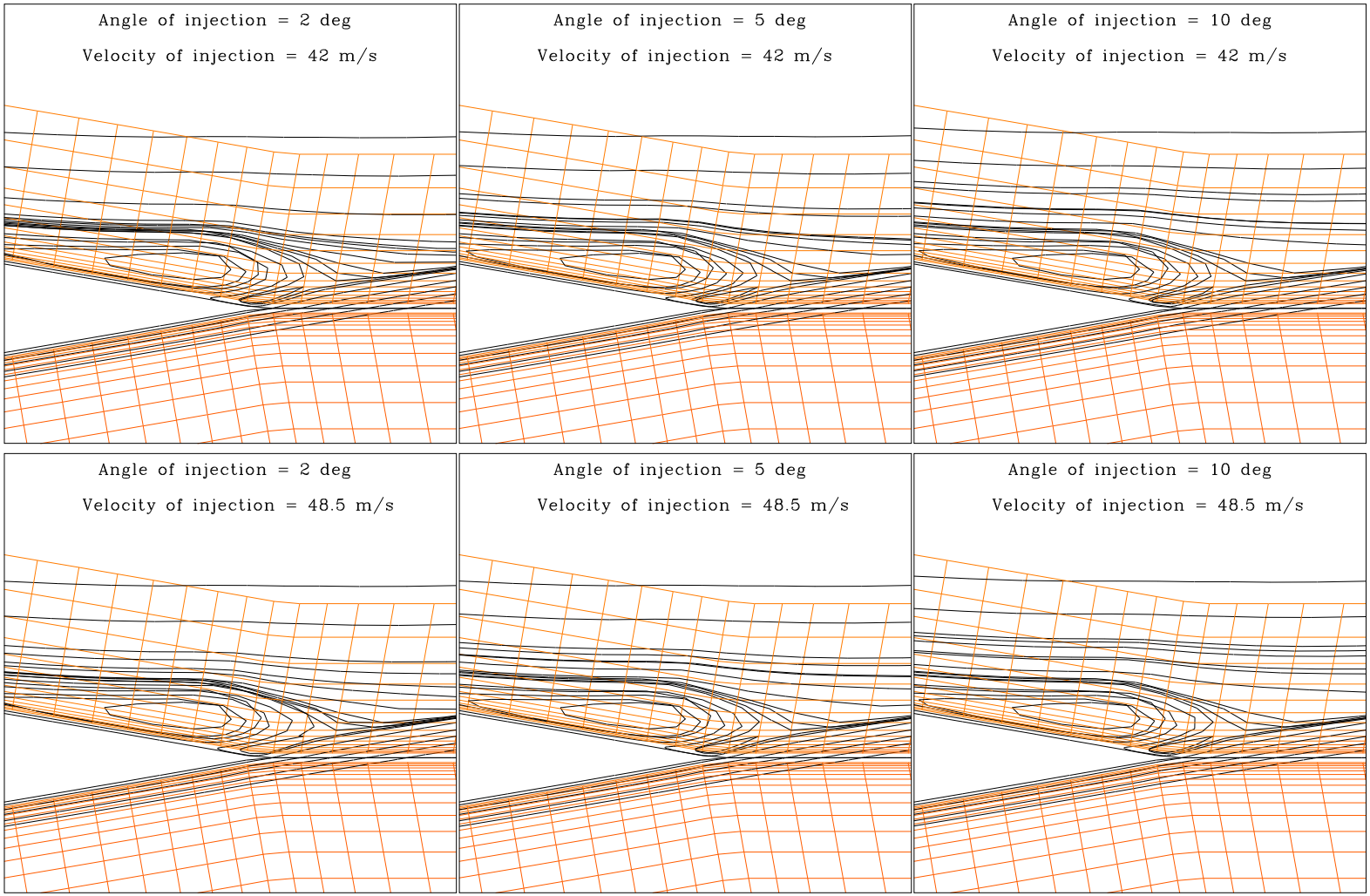

Fig. 65.: Streamlines at trailing edge region. $\theta_{jet} = 2, 5, 10$ deg and $v_{jet} = 42, 48.5$ m/s.

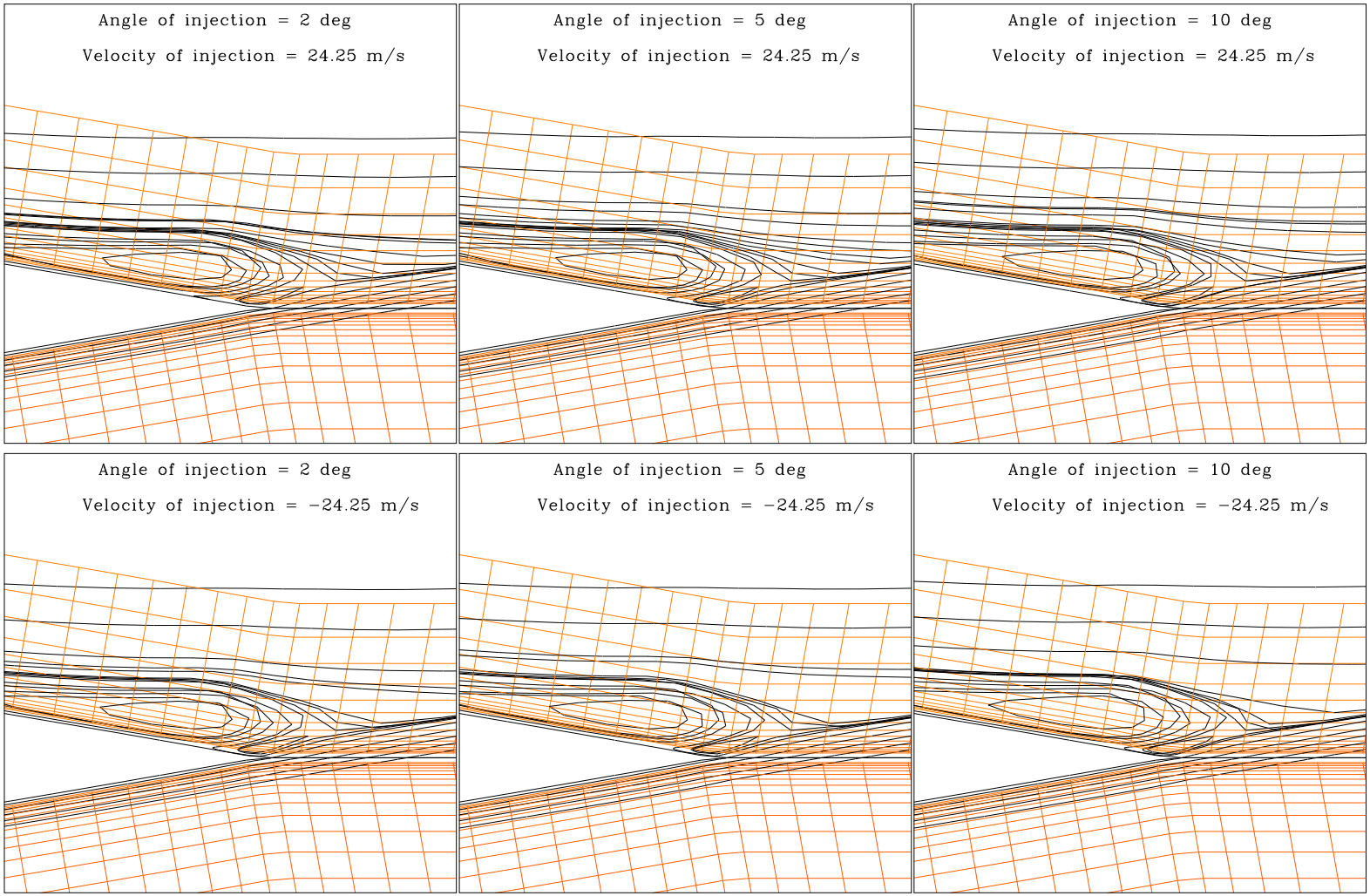

Fig. 66.: Streamlines at trailing edge region. $\theta_{jet} = 2, 5, 10$ deg and $v_{jet} = 24.25, -24.25$ m/s.

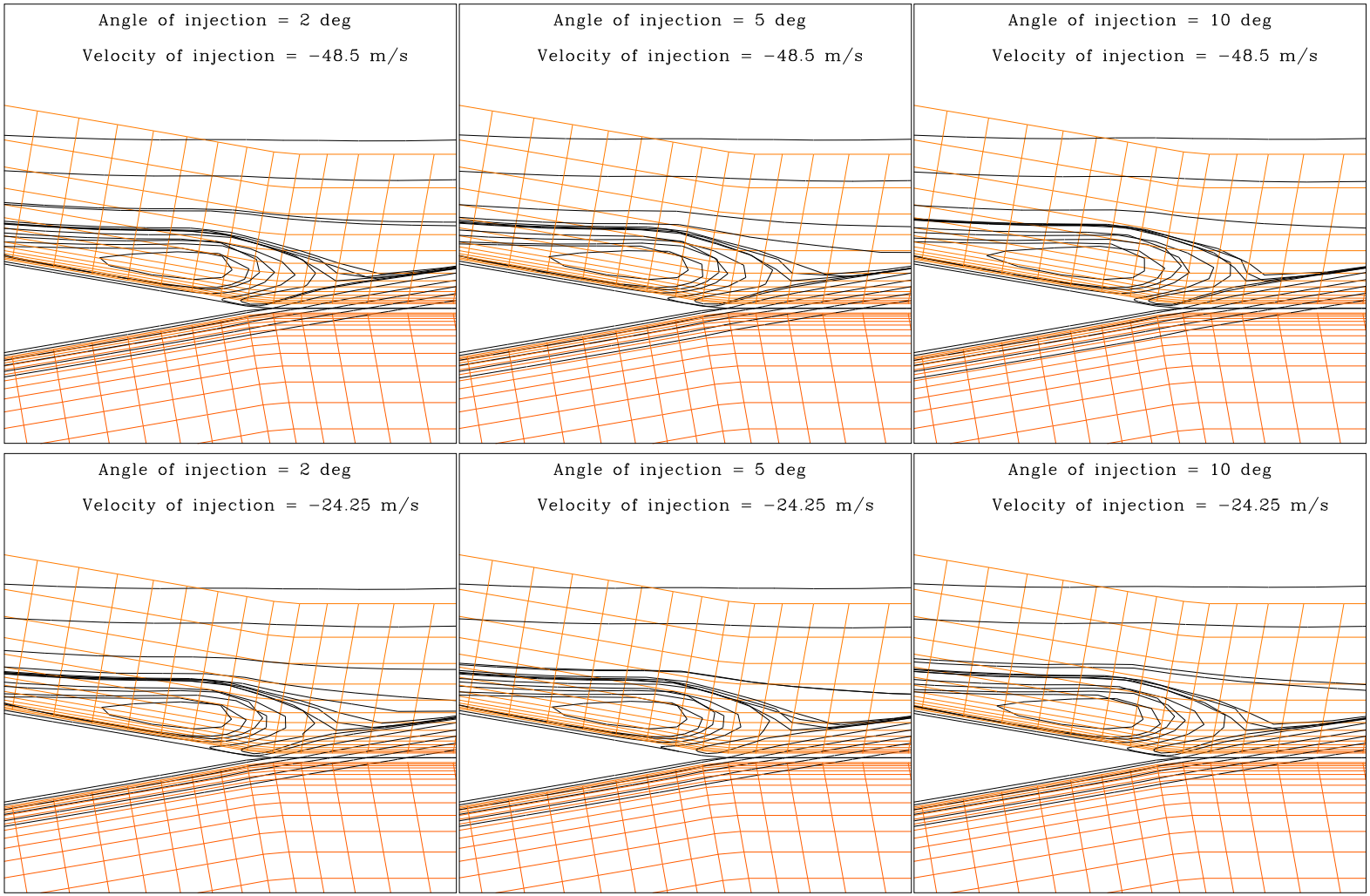

Fig. 67.: Streamlines at trailing edge region. $\theta_{jet} = 2, 5, 10$ deg and $v_{jet} = -48.5, -24.25$ m/s.

Six points of the lift coefficient histories were employed to make Figures 62 to 67. These points correspond approximately to 17%, 25%, 42%, 58%, 75% and 92% of one full velocity injection cycle as shown in Figure 68.

The velocities corresponding to these points are shown in the figures. The values of the lift coefficients for all these figures are summarized in Figure 68.

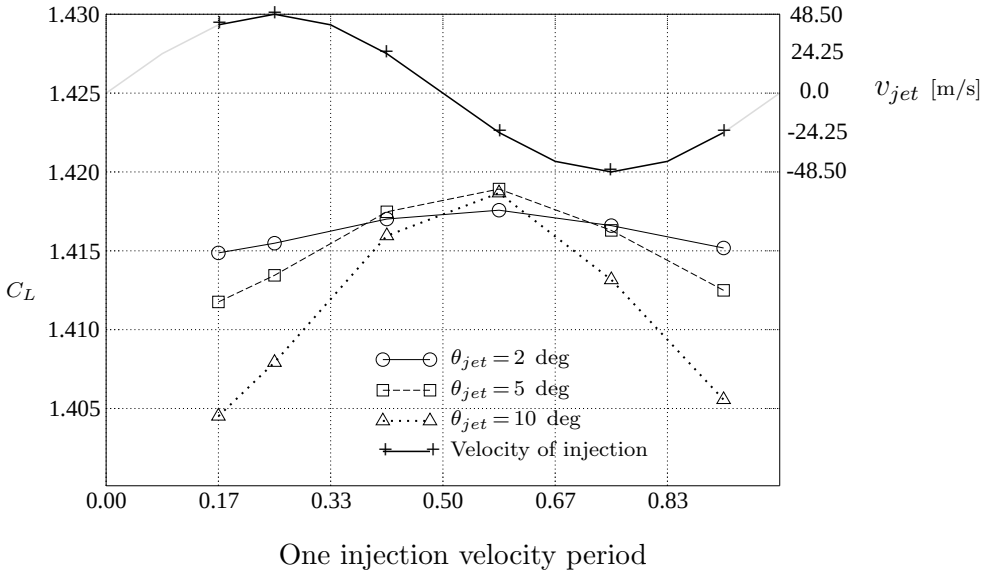

Fig. 68.: Instantaneous lift coefficients for different injection velocities and different injection angles (corresponding to Figures62 to 67).

Figures 62 to 64 clearly show the effect of blowing and suction. Strong separation is observed for angles $\theta_{jet} = 5$ and $\theta_{jet} = 10$ deg when blowing is taking place. On the other hand, the opposite is observed when suction is taking place. That is, suction brings the streamlines closer to the surface.

Regarding the figures corresponding to the trailing edge region (Figures 65 to 67), one can see that higher lift coefficients correspond, in general, to streamlines less

spread around the recirculation region in the trailing edge[5], while low lifts correspond to the opposite situation. One sees that, even though the C_L corresponding the simulation with $\theta_{jet} = 2$ deg does not attain the highest lift coefficient, it does not attain the lowest either (see Figure 68). This is why the mean C_L for $\theta_{jet} = 2$ deg is higher than those for higher angles.

Finally, it should be noted that a "lag" of the lift coefficient response with respect to the actuation is observed. One would expect that for a maximum suction ($v_{jet} = -48.5$ m/s in our simulation) there should correspond a maximum lift but this is not the case[6]. Figure 69 shows this situation. In this figure the velocity of injection has been scaled and translated such that it could be superimposed to the lift coefficient figure.

J. Summary

This chapter presents some fundamentals of flow separation. Techniques for flow separation control are discussed and focus is placed on synthetic jet actuation. The application of synthetic jets to flow separation is based in their ability to energize the boundary layer. The actuators add momentum to the boundary layer in the suction and blowing steps. Furthermore, the oscillatory nature of the device promotes the mixing of the low momentum fluid near the wall with the higher energy fluid close to the edge of the boundary layer. A discussion of the operation principle of the synthetic jet actuator is given.

Important parameters for synthetic jet actuation are introduced and optimum values $F^+ = 1$ and $C_\mu \geq 0.002$ are identified and employed. It is also demonstrated

[5]One has also to look how the streamlines look like at the injection site, the closer to the surface, the higher the lift.

[6]This behavior is observed only at the very beginning of the simulation

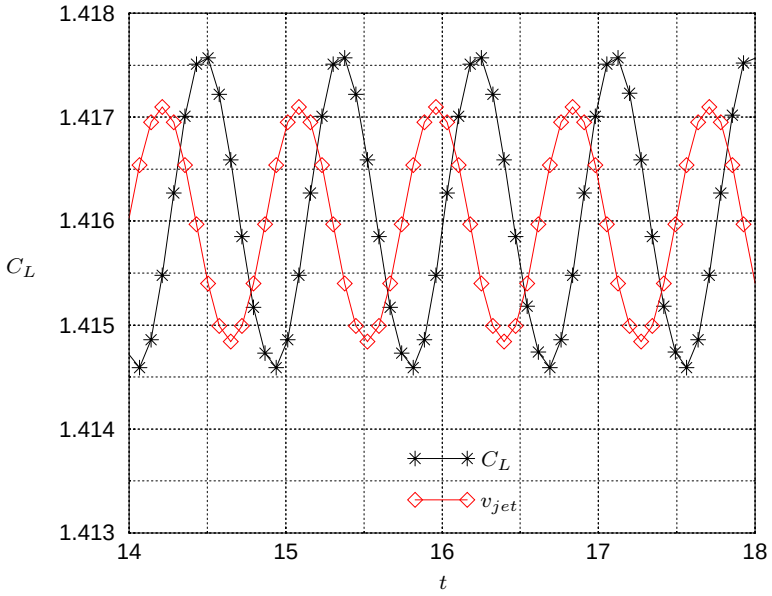

Fig. 69.: C_L and v_{jet} histories. Note: v_{jet} has been scaled and translated such that superposition was possible.

that the optimum direction for the oscillatory injection is tangentially to the airfoil's surface. Results of two numerical simulations on NACA0012 and NACA0015 airfoils are presented and discussed. Two different sets of injection parameters were employed. In both cases, oscillatory injection proved to be beneficial. Finally some future work suggestions and recommendations are given.

CHAPTER VI

CONCLUSIONS

In this work a numerical tool employed for the investigation of flow separation control has been developed and tested. The separation control technique studied is the synthetic jet actuation. The pulsating zero mass jet flow was simulated by imposing a harmonically varying transpiration boundary condition on the airfoil's surface.

The developed code employs a cell centered finite volume scheme which handles viscous, turbulent, steady and unsteady compressible fluid flow problems. The only speeding up technique implemented in this code is the variable time-stepping technique. To reduce the computational time, the pseudo-time stepping method [33] was implemented and this also employs the variable (pseudo) time-stepping technique.

It takes a significant CPU time to obtain converged results, specially if the flow is unsteady and slow. The turbulence model implemented in this code is the Baldwin-Lomax turbulence model [18]. This choice was made because of this model's simplicity, even when it is known that it overestimates the lift for separated flow [53] (as it is confirmed in the computations reported in this dissertation).

Other turbulence models, like the Sparlat and Allmaras [54] one-equation model, give somewhat better agreement with experiments, but the overall flow character with and without control has been found to be the same as that using using the Baldwin-Lomax turbulence model [16]. It is therefore concluded that the turbulence model employed in this dissertation is appropriate for attaining the goals of this work.

The code is validated for steady simulations over NACA0012 airfoils for which there is a large body of experimental data (see e.g. [44]). Good agreement with the experimental data is obtained for the pressure and lift coefficients as shown in Chapter IV. It is noted, though that a small over-prediction in the lift coefficient,

over the post-stall regime, is reported.

As mentioned above, to date, numerical methods for fluid flow simulations suffer the drawback of over-predicting the lift coefficient and in capturing the separation point and the angle of attack for which the maximum lift coefficient is obtained. This code, however, acceptably follows the experimental lift coefficient versus angle of attack plot for the steady run with respect to other, current numerical codes. Furthermore, for the cases with oscillatory fluid injection, the general trend over the post-stall regime is also acceptably captured. Therefore, the present research code reliably determines the benefits of flow separation control by oscillatory fluid injection.

The phenomenon investigated here was flow separation control by means of oscillatory fluid injection. The oscillatory blowing takes advantage of inherent local instabilities in the near wall shear layer that cause the selective amplification of the input oscillation frequency. These amplified disturbances convect downstream along the airfoil as coherent large structures that serve to mix the boundary layer flow and delay separation [50] [51] [1]. The efficiency of the mixing provides substantial increase in lift while concomitantly reducing drag. This has been corroborated experimentally [15] and now, in the present research, this is numerically corroborated as well.

The experimental results of Gilarranz [15] showed that a gain of up to 80% in lift coefficient increase can be obtained by employing what are generally accepted to be optimum injection parameters (i.e. $F^+ = 1$ and $C_\mu \geq 0.002$ %). The code developed in this research predicts a maximum gain in lift coefficient of up to 93%. The general trend is well captured despite the discrepancy which is attributed to the modeling of the injection boundary condition and to the turbulence model.

The second numerical simulation performed in this research was on a faster flow and a different set of injection parameters were tested. The injection location was very close to the leading edge of a NACA0012 airfoil and the momentum of the injection was smaller than the previous case. The numerical results showed this time a gain in lift increase of 30%. The difference with Gilarranz results stems on the different injection parameters, suggesting (or corroborating) that $F^+ = 1$, $C_\mu \geq 0.002$ and the employed injection location are optimum values for flow separation control.

Finally, and in view of the results obtained and presented in this research, it is concluded that a reliable numerical simulation tool has been developed for the study of the flow physics generated by the synthetic jet actuators. This tool can be employed as a support tool in the optimization of the actuator's operation and in the modeling of its operation.

A. Future Work and Recommendations

This research dealt with flow control separation in an open-loop manner, that is, no formal automatic control systems or philosophies were implemented. Actuation was accomplished through a variation of the actuator parameters and the resulting control was monitored, usually in an integral manner. It is beneficial that flow control separation employs feed-back control. The concept of feed-back control implies that some measurable quantity, e.g., wall pressure or wall shear stress, in the downstream location can serve to direct the attributes of the actuator so as to obtain a desired control objective downstream of the actuator. Feed-back control is feasible because the downstream sensors of the monitored quantity (e.g. wall pressure or shear stress) would provide the relevant information to the actuator prior to the actuator encountering a separated flow condition. Also, the downstream sensors can measure and

assess the level of control obtained due to actuation.

The speed of the code developed in this research could still be improved by implementing extra speeding up techniques such as residual smoothing and multigrid method (see e.g. [32] pp. 301-315). Furthermore, additional turbulence modeling schemes should be implemented such that a comparison of results using the different turbulence models can be performed.

REFERENCES

[1] D. Greenblatt, B. Nishiri, A. Dabari and I. Wygnanski, "Some factors affecting stall control with particular emphasis on dynamic stall," *AIAA Paper,* 99-3504, 1999.

[2] A. Seifert and L. G. Pack, "Oscillatory control of separation at high Reynolds numbers," *AIAA Paper,* AIAA 98-0214, 1998.

[3] J. L. Rao, G. J. Ko, T. Stragnac, O. K. Rediniotis, "Flow separation control via synthetic jet actuation," *AIAA Paper,* 2000-0407, Jan. 2000.

[4] G. V. Lachmann, *Boundary Layer and Flow Control. Its Principles and Application*, vol. 1 and 2. New York: Pergamon Press, 1961.

[5] D. Greenblatt and I. J. Wygnansky "The control of flow sepatation by periodic excitation," *Progress in Aerospace Sciences,* vol. 36, no. 7, 2000, pp. 487-545.

[6] M. Gad-el-Hak, *Flow Control: Passive, Active and Reactive Flow Managment.* New York: Cambridge University Press, 2000, pp. 150-188.

[7] D. C. McCormick, "Boundary layer separation control with directed synthetic jets," *AIAA Paper,* 2000-0519, 2000.

[8] I. Wygnansky, "Boundary layer and flow control by periodic addition of momentum," *AIAA Paper,* AIAA-97-2117, 1997.

[9] G. B. Schubauer, H. K. Skramstad "Laminar boundary layer oscillations and transition on a flat plate," *NACA Report* 909, 1948.

[10] F. G. Collins, J. Zelenevitz "Influence of sound upon separated flow over wings," *AIAA J,* vol. 13, no. 3, pp. 408-410, 1975.

[11] C. D. Winant and F. K. Browand, "Vortex pairing: the mechanism of turbulent mixing layer growth at moderate Reynolds number," *J Fluid Mech*, vol. 63, no. 2, pp. 237-256, 1974.

[12] Y. Katz, B. Nishiri, I. J. Wygnanski, "The delay of turbulent boundary layer separation by oscillatory active control," *AIAA Paper,* 89-0975, 1989.

[13] B. Nishiri, I. Wygnanski, "Effects of periodic excitation on turbulent separation from a flap," *AIAA J,* vol. 36, no. 4, pp. 547-556, 1998.

[14] L. S. Huang, L. Maestrello, T. D. Bryant, "Separation control over airfoils at high angles of attack by sound emanating from the surface," *AIAA Paper,* 87-1261, 1987.

[15] J. L. Gilarranz, "Development of high-power, compact synthetic jet actuators for flow separation control," Ph.D. dissertation, Texas A&M University, College Station, Texas, 2001.

[16] J. M. Wu, X. Y. Lu, A. G. Denny, M. Fan and J. Z. Wu, "Post-stall lift enhancement on an airfoil by local unsteady control part I. Lift, drag and pressure characteristics," *AIAA Paper,* 97-2063, 1997.

[17] J. M. Wu, X. Y. Lu and J. Z. Wu, "Post-stall lift enhancement on an airfoil by local unsteady control, part II. Mode competition and vortex dynamics" *AIAA Paper,* 97-2064, 1997.

[18] B. S. Baldwin and H. Lomax, "Thin layer approximation and algebraic model for separated turbulent flows," *AIAA Paper,* 78-257, 1978.

[19] A. A. Hassan and R. D. JanakiRam, "Effects of zero-mass synthetic jets on the aerodynamics of the NACA-0012 airfoil," *AIAA Paper,* 97-2326, 1997.

[20] J. F. Donovan, L. D. Kral and A. W. Cary, "Active control applied to an airfoil," *AIAA Paper,* 98-0210, 1998.

[21] R. Aris, *Vectors, Tensors and the Basic Equations of Fluid Mechanics.* New York: Dover Publ. Inc., 1989.

[22] H. Schlichting, *Boundary Layer Theory.* 7th edition, New York: McGraw-Hill, 1979.

[23] F. M. White, *Viscous Fluid Flow.* New York: McGraw-Hill, 1991.

[24] C. Hirsch, *Numerical Computation of Internal and External Flows*, vol. 1. 8th edition, New York: John Wiley & Sons, 2000.

[25] P. D. Lax, "Weak solutions of non-linear hyperbolic equations and their numerical computation," *Comm. Pure and Applied Mathematics,* vol. 7, pp. 159-9, 1954

[26] W. F. Ames, *Numerical Methods for Partial Differential Equations.* New York: Academic Press, Inc., 1977.

[27] E. Turkel, "Accuracy of schemes with nonuniform meshes for compressible fluid flows," *Applied Numerical Mathematics*, vol. 2, pp. 529–550, 1986.

[28] A. Jameson, W. Schmidt, D. GmbH, E. Turkel, "Numerical solutions of the Euler equations by finite volume methods using Runge-Kutta time-stepping schemes," *AIAA Paper,* 81-1259, 1981.

[29] J. Von Neumann, R. D. Ritchmeyer, "A method for the numerical computation of hydrodynamic shocks," *Journal of Applied Physics*, vol. 21, pp. 232-237, 1950.

[30] P. D. Lax, B. Wendroff, "Systems of conservation laws," *Communications in Pure and Applied Mathematics*, vol. 13, pp. 217-237, 1960.

[31] R. W. MacCormack, B. S. Baldwin, "A numerical method for solving the Navier-Stokes equations with application to shock-boundary layer interactions," *AIAA Paper,* 72-154, 1975.

[32] J. Blazek, *Computational Fluid Dynamics: Principles and Applications*, Oxford: Elsevier, 2001.

[33] A. Jameson, "Time dependent calculations using multigrid, with applications to unsteady flows past airfoils and wings," *AIAA Paper,* 91-1596, 1991.

[34] A. Arnone, M. S. Liou, L. A. Povinelli, "Multigrid time-accurate integration of Navier-Stokes equations," *AIAA Paper,* 93-3361, 1993.

[35] N. D. Melson, "Time-accurate Navier-Stokes calculations with multigrid acceleration," *in Proc. 6th Copper Mountain Conf. on Multigrid Methods,* 1993, pp. 423-439.

[36] T. Cebeci, "Calculation of compressible turbulent boundary layers with heat and mass transfer," *AIAA Paper,* 70-741, 1970.

[37] C. Hirsch, *Numerical Computation of Internal and External Flows*, vol. 2. 8th edition, New York: John Wiley & Sons, 2000.

[38] E. W. Swokowski, *Calculus with Analytic Geometry*, Alternate Edition, Boston: Prindle, Weber & Schmidt, 1983.

[39] D. L. Whitfield, J. M. Janus, "Three-dimensional unsteady Euler equations solution using flux vector splitting," *AIAA Paper,* 84-1552, 1984.

[40] H. O. Kreiss,, "Initial Boundary Value Problems for Hyperbolic Systems," *Comm. Pure Appl. Math.,* 23, pp. 277-298, 1970.

[41] R. D. Joslin, L. G. Horta and F. J. Chen, "Transitioning active flow control to applications," *AIAA Paper,* 99-3575, Jun. 1999.

[42] L. D. Landau, E. M. Lifschitz *Fluid Mechanics*, London: Pergamon, 1959.

[43] R. K. Agarwal, J. E. Deese, "Computation of transonic viscous airfoil, inlet and wing flowfields," *AIAA Paper,* 84-1551, 1984.

[44] C. D. Harris, "Two-dimensional aerodynamic characteristics of the NACA0012 airfoil in the Langley 8-foot transonic pressure tunnel." *NASA Technical Memorandum,* 81927, 1981.

[45] W. K. Anderson, J. L. Thomas and C. L. Rumsey, "Application of thin-layer Navier-Stokes equations near maximum lift," *AIAA Paper,* 84-0049, 1984.

[46] V. J. Modi, F. Mokhtarian, M. Fernando and T. Yokomizo, "Moving surface boundary layer control as applied to 2-D airfoils," *AIAA Paper,* AIAA-89-0296, 1989.

[47] K. McManus, A. Ducharme, C. Goldey and J. Magil, "Pulsed jet actuators for suppressing flow separation," *AIAA Paper,* AIAA-97-1971, 1997.

[48] K. McManus and J. Magil, "Airfoil performance enhancement using pulsed jet separation control," *AIAA Paper,* AIAA-97-1971, 1997.

[49] A. Seifert, A. Darabi and I. Wygnansky, "Delay of airfoil stall by periodic excitation," *Journal of Aircraft*, vol. 33, no. 4, pp. 691-698, July-August 1996.

[50] M. Hites, H. Nagib, T. Bachar and I. Wygnanski, "Enhanced performance of airfoils at moderate Mach numbers using zero-mass flux pulsed blowing," *AIAA Paper,* 2001-0734, 2001.

[51] J. A. Ekaterinaris, "Numerical investigations of dynamic stall active control for incompressible and compressible flows," *AIAA Paper*, AIAA-2000-4333, August, 2000.

[52] A. Seifert, V. Theofillis and R. D. Joslin, "Issues in active flow control: theory, simulation and experimentation," *AIAA Paper,* 2002-3277, June 2002.

[53] S. Ko and W. J. McCroskey, "Computations of unsteady separating flows over an oscillating airfoil," *AIAA Paper,* AIAA 95-0312, 1995.

[54] P. R. Sparlat and S. R. Allmaras, "A one equation turbulence model for aerodynamic flows," *AIAA Paper,* AIAA 92-0439, 1992.

VITA

Celerino Resendiz Rosas

Dom. Con., Lázaro Cárdenas, Zimapán Hgo., México. C.P. 42351.

Phone: (759) 727-4003

E-mail: celerino@parker.tamu.edu

EDUCATION:

M.S., Mechanical Engineering, Instituto Politecnico Nacional, (Mexico). August 1996.

B.S., Mechanical Engineering, Instituto Politecnico Nacional (Mexico). June 1993.